

NASA Contractor Report 4365

11733
~~11733~~

The Mechanisms of Dispersion Strengthening and Fracture in Al-Based XDTM Alloys

R. M. Aikin, Jr.

CONTRACT NAS1-18531
MAY 1991

(NASA-CR-4365) THE MECHANISMS OF DISPERSION
STRENGTHENING AND FRACTURE IN AL-BASED
XD(TM) ALLOYS, PART 1 Final Report (Martin
Marietta Labs.) 153 p

CSCL 11F

N91-24402

Unclass

H1/26 0011733

NASA

NASA Contractor Report 4365

The Mechanisms of Dispersion Strengthening and Fracture in Al-Based XDTM Alloys

R. M. Aikin, Jr.
Martin Marietta Corporation
Martin Marietta Laboratories
Baltimore, Maryland

Prepared for
Langley Research Center
under Contract NAS1-18531



National Aeronautics and
Space Administration
Office of Management
Scientific and Technical
Information Division

1991

ABSTRACT

The influence of reinforcement size, volume fraction, and matrix deformation behavior on room and elevated temperature strength; the fracture toughness; and the fatigue crack growth rate of metal matrix composites of Al-4%Cu-1.5%Mg with TiB₂ have been examined. The influence of reinforcement volume fraction has also been examined for pure aluminum with TiB₂. Higher TiB₂ volume fractions increased the tensile yield strength at both room and elevated temperatures, and reduced the elongation to fracture. Tensile tests also indicate that small particles provided a greater increase in strength for a given volume fraction than larger particles, whereas elongation to fracture appeared to be insensitive to reinforcement size. Interparticle spacing appears to be the factor that controls the strength of these alloys, with the exact nature of the dependence relying on the nature of dislocation slip in the matrix (planar versus diffuse).

The isothermal aging response of the precipitation strengthened Al-4%Cu-1.5%Mg alloys was not accelerated by the presence of TiB₂. Cold work prior to artificial aging created additional geometrically necessary dislocations which served as heterogeneous nucleation sites leading to accelerated aging, a finer precipitate size, and an increase in the strength of the alloy.

The fracture toughness of the Al-4%Cu-1.5%Mg alloys decreased with TiB₂ additions of 0 to 5 vol% and were nearly constant for additions of 10 to 15 vol%. Fatigue crack growth rates were accelerated by the additional TiB₂ loading. For the same TiB₂ loading smaller particles result in a higher fatigue crack growth rate.

FOREWORD

This document is the final report for the program "The Mechanisms of Dispersion Strengthening and Fracture in Al-Based XDTM Alloys." The work was sponsored by the National Aeronautics and Space Administration, Langley Research Center, under contract number NAS1-18531; W.D. Brewer contract monitor. The period of performance of this contract was from June 24, 1987 to September 24, 1990.

The author wishes to thank R.N. Bennett, W.M. Buchta, and P.E. McCubbin for fabricating the alloys, and P. Estep for help with the initial mechanical testing. Special thanks are extended to N.C. Beck Tan for performing the heat treatment and mechanical testing of the age-hardenable alloys. The author also acknowledges the useful discussions with L. Christodoulou and S.L. Kampe on aspects of the deformation behavior of these alloys.

TABLE OF CONTENTS

ABSTRACT.....	iii
FOREWORD.....	v
TABLE OF CONTENTS.....	vii
LIST OF FIGURES.....	ix
LIST OF TABLES.....	xiv
1. INTRODUCTION.....	1
1.1 Program Goals.....	1
1.2 The XD™ Process.....	2
2. XD™ ALUMINUM-TiB ₂ SYSTEM.....	3
2.1 Particle Size.....	3
2.2 Stability of TiB ₂ in Aluminum.....	7
3. TiB ₂ IN PURE ALUMINUM.....	8
3.1 Materials.....	8
3.1.1 Processing.....	8
3.1.2 Microstructure.....	8
3.2 Tensile Properties.....	13
3.3 Elevated-Temperature Tensile Properties.....	23
4. TiB ₂ IN Al-4%Cu-1.5%Mg.....	27
4.1 Materials.....	27
4.1.1 Processing.....	27
4.1.2 As-Cast Microstructure: Particle Pushing.....	27
4.1.3 Extruded Microstructure.....	30
4.2 Elastic Modulus.....	41
5. DISLOCATION GENERATION DUE TO CTE MISMATCH.....	45
5.1 Dislocation Punching Models.....	45
5.1.1 Dislocation Nucleation Model.....	45
5.1.2 Continuum Models.....	48
5.2 Experimental Evidence of Dislocation Punching in MMCs.....	49
5.3 Dislocation Punching in Al-4%Cu-1.5%Mg+TiB ₂	50
6. AGING RESPONSE OF TiB ₂ REINFORCED Al-4%Cu-1.5%Mg.....	55
6.1 Precipitation in Al-Cu-Mg Alloys.....	55
6.2 Aging in Aluminum Based MMCs.....	61
6.3 Isothermal Aging Response of Al-4%Cu-1.5%Mg+TiB ₂	63

6.3.1	Aging Response at 190°C.....	63
6.3.2	The Effect of Aging Temperature.....	71
6.4	Aging of Al-4%Cu-1.5%Mg+TiB ₂ Following Cold Work	76
6.4.1	Geometrically Necessary Dislocations	76
6.4.2	Amount of Cold Work	77
6.4.3	Aging Kinetics	80
6.4.4	Microstructure.....	85
7.	STRENGTHENING MECHANISMS IN METAL MATRIX COMPOSITES	96
7.1	Review of Possible Strengthening Mechanisms at Low Temperatures	96
7.1.1	Continuum Models	96
7.1.2	Single Dislocation-Particle Interaction Model	97
7.1.3	Multiple Dislocation-Particle Interaction Models: Dislocation Pile-Up Models	97
7.1.4	Multiple Dislocation-Particle Interaction Models: Forest Hardening Models	98
7.2	Role of Particle Size and Volume Fraction	99
7.2.1	Al + TiB ₂	99
7.2.2	Al-4%Cu-1.5%Mg + TiB ₂ : Planar Slip	102
7.2.3	Al-4%Cu-1.5%Mg + TiB ₂ : Wavy Slip.....	107
7.2.4	Al-4.5%Cu-1.5%Mg-0.6%Mn + Al ₂ O ₃	107
7.3	Elevated Temperature Properties.....	113
8.	FRACTURE TOUGHNESS	118
8.1	Measurement of Fracture Toughness and K _{IC}	118
8.2	Isothermal-Aging Response.....	120
8.3	Effect of Loading and Particle Size.....	120
9.	FATIGUE.....	123
10.	SUMMARY.....	132
11.	REFERENCES.....	135

LIST OF FIGURES

Figure 2.2	Particle size distributions.....	5
Figure 2.3	Normalized particle size distributions.	6
Figure 3.1	Optical micrographs of pure aluminum with TiB ₂	9
Figure 3.2	Optical micrographs taken with cross-polarized light to show the grain size of the forged and annealed pure aluminum alloys with TiB ₂	12
Figure 3.3	Variation of grain size with volume percent TiB ₂ for forged and annealed aluminum.	14
Figure 3.4	TEM micrographs of annealed pure aluminum with 5 vol% TiB ₂	15
Figure 3.5	Dependence of yield stress on strain rate for the forged and annealed pure aluminum with 0.5-15 vol%, 0.3 μ m TiB ₂	16
Figure 3.6	Tensile properties as a function of volume percent of 0.3 μ m TiB ₂ for forged and annealed pure aluminum.	17
Figure 3.7	Fracture surface of sample of aluminum reinforced with TiB ₂ , pulled in tension at room temperature.	20
Figure 3.8	True stress versus true strain of pure aluminum with 0.3 μ m TiB ₂ pulled in tension at room temperature.	21
Figure 3.9	Strain hardening rate of pure aluminum with 0.3 μ m TiB ₂ pulled in tension at room temperature.	22
Figure 3.10	TEM micrographs taken from gauge section of aluminum reinforced with TiB ₂ , pulled in tension at room temperature.	24
Figure 3.11	Tensile properties as a function of test temperature for forged and annealed pure aluminum with various loadings of 0.3 μ m TiB ₂	25
Figure 4.1	Optical micrographs of the as-cast microstructure of Al-4%Cu-1.5%Mg alloys with 10 vol% TiB ₂ of the two particle sizes (Keller's etch).	29
Figure 4.2	Orthogonal views of the extruded microstructure of Al-4%Cu-1.5%Mg alloys with 10 vol% TiB ₂ of the two particle sizes.	31
Figure 4.3	Optical micrograph of the long transverse direction of the extruded Al-4%Cu-1.5%Mg alloy in the T4 condition (Keller's etch).	33
Figure 4.4	Optical micrograph of the long transverse direction of the extruded Al-4%Cu-1.5%Mg alloys with 0.3 μ m TiB ₂ in the T4 condition (Keller's etch).	34
Figure 4.5	Optical micrograph of the long transverse direction of the extruded Al-4%Cu-1.5%Mg alloys with 1.3 μ m TiB ₂ in the T4 condition (Keller's etch).	36
Figure 4.6	EDS spectra of dark-colored round Al ₂ CuMg particle shown in Fig. 4.3.	38
Figure 4.7	EDS spectra of light-colored rectangular Al ₇ Cu ₂ Fe particle shown in Fig. 4.3.	39

Figure 4.8	Variation of grain size with volume percent TiB_2 for Al-4%Cu-1.5%Mg alloys in naturally aged (T4) condition.....	40
Figure 4.9	Dependence of Young's modulus on volume fraction for two different TiB_2 sizes in the Al-4%Cu-1.5%Mg alloys	43
Figure 5.1	Critical misfit as a function of particle diameter after Ashby and Johnson [14]. Experimental data [12,15-17].	47
Figure 5.2	TEM micrographs showing dislocations in unreinforced Al-4%Cu-1.5%Mg alloy in solutionized, quenched, and naturally aged (T4) condition.	51
Figure 5.3	TEM micrographs showing dislocations near a 0.4 μm diameter TiB_2 particle in Al-4%Cu-1.5%Mg+2vol% TiB_2 . Alloy is in solutionized, quenched, and naturally aged (T4) condition.....	52
Figure 5.4	TEM micrographs showing dislocations near a 0.8 μm diameter TiB_2 particle in Al-4%Cu-1.5%Mg+2vol% TiB_2 . Alloy is in solutionized, quenched, and naturally aged (T4) condition.....	53
Figure 6.1	Limits of solid solubility in Al rich corner of Al-Cu-Mg ternary phase diagram. (Adapted from [10-12]).....	56
Figure 6.2	Electron diffraction pattern of S' with Al matrix at $[001]_\alpha$ zone axis. The small circles are primary reflections while the crosses are due to double diffraction. The variants contributing to the reflections A, B, C, and D are listed (after Gupta, Gaunt, and Chaturvedi [46]).....	59
Figure 6.3	Stereographic projection for a fcc crystal. The lines represent the various $\{120\}$ traces. Various $\langle 100 \rangle$, $\langle 110 \rangle$ and $\langle 120 \rangle$ directions are also shown.	60
Figure 6.4	Arrangement of a group of S' precipitates on (120) and (210) habit planes to yield an apparent (110) habit.	60
Figure 6.5	Variation of matrix microhardness for 2124 with and without SiC whiskers as a function of aging time for alloys solutionized, quenched, and artificially aged at 177°C. Microhardness indents were made with a 5 g load in whisker free regions. Data from Christman and Suresh [29].	62
Figure 6.6	Variation of tensile properties with time of aging at 190°C for the Al-4%Cu-1.5%Mg with and without Mn.....	64
Figure 6.7	Variation of tensile properties with time of aging at 190°C for the Al-4%Cu-1.5%Mg alloys containing 0.3 μm TiB_2 particles.....	67
Figure 6.8	Variation of tensile properties with time of aging at 190°C for the Al-4%Cu-1.5%Mg alloys containing 1.3 μm TiB_2 particles.....	69
Figure 6.9	Variation of yield stress with time of aging at 177°C for the Al-4%Cu-1.5%Mg alloys containing 0.3 μm TiB_2 particles.	72
Figure 6.10	Variation of yield stress with time of aging at 177°C for the Al-4%Cu-1.5%Mg alloys containing 1.3 μm TiB_2 particles.	72
Figure 6.11	Variation of yield stress with time of aging at 204°C for the Al-4%Cu-1.5%Mg alloys containing 0.3 μm TiB_2 particles.	73
Figure 6.12	Variation of yield stress with time of aging at 204°C for the Al-4%Cu-1.5%Mg alloys containing 1.3 μm TiB_2 particles.	73

Figure 6.13	Variation of tensile properties at peak-aged condition for the Al-4%Cu-1.5%Mg alloys containing 0.3 μm TiB_2 particles as a function of aging temperature.	74
Figure 6.14	Variation of tensile properties at peak-aged condition for the Al-4%Cu-1.5%Mg alloys containing 1.3 μm TiB_2 particles as a function of aging temperature.	75
Figure 6.15	Variation of T3 tensile properties with the amount of cold work prior to natural aging for the Al-4%Cu-1.5%Mg alloys.	78
Figure 6.16	Yield stress as a function of the inverse of the square root of the geometric slip distance for Al-4%Cu-1.5%Mg alloys stretched 2% prior to natural aging.	79
Figure 6.17	Variation of tensile properties with time of artificial aging at 190°C for the Al-4%Cu-1.5%Mg alloys with and without cold work prior to aging.	81
Figure 6.18	Variation of tensile properties with time of artificial aging at 190°C for the Al-4%Cu-1.5%Mg alloys containing 0.3 μm TiB_2 following 2% cold work.	82
Figure 6.19	Variation of tensile properties with time of artificial aging at 190°C for the Al-4%Cu-1.5%Mg alloys containing 1.3 μm TiB_2 following 2% cold work.	83
Figure 6.20	Variation of yield stress with time of artificial aging at 190°C for the Al-4%Cu-1.5%Mg alloys following 2% cold work.	84
Figure 6.21	Unreinforced Al-4%Cu-1.5%Mg following 2% cold work and naturally aging. Bright field image at $[001]_\alpha$ zone axis.	86
Figure 6.22	Unreinforced Al-4%Cu-1.5%Mg following 2% cold work and artificially aged at 190°C for 5 hours.	87
Figure 6.23	Unreinforced Al-4%Cu-1.5%Mg following 2% cold work and artificially aged at 190°C for 5 hours. Bright field image at $[001]_\alpha$ zone axis.	88
Figure 6.24	Al-4%Cu-1.5%Mg plus 10 vol% of 0.3 μm TiB_2 following 2% cold work and naturally aging. Bright field image at $[110]_\alpha$ zone axis.	89
Figure 6.25	Al-4%Cu-1.5%Mg plus 10 vol% of 0.3 μm TiB_2 following 2% cold work and naturally aging. Bright field image at $[001]_\alpha$ zone axis.	89
Figure 6.26	Al-4%Cu-1.5%Mg plus 10 vol% of 0.3 μm TiB_2 following 2% cold work and artificially aged at 190°C for 5 hours.	90
Figure 6.27	Al-4%Cu-1.5%Mg plus 10 vol% of 0.3 μm TiB_2 following 2% cold work and artificially aged at 190°C for 5 hours. Bright field image.	92
Figure 6.28	Al-4%Cu-1.5%Mg plus 10 vol% of 0.3 μm TiB_2 following 2% cold work and artificially aged at 190°C for 5 hours. Bright field image at $[001]_\alpha$ zone axis.	92
Figure 6.29	Al-4%Cu-1.5%Mg plus 10 vol% of 1.3 μm TiB_2 following 2% cold work and naturally aging. Bright field image at $[110]_\alpha$ zone axis.	93
Figure 6.30	Al-4%Cu-1.5%Mg plus 10 vol% of 1.3 μm TiB_2 following 2% cold work and natural aging.	94

Figure 6.31	Al-4%Cu-1.5%Mg plus 10 vol% of 1.3 μm TiB_2 following 2% cold work and artificially aged at 190°C for 5 hours.	95
Figure 7.1	Yield stress and proportional limit versus particle loading for pure aluminum alloy with TiB_2	100
Figure 7.2	Yield stress versus the inverse square-root of grain size for pure aluminum alloy with TiB_2	100
Figure 7.3	Yield stress as a function of the interparticle separation for pure aluminum alloy with TiB_2	101
Figure 7.4	Variation of yield stress with volume percent of TiB_2 for Al-4%Cu-1.5%Mg alloys in naturally aged (T4) condition.	103
Figure 7.5	Variation of yield stress and proportional limit with volume percent for Al-4%Cu-1.5%Mg alloys in naturally aged (T4) condition.	104
Figure 7.6	Yield stress versus the inverse square-root of grain size for Al-4%Cu-1.5%Mg alloys in naturally aged (T4) condition.	105
Figure 7.7	Yield stress as a function of the interparticle separation for Al-4%Cu-1.5%Mg alloys in naturally aged (T4) condition.	106
Figure 7.8	Variation of yield stress with volume percent of TiB_2 for Al-4%Cu-1.5%Mg alloys in peak-aged (T6) condition.	108
Figure 7.9	Variation of yield stress and proportional limit with volume percent for Al-4%Cu-1.5%Mg alloys in peak-aged (T6) condition.	109
Figure 7.10	Yield stress versus the inverse square-root of grain size for Al-4%Cu-1.5%Mg alloys in artificially aged (T6) condition.	110
Figure 7.11	Yield stress as a function of the interparticle separation for Al-4%Cu-1.5%Mg alloys in artificially aged (T6) condition.	111
Figure 7.12	Yield stress as a function of the interparticle separation for 2024 in O temper condition. Data of Kamat, Hirth, and Mehrabian [75].	112
Figure 7.13	Elevated temperature properties of Al-4%Cu-1.5%Mg with various loadings of 0.3 μm TiB_2 tested at a strain rate of $1.3 \times 10^{-3} \text{ s}^{-1}$ after a half-hour exposure at temperature.	114
Figure 7.14	Elevated temperature properties of Al-4%Cu-1.5%Mg with various loadings of 0.3 μm TiB_2 tested at a strain rate of $1.3 \times 10^{-3} \text{ s}^{-1}$ after a half-hour exposure at temperature.	116
Figure 8.1	Schematic of load-displacement curve and construction of an ideally elastic material with an equivalent energy used to determine P_e	119
Figure 8.2	Equivalent energy fracture toughness vs aging time at 190°C for the Al-4%Cu-1.5%Mg alloys containing 0.3 μm TiB_2 particles.	121
Figure 8.3	Equivalent energy fracture toughness vs aging time at 190°C for the Al-4%Cu-1.5%Mg alloys containing 1.3 μm TiB_2 particles.	121
Figure 8.4	Equivalent energy fracture toughness vs TiB_2 particle loading for the Al-4%Cu-1.5%Mg materials.	122
Figure 9.1	Fatigue crack growth rate of Al-4%Cu-1.5%Mg with 0.3 μm TiB_2	124
Figure 9.2	Fatigue crack growth rate of Al-4%Cu-1.5%Mg with 1.3 μm TiB_2	125
Figure 9.3	Fatigue crack growth rate of Al-4%Cu-1.5%Mg with 2 vol% TiB_2	126

Figure 9.4	Fatigue crack growth rate of Al-4%Cu-1.5%Mg with 5 vol% TiB ₂	127
Figure 9.5	Fatigue crack growth rate of Al-4%Cu-1.5%Mg with 10 vol% TiB ₂	128
Figure 9.6	Plot of m versus ln(C) for stage II region of crack growth rate of Al-4%Cu-1.5%Mg with and without TiB ₂	130
Figure 9.7	Fatigue crack growth rate of 2124+20vol%SiC whiskers compared to Al-4%Cu-1.5%Mg+15vol% TiB ₂ and unreinforced alloy: All alloys in T6 condition with R=0.1. 2124+SiC data from Logsdon and Liaw [80].	131

LIST OF TABLES

Table 3.1	Strain hardening exponent for pure aluminum reinforced with 0.3 μm TiB_2	19
Table 4.1	Chemical composition of unreinforced and TiB_2 reinforced Al-Cu-Mg Alloys.	28
Table 4.2	Young's modulus of Al-4%Cu-1.5%Mg extrusion vs direction in extruded bar.	44
Table 5.1	The elastic constants of aluminum and potential reinforcements along with the stress free transformation strain and constrained strain produced in MMCs reinforced with the indicated particles when quenched from 500°C to room temperature.....	47
Table 8.1	Plane-strain fracture toughness (K_{IC}) of Al-4%Cu-1.5%Mg alloys aged at 190°C from the T4 condition.	119
Table 9.1	Coefficients of least-squares fit to stage II data.	130

1. INTRODUCTION

Aluminum-based discontinuously reinforced metal matrix composites (MMCs) have received attention because of their improved strength, high modulus, and increased wear resistance over conventional aluminum alloys. Clearly, an alloy reinforced with non-deformable, non-shearable particles that are stable to the melting point of the alloy (and beyond) has a fundamental advantage over conventional alloys, which are reinforced with precipitates that can be sheared by dislocations and coarsen or go into solution if exposed to elevated temperature. Although the specific strength of discontinuously reinforced MMCs is not as high as that of continuously reinforced composites, the isotropic properties and reasonable cost of discontinuous MMCs make them potentially useful structural materials.

1.1 Program Goals

The objective of this program is to determine the mechanism governing the mechanical behavior of alloys reinforced with equiaxed particles which are approximately 1 μm in diameter. The specific goal of this program is to examine the influence of reinforcement size, volume fraction, and matrix deformation behavior on the strength, fracture toughness, fatigue, and aging characteristics of an aluminum MMC. Understanding how these parameters affect the properties of MMCs will allow us to engineer these elements to produce composites with superior properties tailored to a specific application.

This is an “experimentally based” program but an attempt will be made, where possible, to correlate the data of this work with previously developed theories and results. Unfortunately, the mechanisms governing the properties of an alloy reinforced with equiaxed particles approximately 1 μm in diameter is not well understood. Alloys reinforced with particles of this size occupy the middle ground between the true dispersion-strengthened metals, which have particles less than 0.1 μm , and conventional MMCs, which have reinforcements greater than 10 μm . This middle ground is made more tenuous by the fact that the mechanisms associated with strengthening, deformation, and fracture in dispersion-strengthened alloys are well understood, whereas much of the understanding of conventional MMCs is incomplete.

To meet the goals of this program, two sets of MMCs were produced by the XDTM process. The first set contained 0.3 μm TiB₂ particles in pure aluminum. The volume fraction of these alloys was varied from 0.5 to 15 vol%. The second set consisted of TiB₂ particles either 0.3 μm or 1.3 μm in diameter in a matrix of Al-4%Cu-1.5%Mg (a model ternary alloy similar to 2024 but without Mn). The volume fraction in these alloys was varied from 0 to 15

vol%. In most of the heat-treated conditions considered, the Al-4%Cu-1.5%Mg alloy has both the TiB_2 ceramic reinforcement and either the G.P. zones or S' (Al_2CuMg) precipitates of the 2000-series aluminum matrix. Because G.P. zone and S' nucleation is not dependent on excess vacancies for heterogeneous nucleation, this 2000-series alloy serves as a much simpler system for study than alloys which are sensitive to vacancy concentration, such as 7000-series alloys.

1.2 The XDTM Process

The XDTM process is a patented technique developed by Martin Marietta Corporation, in which ceramic particles are produced *in situ* in a molten metal [1]. The process enables the production of MMCs reinforced with a wide variety of transition metal carbide, boride, nitride, and silicide particles. The reinforcements are typically single crystals of high purity, which because they were formed *in situ*, have clean unoxidized interfaces. By suitably altering the parameters of the *in situ* formation step, the size of the reinforcements can be varied from approximately 0.2 μm to 10 μm and the volume fraction can be varied from a few percent up to approximately 80%.

Typically, a two-step process is used to produce aluminum alloys with a low particle loading (0 to 30%) . In the first step a master alloy containing a large volume fraction of the desired reinforcement is produced by the XDTM process in pure aluminum. In a subsequent casting process, this master alloy is diluted to the desired ceramic particle loading and the matrix alloying additions are added [2,3]. By using this two-step master alloy approach, the amount of material produced by the XDTM process is kept to a minimum, thereby reducing production costs.

2. XD™ ALUMINUM-TiB₂ SYSTEM

2.1 Particle Size

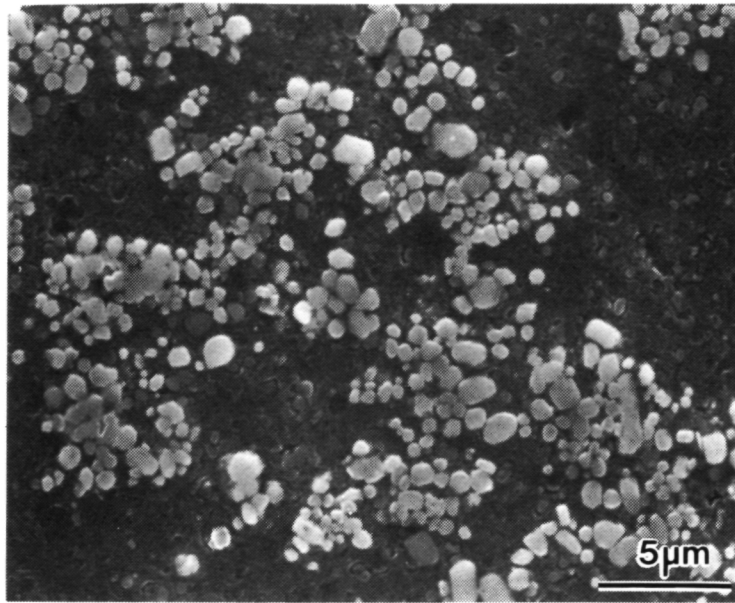
In this study XD™ master alloys containing TiB₂ particles of two sizes were produced and examined. The TiB₂ particles present in both materials are roughly spherical; many are hexagonal cylinders with planar features along the (0001) and {11 $\bar{2}$ 0} crystallographic planes. The typical shapes and size distributions of the lightly etched Al+10vol%TiB₂ samples are shown in the scanning electron microscope (SEM) micrographs in Fig. 2.1.

Although the size distributions of major and minor diameters could be used as a direct measure of particle size, we use an alternative definition of particle size, the equivalent diameter. The equivalent diameter of the particle is defined as the diameter of a circular particle with the same area as the area of the elliptical particle. In determining the equivalent diameter, individual particles were assumed to be ellipsoidal. The effective area of each particle was calculated from the measured major and minor diameters.

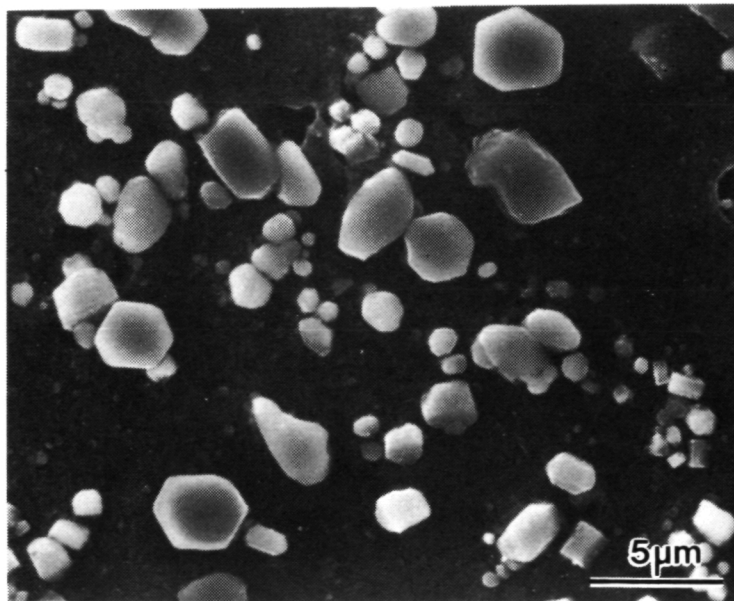
The polished surfaces of alloys containing 5 vol% TiB₂ were lightly etched and the major and minor diameters of individual particles were measured from micrographs taken on the SEM to determine the particle size. Because only two different master alloys were used, there was no need to determine the particle size of the alloys as a function of particle loading. The equivalent diameters of approximately 600 particles were determined, for each of the two particle sizes, and the mean diameter and frequency distributions were calculated from these measurements. The equivalent diameter distributions of the two master alloys are shown in Fig. 2.2. The ordinate is normalized to unity in each plot. The means of these distributions are 0.34 μm ($0.34 \pm 0.06 \mu\text{m}$) and 1.29 μm ($1.31 \pm 0.10 \mu\text{m}$), respectively. Although the shape of the major and minor diameter distributions are similar to that of the equivalent diameter distribution it is believed that the mean equivalent diameter represents the particle size of different materials better than the mean of either the minor or the major diameter. Measurements of major and minor diameters show the aspect ratio to be 1.29 ± 0.32 for the 0.3 μm particles and 1.29 ± 0.02 for the 1.3 μm particles.

Comparing the breadth of the distributions of particle diameter shown in Fig. 2.2(a) with those in Fig. 2.2(b), it might appear that the size distribution is broader in the 1.3 μm TiB₂ material than in the 0.3 μm material. However, the normalized distributions in Fig. 2.3 (obtained by normalizing the abscissa by the mean diameter) show that the breadth and roughly symmetric shapes of the two distributions are quite similar. Thus, the difference between the

ORIGINAL PAGE
BLACK AND WHITE PHOTOGRAPH

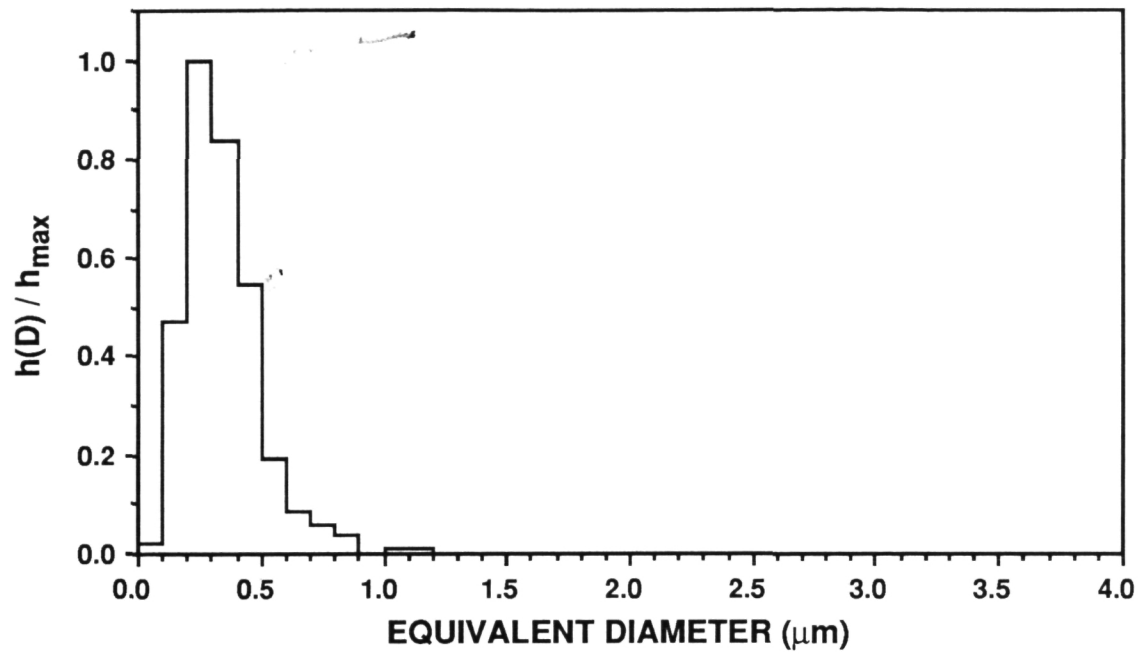


(a) Small particles with mean diameter of 0.34 μm .

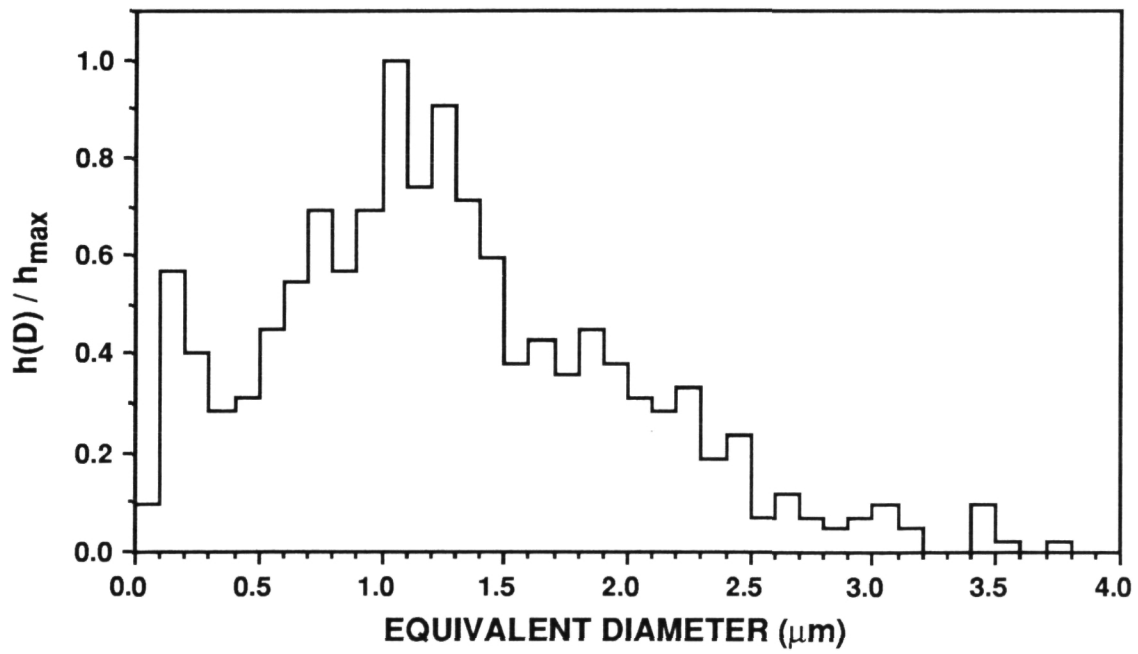


(b) Large particles with mean diameter of 1.31 μm .

Figure 2.1 SEM micrographs of etched Al+10vol%TiB₂ made with two sizes of TiB₂.

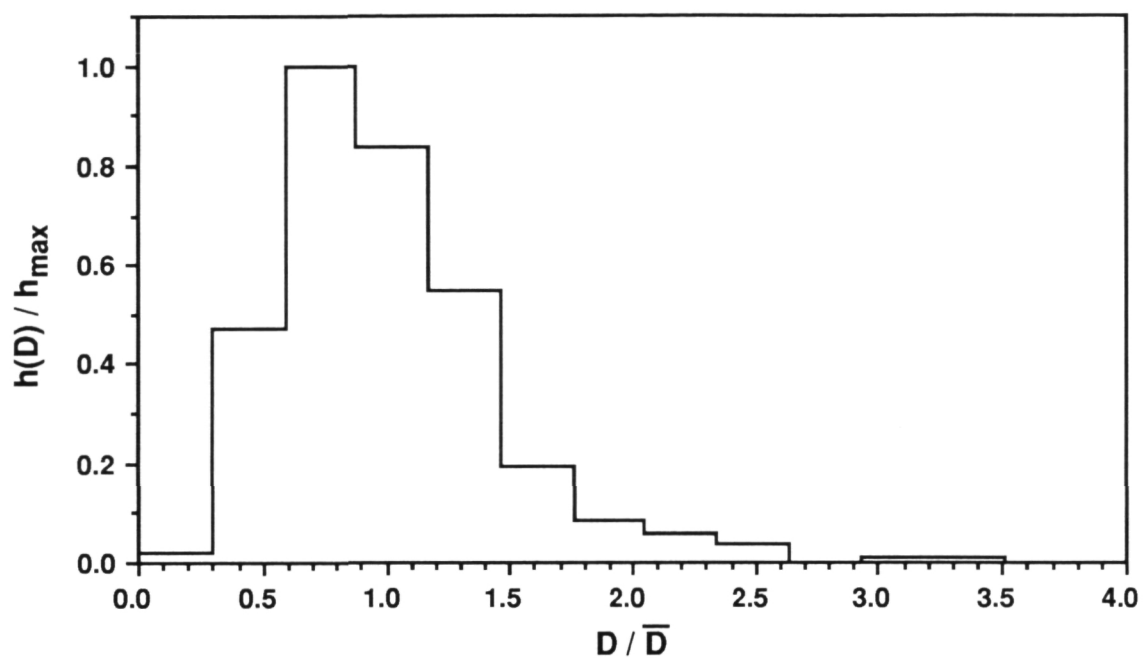


(a) Small particles with mean diameter of 0.34 μm .

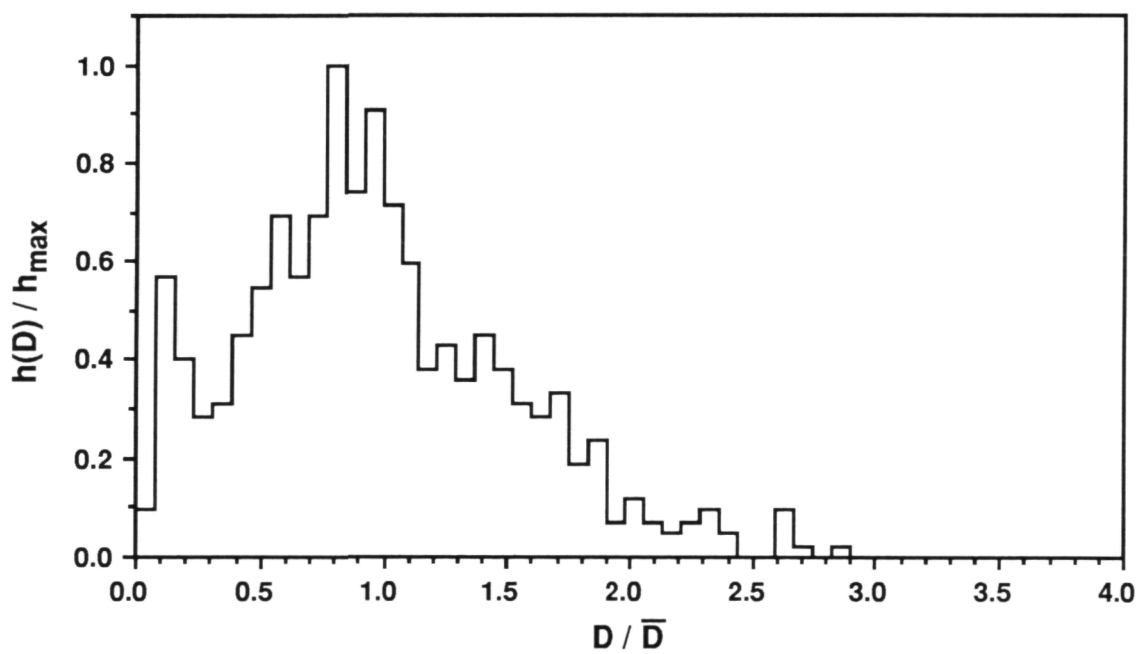


(b) Large particles with mean diameter of 1.31 μm .

Figure 2.2 Particle size distributions.



(a) Small particles with mean diameter of $0.34 \mu\text{m}$.



(b) Large particles with mean diameter of $1.31 \mu\text{m}$.

Figure 2.3 Normalized particle size distributions.

distributions in Fig. 2.2 is due to the difference in scale (i.e., the difference in the size of the particles), not a difference in the shape or nature of the distribution.

2.2 Stability of TiB_2 in Aluminum

The thermodynamic stability of TiB_2 in aluminum is well documented as demonstrated by the use of TiB_2 for the liners of alumina reduction cells in the primary production of aluminum. The stability of TiB_2 with respect to molten aluminum allows for molten metal processing of TiB_2 reinforced composites without concern for bulk or interfacial reactions between the melt and reinforcement.

3. TiB₂ IN PURE ALUMINUM

To help understand the role of the TiB₂ on the mechanical behavior of aluminum alloys it is necessary to understand the impact of TiB₂ on the pure metal. Therefore, the structure and properties of TiB₂ in pure aluminum will be briefly examined in this chapter prior to considering an aluminum alloy in ensuing chapters.

3.1 Materials

3.1.1 Processing

Alloys with 0.5, 2, 5, 10, and 15 vol% TiB₂ were fabricated using the master alloy with 0.3 μm TiB₂. The alloys were induction melted using the XDTM master alloy and 99.99% pure aluminum, and then casting it into a 7.6 cm (3 in.) diameter mold. These 2 kg (5 lb) ingots were then hot forged in three orthogonal directions. After forging, the alloys were heat treated at 500°C (932°F) for 2 hours and furnace cooled. This high-temperature heat treatment allowed the alloys to recrystallize. The alloys were slow cooled to minimize the possibility of dislocation punching due to the coefficient of thermal expansion (CTE) mismatch between particle and matrix (dislocation punching will be discussed in detail in Chapter 5).

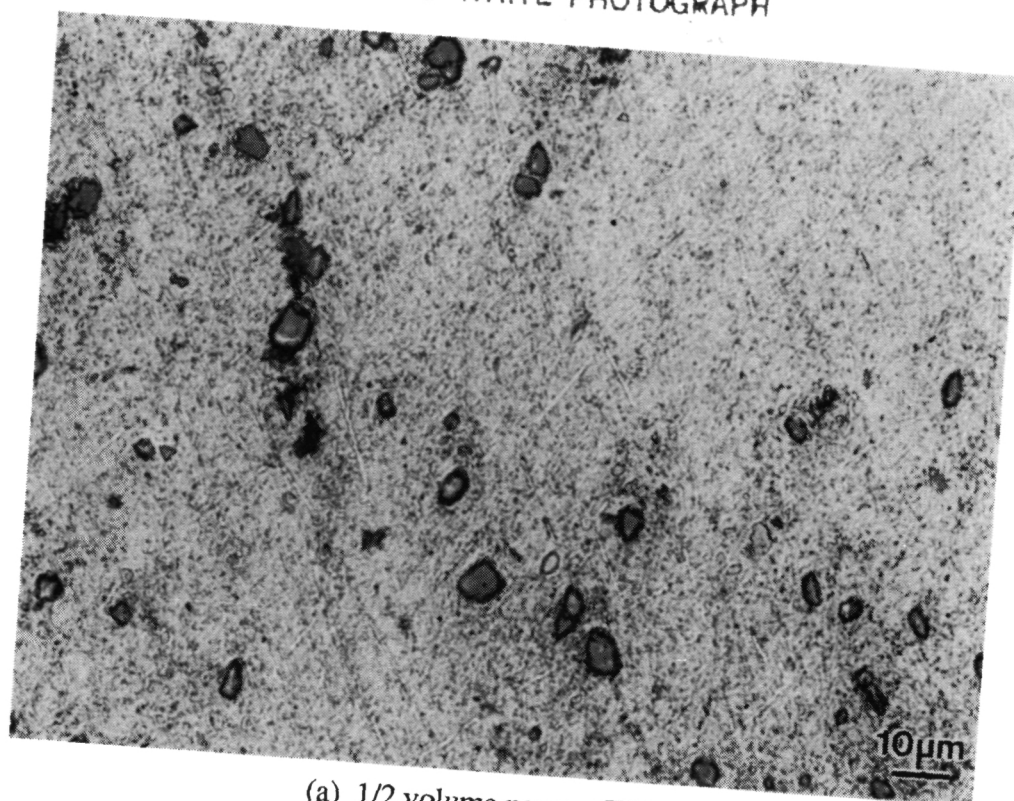
3.1.2 Microstructure

Optical micrographs of the unetched surface of the pure Al plus TiB₂ alloys in the annealed condition are shown in Fig. 3.1. Energy dispersive x-ray spectroscopy (EDS) indicates that the large 200 to 600 μm particles visible in the 0.5 and 2% alloys {Figs. 3.1(a) and (b)} are Si. The alloys with a higher TiB₂ content also appear to contain large Si precipitates, though the presence of the small TiB₂ particles render the Si less conspicuous.

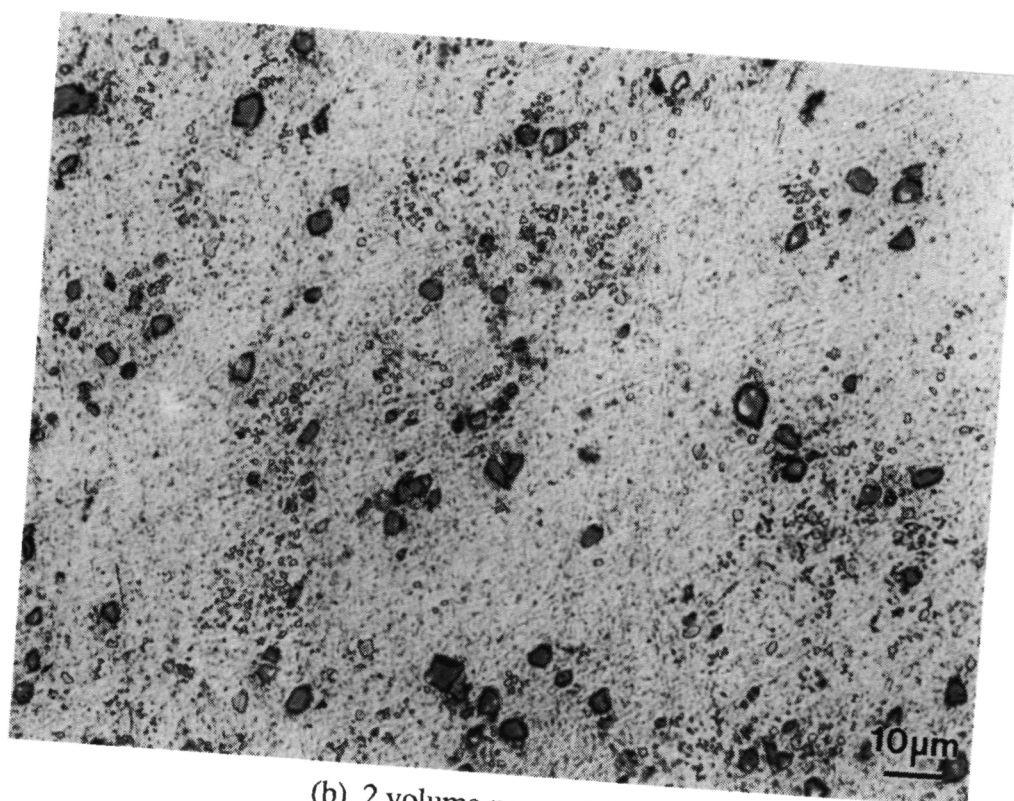
In the 0.5, 2, and 5% alloys there is some evidence of clustering of the TiB₂ particles {Figs. 3.1(a)-(c)}. It is believed that this clustering is due to particle pushing by the solidification front during casting (particle pushing is further discussed in Section 4.1.2). Although the segregation is not particularly severe, with increasing TiB₂ loading, the particle distribution improved such that it is uniform for the 10 and 15% alloys {Figs. 3.1(d) and (e)}.

The grain size of these alloys was found to depend greatly on particle loading. The TiB₂ particles refined the as-cast grain size and prevented grain growth during the long high-temperature anneal. The micrographs seen in Fig. 3.2 shows the grain size of anodized samples taken in cross-polarized light. The alloys were anodized using Barker's solution, in the same manner as conventional aluminum alloys. The materials with higher loadings of TiB₂

ORIGINAL PAGE
BLACK AND WHITE PHOTOGRAPH



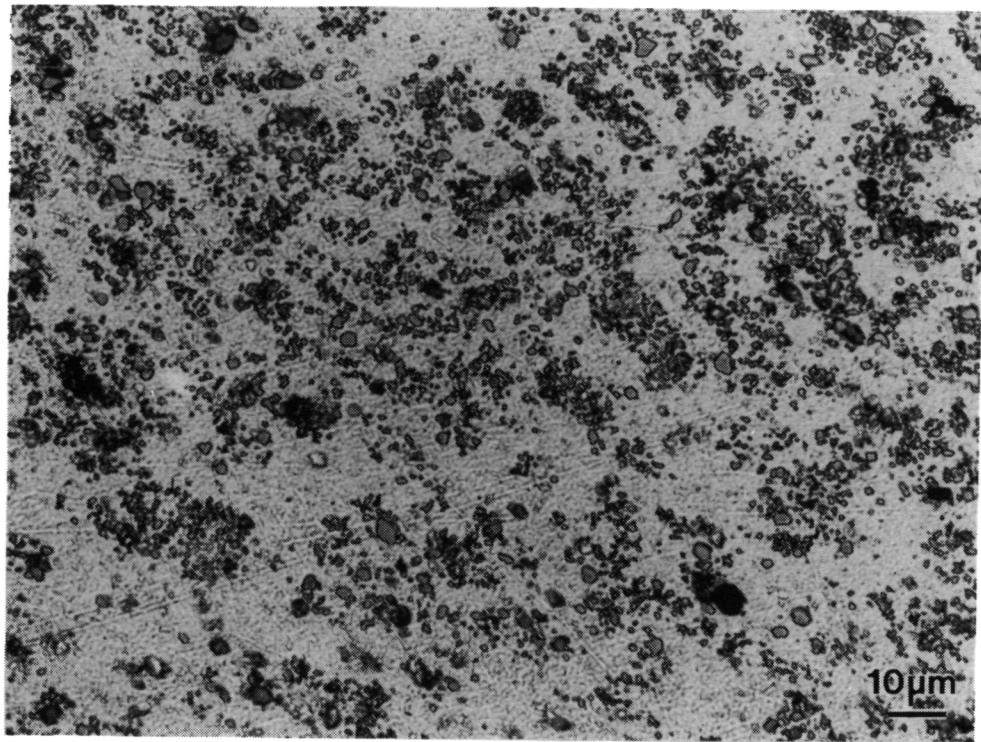
(a) 1/2 volume percent TiB_2



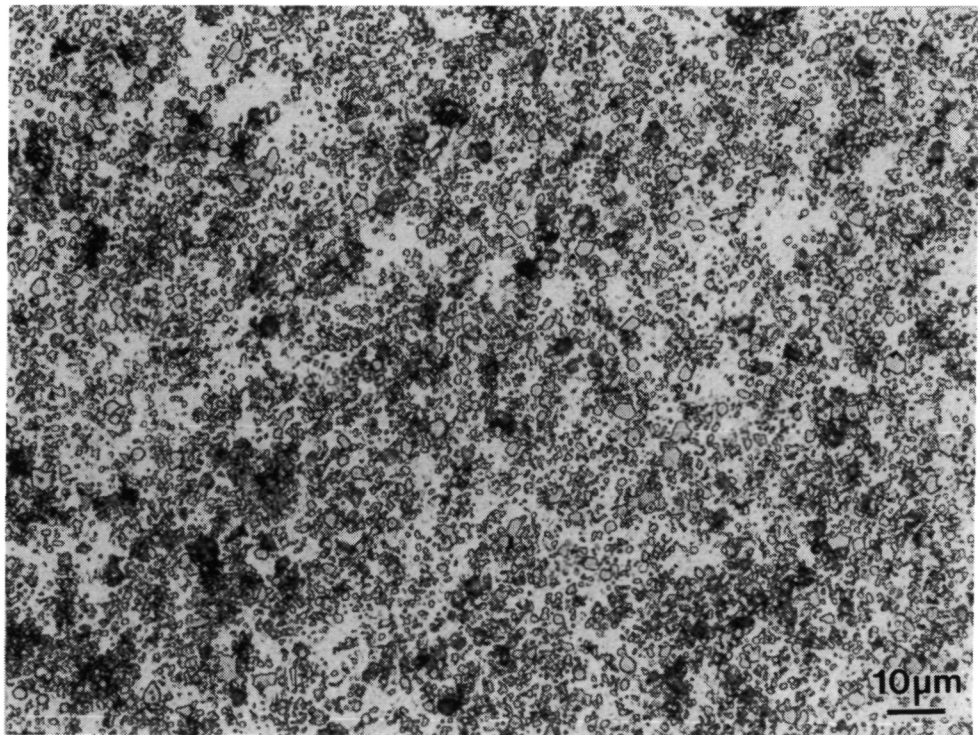
(b) 2 volume percent TiB_2

Figure 3.1 Optical micrographs of pure aluminum with TiB_2 .

ORIGINAL PAGE
BLACK AND WHITE PHOTOGRAPH

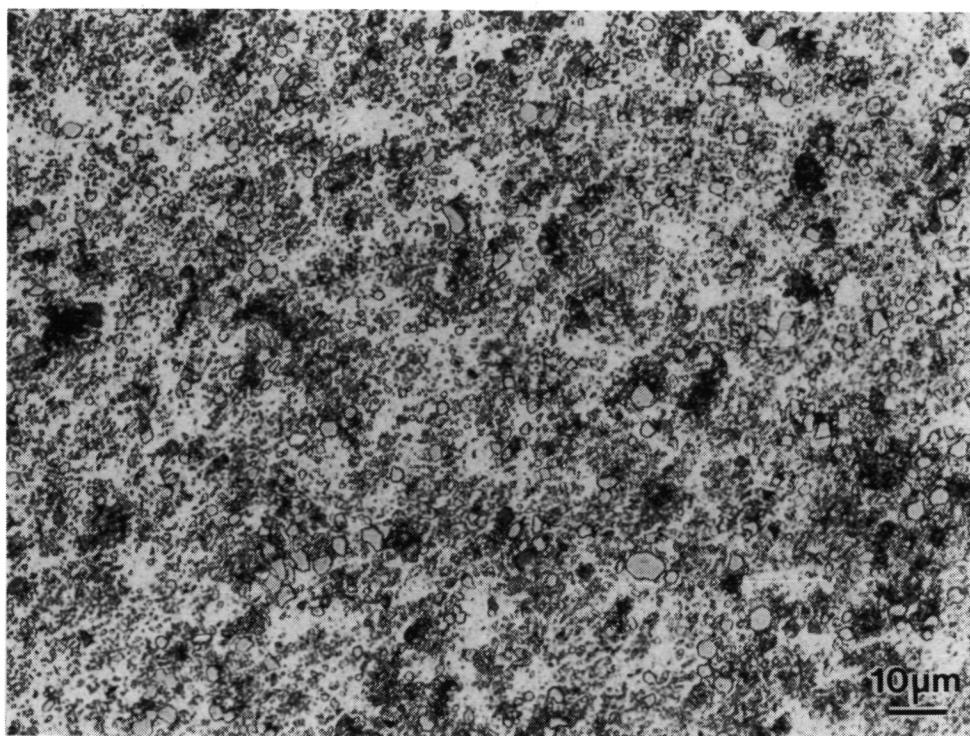


(c) 5 volume percent TiB_2



(d) 10 volume percent TiB_2

Figure 3.1 (cont.) Optical micrographs of pure aluminum with TiB_2 .

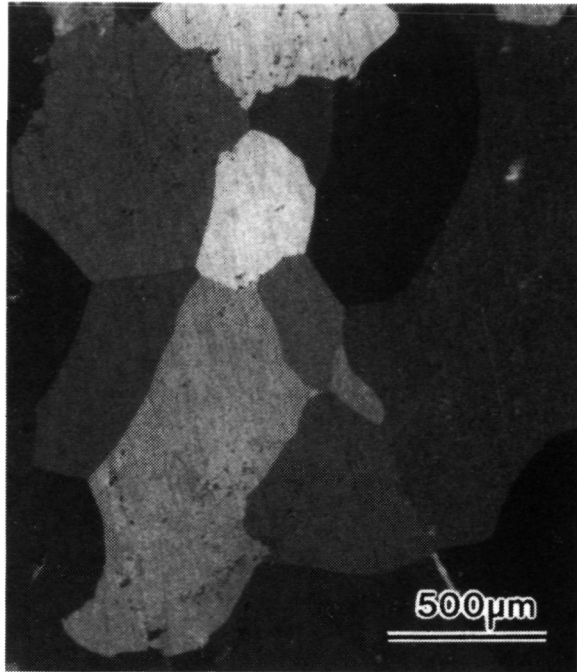


(e) 15 volume percent TiB_2

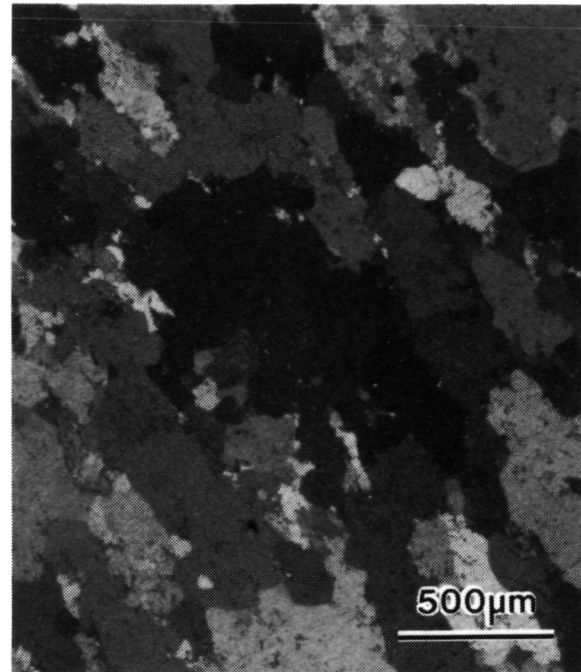
Figure 3.1 (cont.) Optical micrographs of pure aluminum with TiB_2 .

ORIGINAL PAGE
BLACK AND WHITE PHOTOGRAPH

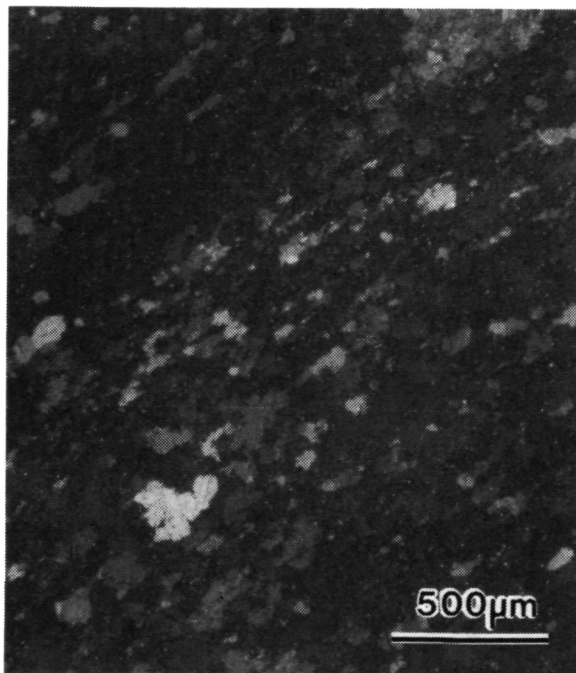
ORIGINAL PAGE
BLACK AND WHITE PHOTOGRAPH



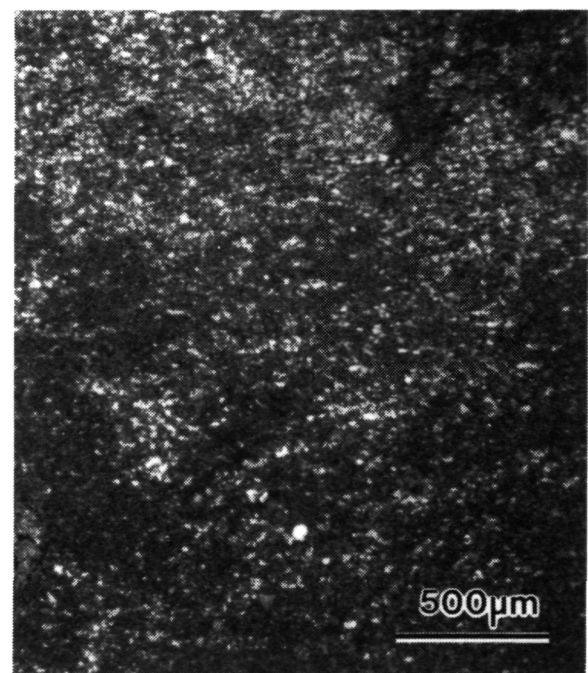
(a) 1/2 volume percent TiB_2 .



(b) 2 volume percent TiB_2 .



(c) 5 volume percent TiB_2 .



(d) 10 volume percent TiB_2 .

Figure 3.2 Optical micrographs taken with cross-polarized light to show the grain size of the forged and annealed pure aluminum alloys with TiB_2 .

have a much smaller grain size; in fact, the grains are so small that the size cannot be accurately be resolved by this technique.

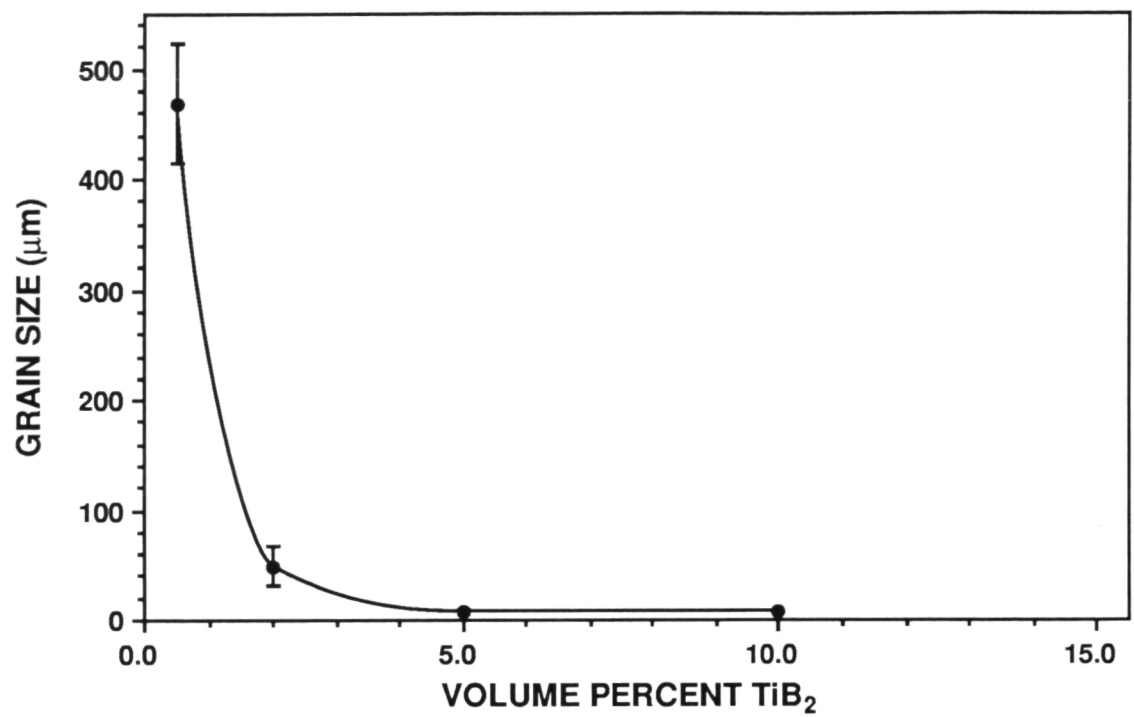
The grain size was quantitatively determined by a combination of transmission electron microscopy (TEM) and optical microscopy. For our purposes grain diameter will be taken as \bar{L}_3 , the measured mean intercept length of grain boundaries. For the low loading, large grain size materials, the mean intercept length of grain boundaries was measured from optical micrographs of anodized samples taken using cross-polarized light. For the higher loading, small grain size materials, the grain size was too small to measure from anodized samples. Here the mean intercept length was measured from TEM micrographs. In Fig. 3.3 the grain size, d , is plotted against the volume percent of TiB_2 . For the alloy with 2 vol% TiB_2 the grain size was determined by both methods and there is good agreement between the two techniques. In Fig. 3.3 (b) the logarithm of the grain size is plotted against the log of the volume percent TiB_2 in order to expand the ordinate for clarity; this is not meant to imply any functional dependence of grain size on TiB_2 loading.

In Fig. 3.4 representative TEM micrographs of the 5 vol% TiB_2 alloy are shown to illustrate the presence of particles both at the grain boundary and intergranularly. Also note in Fig. 3.4(b) the low dislocation density in these annealed samples and the apparent lack of dislocation loops. This suggests that either dislocations produced during the slow cool from the annealing temperature have annealed out or there was not a significant amount of dislocation punching to begin with (perhaps stress was relaxation by a diffusional mechanism).

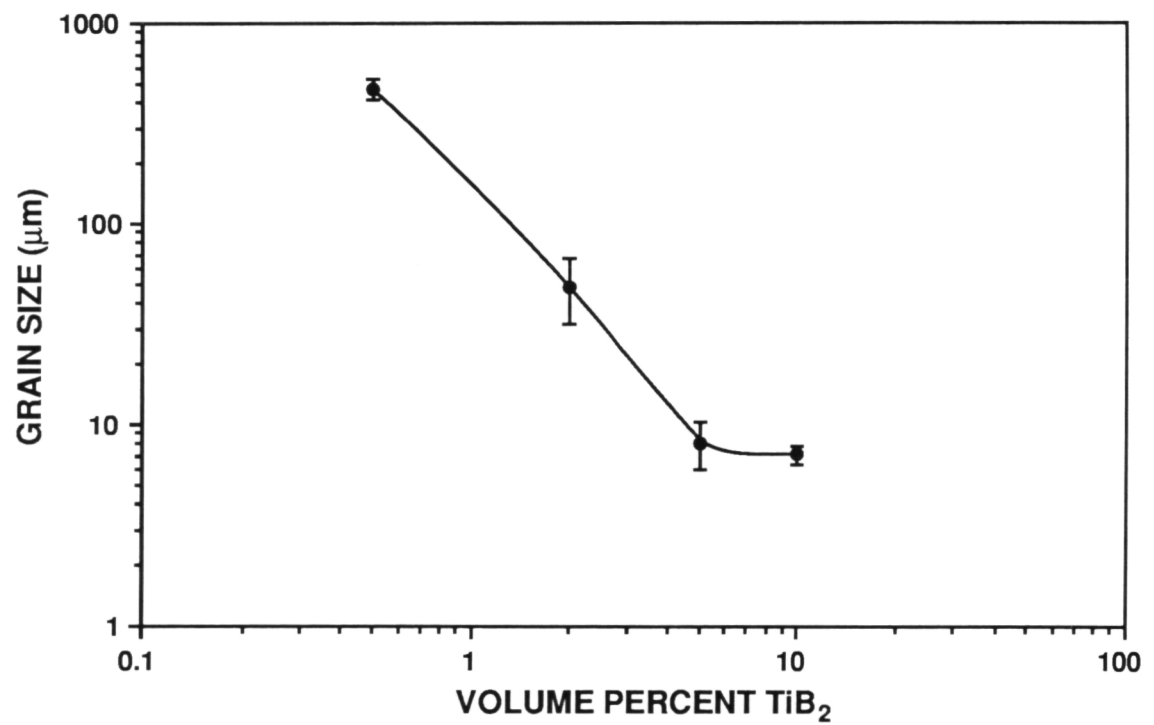
3.2 Tensile Properties

The tensile tests were performed in a screw-driven mechanical test frame using a clip-on extensometer and threaded samples with a 0.64 cm (0.25 in.) diameter by 2.54 cm (1 in.) gauge section. In Fig. 3.5, the 0.2% offset yield stress is shown as a function of strain rate for the five particle loadings used. The yield stress was not dependent on strain rates ranging from 1.3×10^{-4} to 0.13 sec^{-1} at room temperature. This is not unexpected; typically strain-rate-dependent deformation is a thermally activated process. Because the mechanical properties do not depend on strain rate at room temperature, further discussion in this report is confined to tests performed at a strain rate of $1.3 \times 10^{-3} \text{ sec}^{-1}$.

Figure 3.6 shows the dependence of the 0.2% offset yield stress and the ultimate tensile strength (UTS) on TiB_2 loading for the pure aluminum with TiB_2 . Also shown is the 95% confidence interval for these data. Both the yield stress and UTS increased with increased particle loading.

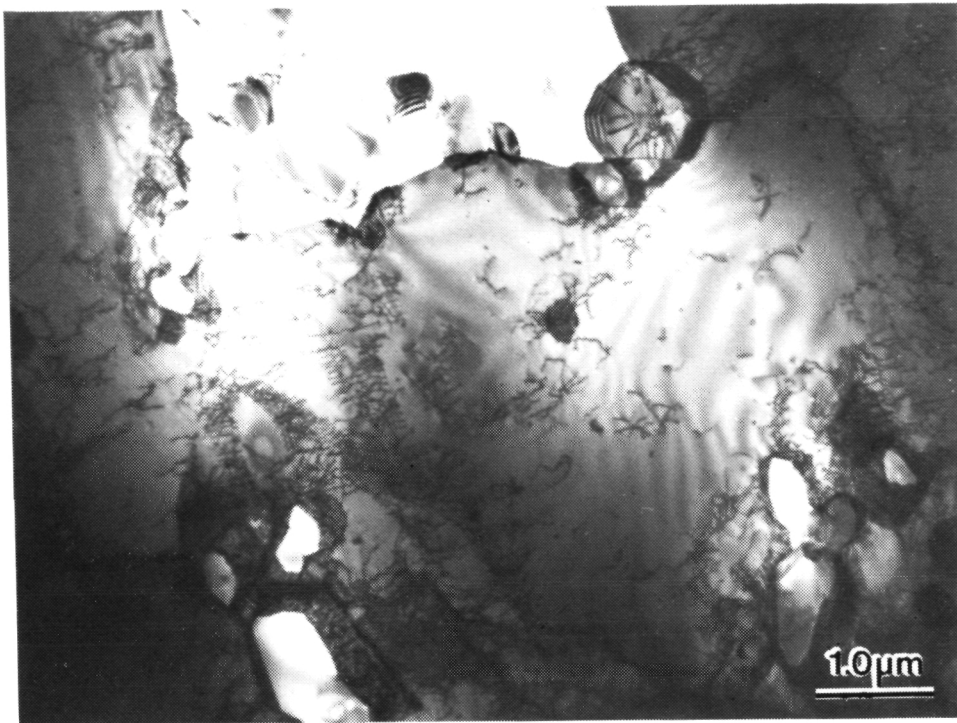


(a)

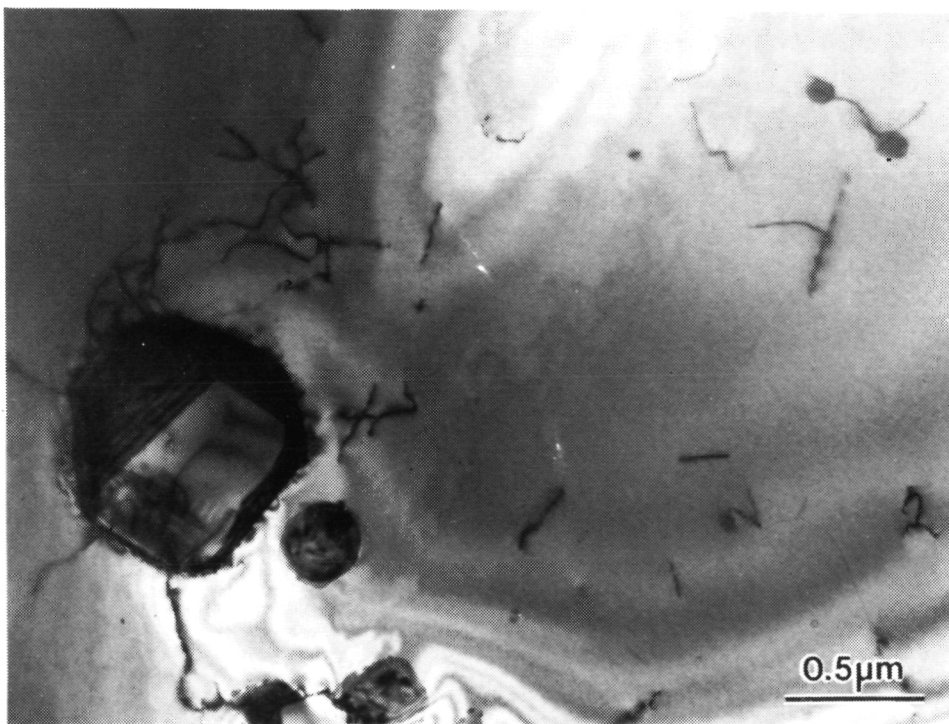


(b)

Figure 3.3 Variation of grain size with volume percent TiB_2 for forged and annealed aluminum.



(a) Low magnification



(b) Micrograph taken at $[110]_{\alpha}$ zone axis, multi-beam condition.

Figure 3.4 TEM micrographs of annealed pure aluminum with 5 vol% TiB_2 .

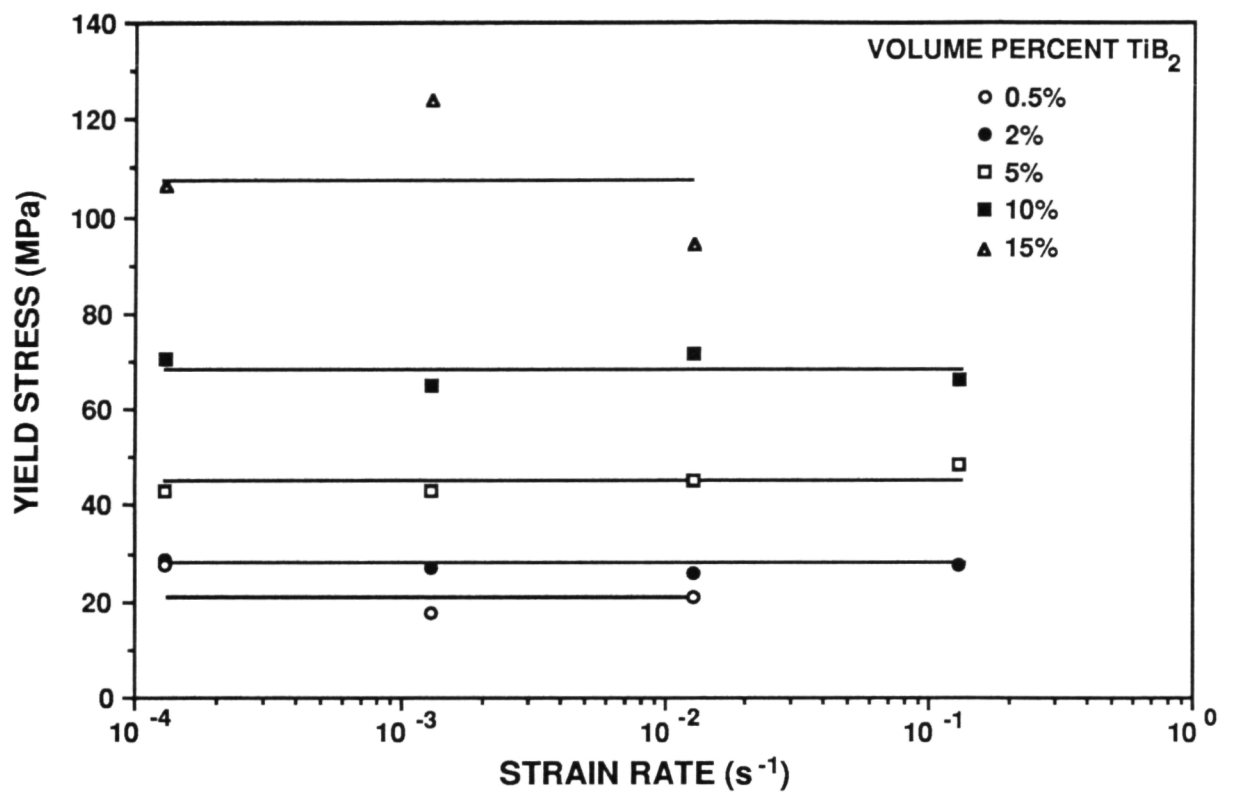
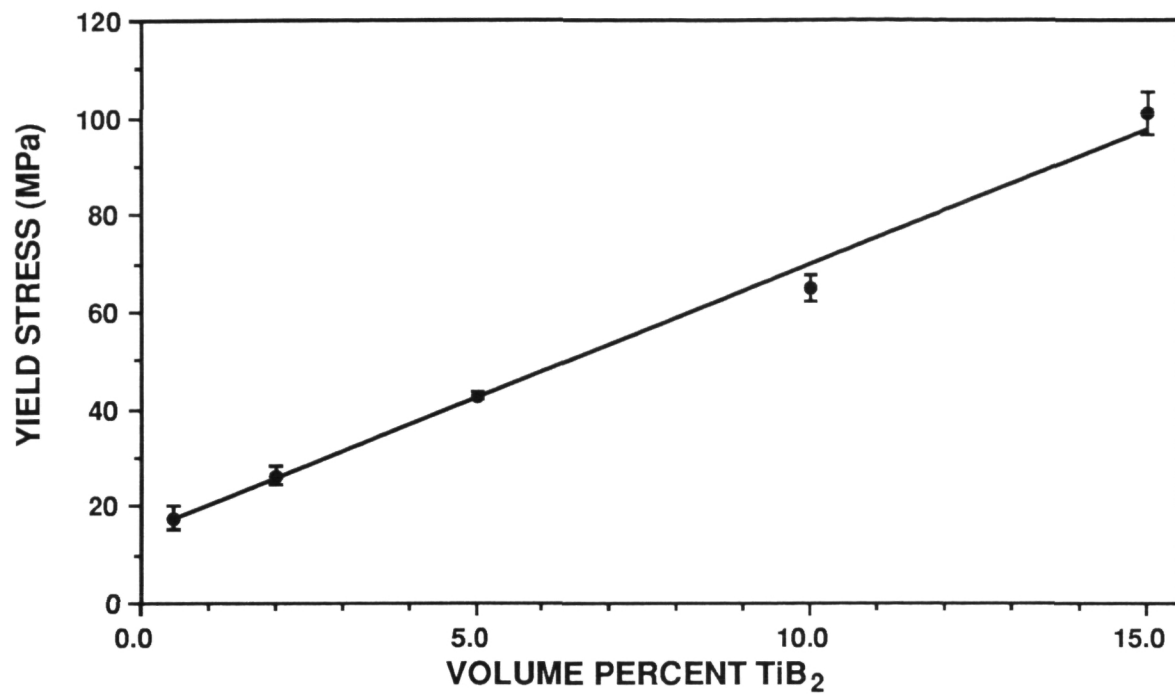
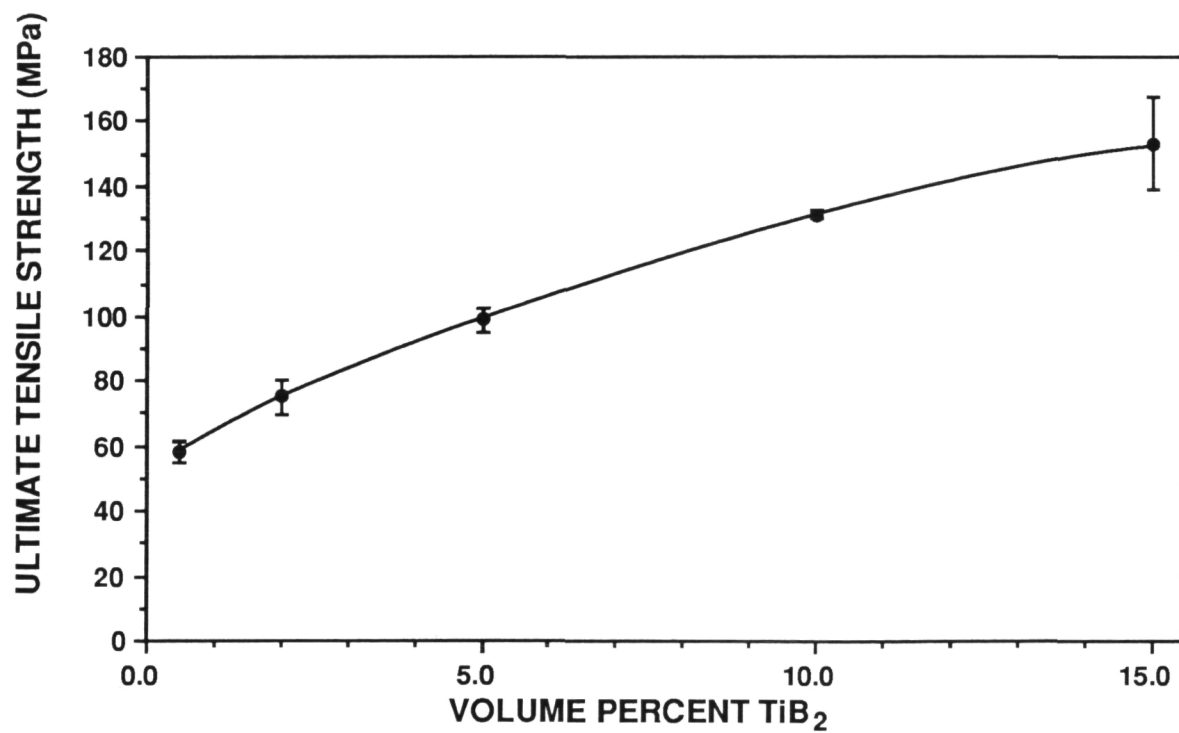


Figure 3.5 Dependence of yield stress on strain rate for the forged and annealed pure aluminum with 0.5-15 vol%, 0.3 μm TiB_2 .

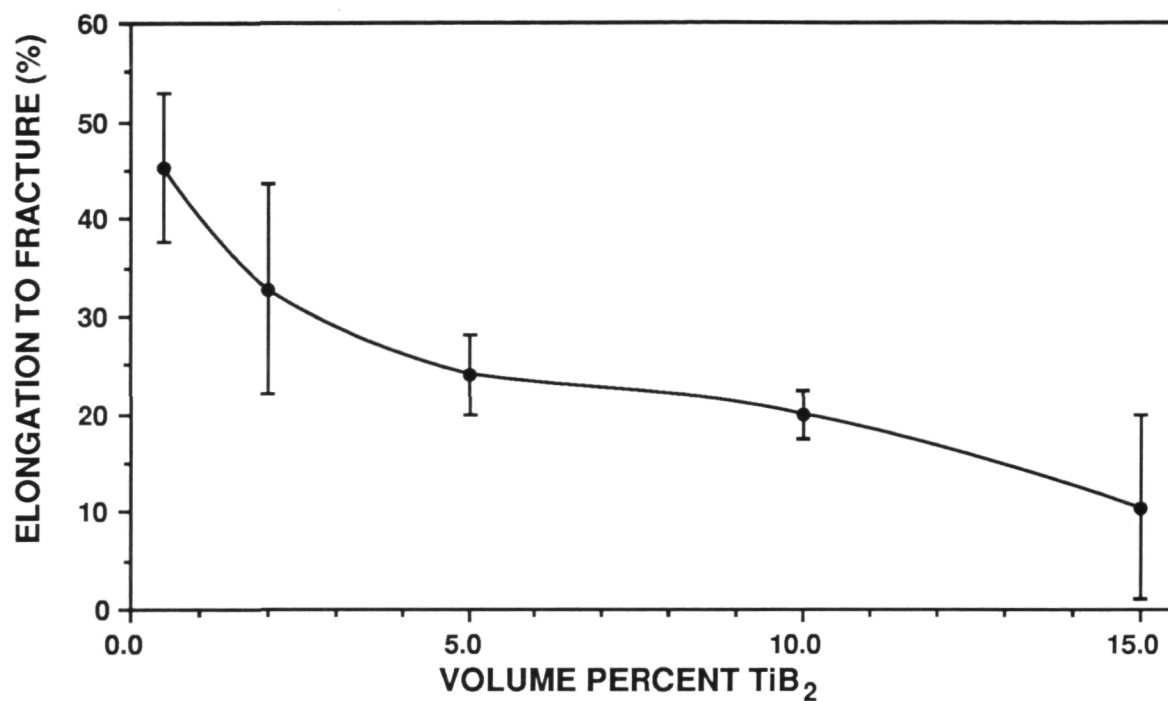


(a) Yield stress

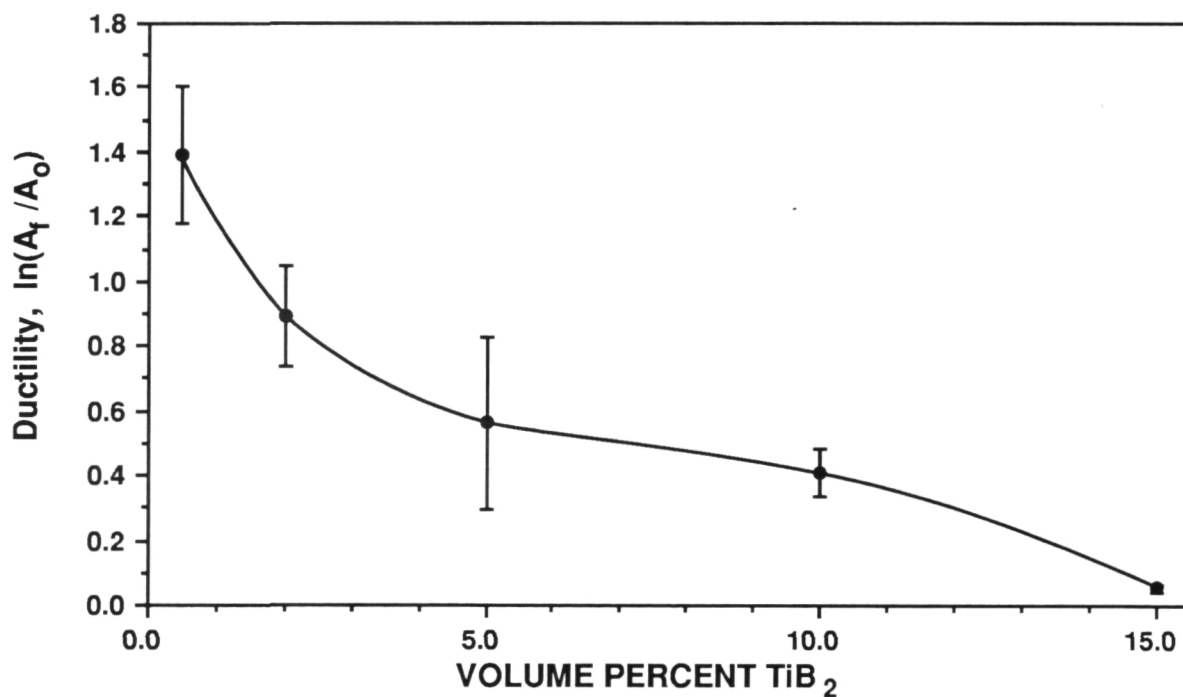


(b) Ultimate tensile strength

Figure 3.6 Tensile properties as a function of volume percent of $0.3 \mu\text{m}$ TiB_2 for forged and annealed pure aluminum.



(c) Elongation to fracture



(d) Ductility determined from reduction in area

Figure 3.6 Tensile properties as a function of volume percent of $0.3 \mu\text{m}$ TiB_2 for forged and annealed pure aluminum.

The elongation to fracture in a 2.54 cm (1 in.) gauge section is plotted in Fig. 3.6(c) as a function of particle loading. Elongation decreased monotonically with increasing volume fraction, a typical trend in composites. Ductility, as determined from the reduction in cross-sectional area, is plotted in Fig. 3.6(d). Ductility also decreased with increasing TiB₂ volume fraction. Although both the elongation to fracture and the ductility of these alloys decreased significantly with increasing particle loadings, the fracture mode remains ductile rupture. As shown in Fig. 3.7, these alloys exhibit a cup-and-ball fracture surface, in which dimple size is strongly dependent on particle loading. Roughly 50% of these dimples are occupied by a TiB₂ particle. It is thus quite likely that voids initiated at the particle/matrix interface.

The initial portions of representative tensile true-stress true-strain curves for the 0.5, 2, 5, and 10 vol% TiB₂ alloys are shown in Fig. 3.8(a). In Fig. 3.8(b) the data beyond the 0.2% yield stress are plotted as the logarithm of the true strain versus the logarithm of the true stress. Also in Fig. 3.8 are the lines corresponding to a least-squares fit of the data to the power law equation $\sigma = A\epsilon^n$. The strain hardening exponent, n , obtained from this fit are presented in Table 3.1. The observed n decreases with increasing particle loading, though because of the large differences in the stress of these alloys it is felt that n serves as a poor measure of strain hardening in this case*.

Table 3.1
Strain Hardening Exponent for Pure Aluminum Reinforced with 0.3 μm TiB₂

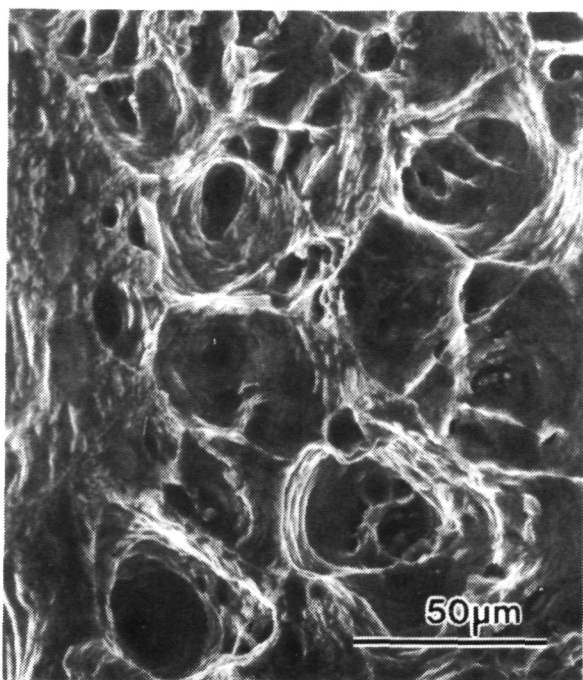
TiB ₂ content	n
0.5%	0.34
2%	0.28
5%	0.24
10%	0.20

To further examine the strain hardening of these alloys the stress-strain curves of Fig. 3.9 were differentiated to obtain the slope, $d\sigma/d\epsilon$, as a function of strain. Because numerical differentiation of data that contains experimental scatter will amplify that noise, we've chosen

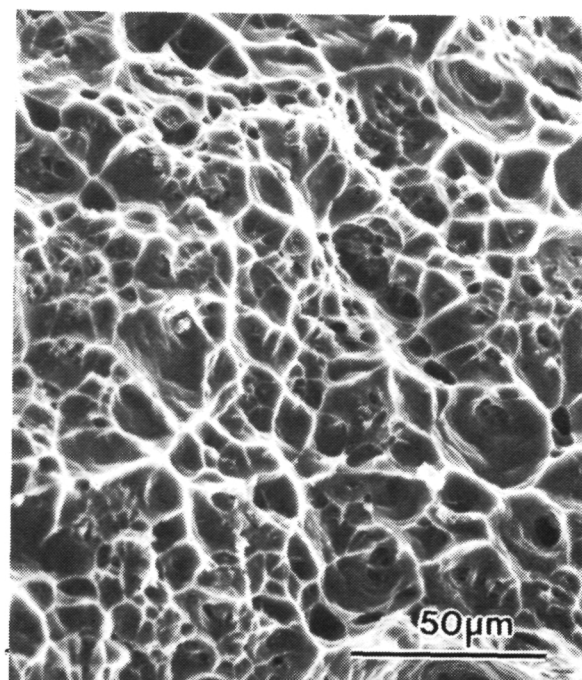
* Consider that differentiation of $\sigma = A\epsilon^n$ yields the relation

$$n = \frac{\epsilon}{\sigma} \frac{d\sigma}{d\epsilon}.$$

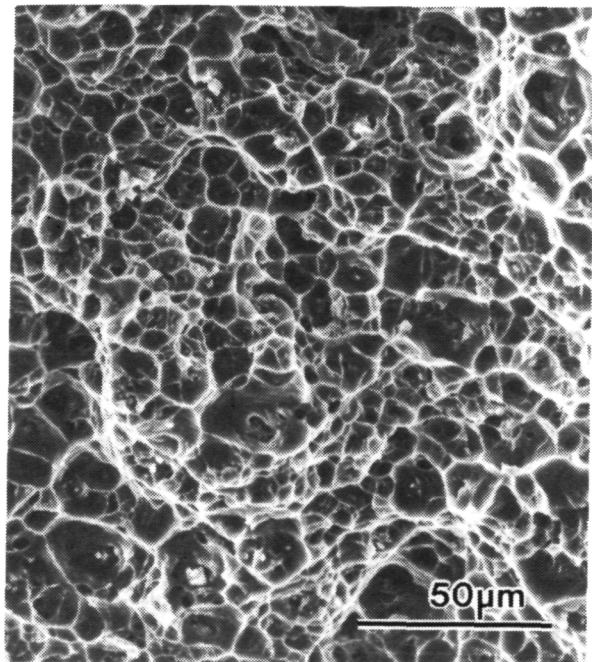
The inverse dependence of n on σ overwhelms the $d\sigma/d\epsilon$ term, yielding a lower value of n for an alloy which has a high $d\sigma/d\epsilon$.



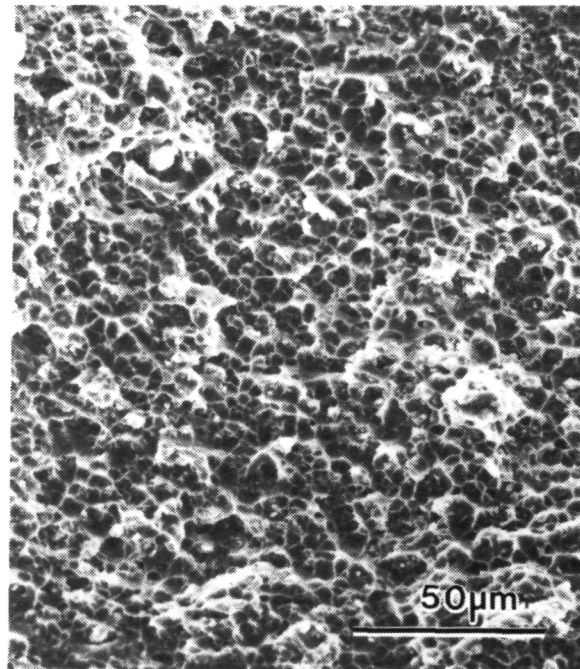
(a) 1/2 volume percent TiB_2 .



(b) 2 volume percent TiB_2 .

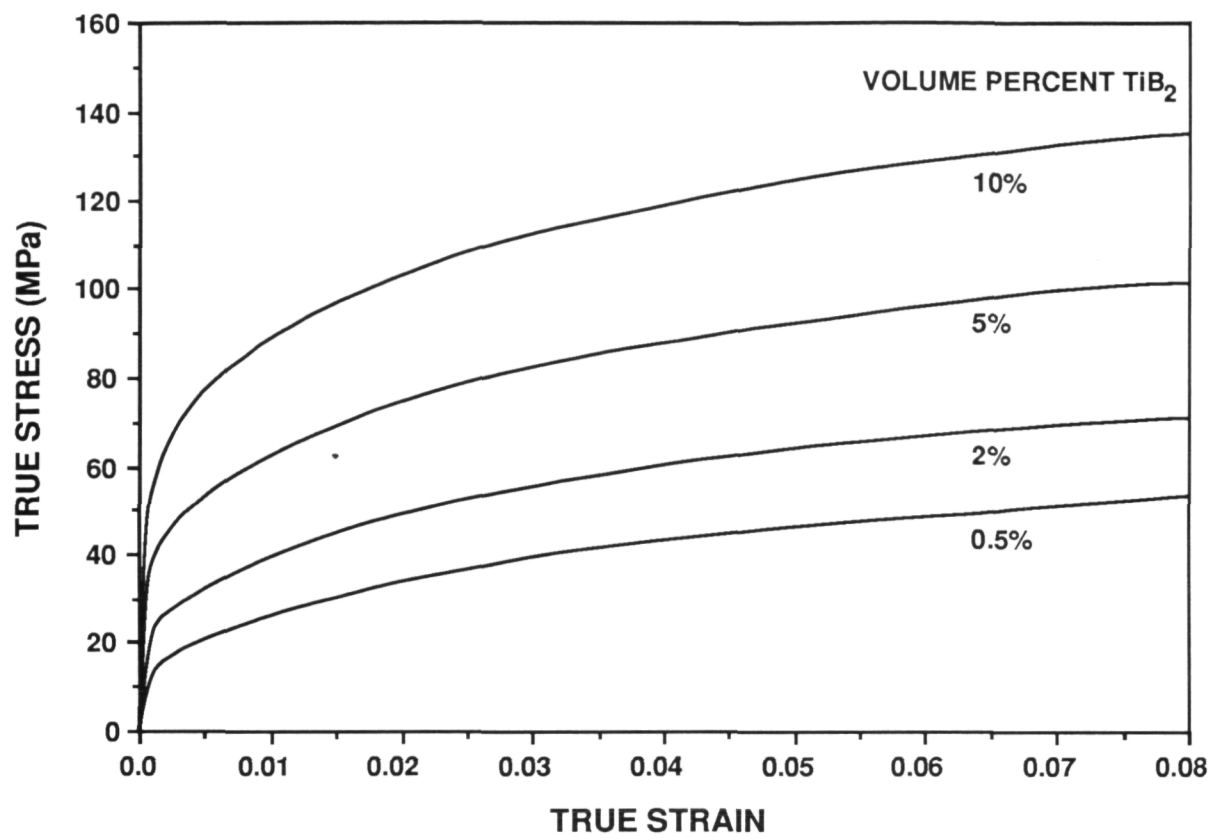


(c) 5 volume percent TiB_2 .

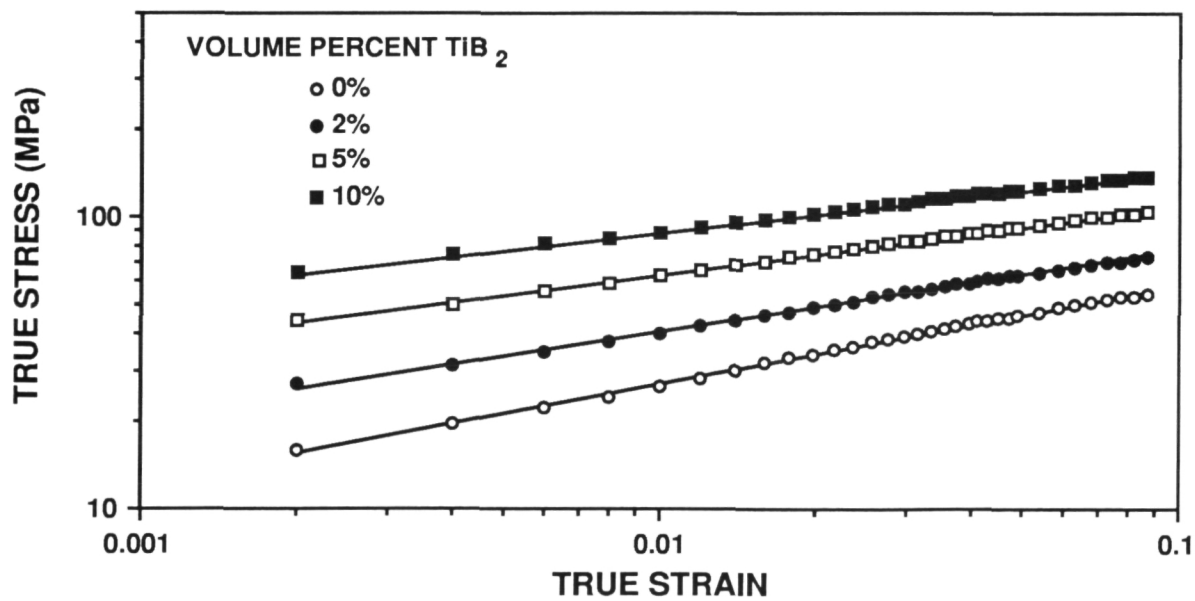


(d) 10 volume percent TiB_2 .

Figure 3.7 Fracture surface of sample of aluminum reinforced with TiB_2 , pulled in tension at room temperature.

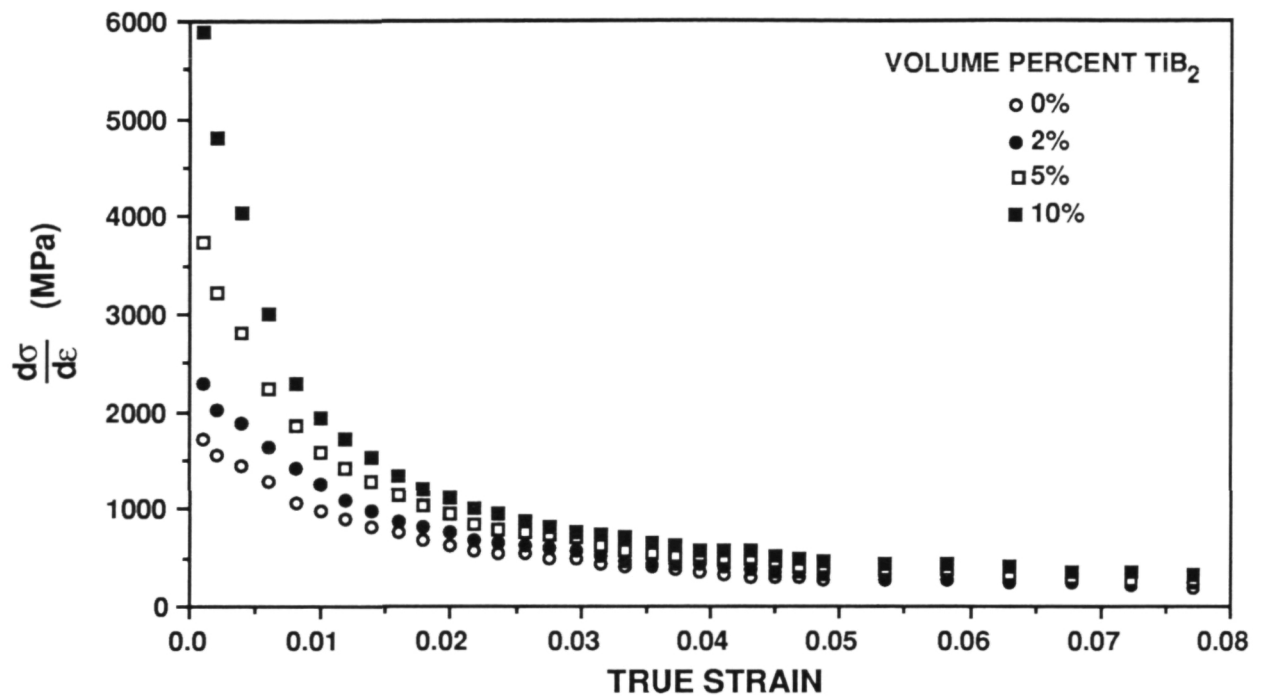


(a)

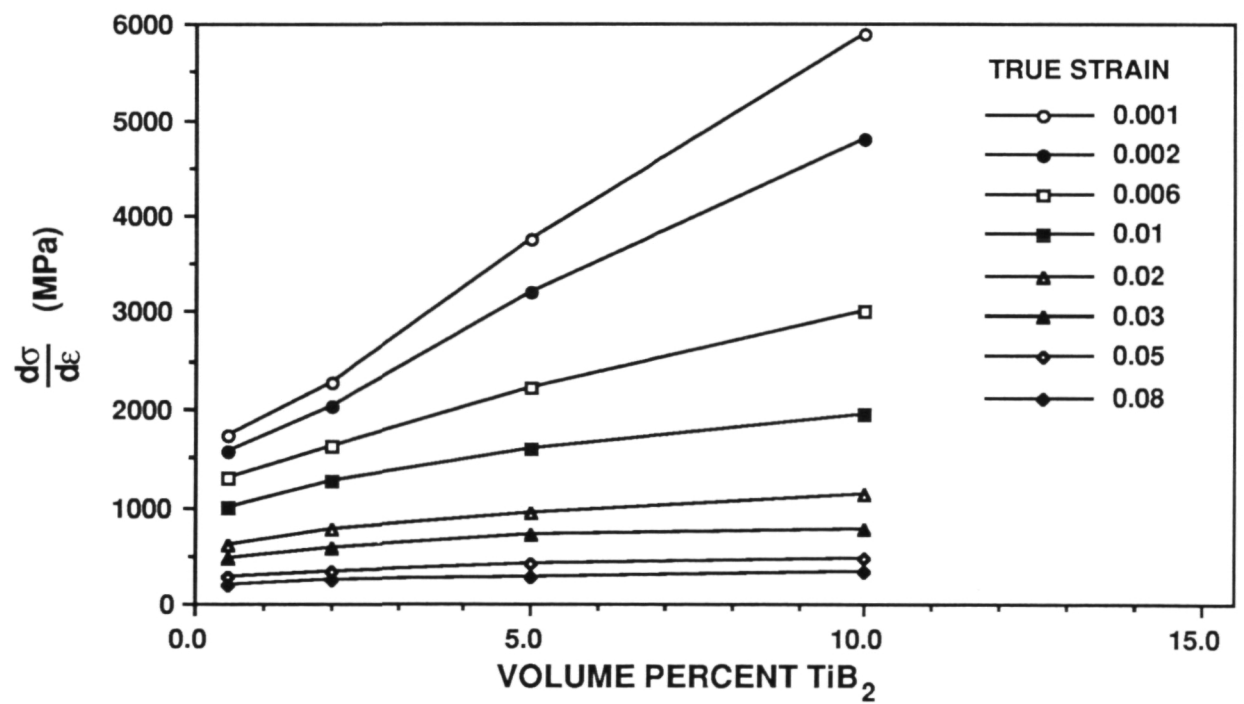


(b)

Figure 3.8 True stress versus true strain of pure aluminum with 0.3 μm TiB_2 pulled in tension at room temperature.



(a) Strain hardening rate versus true strain



(b) Strain hardening rate versus TiB_2 loading

Figure 3.9 Strain hardening rate of pure aluminum with $0.3 \mu\text{m}$ TiB_2 pulled in tension at room temperature.

to fit the data to a line segment then analytically differentiate the fitted segment. This procedure significantly reduces noise. Thus to obtain the slope, a data point along with 2 points prior to it and 2 points following it were fit to a linear segment using a least-squares fit of these 5 points. The slope of this segment was then obtained directly. In Fig. 3.9(a) $d\sigma/d\varepsilon$ is plotted as a function of true strain. In Fig. 3.9(b) the data are replotted as $d\sigma/d\varepsilon$ versus the volume fraction of TiB_2 for various strains. The strain hardening rate is initially very high and then decreases with increasing strain. It also is highly dependent on the TiB_2 content of the alloy and increases with increasing particle loading. At higher strains the strength of the alloys reaches a plateau and the strain hardening rate of the alloys becomes independent of particle loading.

To help understand the role that particles play on the strain hardening of these alloys TEM foils were prepared from the gauge section of various materials. Selected tensile samples were strained to a predetermined amount and unloaded. Thin slices were then taken out of the tensile gauge parallel to the tensile axis using a slow speed diamond saw. The slices were then thinned using 400 and 600 grit SiC papers and 3 mm foils were mechanically punched. The reduction in area at that point in the gauge was determined for each disk. TEM foils were then prepared by electropolishing the disks in a twin-jet electropolisher until perforation. Electropolishing was performed at -30°C and 10V using a 10% perchloric acid in ethanol solution. These conditions thinned the aluminum and TiB_2 at nearly identical rates. Once perforated the samples were rinsed in 3 ethanol baths and dried. The samples were examined at 100 KV in a JEOL 100CX microscope using a double tilt goniometer.

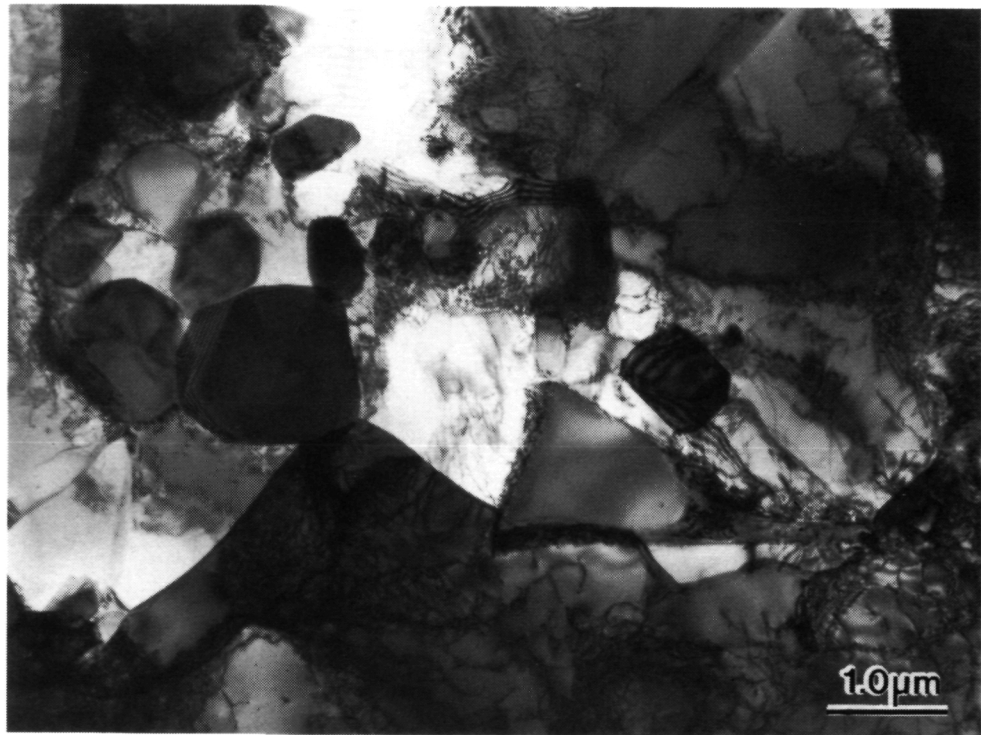
In Fig. 3.10 bright field micrographs of 0.5% and 5% samples strained to a reduction in area of approximately 10% are shown. In the 0.5% alloy {Fig. 3.10(a)}, dislocations are observed as single dislocations in the matrix, dislocations associated with the TiB_2 particles, and dislocations in weakly developed dislocations cells. In the 5% alloy {Fig. 3.10(b)}, the dislocation cells seem to be better developed and there are numerous dislocation tangles. The difference in dislocation substructure between the two materials is consistent with the observed strain hardening rate.

3.3 Elevated-Temperature Tensile Properties

Elevated-temperature tensile tests were performed at a strain rate of $1.3 \times 10^{-3} \text{ sec}^{-1}$. The 0.2% offset yield stress as a function of temperature is plotted in Fig. 3.11(a). The yield stress of the alloys decreased with increasing temperature, though the decrease was less pronounced among the weaker, lower loading alloys than in the stronger, higher loading alloys. Figure 3.11(a) also shows that yield stress increased with increased particle loadings, although at the highest temperature there is a smaller proportional increase in strength between alloys. A

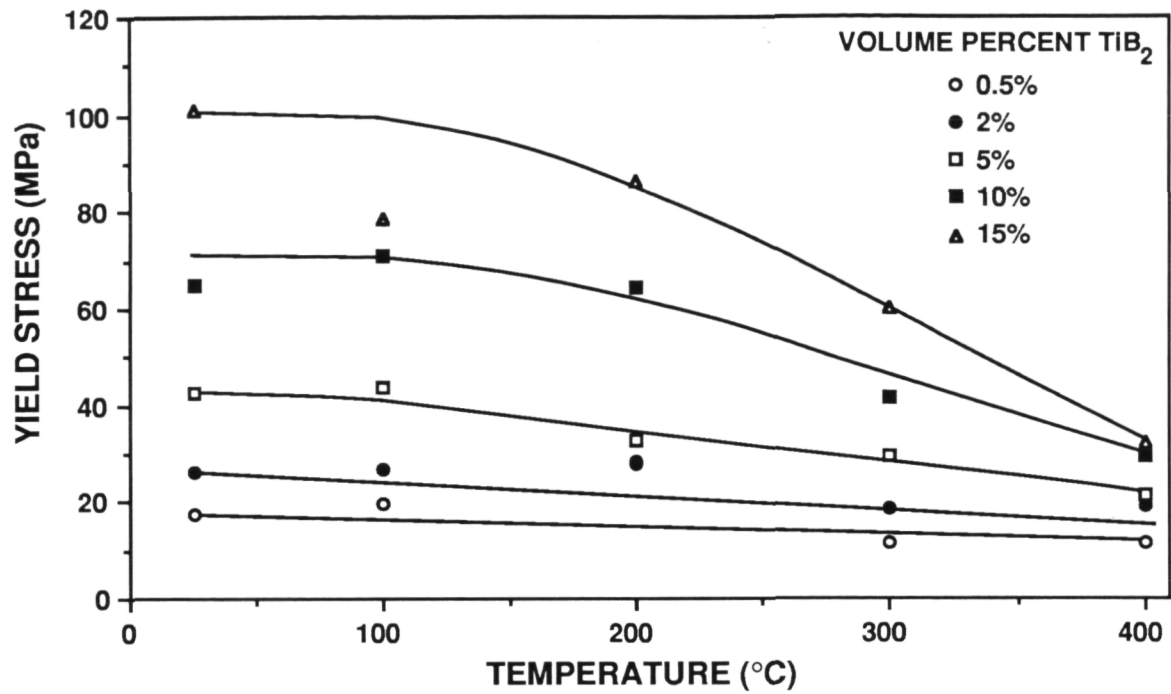


(a) Pure aluminum plus 1/2 vol% TiB_2 , reduction in area 9.6%.

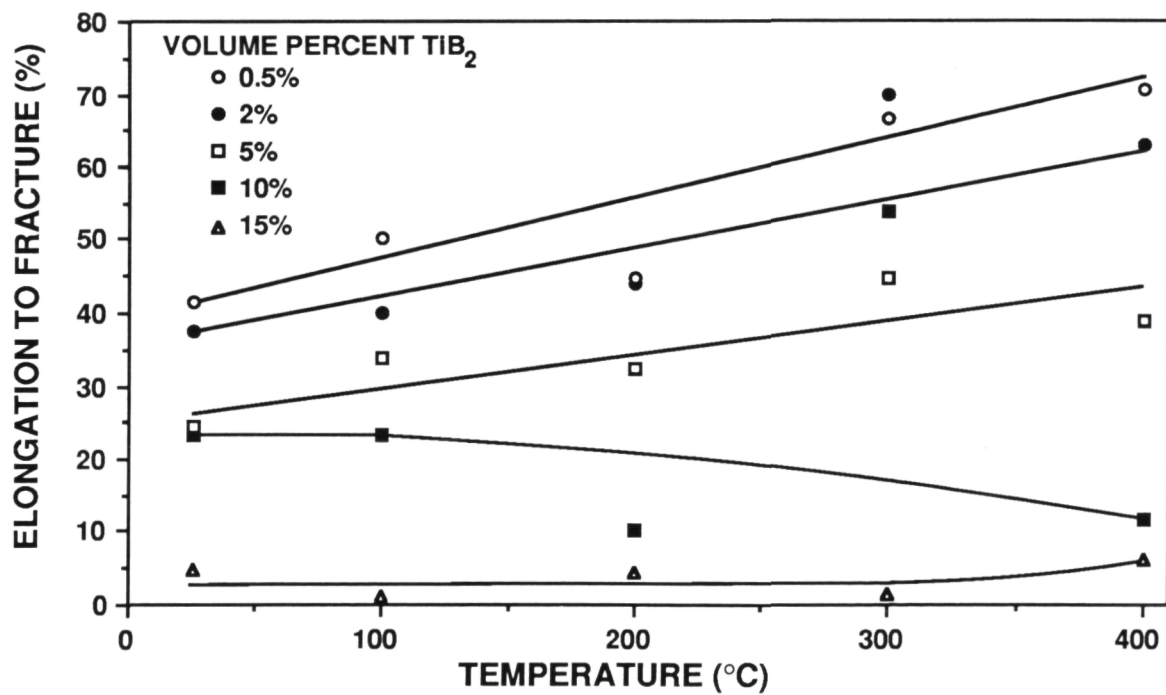


(b) Pure aluminum plus 5 vol% TiB_2 , reduction in area 11.7%.

Figure 3.10 TEM micrographs taken from gauge section of aluminum reinforced with TiB_2 , pulled in tension at room temperature.



(a) Yield stress



(b) Elongation to fracture

Figure 3.11 Tensile properties as a function of test temperature for forged and annealed pure aluminum with various loadings of $0.3 \mu m$ TiB_2 .

corresponding plot, Fig. 3.11(b), shows the elongation to fracture as a function of temperature. In general, the elongation of these materials increased gradually with increasing temperature.

4. TiB₂ IN Al-4%Cu-1.5%Mg

In subsequent chapters various aspects of the structure and properties of TiB₂ reinforced Al-4%Cu-1.5%Mg alloys will be examined such as the aging kinetics, strengthening mechanisms, fracture toughness, and fatigue. Prior to dealing with these specific topics, generic aspects of the microstructure will be examined in this chapter. This chapter also contains some topics which do not fit into sections of their own, such as the discussion of elastic modulus in Section 4.2.

4.1 Materials

4.1.1 Processing

Alloys with 0, 2, 5, 10, and 15 vol% TiB₂ were fabricated in an Al-4wt%Cu-1.5wt%Mg matrix using both master alloys described in Section 2.1. The alloys were produced by induction melting 99.99% pure aluminum, master alloys of Cu and Mg, and the XD™ master alloy. Thirty kilogram (60 lb) melts were cast into a 15.2 cm (6 in.) diameter mold and allowed to solidify. The ingots were then hot extruded into 7.0 cm by 1.6 cm (2.75 in. by 0.63 in.) bar at an aluminum extrusion house. The resulting extrusion ratio was 16:1. The chemical compositions of these alloys are listed in Table 4.1. Although the actual composition is slightly low in copper (Cu ~3.7%), it is quite close to the intended composition of Al-4%Cu-1.5%Mg.

4.1.2 As-Cast Microstructure: Particle Pushing

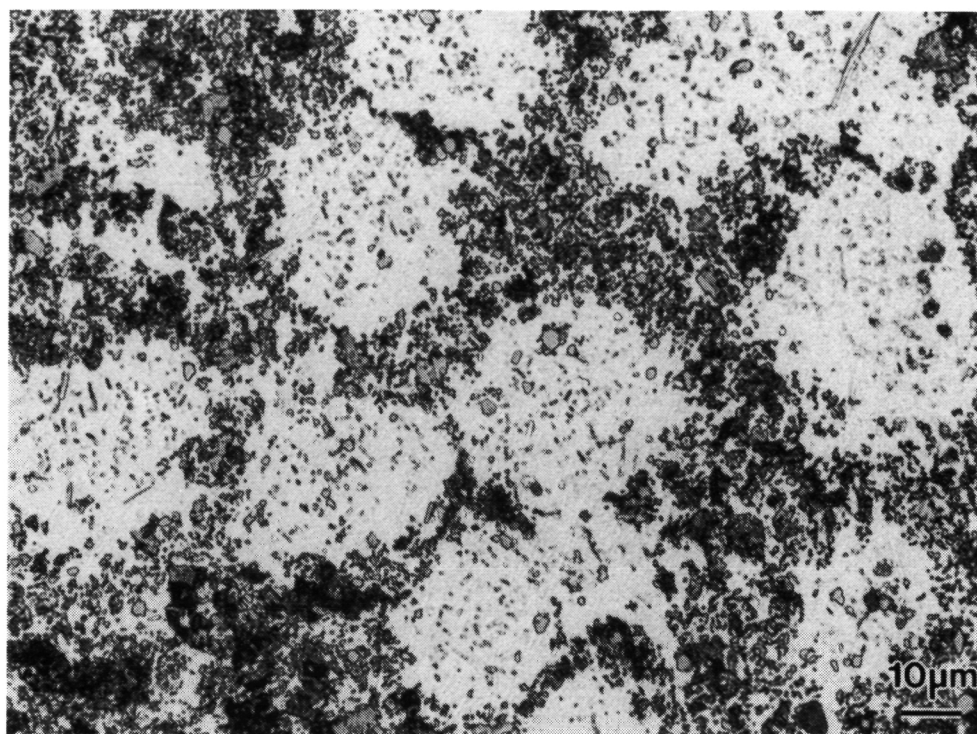
There are two distinct distributions of TiB₂ in the as-cast ingots. In the alloys with 1.3 μm TiB₂, the particle distribution is uniform, whereas the alloys with 0.3 μm TiB₂ show a pronounced cellular solidification structure. Figure 4.1(a-b) shows the difference in the as-cast microstructures in the two 10 vol% ingots. The circular lightly shaded areas of Fig. 4.1(a) are regions of very low TiB₂ content. Also present in these micrographs are the intermetallic particles CuAl₂, CuMgAl₂, and Cu₂FeAl₇ (both primary and eutectic).

When an insoluble particle is intercepted by a moving solidification front it can either be pushed or engulfed. Engulfment occurs through the growth of the solid over the particle and its subsequent enclosure in the solid. If the solidification front breaks down into cells, dendrites, or equiaxed grains, two or more solidification fronts can converge on the particle. In this case, the particle can be pushed between the solidification fronts, finally being entrained in the solid at the end of local solidification.

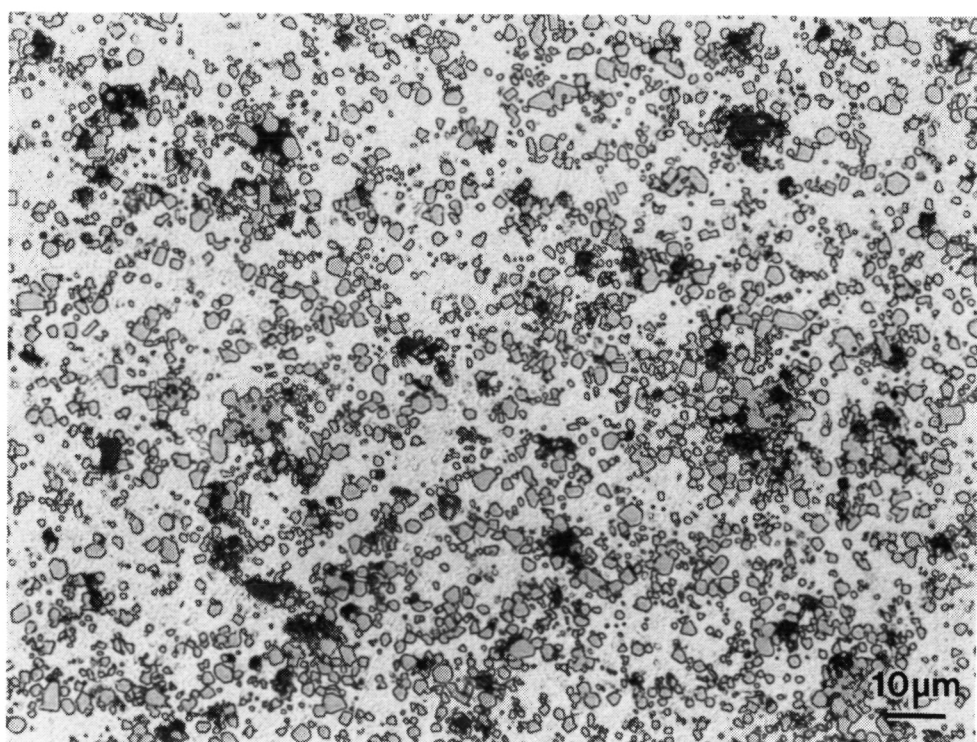
Table 4.1

Chemical composition of unreinforced and TiB₂ reinforced Al-Cu-Mg Alloys.

Alloy Designation	Nominal Loading (vol%)	Mean Size (μm)	Chemical Analysis (wt%)			
			Cu	Mg	Si	Fe
0401	Unreinforced		3.47	1.47	0.03	0.05
0202	2	0.3	3.67	1.54	0.03	0.06
0205	5	0.3	3.68	1.50	0.04	0.14
0210	10	0.3	3.83	1.38	0.06	0.17
0302	2	1.3	3.55	1.57	0.03	0.06
0305	5	1.3	3.84	1.56	0.03	0.08
0310	10	1.3	3.84	1.55	0.04	0.10
0315	15	1.3	3.92	1.57	0.04	0.12



(a) 0.3 μm TiB_2



(b) 1.3 μm TiB_2

Figure 4.1 Optical micrographs of the as-cast microstructure of Al-4%Cu-1.5%Mg alloys with 10 vol% TiB_2 of the two particle sizes (Keller's etch).

As discussed by Stefanescu, Dhindaw, Kacar, and Moitra [4] there is a critical solidification-front velocity, V_{cr} , above which the particles are engulfed at the liquid/solid interface. Below the critical velocity the particles are pushed. Omenyi and Neumann [5] showed that the critical velocity is empirically related to the particle radius by:

$$V_{cr} = \frac{K}{r^n} \quad (4.1)$$

where K is a constant and the exponent, n , ranges from 0.28 to 0.90. This equation shows that small particles are more likely to be rejected from the solidification front than large particles.

All of the Al-4%Cu-1.5%Mg alloys were cast under the same conditions, with the same amount of super heat, and thus the same solidification rate; only the particle size of the TiB_2 reinforcement was different. Therefore, the difference in the as-cast structures of the alloys must be attributable to the difference in the critical velocities at these two particle sizes. In the 0.3 μm TiB_2 ingots, the solidification rate was less than the critical velocity and the particles were rejected; in the 1.3 μm ingots, the solidification rate was greater than the critical velocity and the particles were engulfed.

It is interesting to note that the interface of the *in situ* XDTM composite affects the solidification behavior of these alloys. McCoy and Wawner [6] produced a Al-1.5%Mg+ TiB_2 composite by compo-casting an Al-Mg alloy with a commercially available 5 μm TiB_2 powder. These composites were directionally solidified over a range of solidification velocities and examined for particle pushing. For all solidification velocities examined, the 5 μm TiB_2 particles were pushed by the solidifying aluminum dendrites. The discrepancy between McCoy and Wawner's results and the results showing no pushing of the 1.3 μm TiB_2 used in this study could possibly be due to the presence of a thin non-wetting oxide on the surface of the TiB_2 used by McCoy and Wawner*. Such a non-wetting layer would drastically affect the particle rejection behavior of the system.

4.1.3 Extruded Microstructure

The solidification cell structure of the 0.3 μm TiB_2 ingots was not eliminated by subsequent processing. Figure 4.2(a-b) shows orthogonal views of the extruded microstructure for the two 10% alloys. The 0.3 μm TiB_2 alloy {Fig. 4.2(a)} has particle-

* It is not envisioned that the difference in the alloy compositions and the subsequent difference in the partition coefficients and solidification ranges, are significant enough to be responsible for the observed difference in behavior, though the possibility does exist.

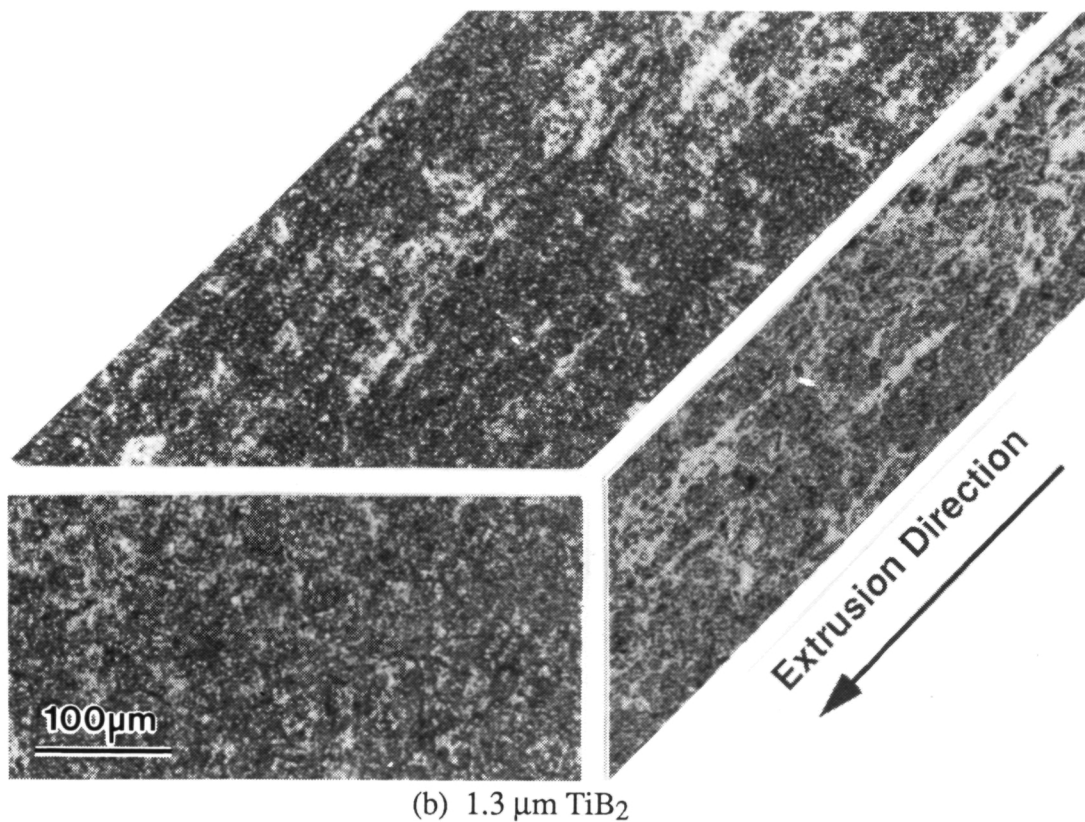
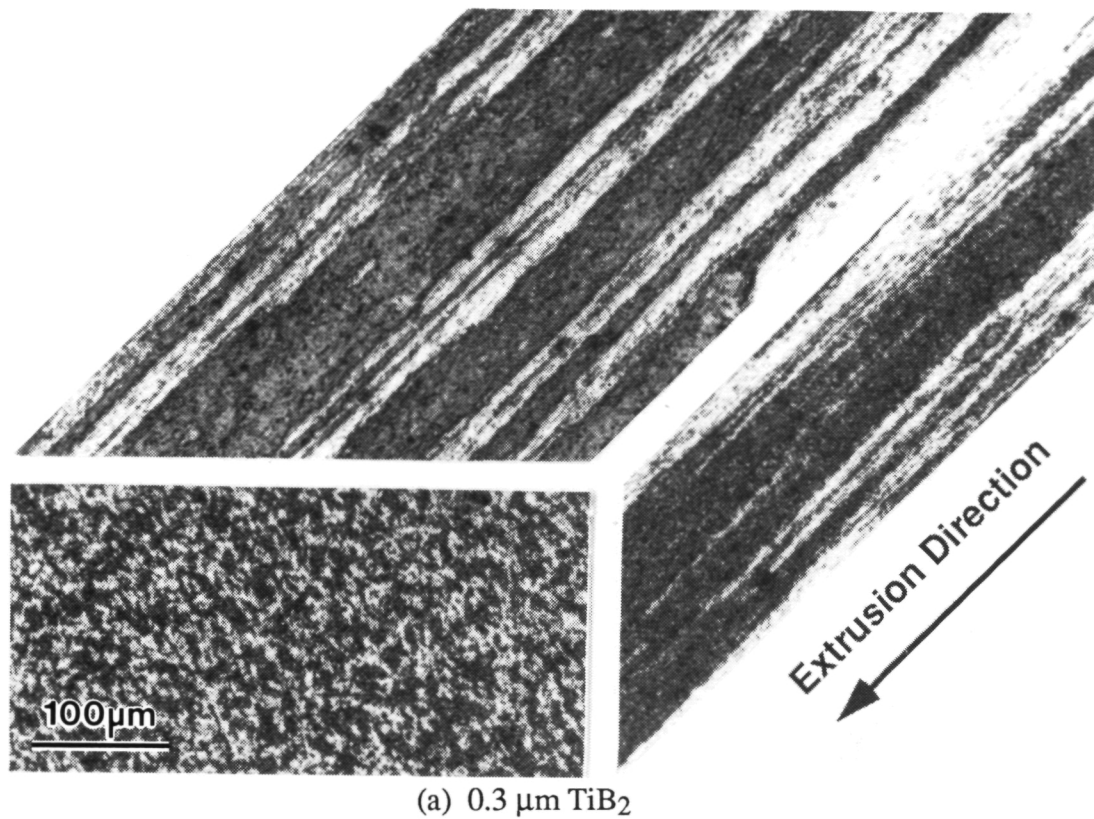


Figure 4.2 Orthogonal views of the extruded microstructure of Al-4%Cu-1.5%Mg alloys with 10 vol% TiB₂ of the two particle sizes.

deficient regions that are elongated in the direction of extrusion, whereas the 1.3 μm TiB_2 alloy {Fig. 4.2(b)} has a uniform distribution of particles.

The long transverse sections of the extruded unreinforced, 0.3 μm , and 1.3 μm alloys are shown in Figs. 4.3, 4.4(a-c), and 4.5(a-d), respectively, in the solutionized and naturally aged, T4, condition. The strung-out particles present in the unreinforced alloy (see Fig. 4.3) are the coarse intermetallics typically observed in 2000-series alloys. These are identified by their response to Keller's etch as the dark-colored round Al_2CuMg particles and the light-colored rectangular Cu_2FeAl_7 particles. This identification is confirmed and by energy dispersive spectroscopy, as shown in Figs. 4.7 and 4.8. These two intermetallics typically are present as the remaining insoluble phases in commercial 2024 alloys following solutionizing.

Although not as clearly defined as in the unreinforced alloy, the same dark-colored round Al_2CuMg particles are present in the reinforced alloys. The light-colored rectangular $\text{Al}_7\text{Cu}_2\text{Fe}$ particles are not as extensive in the 0.3 μm alloys and are difficult to discern in the 1.3 μm alloys. In the extruded 0.3 μm TiB_2 alloys (shown in Fig. 4.4), the intermetallics are present as clusters along with the TiB_2 particles. Because both intermetallics are associated with the last eutectic liquid to solidify, these clusters represent the TiB_2 particles and eutectic liquid that were rejected during solidification. In the extruded 1.3 μm TiB_2 alloys the intermetallics are associated with TiB_2 particle clumps in the 2% loading alloy {Fig. 4.4(a)}, whereas in the alloys with higher loadings the intermetallics are randomly distributed and TiB_2 clumps are not observed. This indicates that, except in the 2% loading, the 1.3 μm TiB_2 particles were not pushed by the advancing solidification front.

In a manner similar to the pure aluminum TiB_2 alloys, the grain size was determined by a combination of TEM and optical microscopy. As before, the grain diameter is taken to be \bar{L}_3 , the measured mean intercept length of grain boundaries. For the low loading, large grain size material, the mean intercept length of grain boundaries was measured from optical micrographs of samples heavily etched in Keller's etch to bring out the grain boundaries. For the higher loading, small grain size alloys, the grain size was too small to measure from etched samples. Here the mean intercept length was measured from TEM micrographs. In Fig. 4.8 the grain size, d , is plotted against the volume percent of TiB_2 . For the alloys with 5 vol% TiB_2 the grain size was determined by both methods and as shown in Fig. 4.8, there is good agreement between the two techniques.

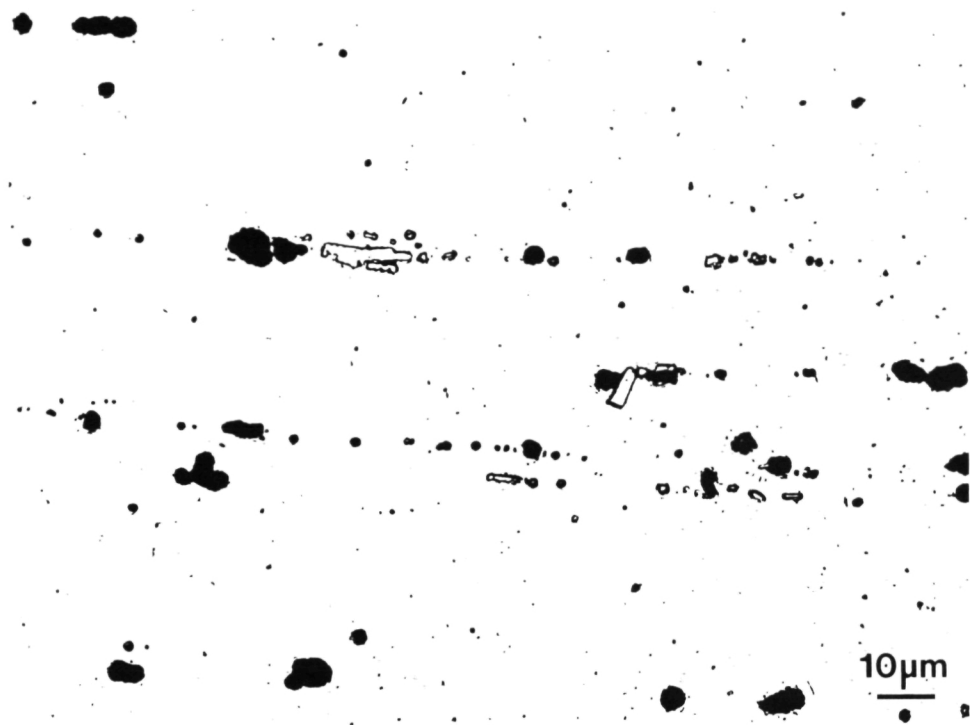
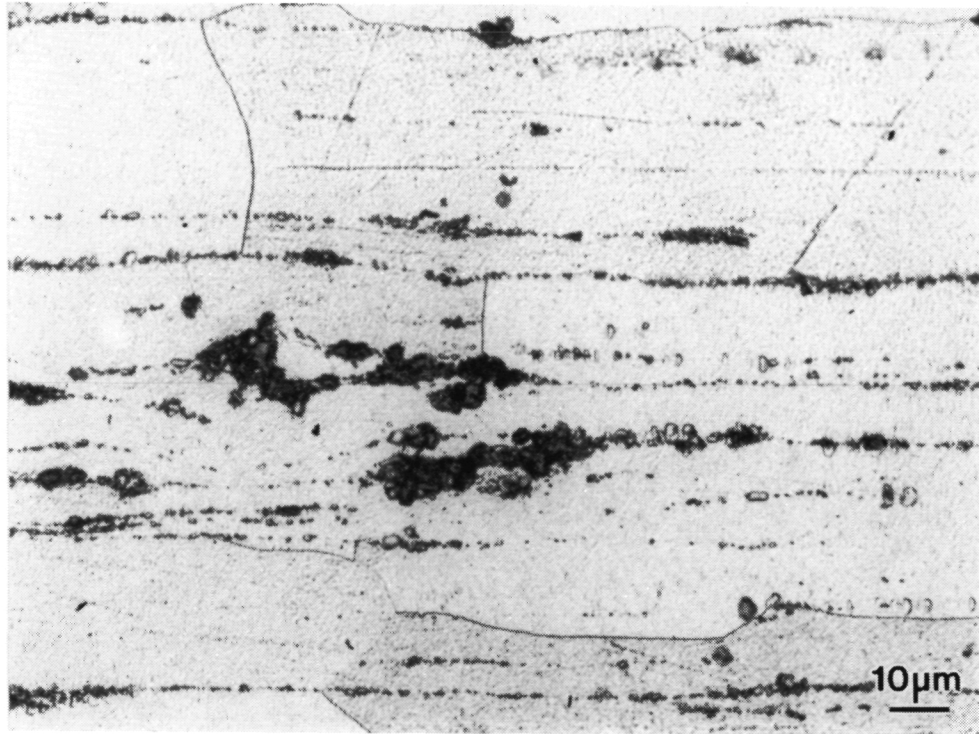
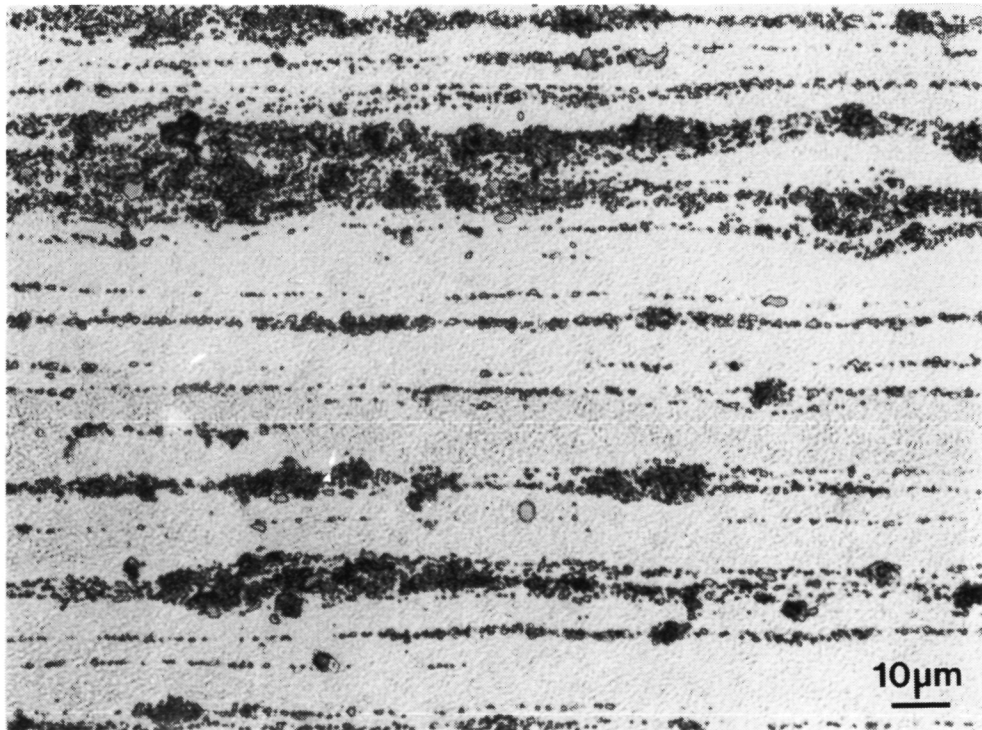


Figure 4.3 Optical micrograph of the long transverse direction of the extruded Al-4%Cu-1.5%Mg alloy in the T4 condition (Keller's etch).

ORIGINAL PAGE
BLACK AND WHITE PHOTOGRAPH

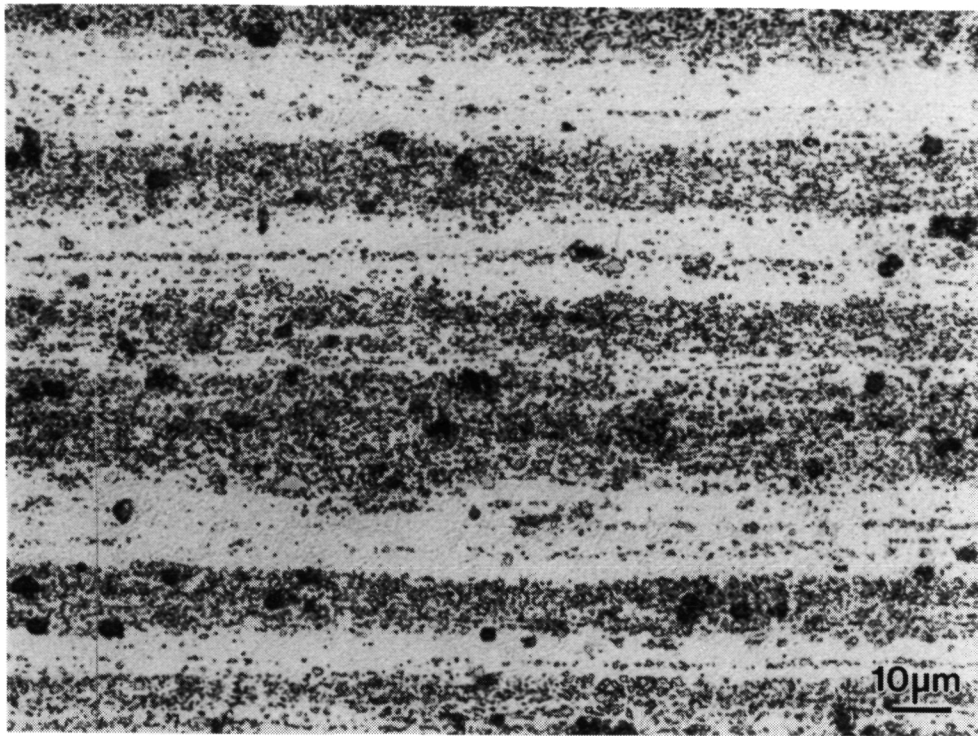


(a) 2 volume percent TiB_2



(b) 5 volume percent TiB_2

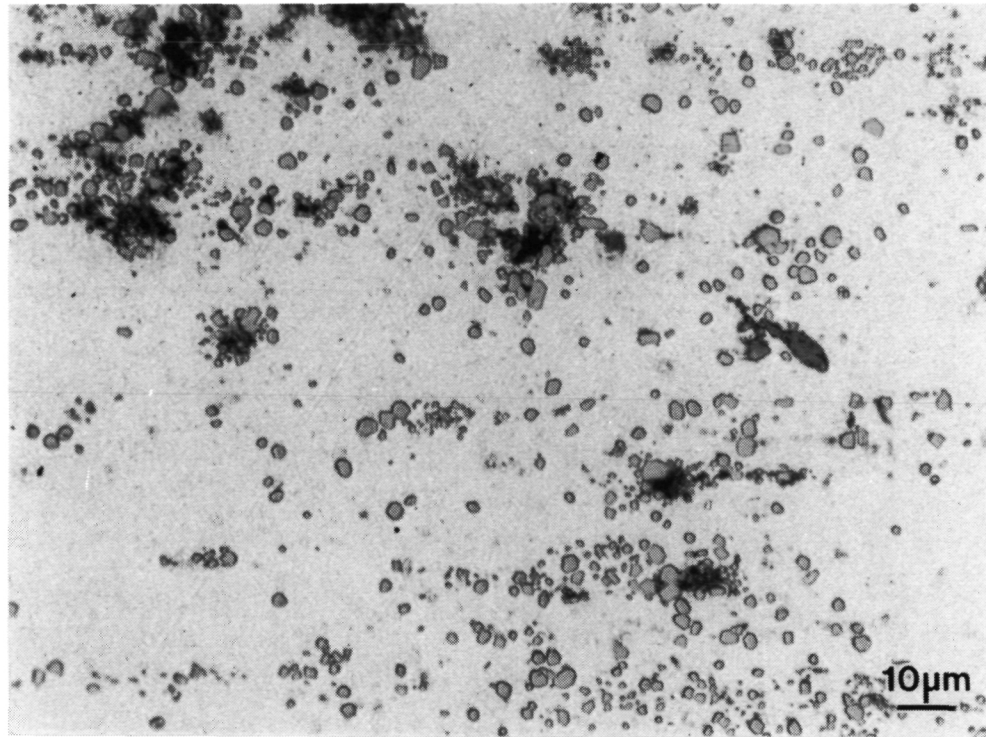
Figure 4.4 Optical micrograph of the long transverse direction of the extruded Al-4%Cu-1.5%Mg alloys with $0.3 \mu\text{m}$ TiB_2 in the T4 condition (Keller's etch).



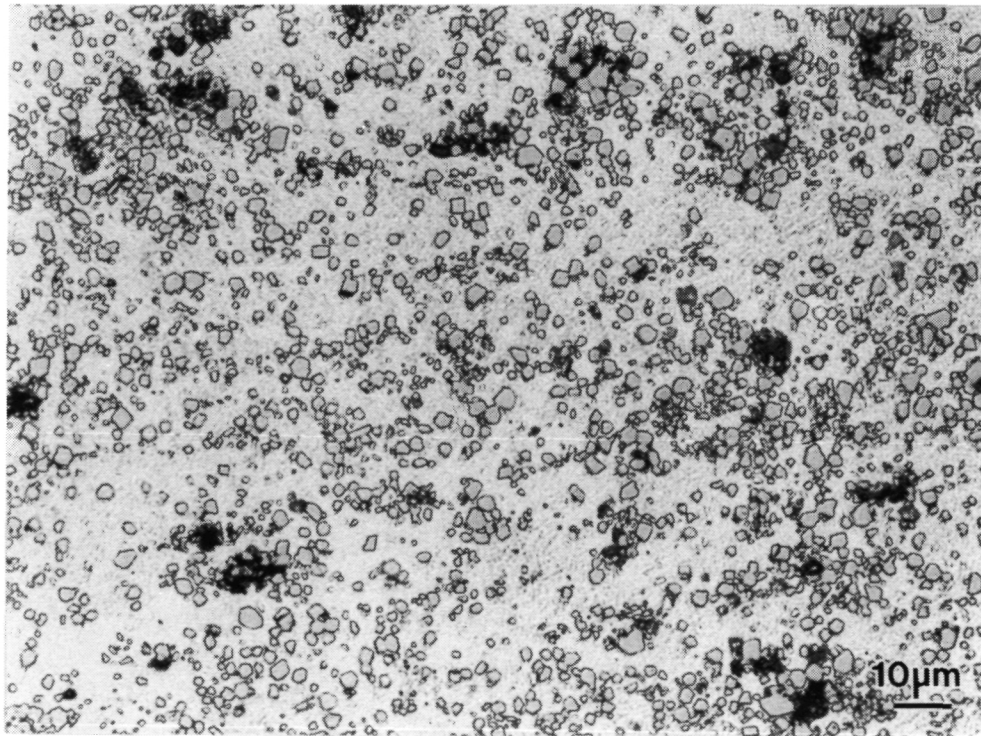
(c) 10 volume percent TiB₂

Figure 4.4 (cont) Optical micrograph of the long transverse direction of the extruded Al-4%Cu-1.5%Mg alloys with 0.3 μm TiB₂ in the T4 condition (Keller's etch).

ORIGINAL PAGE
BLACK AND WHITE PHOTOGRAPH

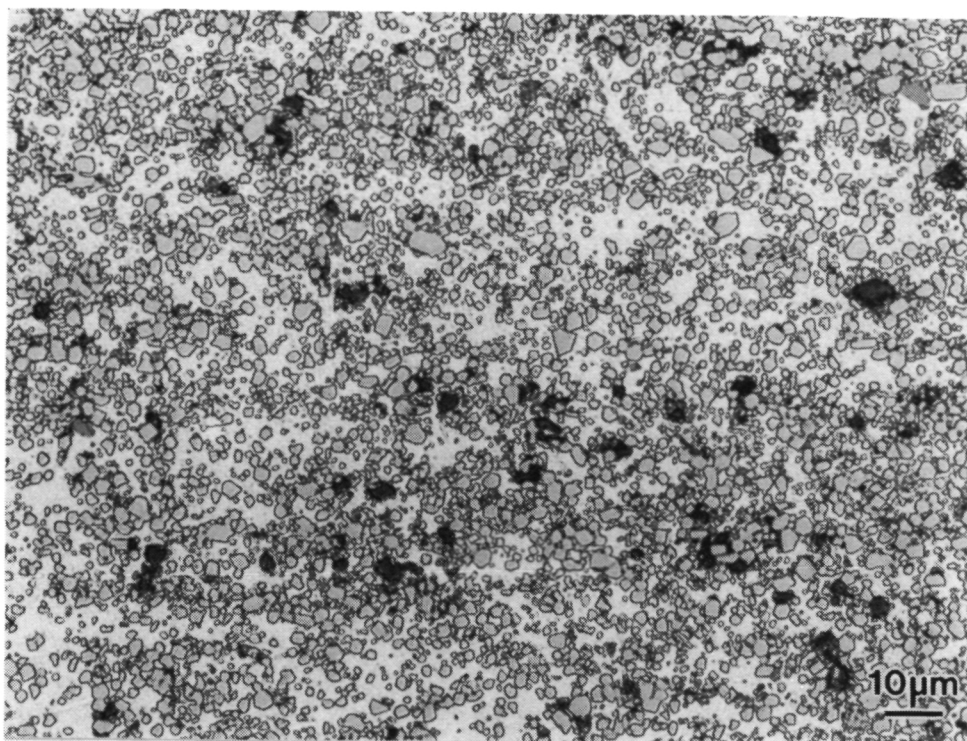


(a) 2 volume percent TiB_2

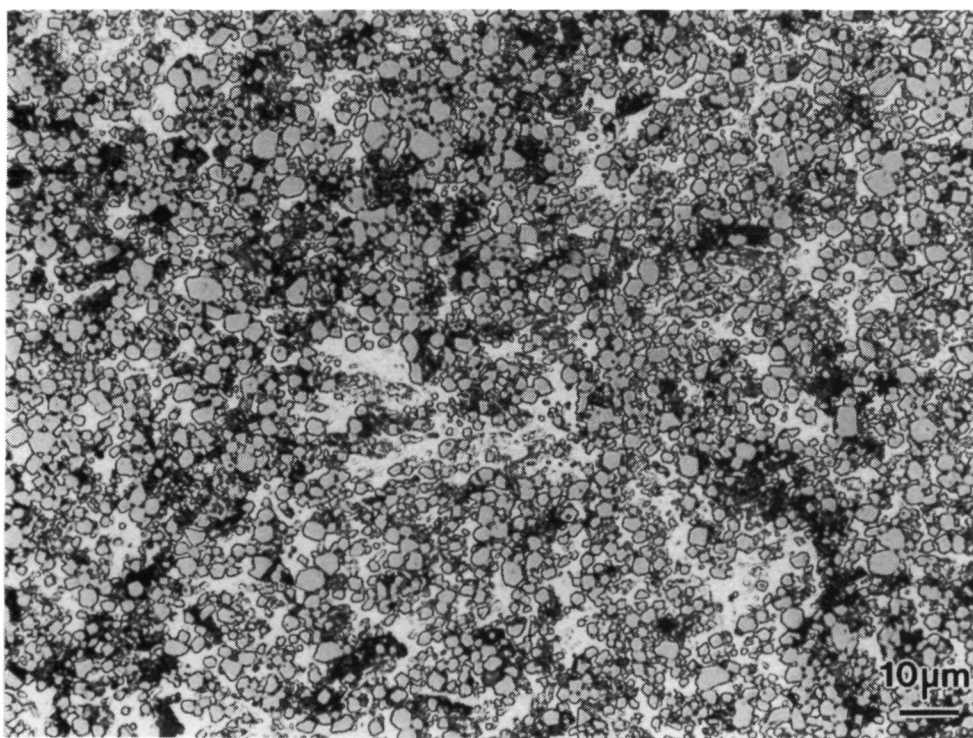


(b) 5 volume percent TiB_2

Figure 4.5 Optical micrograph of the long transverse direction of the extruded Al-4%Cu-1.5%Mg alloys with 1.3 μm TiB_2 in the T4 condition (Keller's etch).



(c) 10 volume percent TiB_2



(d) 15 volume percent TiB_2

Figure 4.5 (cont.) Optical micrograph of the long transverse direction of the extruded Al-4%Cu-1.5%Mg alloys with 1.3 μm TiB_2 in the T4 condition (Keller's etch).

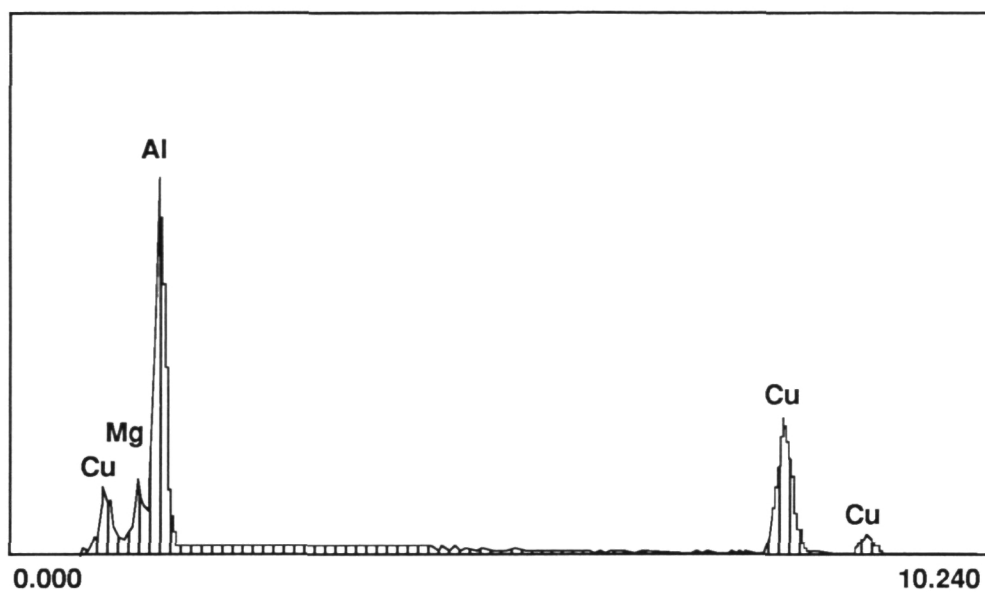
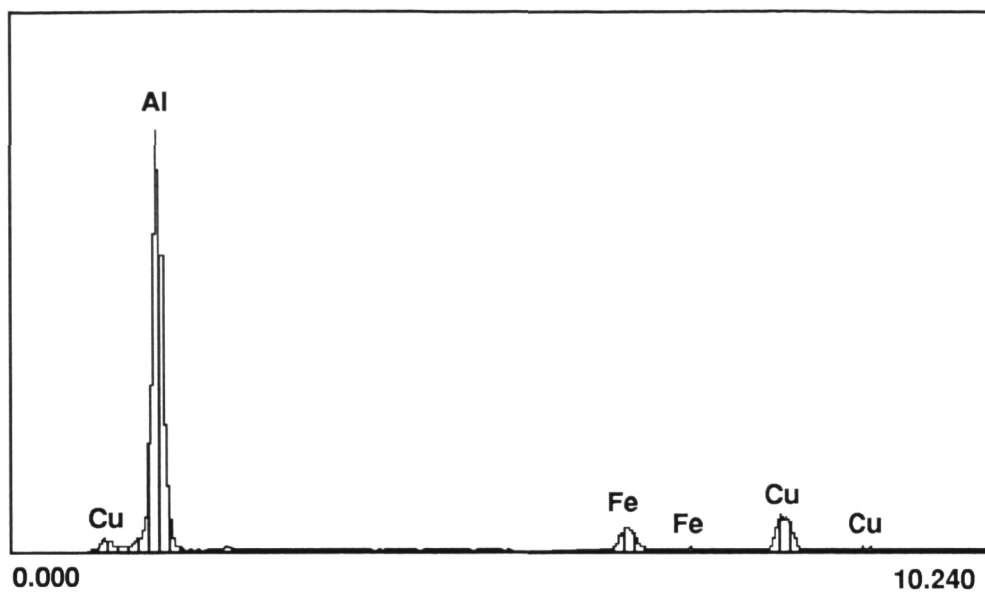
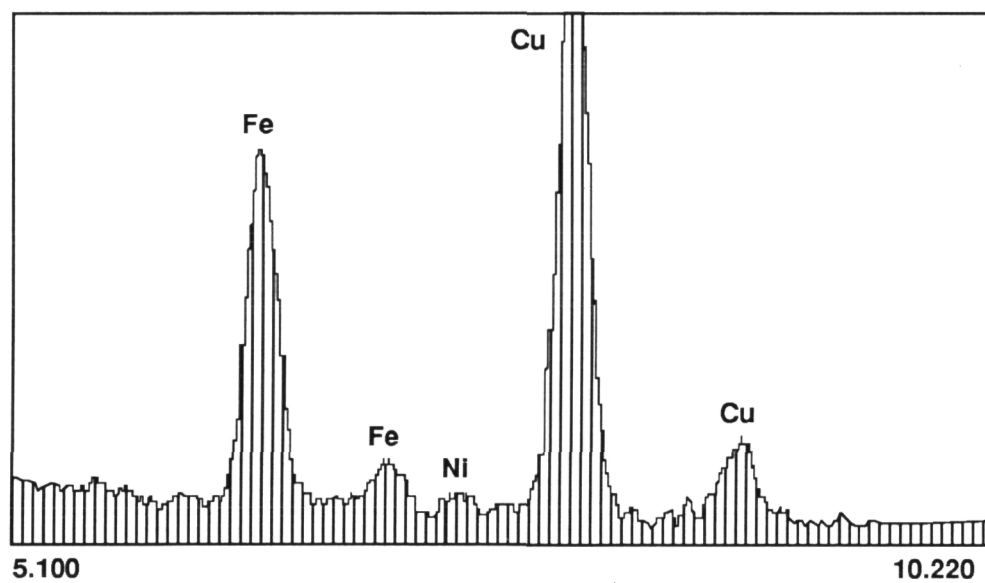


Figure 4.6 EDS spectra of dark-colored round Al_2CuMg particle shown in Fig. 4.3.



(a)



(b)

Figure 4.7 EDS spectra of light-colored rectangular $\text{Al}_7\text{Cu}_2\text{Fe}$ particle shown in Fig. 4.3.

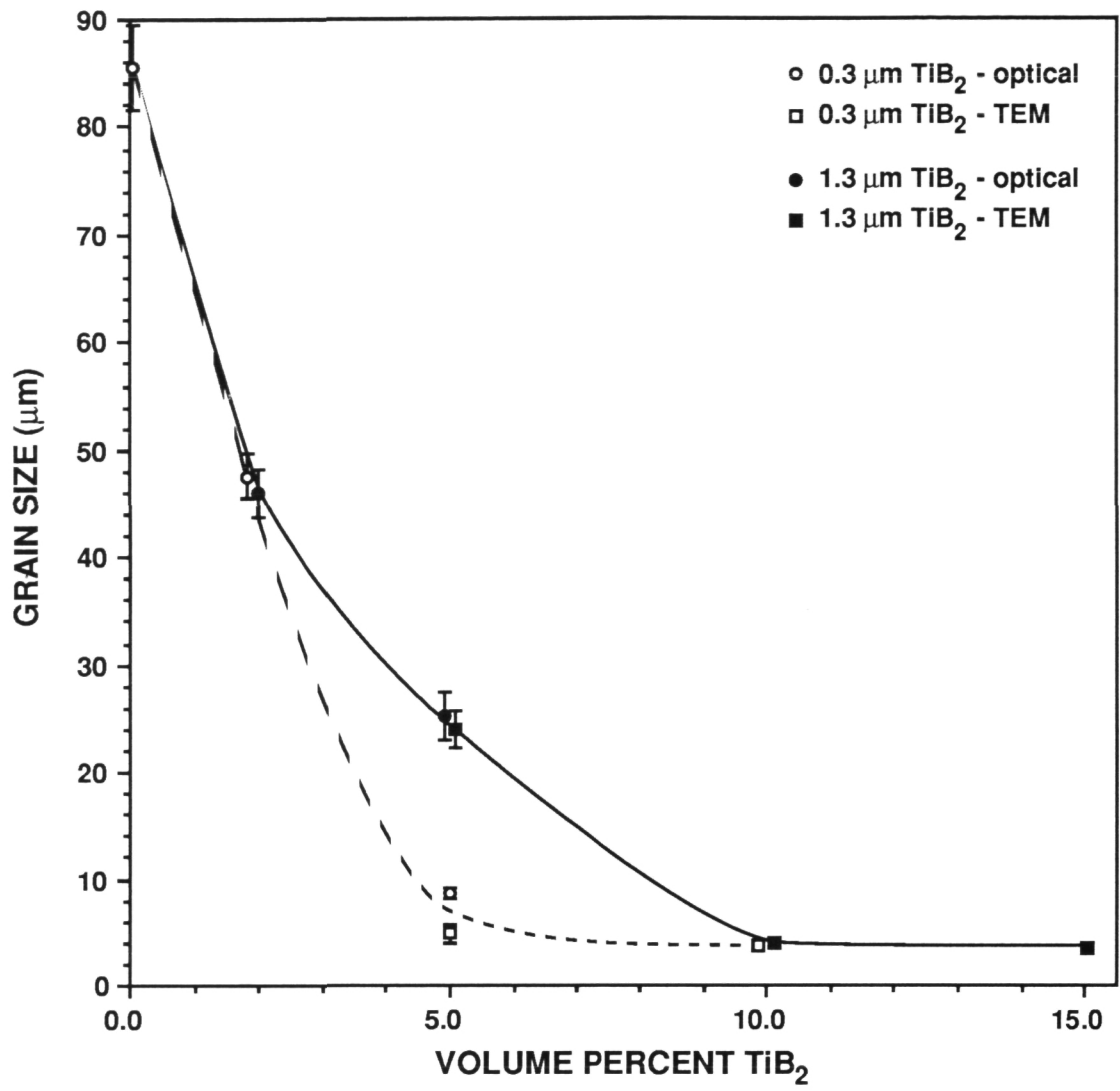


Figure 4.8 Variation of grain size with volume percent TiB₂ for Al-4%Cu-1.5%Mg alloys in naturally aged (T4) condition.

4.2 Elastic Modulus

An important advantage of the MMCs is that they have a much higher modulus than the unreinforced matrix.

Hashin and Shtrikman [7] have used a variational technique in the linear theory of elasticity to derive the upper and lower bound to the elastic constants for the case of a two phase material. Although other approximations such as the rule of mixtures, shear lag theory [8], and Eshelby's technique [8] have been used to determine the modulus of MMCs, the agreement between theory and experiment is poor. On the other hand the Hashin-Shtrikman lower bound consistently yields accurate results.

The Hashin-Shtrikman relations predict the effective bulk and shear moduli, K^* and G^* , of a two-phase material to be

$$K^*_{\text{lower}} = K_m + \frac{f}{\frac{1}{K_p - K_m} + \frac{3(1-f)}{3K_m + 4G_m}} \quad (4.2)$$

$$K^*_{\text{upper}} = K_p + \frac{(1-f)}{\frac{1}{K_m - K_p} + \frac{3f}{3K_p + 4G_p}} \quad (4.3)$$

$$G^*_{\text{lower}} = G_m + \frac{f}{\frac{1}{G_p - G_m} + \frac{6(K_m + 2G_m)(1-f)}{5G_m(3K_m + 4G_m)}} \quad (4.4)$$

$$G^*_{\text{upper}} = G_p + \frac{(1-f)}{\frac{1}{G_m - G_p} + \frac{6(K_p + 2G_p)f}{5G_p(3K_p + 4G_p)}} \quad (4.5)$$

where f is the volume fraction of particle, K the bulk modulus, G the shear modulus, and the subscripts p and m refer to the particle and matrix phases, respectively. The lower bound physically describes the situation where the "matrix" is the continuous phase, whereas the upper bound describes the situation where the "particle" is the continuous phase. The Young's modulus or modulus of elasticity can then be determined for the composite using the relationship

$$E = \frac{9KG}{3K + G}. \quad (4.6)$$

In Fig. 4.9, Young's modulus (determined by ultrasonic measurements) is plotted as a function of volume fraction and particle size. These measurements were taken from extruded samples that were solutionized and naturally aged, although typically the modulus of aluminum alloys is independent of heat treatment. Included in Fig. 4.9 are the Hashin-Shtrikman bounds, where the elastic constants $E_m=73$ GPa, $\nu_m=1/3$, $E_p=565$ GPa, and $\nu_p=0.13$ [9] have been used to calculate the bounding curves. As the figure shows, the modulus of the alloy increased with increasing TiB_2 additions. The experimental points lie close to the Hashin-Shtrikman lower bounds, as expected, since the aluminum matrix is the continuous phase. Within the accuracy of the experimental technique, particle size had no effect on modulus.

Because of the anisotropic distribution of particles observed in the extruded microstructure, the variation of modulus with orientation was examined for the unreinforced and the two 10% TiB_2 alloys. As Table 4.2 shows, there was a very slight increase in elastic modulus, i.e. approximately 1 GPa, in the longitudinal direction of both the reinforced and unreinforced alloys which is likely due to a slight crystallographic texture as a result of extrusion. Hence, the anisotropic distribution of particles in the 0.3 μm TiB_2 alloys is not manifested in the elastic modulus.

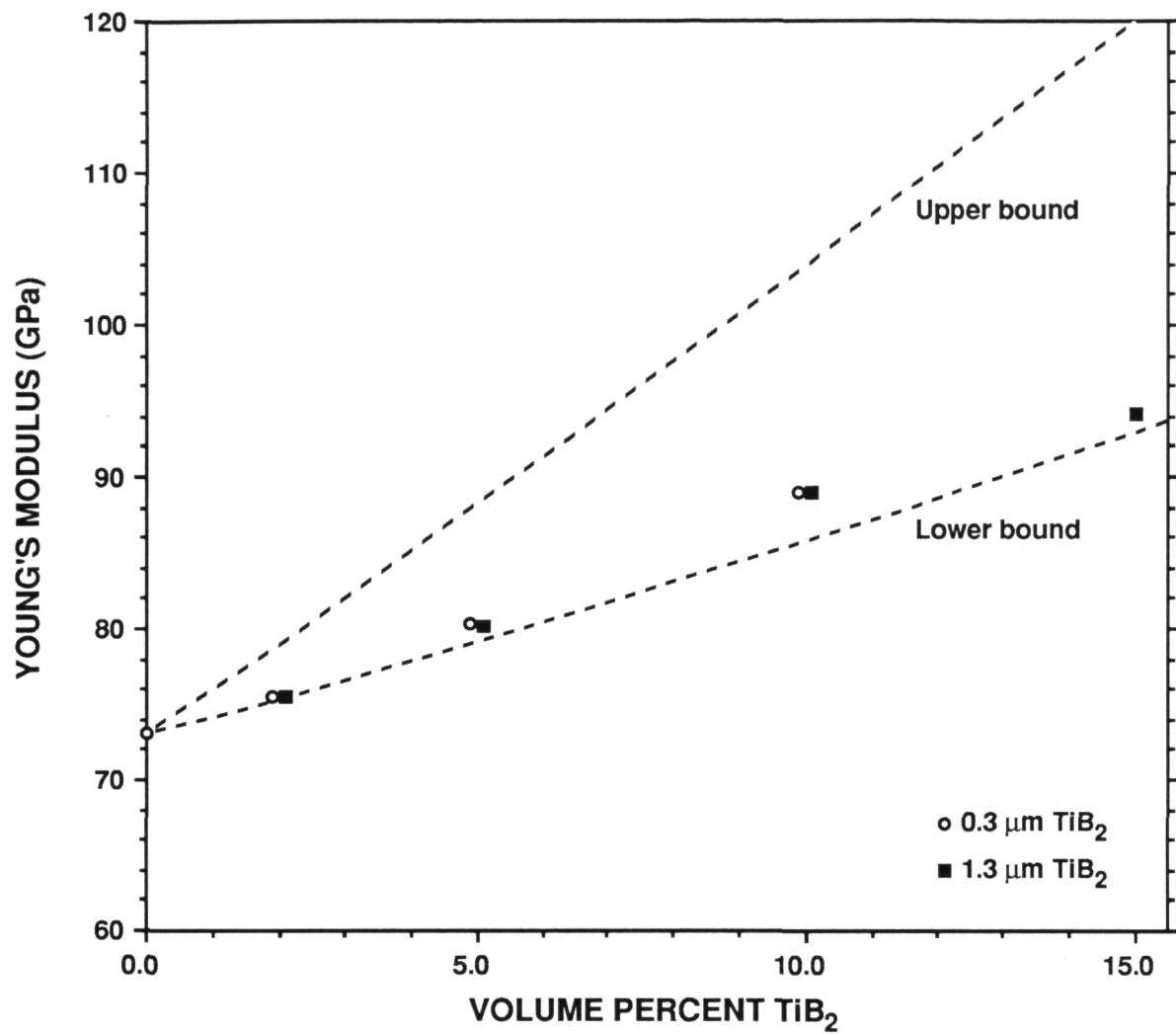


Figure 4.9 Dependence of Young's modulus on volume fraction for two different TiB_2 sizes in the Al-4%Cu-1.5%Mg alloys; also shown are the upper and lower bounds predicted by the Hashin-Shtrikman relationship.

Table 4.2

Young's modulus of Al-4%Cu-1.5%Mg extrusion vs direction in extruded bar.

	Young's Modulus (GPa)			Density (g/cm ³)
	Short Transverse	Long Transverse	Longitudinal	
Unreinforced	73.0	73.0	73.7	2.73
10vol% 0.3 μ m TiB ₂	88.9	88.2	89.6	2.93
10vol% 0.3 μ m TiB ₂	88.9	88.2	89.9	2.92

5. DISLOCATION GENERATION DUE TO CTE MISMATCH

When a MMC is held at a high temperature, such as occurs during solutionizing of the matrix, the matrix and particle equilibrate and reach a state of zero stress through plastic or diffusional relaxation. Hence, the hole in which the particle resides becomes a “perfect fit.” If the material is then cooled, both the particle and matrix change their dimensions due to thermal expansion. If the CTE of the particle and matrix differ then the hole will no longer be the correct size for the particle. This mismatch creates stresses which in turn are capable of generating dislocations around the particle. Because dislocations can affect both the mechanical properties and aging response of the composite we will examine the process of dislocation generation due to CTE mismatch in this chapter.

5.1 Dislocation Punching Models

The stress field around a misfitting inclusion is a classic problem of engineering mechanics and has been examined by a number of authors, including Eshelby in his classic work [10]. The extension of this problem to the elasto-plastic case fall into two classes: those that utilize a dislocation nucleation model and those that use the continuum mechanics approach of generalized yielding.

5.1.1 Dislocation Nucleation Model

Models that determine the critical misfit required to nucleate dislocations at a misfitting particle have been proposed by Weatherly [11]; Brown, Woolhouse, and Valdré [12]; Brown and Woolhouse [13]; and Ashby and Johnson [14]. Weatherly's criterion simply requires that the maximum shear stress at the particle-matrix interface exceed the theoretical shear stress for the matrix; this defines an upper limit to the critical misfit. A lower limit to the critical misfit is obtained by requiring that the energy of the system be decreased if the dislocation loop is generated at a particle. In this way, Brown et al. obtained a lower limiting misfit for the generation of a prismatic loop at the particle-matrix interface. Ashby and Johnson propose a model where a shear loop is nucleated at the particle. The shear loop then transforms by cross-slip into a prismatic loop, a mechanism that is perhaps more physically realistic than the punching of a prismatic loop directly.

The results of the Ashby-Johnson model are cast in terms of the constrained strain of the particle which, in turn, is determined from the stress free transformation strain. The stress free transformation strain is the strain that arises due to a particle misfit where it is assumed that the matrix and particle can move independently of each other, i.e., as if the particle had been

removed from the matrix and the particle and hole change size independently. In terms of the cooling problem, the stress free transformation strain is

$$e_{11}^t = (\alpha_m - \alpha_p) \Delta T \quad (5.1)$$

where α is the CTE, ΔT is the temperature difference, and the subscripts p and m refer to the particle and matrix, respectively. The strain produced once the particle is replaced in the hole and allowed to elastically relax is the constrained strain. The constrained strain is

$$e_{11}^c = \left(\frac{3K_p}{3K_p + 4G_m} \right) e_{11}^t \quad (5.2)$$

where K is the bulk modulus, G is the shear modulus, and the subscripts are as defined above. A critical misfit is then defined as the minimum constrained strain that allows for dislocation generation for a given particle size.

Ashby and Johnson's results are shown in Fig. 5.1 where the critical misfit is plotted against particle diameter. The upper limit represents the generation of dislocations by exceeding the theoretical shear strength of the matrix, essentially $G/2\pi$. Nucleation of new dislocations at a coherent interface is extremely difficult and is experimentally found to be on the order of $G/2\pi$. The lower limit represents the generation of dislocations over an activation energy barrier. Nucleation of new dislocations at an incoherent interface tends to follow the lower limit as shown by the experimentally determined values obtained for various particle types and degrees of misfit. The stresses are much lower, on the order of $G/100$, and decrease as the particle size becomes larger.

In Table 5.1 the stress free transformation strain and constrained strain for various reinforcements in an aluminum matrix are tabulated along with the physical constants [9] used to calculate them. It has been assumed that the misfit arises from the CTE mismatch created by quenching from 500°C to room temperature and that no relaxation or dislocation punching occurs during the quenching operation. This is the same temperature change produced when quenching from the solutionizing temperature in many age-hardenable aluminum alloys. The calculated constrained strains and Ashby-Johnson's lower bound (Fig. 5.1) are used to determine a critical particle diameter, D_{crit} , above which dislocation punching due to CTE mismatch might be expected; values of D_{crit} are tabulated in Table 5.1.

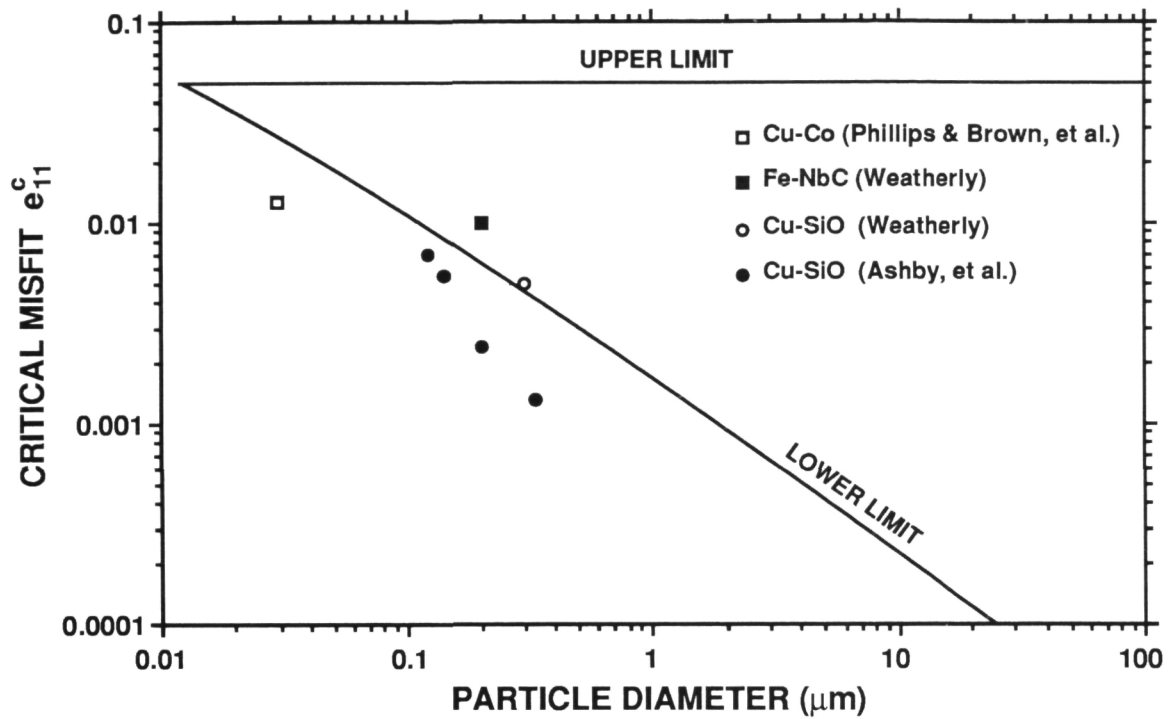


Figure 5.1 Critical misfit as a function of particle diameter after Ashby and Johnson [14]. Experimental data [12,15-17].

Table 5.1

The elastic constants of aluminum and potential reinforcements along with the stress free transformation strain and constrained strain produced in MMCs reinforced with the indicated particles when quenched from 500°C to room temperature.

Material	ν	E (GPa)	CTE (10^{-6} K^{-1})	e_{11}^t	e_{11}^c	D_{crit} (μm)
Al	0.33	73	22.0	-	-	-
TiB ₂	0.13	565	8.10	0.0066	0.0058	0.22
SiC	0.19	483	4.95	0.0081	0.0071	0.16
TiC	0.19	430	8.00	0.0067	0.0057	0.22
Al ₂ O ₃	0.26	380	7.90	0.0067	0.0059	0.21
TiN	0.24	251	8.00	0.0067	0.0054	0.23

5.1.2 Continuum Models

For larger particles, generalized yielding has been used as a criterion for the elasto-plastic deformation of a misfitting inclusion. For a misfitting sphere the problem is essentially that of elasto-plastic deformation of a thick hollow sphere under internal pressure [18-20]. Lee, Earmme, Aaronson, and Russell [21] have used the continuum method of Christian [22] to consider a misfitting sphere in both an elastic and elasto-plastic matrix. The stress as a function of position from the particle-matrix interface is determined as well as the strain energy. This model assumes a perfectly plastic matrix (no work hardening). For large particles the effective yield stress is determined from the von Mises yielding criterion; for smaller precipitates a size-dependent yield stress is obtained from the Ashby-Johnson model. The model of Lee et al. [21] has been extended by Earmme, Johnson, and Lee [23] to include work hardening effects and by Kim, Lee, and Plichta [24] to include volume fraction effects.

For whisker reinforced materials, Taya and Mori [25] model a particle in an elasto-plastic matrix by considering two concentric prolate ellipsoids with the same minor axis but differing major axis. The smaller ellipse represents the particle and the larger the limit of the plastic zone. The stress field is determined using Eshelby's equivalent inclusion method [10], and the plastic zone size is determined by equating the gradient of the potential energy to the gradient of the work done by the motion of the punched dislocation loops. The resulting plastic zone size is a function of particle aspect ratio, ΔT , and matrix friction stress.

Dutta, Bourell, and Latimer [26] use finite element methods and the method of Hill [18] to calculate the plastic zone size and shape around reinforcements with various morphologies including plates and whiskers.

Arsenault and Shi [27] used a geometric model to consider a rectangular inclusion which punched dislocations from its edges due to CTE mismatch. The model calculates dislocation density for a given volume fraction, ΔCTE , ΔT , and particle size. It was assumed that all of the thermal strain was relieved by dislocation punching; thus, there is no yield criteria. It was also assumed that there is no dislocation drag and no dislocation interaction; thus, dislocations filled the matrix uniformly. The model includes volume fraction effects, and since dislocation density is proportional to the sum of the inclusion edges, smaller particle sizes yield a higher dislocation density, for a given volume fraction.

5.2 Experimental Evidence of Dislocation Punching in MMCs

Flom and Arsenault [28] examined the plastic zone size of a cylindrical macro-composite of polycrystalline SiC in pure Al by observing slip bands on a polished surface as a function of cooling rate.

Arsenault and Shi [27] measured bulk dislocation density of 6061 reinforced with SiC plates which was thermally cycled in a high voltage TEM with a hot stage. The samples were heated and then cooled over an approximately 1 hour period. During the cooling cycle the generation of dislocations at the SiC-matrix interface as observed. This work was expanded upon by Volgelsang, Arsenault, and Fisher, [29] who examined 6061 with 0, 5, and 20 vol% SiC whiskers and 6061 with 20 vol% SiC plates and observed that the intensity of dislocation generation at the particle-matrix interface is related to the size and shape of the SiC particles. Dislocation generation is lowest for small, nearly spherical particles and increases with increasing particle size. Particle corners acted as stress concentrators. These authors also observed precipitates nucleating upon dislocations during cooling.

Christman and Suresh [30] use Taya and Mori's model to calculate dislocation density. Experimentally they observe higher dislocation density in SiC whisker reinforced 2024 than in unreinforced alloy. They also observe a higher concentration of helical dislocation loops in the reinforced alloy than in the base alloy, which they attribute to a higher density of quenched-in vacancies in the composite.

Kim, Lee, and Plichta [24] examined 2024 with several sizes of SiC (22, 14, and 5 μm) and 2024+TiC of several loadings (0, 2, and 10 vol%). Alloys were produced by hot pressing powders, hot rolling the resulting ingots, solutionizing, and water quenching. Thin foil samples were prepared by electropolishing. Dislocation density was then determined as a function of distance from the particle-matrix interface using TEM. For large particles ($\sim 10 \mu\text{m}$), a gradient was observed with dislocation density increasing as the particle-matrix interface was approached. As the SiC volume fraction increased, dislocation density increased and the dislocations occupied a wider area. Like the findings of Volgelsang et al. [29], the intensity of dislocation generation is related to the size and shape of the SiC particles. Very few dislocations were associated with small submicron particles, while with increased particle size dislocation density near the particle increased significantly. The dislocation density observed in the 2024+TiC composites was significantly less than in the 2024+SiC composites. This is attributed to the smaller ΔCTE and difference in elastic constants.

5.3 Dislocation Punching in Al-4%Cu-1.5%Mg+TiB₂

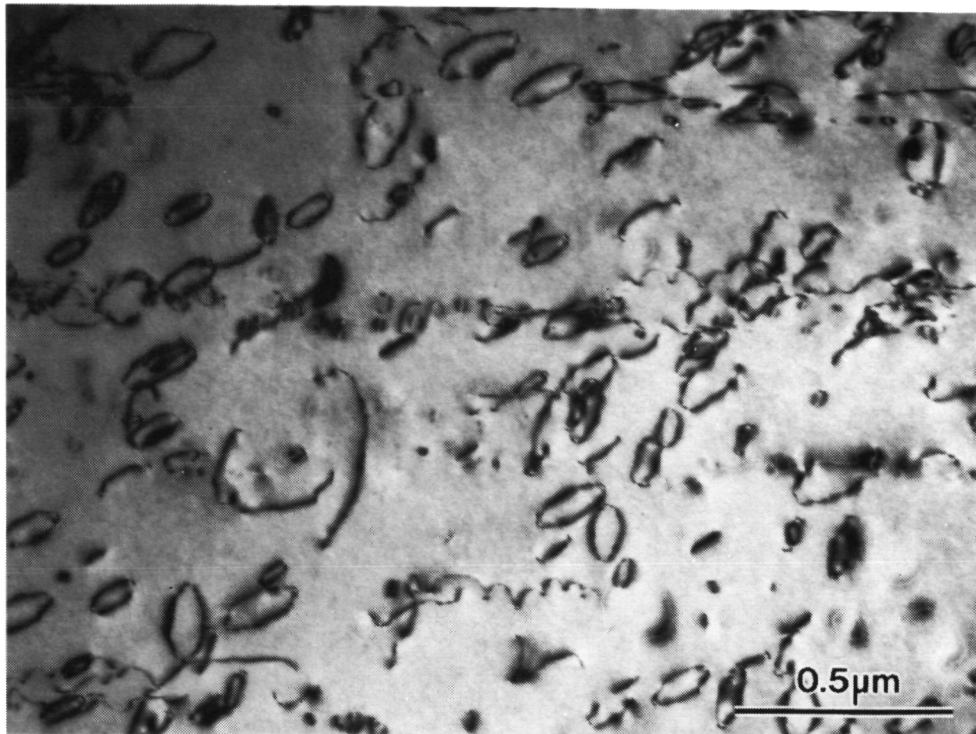
In this section we will examine the dislocation structures in Al-4%Cu-1.5%Mg alloys, with and without TiB₂. The microstructural condition examined is the T4 condition, where the alloys have been solutionized at 493°C, cold water quenched, and then allowed to naturally age at room temperature for several months. Since this is the microstructural state from that subsequent artificial aging was initiated (see Chapter 6) this is the condition which impacts the aging kinetics and, in turn, is the reason for our primary interest in dislocation punching. It might appear that the as-quenched condition would be a better condition in which to study dislocation punching because of the possibility of dislocation recovery and the formation of dislocation loops from vacancy condensation. However, the naturally aged condition offers the advantage that the G.P. zones will act to pin dislocations and thus reduce dislocation rearrangement during TEM thin foil preparation.

The TEM foils were prepared by mechanically thinning quenched and naturally aged bulk samples down to 0.25 mm (0.010 in.). Three millimeter disks were then punched and the foils were electropolished until perforation in a twin-jet electropolisher at -30°C and 15V using a solution of 25% nitric acid in methanol. Once perforated the samples were rinsed in 3 methanol baths, dried, and examined at 100 KV in a JEOL 100CX microscope using a double-tilt goniometer.

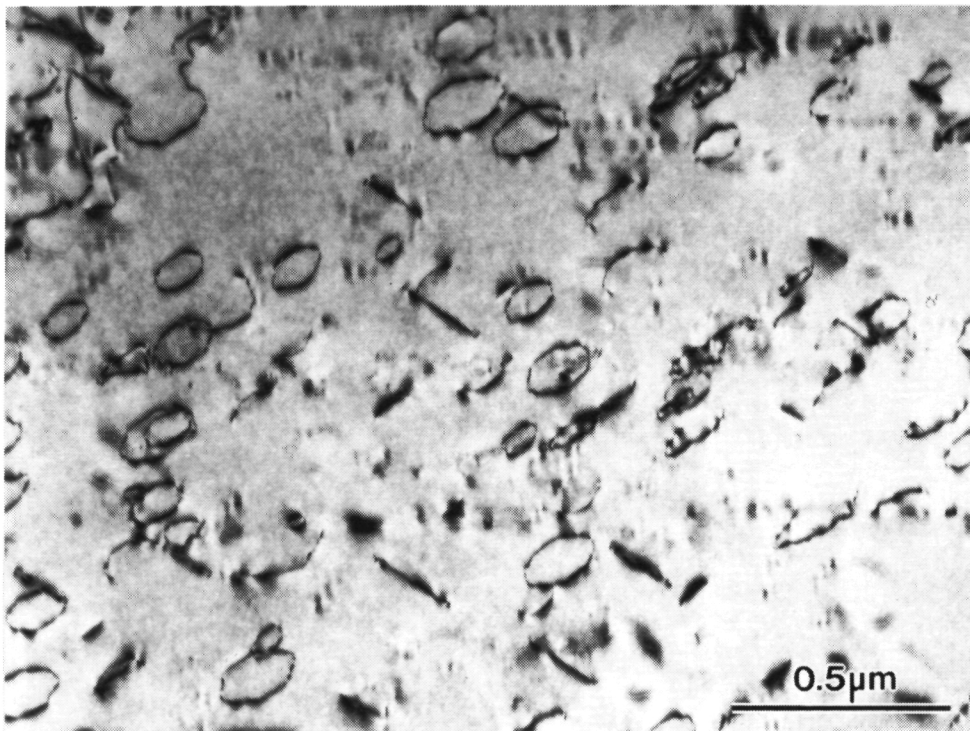
Figure 5.2 is a bright field TEM image taken using the indicated two-beam conditions showing the dislocation structure of an unreinforced Al-4%Cu-1.5%Mg alloy that was solutionized at 493°C, cold water quenched, and then allowed to naturally age at room temperature for several months. The dislocations are primarily in the form of dislocation loops although some linear and helical dislocations are present. The dislocation loops occur by the condensation of vacancies and are a very typical microstructure of aluminum alloys in the T4 condition.

In Figs. 5.3 and 5.4 the dislocation substructure of an alloy with 2 vol% TiB₂ in Al-4%Cu-1.5%Mg is shown. Figure 5.3 contains a TiB₂ particle which is approximately 0.4 μm in diameter. There are more linear dislocations in this sample than in the unreinforced alloy and fewer dislocation loops. Some of the linear dislocations appear to be associated with the particle, but the association could be incidental. Figure 5.4 contains a TiB₂ particle approximately 0.8 μm in diameter. In this sample dislocation loops are clearly being punched out at the corners of the particle. Also observe that the uniform dislocation loops from vacancy condensation in this region are much fewer than in the unreinforced alloy.

As shown in Table 5.1, the Ashby-Johnson model predicts that the critical diameter for TiB₂ is 0.2 μm for these conditions. The critical diameter is the lower limit that requires the

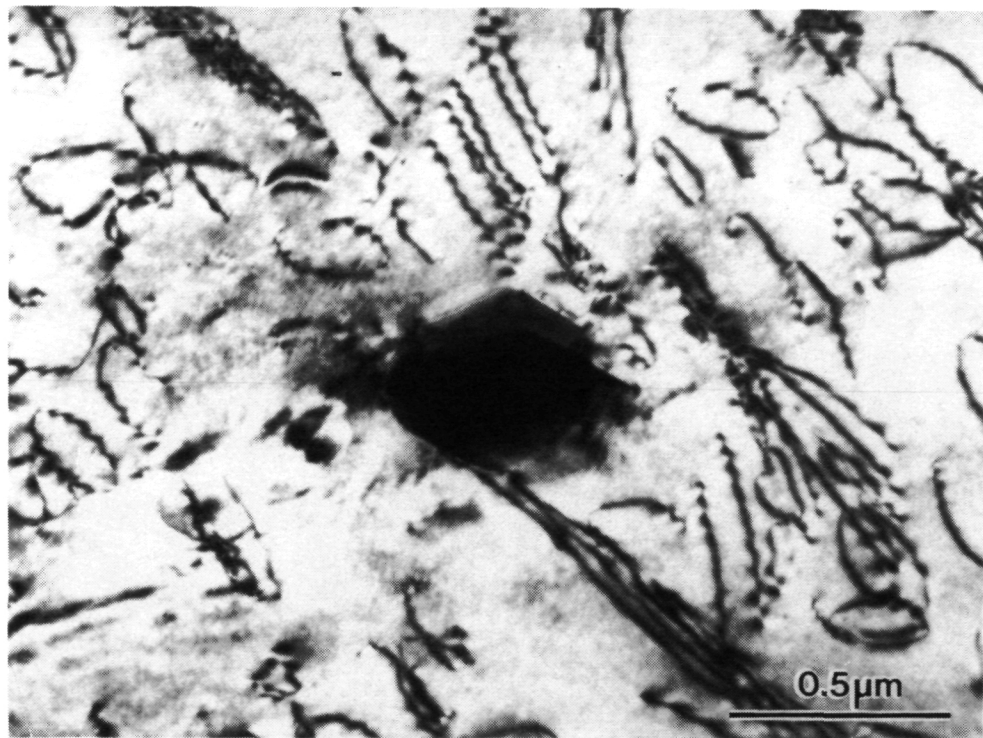


(a) Two-beam condition with $\vec{g} = (002)$ near $[110]$.

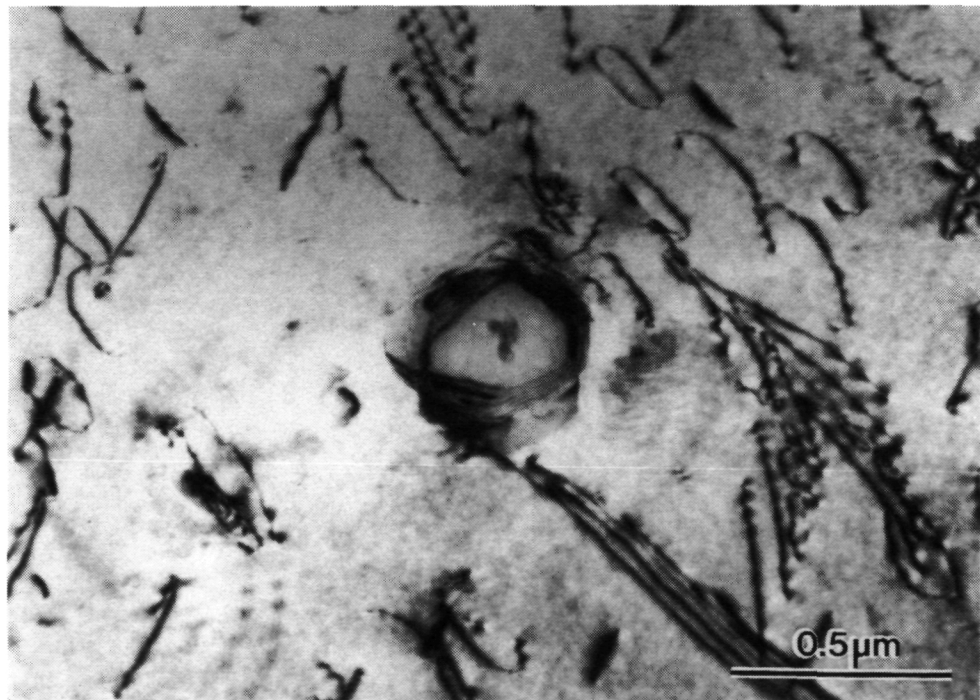


(b) Two-beam condition with $\vec{g} = (1\bar{1}1)$ near $[110]$.

Figure 5.2 TEM micrographs showing dislocations in unreinforced Al-4%Cu-1.5%Mg alloy in solutionized, quenched, and naturally aged (T4) condition.

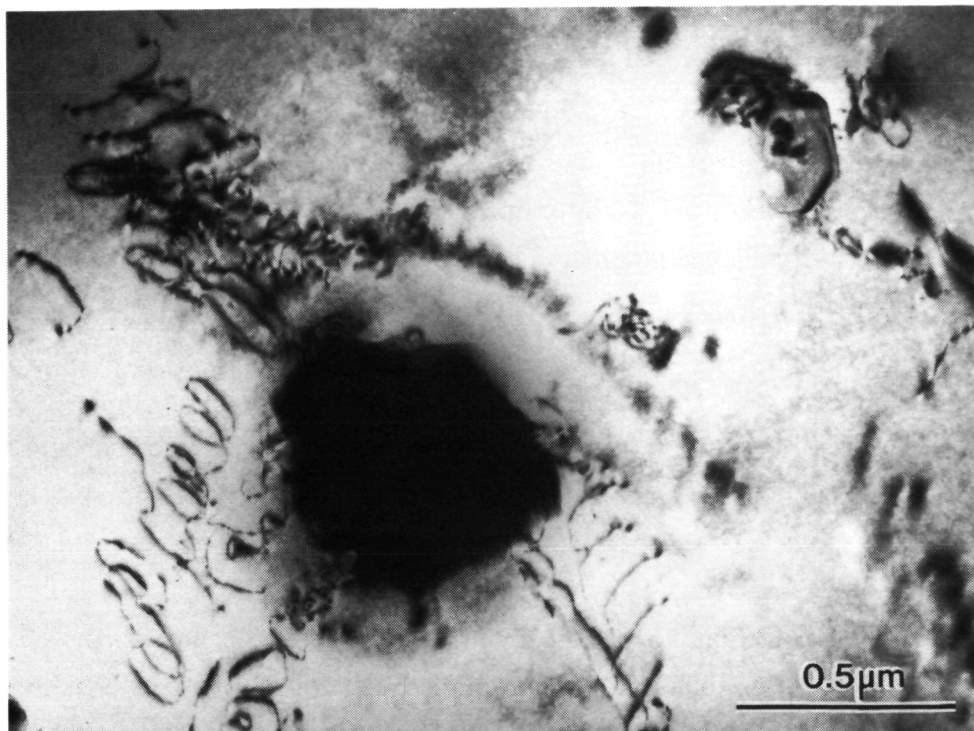


(a) Two-beam condition with $\vec{g} = (002)$ near $[110]$.

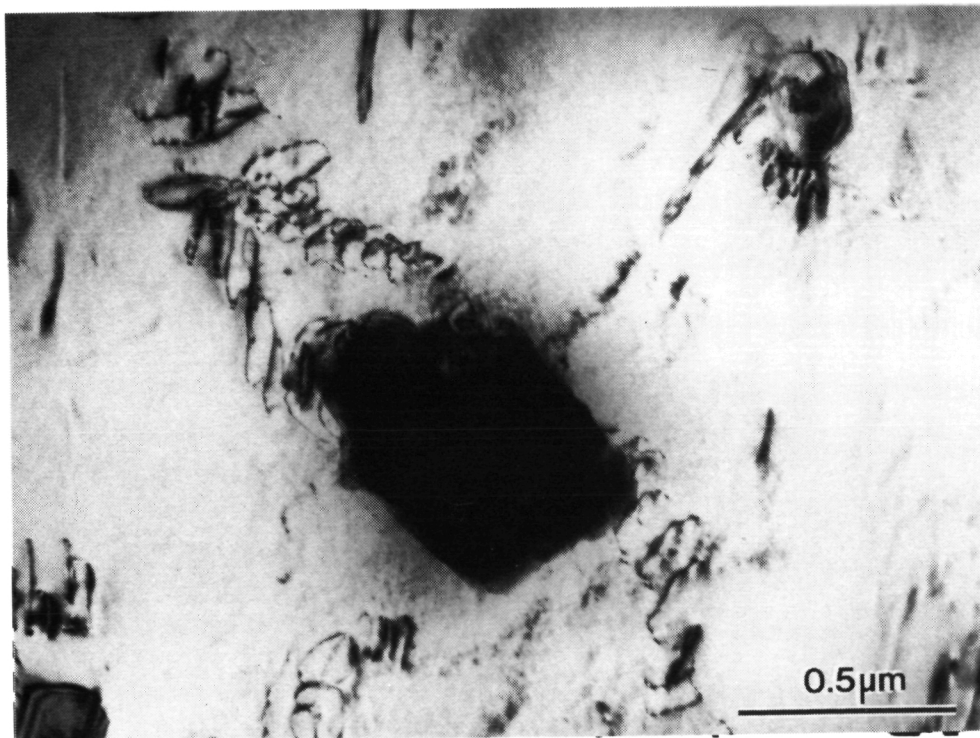


(b) Two-beam condition with $\vec{g} = (1\bar{1}1)$ near $[110]$.

Figure 5.3 . TEM micrographs showing dislocations near a 0.4 μm diameter TiB₂ particle in Al-4%Cu-1.5%Mg+2vol%TiB₂. Alloy is in solutionized, quenched, and naturally aged (T4) condition.



(a) Two-beam condition with $\vec{g} = (002)$ near $[110]$.



(b) Two-beam condition with $\vec{g} = (1\bar{1}1)$ near $[110]$.

Figure 5.4 TEM micrographs showing dislocations near a 0.8 μm diameter TiB₂ particle in Al-4%Cu-1.5%Mg+2vol%TiB₂. Alloy is in solutionized, quenched, and naturally aged (T4) condition.

dislocation nuclei to overcome an activation barrier, thus the true critical diameter is likely to be slightly higher than $0.2\ \mu\text{m}$. The observation that the $0.8\ \mu\text{m}$ particle is punching dislocations while the $0.4\ \mu\text{m}$ particle is not, is therefore consistent with this model. The incorporation of a particle size effect in the Ashby-Johnson model and the lack of a particle size effect in the continuum models, makes the Ashby-Johnson model useful.

The observation that the number of dislocation loops from vacancy condensation decreases as the number of loops from dislocation punching increases may be due to the annihilation of vacancies by diffusion to neighboring dislocations. With a lower vacancy concentration the number of vacancies available for condensation to form dislocation loops is less. Furthermore, the lower number of dislocation loops from vacancy condensation in the reinforced alloys that do not exhibit significant dislocation loop punching, may arise from a greater density of vacancy sinks such as the incoherent Al-TiB₂ interfaces and the large grain boundary area present in these alloys due to their small grain size.

Although the quantitative microscopy to measure the dislocation density of these alloys has not been performed, qualitatively the overall dislocation density between the reinforced and unreinforced alloys is similar. This similar dislocation density will have important consequences for the aging kinetics, as will be examined in detail in the next chapter.

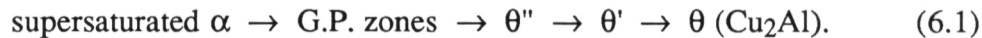
6. AGING RESPONSE OF TiB₂ REINFORCED Al-4%Cu-1.5%Mg

One of the most fundamental properties of age-hardenable aluminum alloys is their aging kinetics. In this chapter we will examine the aging of TiB₂ reinforced Al-4%Cu-1.5%Mg both with and without cold work prior to artificial aging. To start this examination we will first review aging in conventional Al-Cu-Mg alloys and the aging of MMCs.

6.1 Precipitation in Al-Cu-Mg Alloys

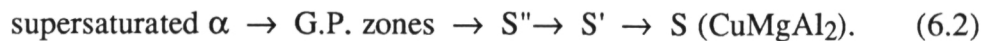
Aluminum rich Al-Cu-Mg alloys with a Cu:Mg weight ratio of 2.6:1 (Cu:Mg atom ratio of 1:1) form the pseudo-binary system aluminum-S (CuMgAl₂) [31-33]. As shown in the aluminum rich end of the Al-Cu-Mg ternary phase diagram (Fig. 6.1), in alloys with a Cu:Mg ratio of greater than 8:1 the equilibrium precipitate is θ (Cu₂Al); in alloys with a ratio of between 8:1 and 4:1, both θ and S are present; in alloys with a ratio of between 4:1 and 1.5:1 the equilibrium precipitate is S; while in alloys below 1.5:1 the precipitate is CuMg₄Al₆. In the alloys considered in this study, the Cu:Mg ratio is 2.4:1 and thus S is the equilibrium precipitate.

The precipitation sequence in aluminum-rich Al-Cu alloys is



This precipitation sequence has been termed the “classical” example of an age-hardening alloy. The large free-energy barrier that opposes the nucleation of the equilibrium phase is circumvented by the formation of a series of intermediate phases which are coherent or semicoherent with the parent matrix. Although the reduction in the free-energy (ΔG_{volume}) accompanying the precipitation of each intermediate phase is less than the free energy reduction accompanying the precipitation of the equilibrium phase, the activation energy opposing nucleation of the intermediate phase is less due to its lower misfit strain-energy and surface free-energy.

The precipitation sequence in Al-Cu-Mg alloys with a Cu:Mg ratio of approximately 2.6:1 following solutionizing and quenching is



Age hardening of solutionized and quenched (supersaturated) Al-Cu-Mg alloys at room and elevated temperatures occurs through the formation of G.P. zones. Bagaryatsky [34] reported

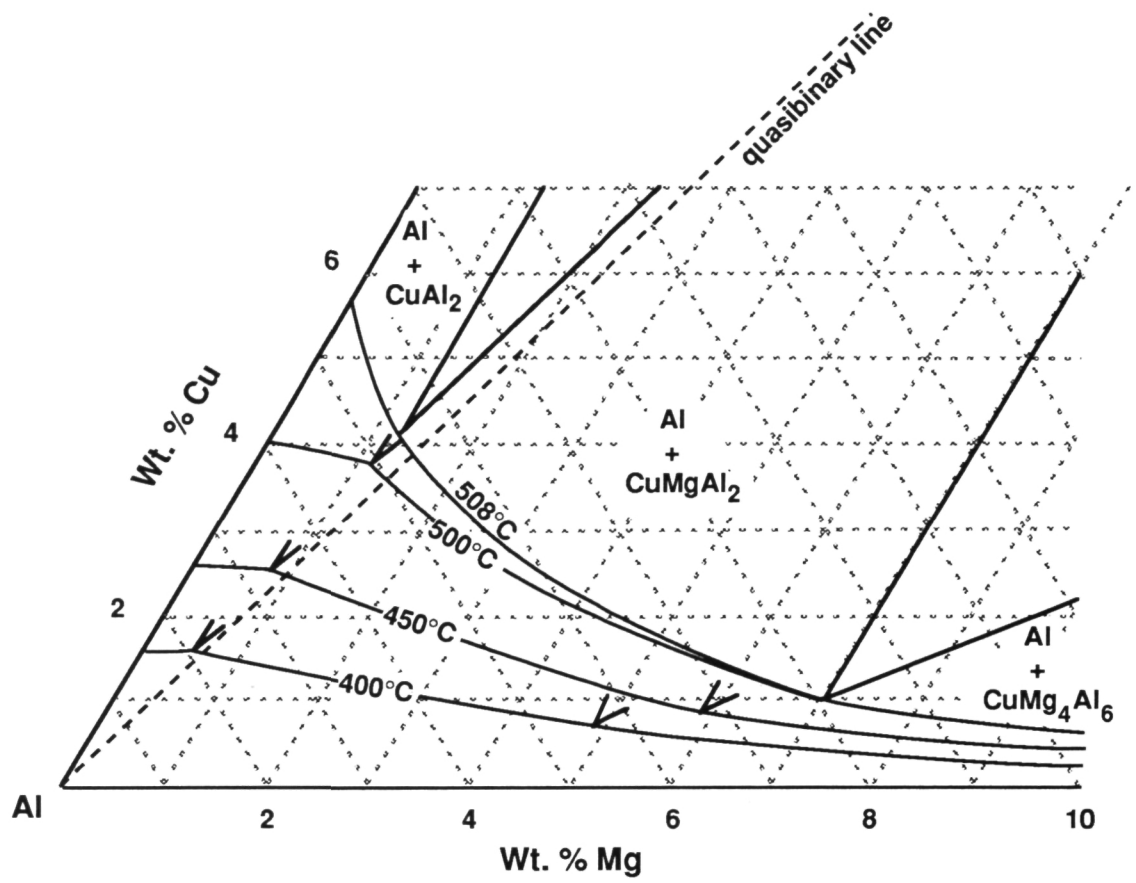


Figure 6.1 Limits of solid solubility in Al rich corner of Al-Cu-Mg ternary phase diagram. (Adapted from [10-12]).

that aging causes precipitation of G.P. zones, as shown by diffuse x-ray scattering from rods along $\langle 110 \rangle$ in alloys aged at room temperature. Building on Hardy's [35] age-hardening study of two Al-Cu-Mg alloys with Cu:Mg ratios of 7.1 and 2.2:1, Silcock [36] used single crystal x-ray methods to relate the structural changes to the hardening. In the 2.2:1 alloy the zones formed as cylinders 10-20 Å in diameter by 40 Å long. The zones are heterogeneously nucleated and excess vacancies are not believed to be involved in zone formation. Hence, precipitate free zones near the grain boundaries are not observed.

A slightly distorted S structure was suggested for S'' [34], and a monoclinic structure has been reported [37]. Additional resistivity [38] and eddy current [39] measurements support the existence of both G.P. zones and S'' at low aging temperatures ($<100^\circ\text{C}$). However, other investigators [35,40-43] have not observed the S'' phase.

The orthorhombic intermediate S' phase has the orientation relationship [34,36]

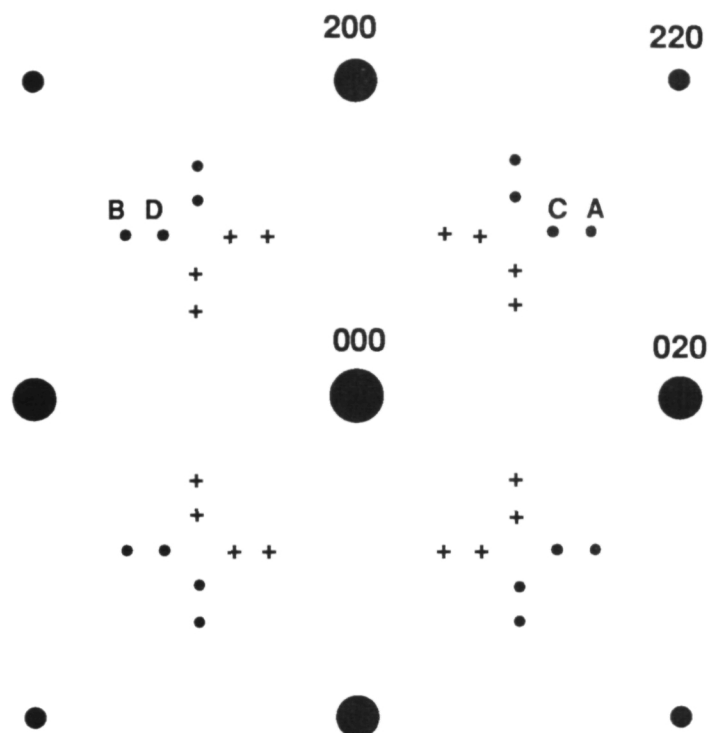
$$[100]_\alpha \parallel [100]_{S'}; \quad [021]_\alpha \parallel [010]_{S'}; \quad [01\bar{2}]_\alpha \parallel [001]_{S'} \quad (6.3)$$

with respect to the α -aluminum matrix. Wilson and Partridge [40] showed that the S' phase has the same crystal structure as the S phase with lattice parameters $a=4.04$ Å, $b=9.25$ Å, and $c=7.18$ Å. Site occupancy models based on x-ray and TEM data have been developed by Mondolfo [31] and Cuisiat, Duval, and Graf [44], while a model based on high resolution TEM, coupled with image simulation, has been presented by Yan, Chunzhi, and Minggao [45].

Wilson and Partridge examined the nucleation and growth of S' in an alloy with Cu:Mg of 2.1:1 at 190°C [40]. They found that S' nucleated heterogeneously on dislocations and grows as laths on $\{210\}_\alpha$ in the $\langle 001 \rangle_\alpha$ direction. Corrugated S' sheets are formed and intersect during the later stages of growth. Eventually, the S' phase grows to the point that it loses coherency with the matrix, and the equilibrium S phase replaces it. Gupta, Gaunt, and Chaturvedi [46] examined the artificial aging of an alloy with a Cu:Mg ratio of 1.9:1 at 190°C and found that the S' precipitates are only a slightly strained version of the S phase and that they grow as rods along the $\langle 100 \rangle_\alpha$ direction with a slight tendency to cluster in groups on $\{110\}_\alpha$ planes; it was suggested that lath formation is dependent upon the Cu:Mg ratio. Zhang, Sun, and Ye [47] have examined a commercial 2024 alloy (Cu:Mg ratio of 2.2:1 with 0.5%Mn) using high resolution TEM. They report homogeneously nucleated S' rods growing along $\langle 100 \rangle_\alpha$ directions and S' precipitates that were nucleated on helical and irregular lines of dislocations and grew into coarser laths. In all of these studies, irrespective of the S' morphology, the orientation relationship given in (6.3) held.

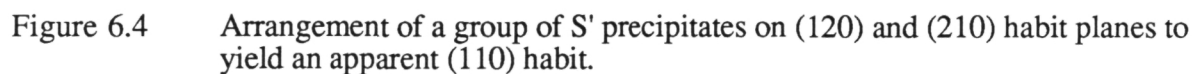
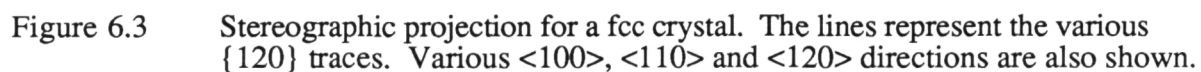
If the $[100]_{\alpha}$ direction is parallel to the $[100]_{S'}$ direction, four variants of S' are possible. This occurs because there are four $\langle 021 \rangle_{\alpha}$ directions that are 90° to $[100]_{\alpha}$, and that can be aligned with $[001]_{S'}$. Since there are three $\langle 100 \rangle_{\alpha}$ axes that can be parallel to $[100]_{S'}$, there are a total of 12 possible crystallographic variants of the S' phase. The diffraction pattern which is observed at a $[100]_{\alpha}$ zone axis is shown in Fig. 6.2. Although other reflections appear in the electron diffraction patterns obtained from overaged samples containing S' [47] only the strongest reflections are represented in Fig. 6.2. The subscripts 1, 2, 3, and 4 refer to the precipitates on the $[0\bar{1}2]_{\alpha}$, $[021]_{\alpha}$, $[0\bar{2}1]_{\alpha}$, and $[012]_{\alpha}$ habit planes, respectively

The observation of laths of S' on apparent $\{110\}$ habit planes [46] and the apparently contradictory observation of S' laths on $\{210\}$ habits can be rationalized in the following manner. The angle between neighboring $\langle 210 \rangle$ directions (such as $[210]$ and $[120]$) as shown in Fig. 6.3 is 36.9° . The angle between precipitates on neighboring $\{210\}$ planes is 143.1° . Corrugated laths of (201) and (120) can be constructed which exhibit an apparent (110) habit as shown in Fig. 6.4. Such an arrangement of neighboring plates may reduce the strain energy of the system.



Label	Reflection/Variant	
A	$(13\bar{1})_1$	$(131)_4$
B	$(1\bar{3}1)_1$	$(1\bar{3}\bar{1})_4$
C	$(112)_2$	$(11\bar{2})_3$
D	$(1\bar{1}\bar{2})_2$	$(1\bar{1}1)_3$

Figure 6.2 Electron diffraction pattern of S' with Al matrix at $[001]_\alpha$ zone axis. The small circles are primary reflections while the crosses are due to double diffraction. The variants contributing to the reflections A, B, C, and D are listed (after Gupta, Gaunt, and Chaturvedi [46]).



6.2 Aging in Aluminum Based MMCs

Studies using hardness have shown that the isothermal aging kinetics of 6061+B₄C particles [48], 6061+SiC whiskers [28,49-50], 2214+SiC whiskers [30], Al-3.5%Cu+SiC particles [51], 8090+SiC particles [52], and 9021+SiC particles [53] are accelerated whereas differential scanning calorimetry and TEM have shown that the precipitation sequence of SiC reinforced 2024, 2219, 6061, 7091, and 7475 [49,54-55] alloys remain the same. Typical of the observed accelerated aging results are the data of Christman and Shuresh, which are presented in Fig. 6.5. Here the microhardness versus artificial aging time for a 2124 alloy reinforced with 0.5 μm by 5 μm whiskers is shown. The alloys were solutionized, quenched, and artificially aged at 177°C. Microhardness indents were made with a 5 g load in whisker free regions.

The acceleration in aging kinetics of an MMC is typically attributed to enhanced nucleation and/or growth of precipitates due to the high dislocation density in the MMC matrix. As discussed in the previous chapter, this increased dislocation density derives from the punching of dislocations upon quenching from the solutionizing temperature due to a CTE mismatch between the ceramic reinforcement and the Al matrix. Dislocations are known to be sites for heterogeneous nucleation of precipitates as well as paths for increased atomic transport during growth, both of which may account for the observed acceleration in aging kinetics. With a higher nucleation density, the aging of the composites is accelerated, in a fashion similar to the acceleration in aging kinetics observed following cold work.

Two alternative explanations for the accelerated aging kinetics are that the residual stress field around the reinforcements results in stress-assisted diffusion or that the particle-matrix interface acts as a high diffusivity path for solute. Through a combination of continuum and dislocation models, Dutta and Bourell [48] conclude that for MMCs with large particles and high dislocation densities, dislocation generation is the principal contributor to accelerated aging. These authors show that only in the case of very small particles and low dislocation densities is residual stress a predominant mechanism. Christman and Suresh [29] and Kim, Lee, and Plichta [23] note that since a higher precipitate density is not observed at the particle-matrix boundary the combination of residual stresses and a “high diffusivity” path at the particle-matrix interface is not responsible for accelerated aging in 2024+SiC composites.

Friend, Horsfall, Luxton, and Young [56] report observing a suppression of the aging response in a 6061 alloy reinforced with amorphous Al₂O₃ whiskers having a diameter of 3 μm (Saffil). They note that the composite no longer responds to artificial aging though it is unclear whether this is due to the nature of the reinforcement or the processing of the composite.

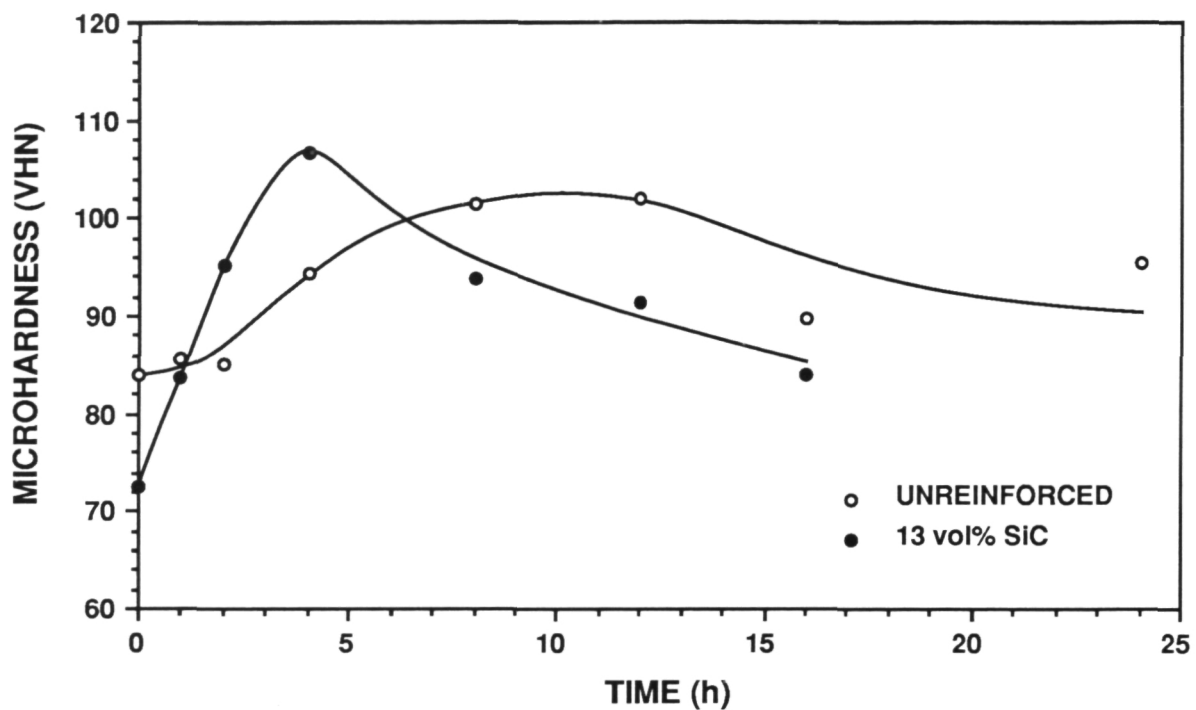


Figure 6.5 Variation of matrix microhardness for 2124 with and without SiC whiskers as a function of aging time for alloys solutionized, quenched, and artificially aged at 177°C. Microhardness indents were made with a 5 g load in whisker free regions. Data from Christman and Suresh [29].

6.3 Isothermal Aging Response of Al-4%Cu-1.5%Mg+TiB₂

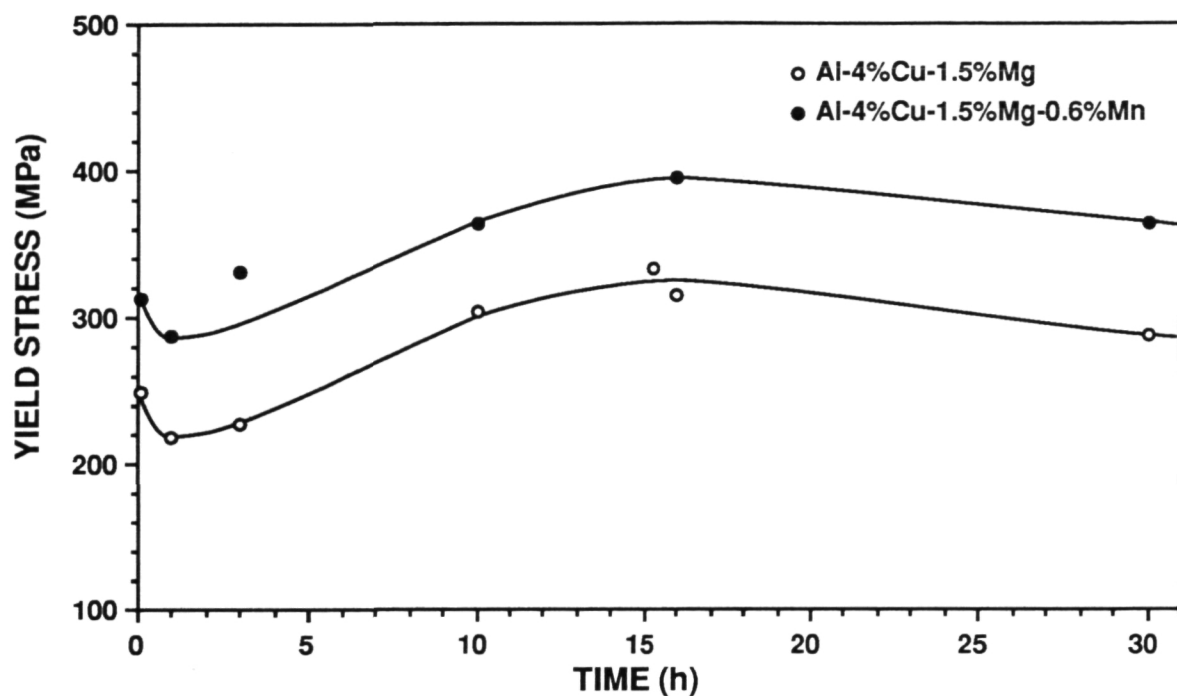
To determine the proper solutionizing temperature for these materials, differential thermal analysis (DTA) was performed on several of the TiB₂ reinforced alloys and the unreinforced alloy. In all the alloys tested the onset of melting was found to occur at 504°C (940°F). There was no notable variation in this temperature with either loading or particle size. This temperature is consistent with the ternary phase diagram and is within experimental error of the reported Al-Al₂Cu-Al₂CuMg eutectic temperature of 503°C (937°F) [10]. For Al-4%Cu-1.5%Mg the ternary phase diagram indicates that the solvus and solidus are separated by approximately 22°C (40°F). Based on these results a solutionizing temperature of 493°C (920°F) was chosen.

After solutionizing for 2 hours at 493°C, the alloys were quenched into cold water and allowed to naturally age for a minimum of 7 days. The hardness following solutionizing became constant after about 3 days; thus, 7 days represents a substantially stable condition. Tensile blanks of the alloys were then artificially aged for various lengths of time at 177°C (350°F), 190°C (375°F), and 204°C (400°F) and allowed to air cool. These tensile samples were then tested in a screw-driven mechanical test frame using either an extensometer or a strain gauge. The strain gauges were used to obtain an accurate measurement of the proportional limit and initial work-hardening rate, whereas the extensometer was used to simplify the tests for which an accurate 0.2% offset yield was sufficient.

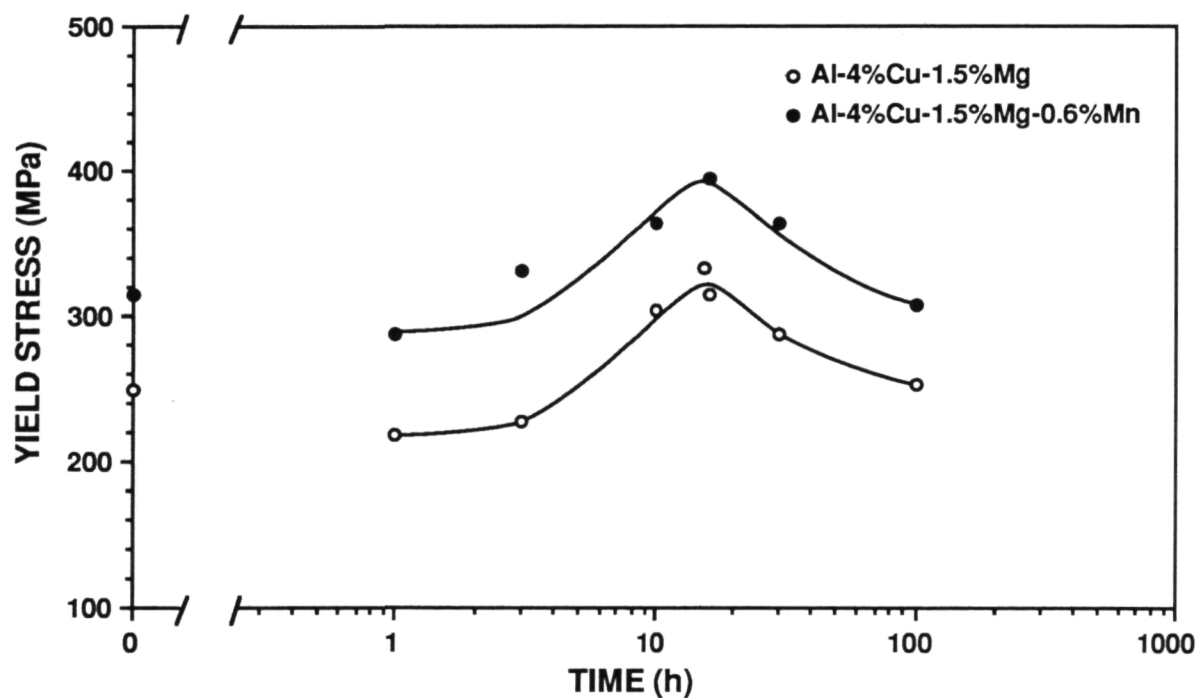
Typically, the aging behavior of an aluminum alloy can be examined through hardness measurements taken as a function of aging time. However, hardness measurements on these MMCs showed a great deal of scatter and were deemed unreliable. For example, the artificial aging response of Al-4%Cu-1.5%Mg reinforced with 10% of the small (0.3 μm) TiB₂ as determined by Vicker's and Rockwell B hardness did not follow the trend in the tensile results for this material. In contrast, the tensile aging response of Al-4%Cu-1.5%Mg with 10% of the large (1.3 μm) TiB₂ correlated quite well with the hardness results. The disparity between the tensile and hardness results for the 0.3 μm TiB₂ alloys is believed to be related to their poor TiB₂ distribution. Because the aging behavior could not be tracked reliably using hardness measurements for the small-particle TiB₂ alloys, it was decided to use tensile tests to determine the aging response throughout this study.

6.3.1 Aging Response at 190°C

Figure 6.6(a) shows the variation of yield stress with aging time at 190°C for the base Al-4%Cu-1.5%Mg. To provide some comparison with commercial aluminum alloys data for 2124 (Al-4%Cu-1.5%Mg-0.6%Mg) cast and extruded under identical conditions are included.

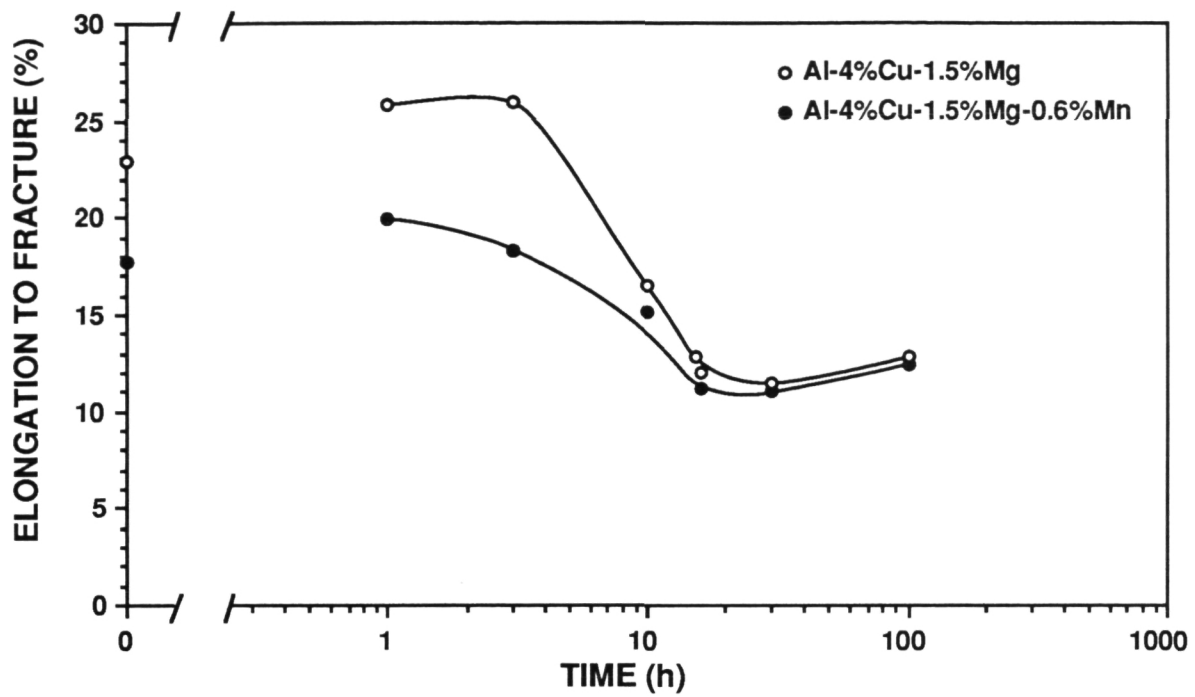


(a) Yield stress versus linear time scale



(b) Yield stress versus logarithmic time scale

Figure 6.6 Variation of tensile properties with time of aging at 190°C for the Al-4%Cu-1.5%Mg with and without Mn.



(c) Elongation to fracture

Figure 6.6 Variation of tensile properties with time of aging at 190°C for the Al-4%Cu-1.5%Mg with and without Mn.

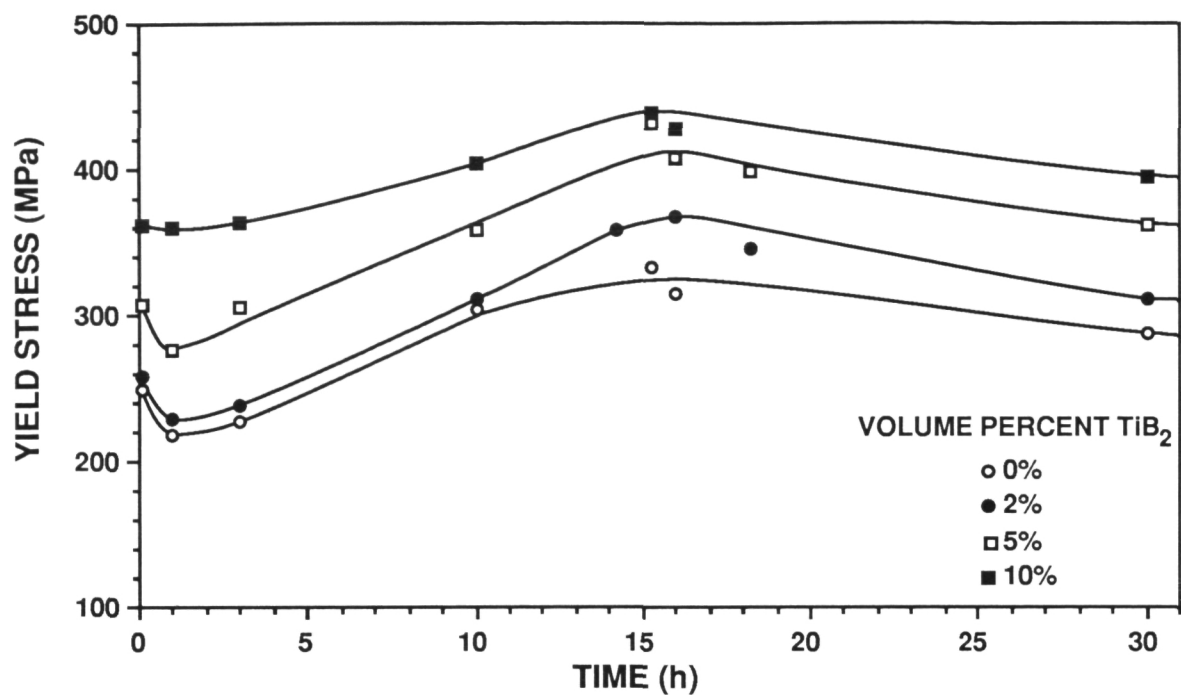
In samples aged from the T4 condition, strength initially dropped (regression) and then increased until it reached a maximum (the peak-aged, i.e., T6, condition), and then declined. Materials aged beyond the peak-aged condition are referred to as overaged. The isothermal-aging response is plotted on a logarithmic time scale in Fig. 6.6(b). Silcock [36] has shown that the sharp rise in the curve is associated with the precipitation of S' in the presence of G.P. zones. At the peak, some G.P. zones are still present along with the S'. Just past the peak, as the strength begins to drop off the last of the G.P. zones disappear. With further aging the strength continues to fall as the S' loses coherency with the matrix and converts to S.

Regression is not observed in samples which are aged directly after quenching. Because S'' is not stable at temperatures above approximately 100°C [38], it is likely that the regression is due to dissolution of S'' precipitates which formed during natural aging at room temperature.

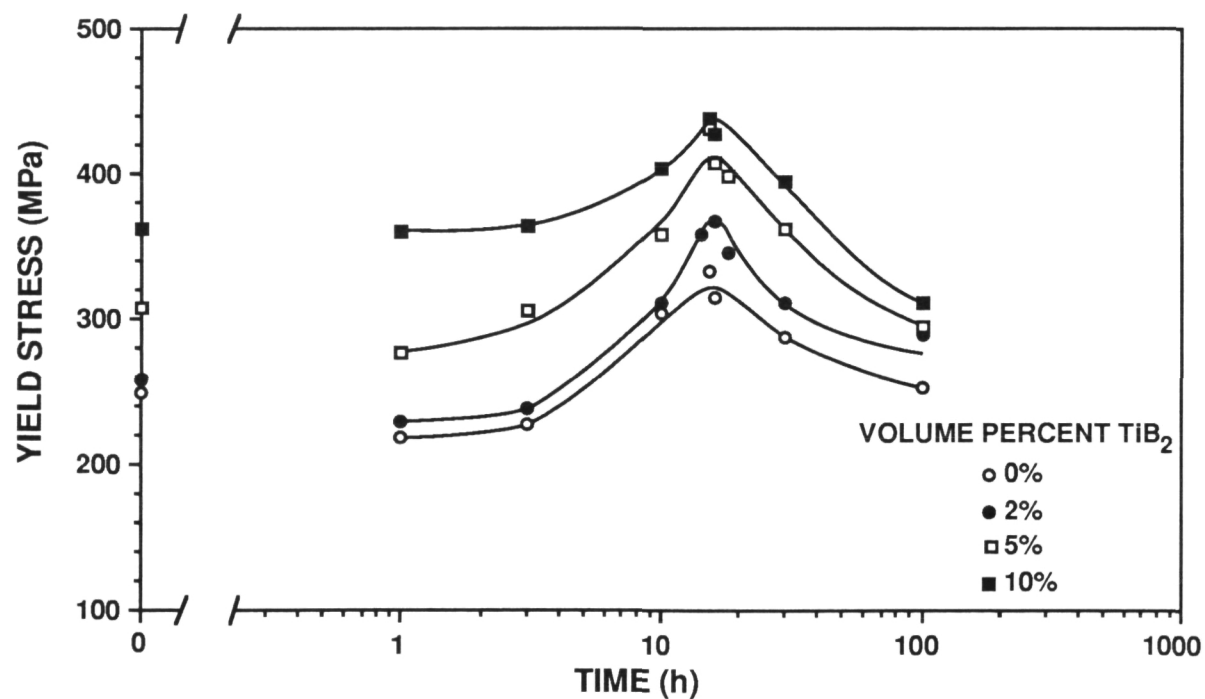
As shown in Fig. 6.6(a), the presence of Mn in the 2124 alloy increases the yield stress by approximately 60 MPa over Al-4%Cu-1.5%Mg for the entire aging history but does not alter either the aging behavior or kinetics. Mn is added to 2124 as a dispersoid former; it forms $\text{Cu}_2\text{Mn}_3\text{Al}_{20}$ which acts as a grain refiner. In Fig. 6.6(c), the elongation to fracture in a 1 in. gauge length is plotted. Elongation decreased with aging, reaching a minimum at the peak-aged condition. Beyond this point, elongation increased, but only by a few percent. Although the initial elongation of the Al-4%Cu-1.5%Mg alloy is greater than 2124 for underaged samples, by the time the alloys reached peak strength at 16 hours the elongation is identical.

Figure 6.7(a) shows the variation of yield stress with aging time at 190°C for the 0.3 μm TiB_2 containing alloys aged from the T4 condition. In a manner identical to the base alloy, strength initially dropped and then increased until it reached a maximum at the peak-aged condition, and then declined. The isothermal-aging response is plotted on a logarithmic time scale in Fig. 6.7(b). Within the experimental error of this data there is no shift in the aging kinetics with the addition of TiB_2 . The elongation to fracture in a 2.5 cm gauge length is plotted for the 0.3 μm alloys on a linear time scale in Fig. 6.7(c) and on logarithmic time scale in Fig. 6.7(d). For all volume fractions of TiB_2 , elongation decreased with aging, reaching a minimum at the peak-aged condition. Beyond this point, elongation increased, but not dramatically.

Figure 6.8(a-c) shows the isothermal-aging behavior at 190°C for the 1.3 μm TiB_2 containing alloys. The behavior was nearly identical to that observed in the alloys containing 0.3 μm TiB_2 , although the smaller particles showed greater strength at the same loading. Again no shift in the aging kinetics was observed with the addition of TiB_2 .

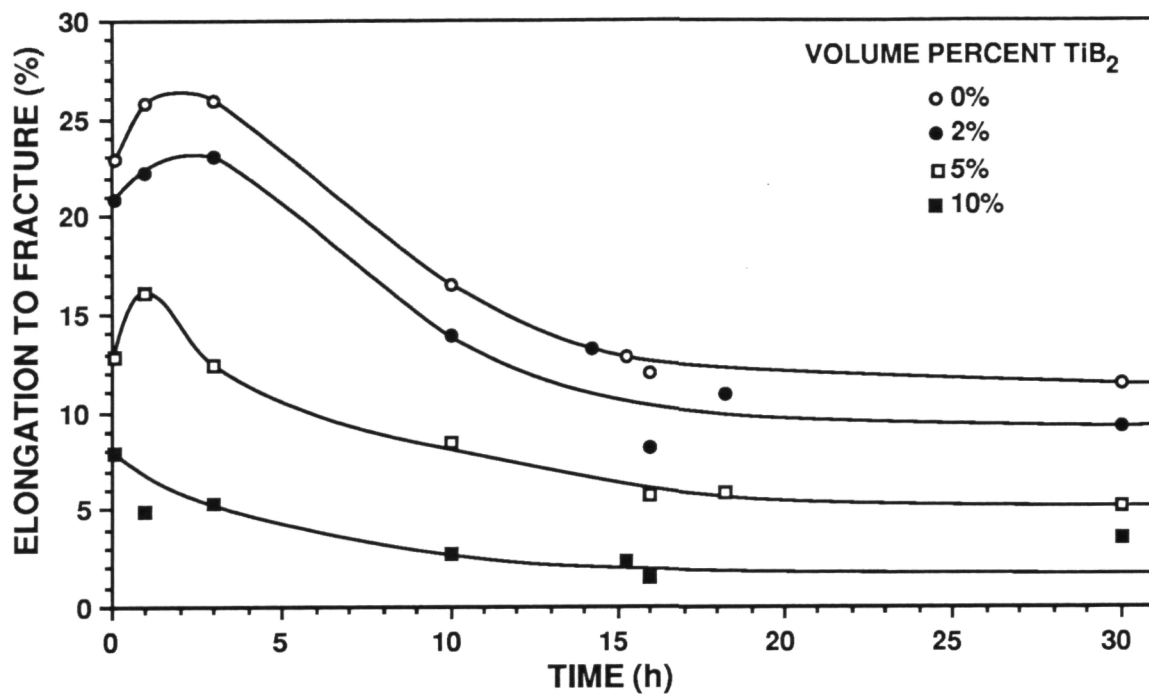


(a) Yield stress versus linear time scale

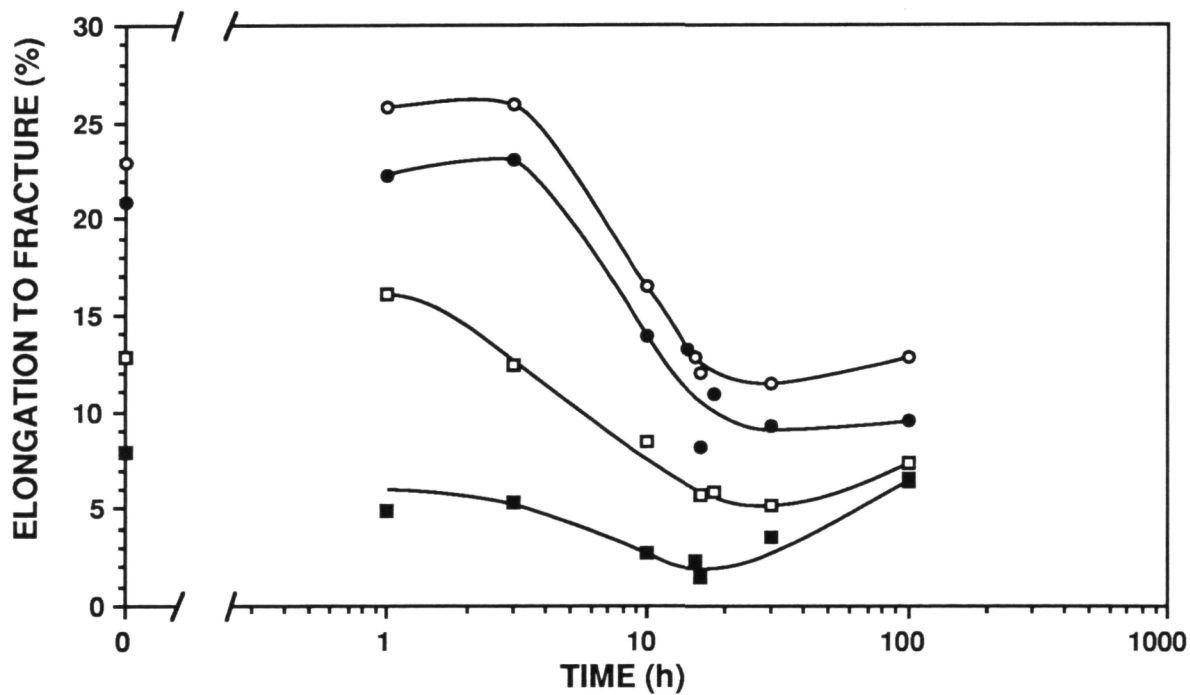


(b) Yield stress versus logarithmic time scale

Figure 6.7 Variation of tensile properties with time of aging at 190°C for the Al-4%Cu-1.5%Mg alloys containing 0.3 μm TiB_2 particles.

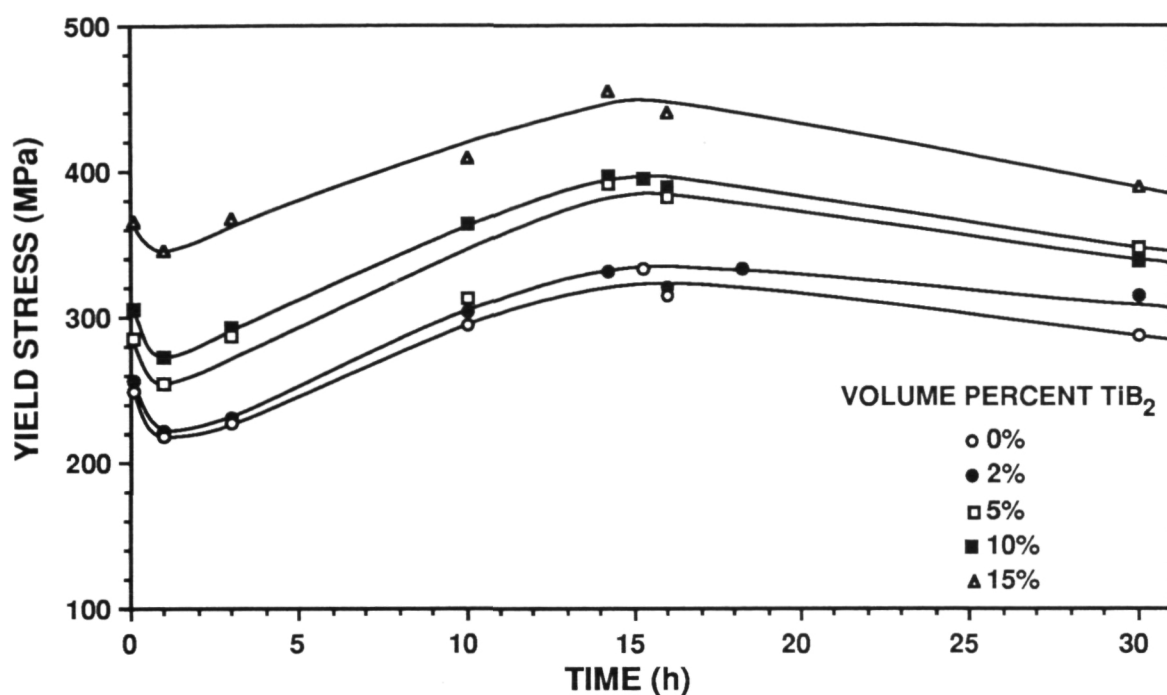


(c) Elongation to fracture versus linear time scale

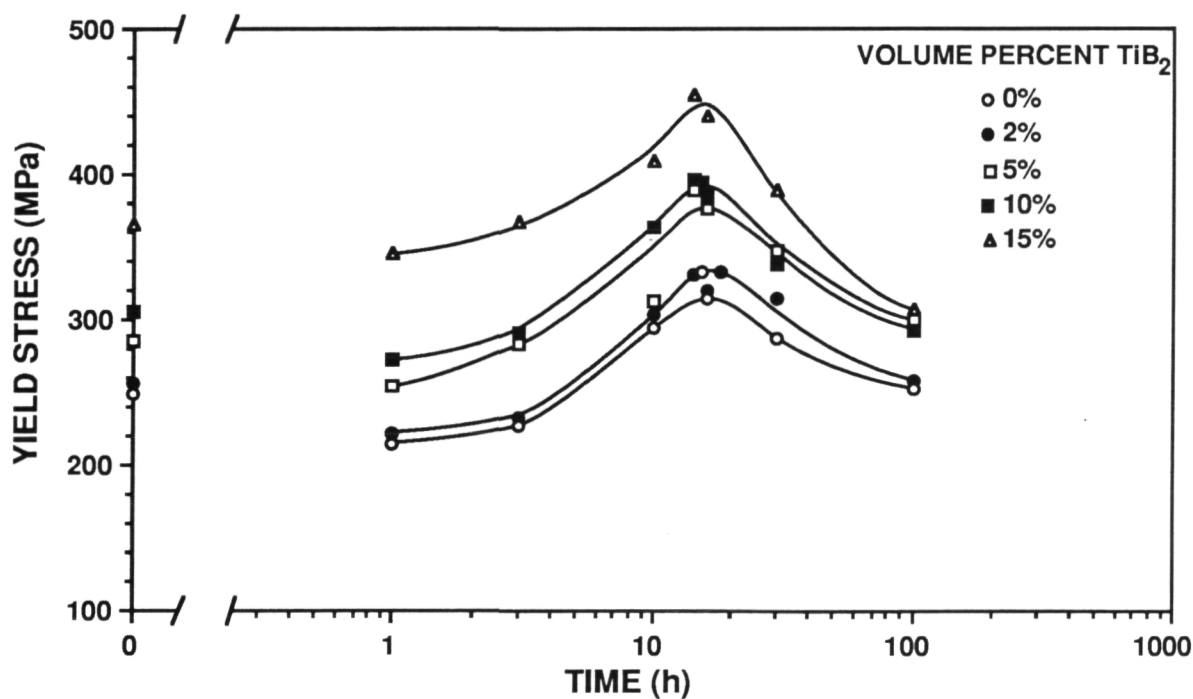


(d) Elongation to fracture versus logarithmic time scale

Figure 6.7 (cont.) Variation of tensile properties with time of aging at 190°C for the Al-4%Cu-1.5%Mg alloys containing $0.3\ \mu\text{m}$ TiB_2 particles.

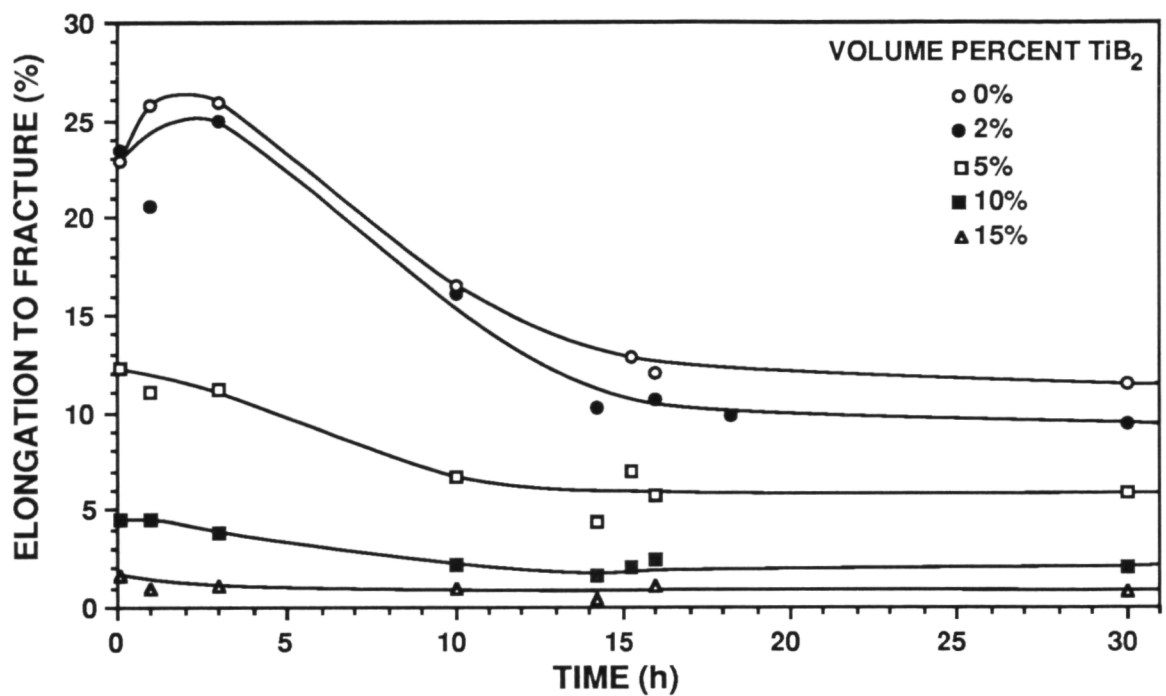


(a) Yield stress versus linear time scale

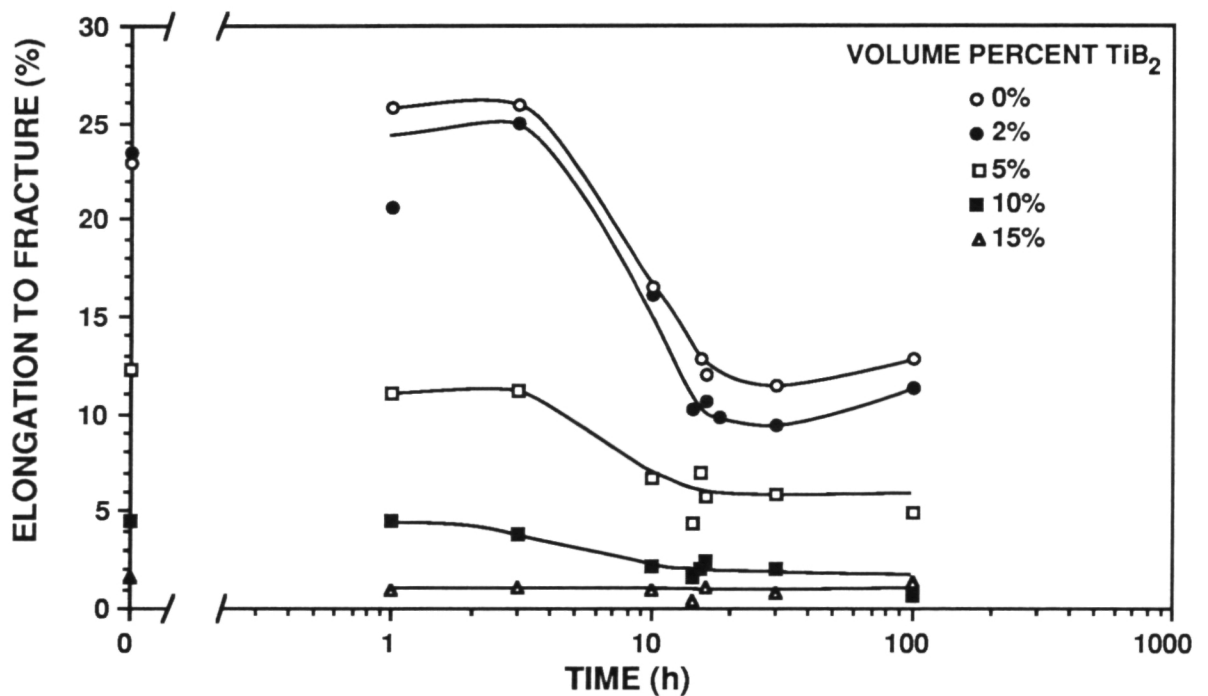


(b) Yield stress versus logarithmic time scale

Figure 6.8 Variation of tensile properties with time of aging at 190°C for the Al-4%Cu-1.5%Mg alloys containing 1.3 μm TiB_2 particles.



(c) Elongation to fracture versus linear time scale



(d) Elongation to fracture versus logarithmic time scale

Figure 6.8 (cont.) Variation of tensile properties with time of aging at 190°C for the Al-4%Cu-1.5%Mg alloys containing $1.3\ \mu\text{m}$ TiB_2 particles.

6.3.2 The Effect of Aging Temperature

Figures 6.9 and 6.10 show the variation of yield stress with time of aging at 177°C (350°F) for the 0.3 μm and 1.3 μm TiB_2 containing alloys. As expected, aging at a lower temperature resulted in slower aging kinetics and a longer time to peak strength. Figures 6.11 and 6.12 show the variation of yield stress with time of aging at 204°C (400°F) for the 0.3 μm and 1.3 μm TiB_2 containing alloys. The higher aging temperature results in faster aging kinetics and a much shorter time to peak strength. At all three of the temperatures considered the TiB_2 loading does not affect the aging kinetics.

To further examine the role of aging temperature, the time to peak strength is taken to be at 30 hours at 177°C, 16 hours at 190°C, and 3 hours at 204°C. Although the spacing of the data at 177°C and 204°C makes these times somewhat approximate, the general trend is correct. In Fig. 6.13 the yield stress and elongation to fracture at the time of peak stress (e.g., 30 hours at 177°C, 16 hours at 190°C, and 3 hours at 204°C) are plotted versus the artificial aging temperature for the alloys reinforced with 0.3 μm TiB_2 . The companion plot for the alloys with 1.3 μm TiB_2 is shown in Fig. 6.14. Along with the data points are the least-squares fit of these data. For the unreinforced alloy, a lower aging temperature results in a higher peak yield stress. Lower aging temperatures favor a higher nucleation rate, which results in a greater number of precipitates per unit area. The greater number of obstacles typically results in higher yield strength. With the addition of TiB_2 , the trend of increasing strength with lower aging temperature weakens and for alloys with 5 vol% or more the strength is independent of the aging temperature. The mechanism responsible for this trend is not understood. The elongation to fracture, at the peak stress, is roughly independent of the aging temperature.

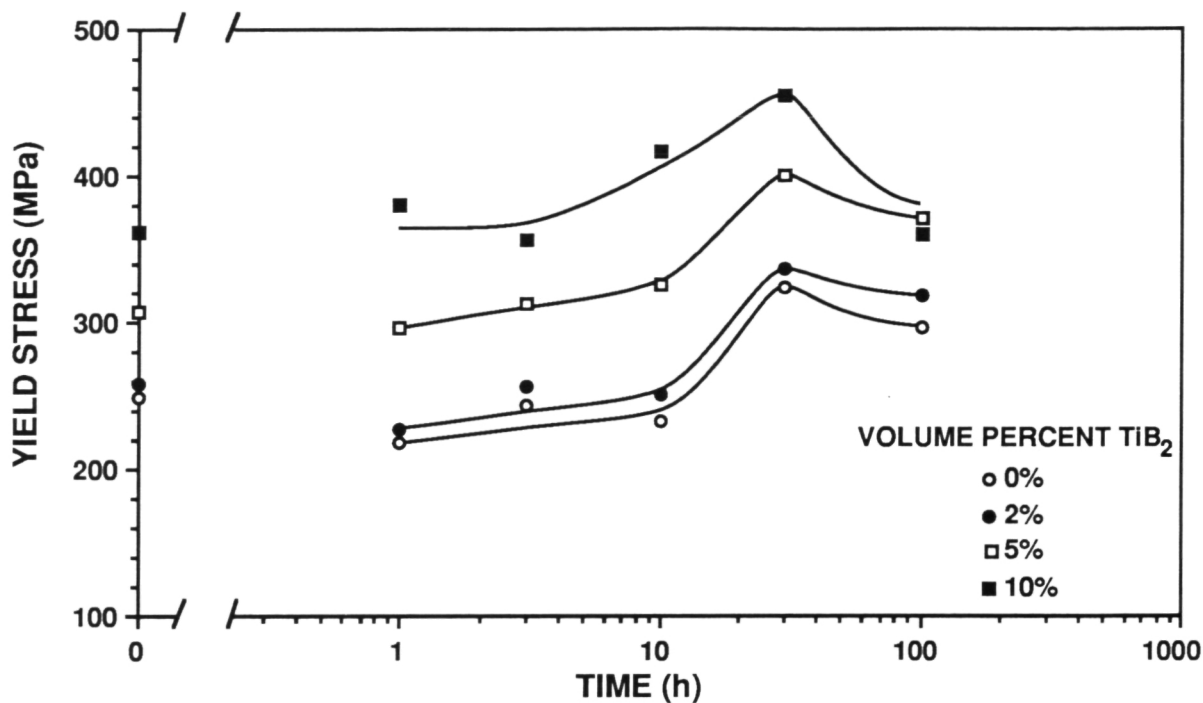


Figure 6.9 Variation of yield stress with time of aging at 177°C for the Al-4%Cu-1.5%Mg alloys containing 0.3 μm TiB_2 particles.

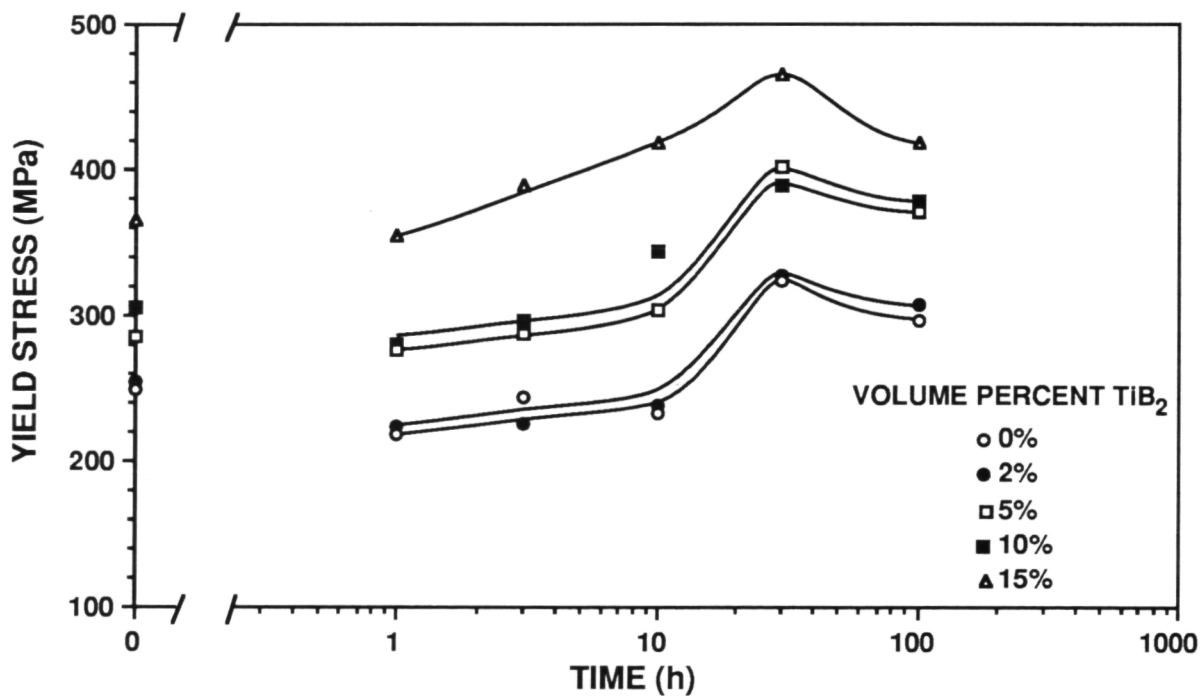


Figure 6.10 Variation of yield stress with time of aging at 177°C for the Al-4%Cu-1.5%Mg alloys containing 1.3 μm TiB_2 particles.

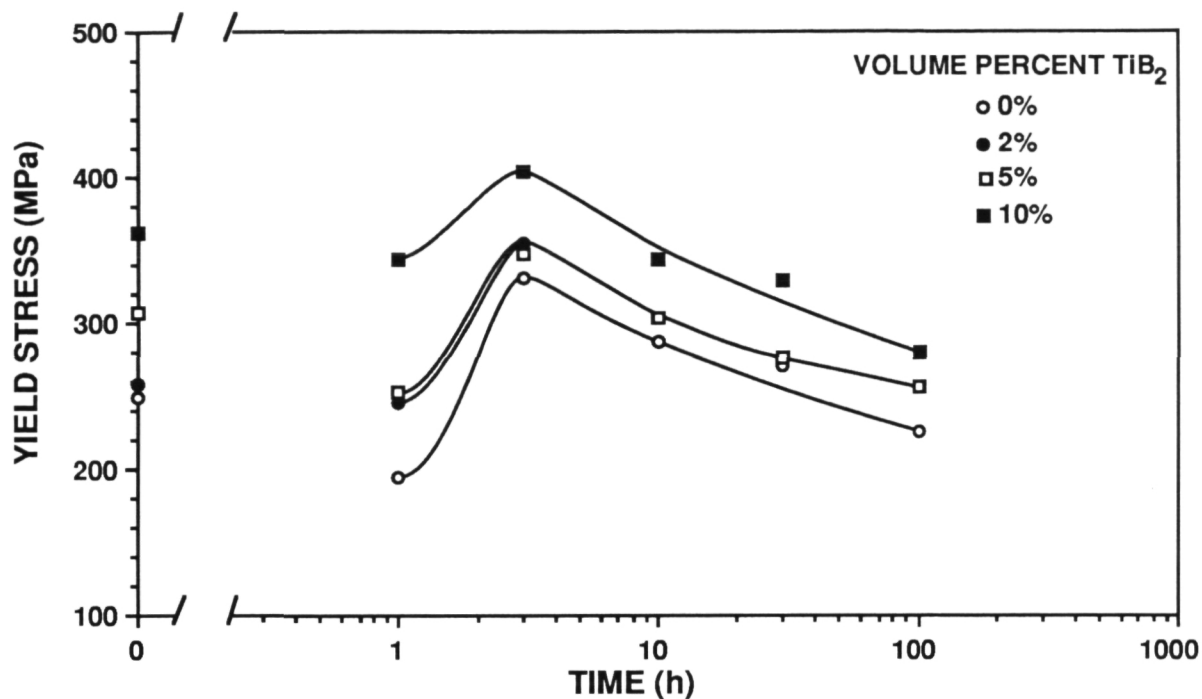


Figure 6.11 Variation of yield stress with time of aging at 204°C for the Al-4%Cu-1.5%Mg alloys containing 0.3 μm TiB_2 particles.

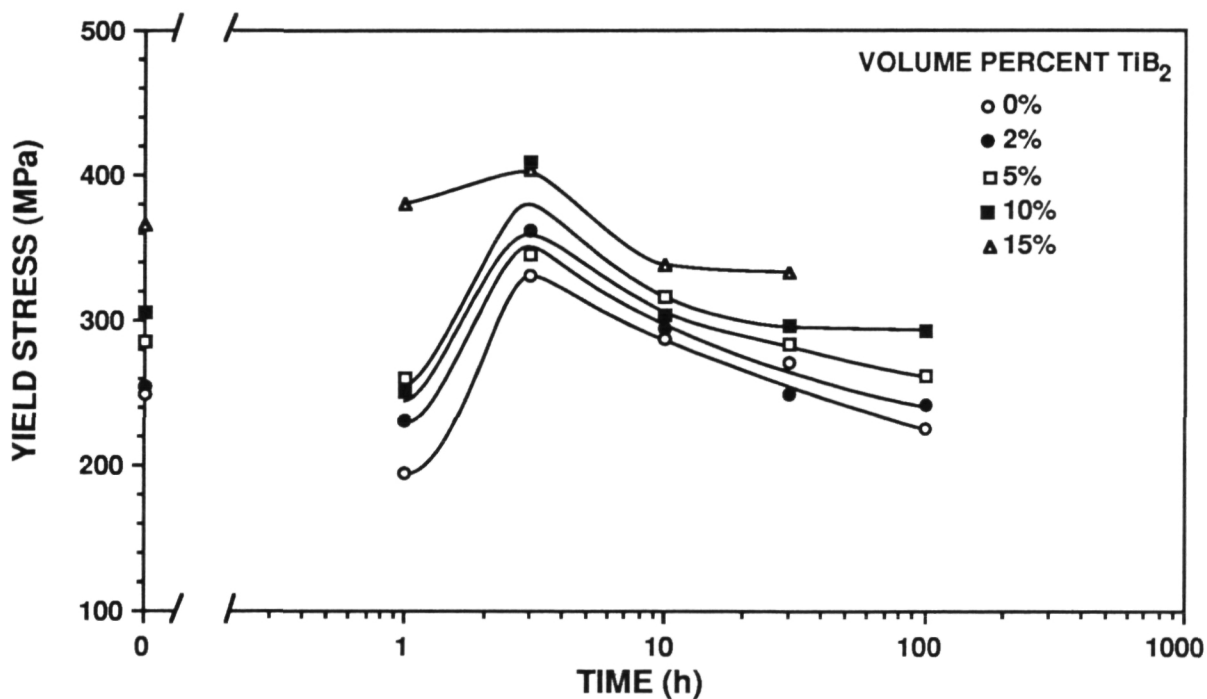
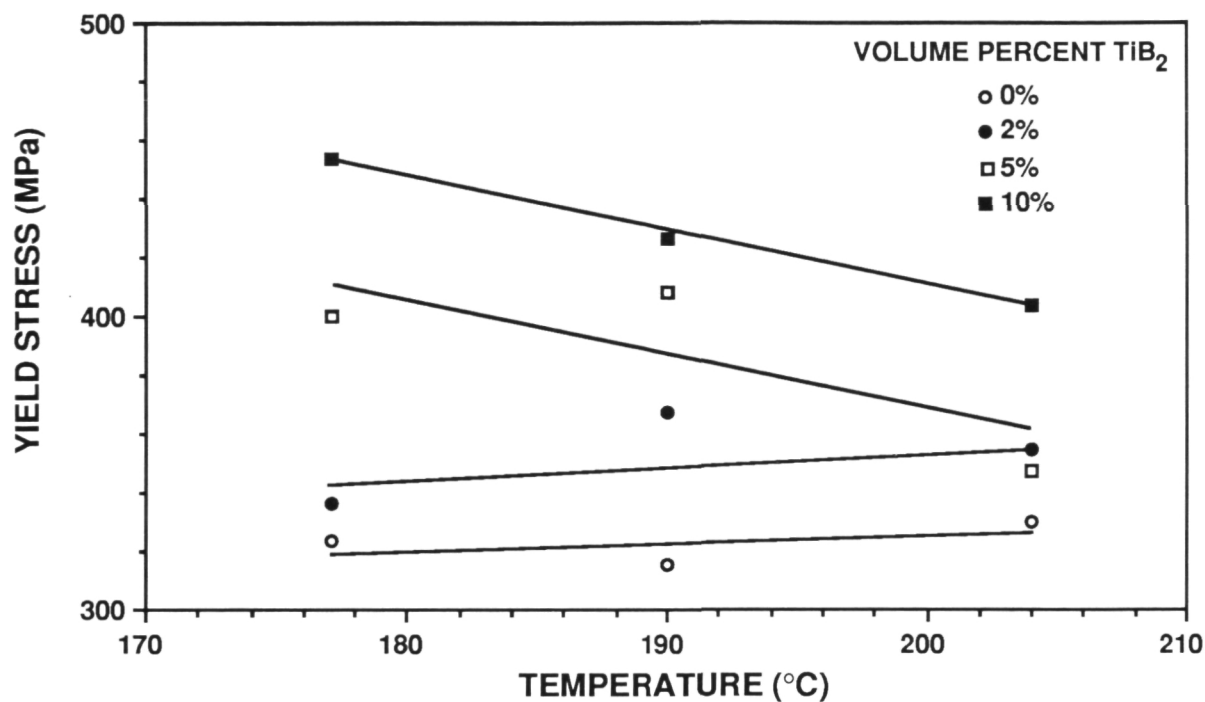
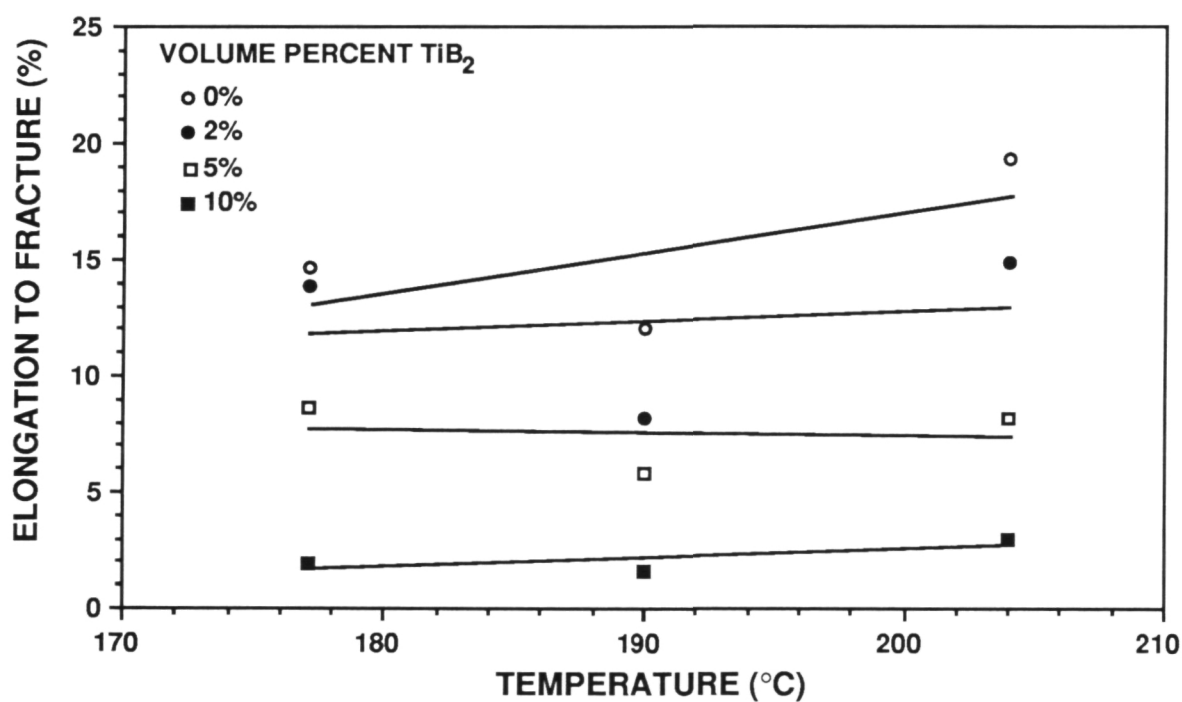


Figure 6.12 Variation of yield stress with time of aging at 204°C for the Al-4%Cu-1.5%Mg alloys containing 1.3 μm TiB_2 particles.

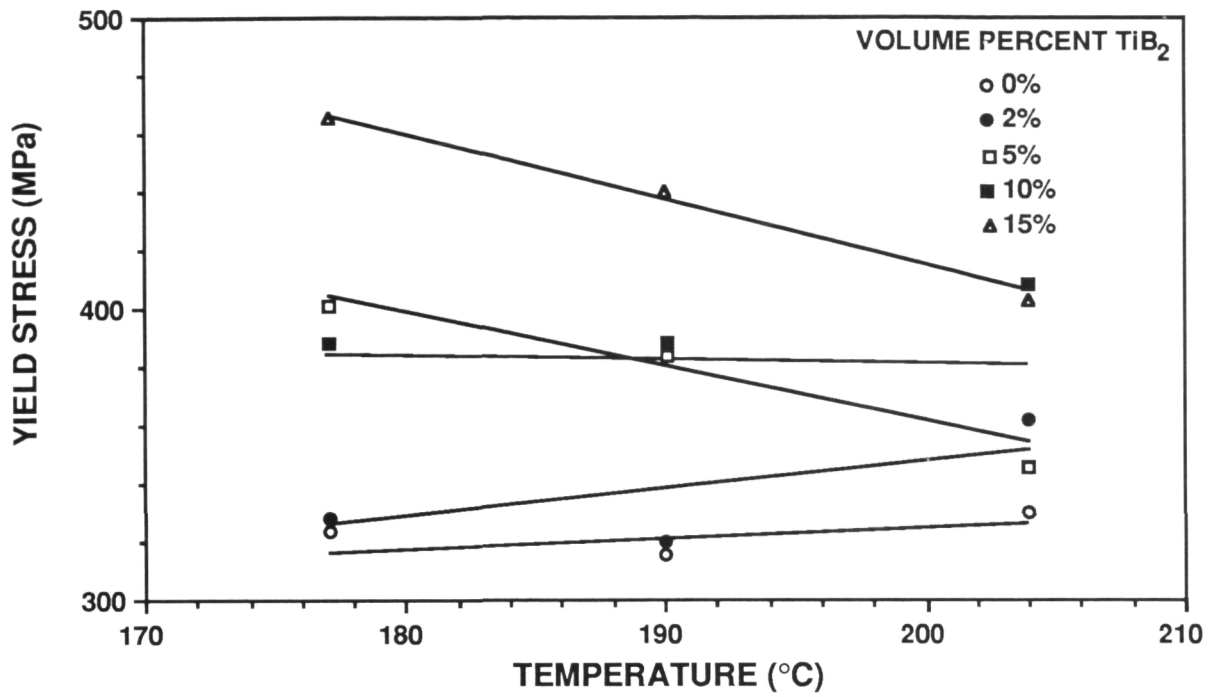


(a) Yield stress

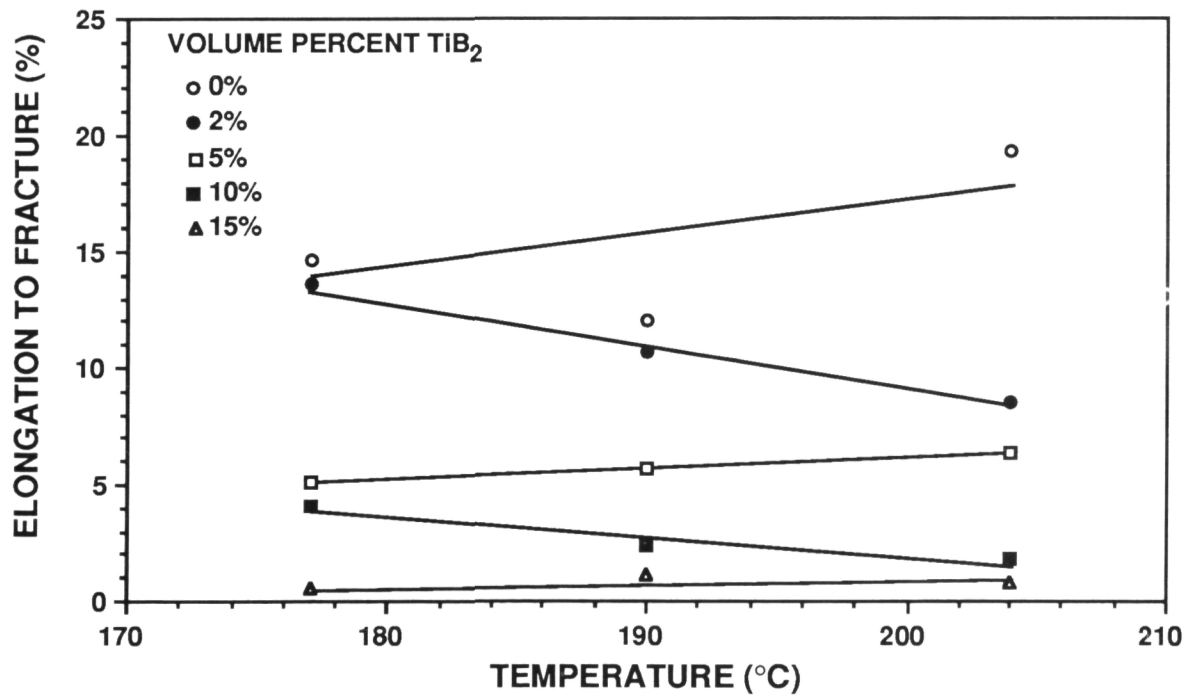


(b) Elongation to fracture

Figure 6.13 Variation of tensile properties at peak-aged condition for the Al-4%Cu-1.5%Mg alloys containing $0.3 \mu\text{m}$ TiB_2 particles as a function of aging temperature.



(a) Yield stress



(b) Elongation to fracture

Figure 6.14 Variation of tensile properties at peak-aged condition for the Al-4%Cu-1.5%Mg alloys containing $1.3 \mu m$ TiB_2 particles as a function of aging temperature.

6.4 Aging of Al-4%Cu-1.5%Mg+TiB₂ Following Cold Work

Stretching following solutionizing and prior to either natural or artificial aging is a common thermomechanical treatment for age-hardenable aluminum alloys. The stretching (or other deformation process) introduces dislocations into the matrix which act as heterogeneous nucleation sites for precipitates. Following aging, the reinforcing precipitates are of the same volume fraction as in the unstretched material but they are finer due to the initially higher nucleation rate. Such thermomechanical processes are designated T3 for the stretched and naturally aged, and T8 for the stretched and artificially aged.

Although T3 and T8 are common tempers for conventional aluminum alloys there are no data in the literature on the effect of stretching and aging thermomechanical treatments on MMCs. With this in mind, two sets of experiments were undertaken on the Al-4%Cu-1.5%Mg+TiB₂ alloys. In the first the role of the amount of stretch was examined using alloys stretched to either 1.5%, 2.0%, 2.5%, or 3.5% plastic elongation and allowed to naturally age. In the second, the kinetics of alloys stretched 2% and then artificially aged at 190°C (375°F) were examined.

To examine the aging kinetics of the alloys with cold work prior to artificial aging oversized tensile samples were solutionized for 2 hours and quenched into cold water. The samples were then immediately stretched to either 1.5%, 2.0%, 2.5%, or 3.5% plastic elongation using a screw-driven tensile frame and a clip-on extensometer and then allowed to naturally age for a minimum of 7 days to the T3 condition. Standard 2.5 cm gauge length tensile samples were then machined from the initially oversized blanks. For the artificial aging experiments the tensile blanks in the T3 condition were artificially aged for various lengths of time at 190°C (375°F) and allowed to air cool. These tensile samples were then tested in a screw-driven mechanical test frame.

6.4.1 Geometrically Necessary Dislocations

To help understand the deformation of nonhomogeneous materials, Ashby has advanced the concept of geometrically necessary dislocations [59]. When a plastically non-homogeneous material is deformed, dislocations are generated in order to maintain mechanical continuity between adjoining constituents of the microstructure. These dislocations are called geometrically necessary dislocations as distinguished from the statistically-stored dislocations that accumulate in pure single crystals and are responsible for their normal 3-stage strain hardening. The density of geometrically necessary dislocations can be determined from

$$\rho^G = \frac{4\gamma}{B} \frac{1}{\lambda^G} \quad (6.4)$$

where ρ^G is the geometrically necessary dislocation density, γ is the shear stress, B is the Burgers vector, and λ^G is the geometric slip distance. For alloys containing a dispersion of spherical particles the geometric slip distance typically is

$$\lambda^G = \frac{r}{f} \quad (6.5)$$

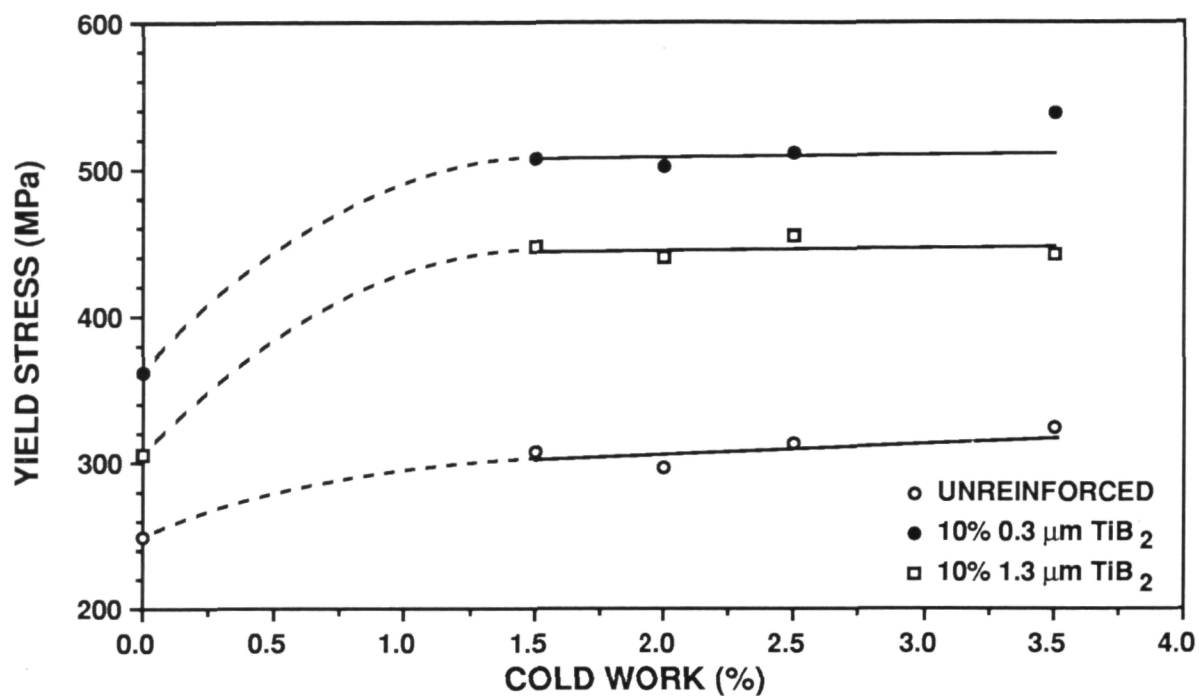
where r is the particle radius and f is the volume fraction. For pure polycrystals λ^G is proportional to the grain size.

6.4.2 Amount of Cold Work

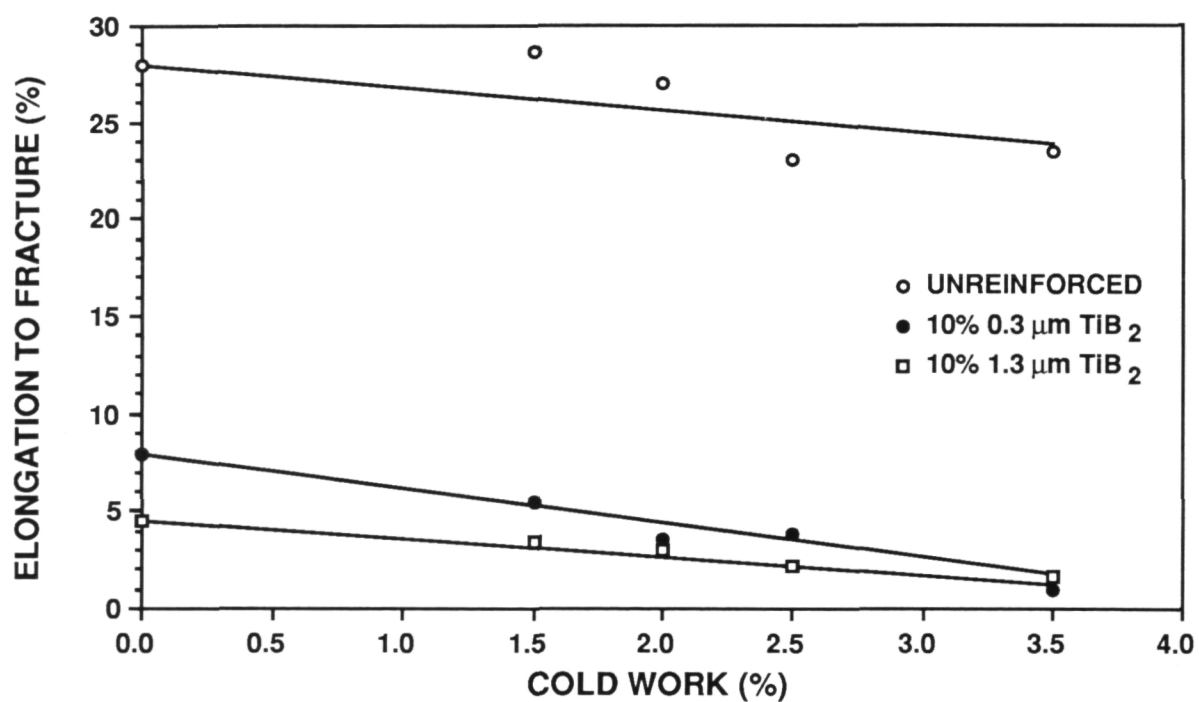
Figure 6.15 shows the tensile behavior of Al-4%-Cu-1.5%Mg unreinforced and also reinforced with 10 vol% of either 0.3 μm or 1.3 μm TiB₂ in the naturally aged condition as a function of the amount of stretch prior to natural aging. As shown in Fig. 6.15(a), the increase of the 0.2% offset yield stress is quite rapid from 0 to 1.5% stretch, whereas further increases in the amount of stretching have relatively little effect. The yield stress of the unreinforced alloy does seem to continue to increase slightly with greater amounts of stretch. As shown in Fig. 6.15(b) the elongation tends to decrease slightly with increasing amount of cold work prior to aging.

Although the next chapter is devoted to the discussion of the strengthening mechanisms in MMCs, in this section we will briefly consider the strengthening increment in these MMCs due to stretching. The dislocation density due to the initial stretch of these alloys should not have been significantly altered by the aging at room temperature undergone by these samples between stretching and testing. Hence, the dislocation density present in these alloys should be equal to the initial density plus the geometrically necessary dislocations given by Eqn. 6.4. Since the yield stress is proportional to the square root of dislocation density, the increment of strengthening due to geometrically necessary dislocations should be proportional to $(\lambda^G)^{-1/2}$. In Fig. 6.16 the yield stress of the alloys in the T3 condition is plotted against $(\lambda^G)^{-1/2}$. For the reinforced alloys the geometric slip distance was taken as the average interparticle spacing on the slip plane

$$\lambda^G = \lambda - 2r_s \quad (6.6)$$



(a) Yield stress



(b) Elongation to fracture

Figure 6.15 Variation of T3 tensile properties with the amount of cold work prior to natural aging for the Al-4%Cu-1.5%Mg alloys.

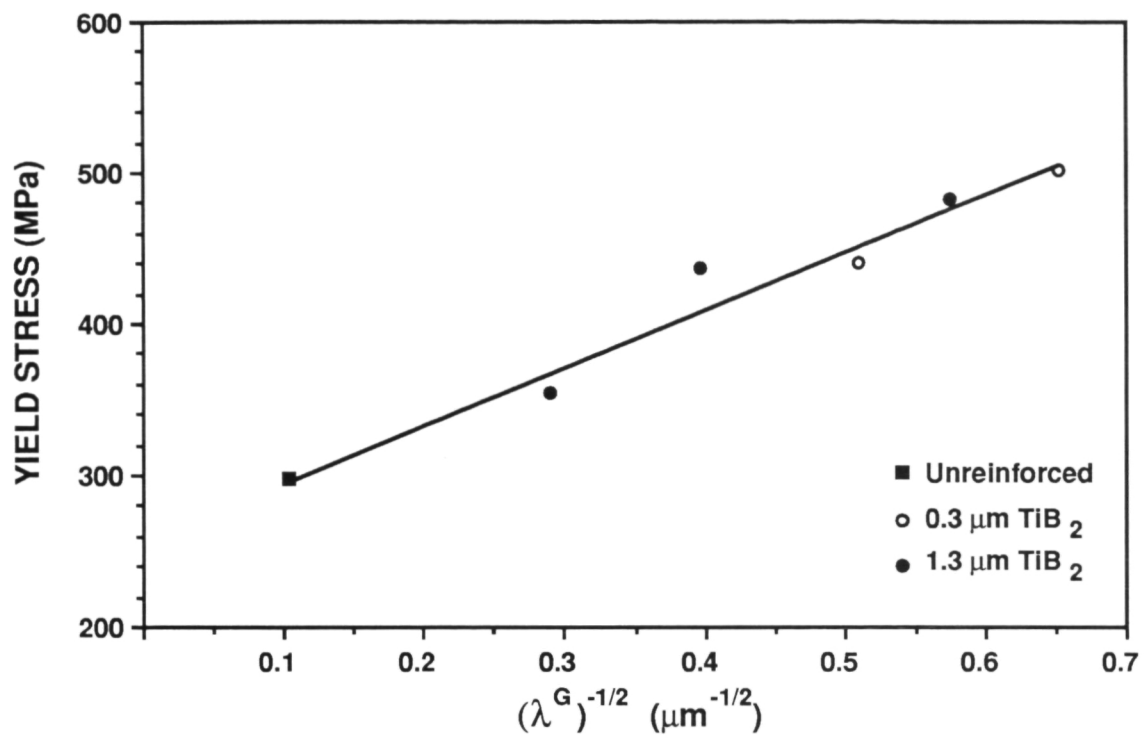


Figure 6.16 Yield stress as a function of the inverse of the square root of the geometric slip distance for Al-4%Cu-1.5%Mg alloys stretched 2% prior to natural aging.

where λ is the average interparticle spacing and r_s is the mean radius of intersection of a random plane with a spherical particle of radius r which is

$$r_s = \sqrt{2/3} r. \quad (6.7)$$

Measurement of average interparticle spacing on a plane of polish, λ , was performed by the line intersect method using SEM micrographs. For the unreinforced alloy λ^G is taken as the grain size.

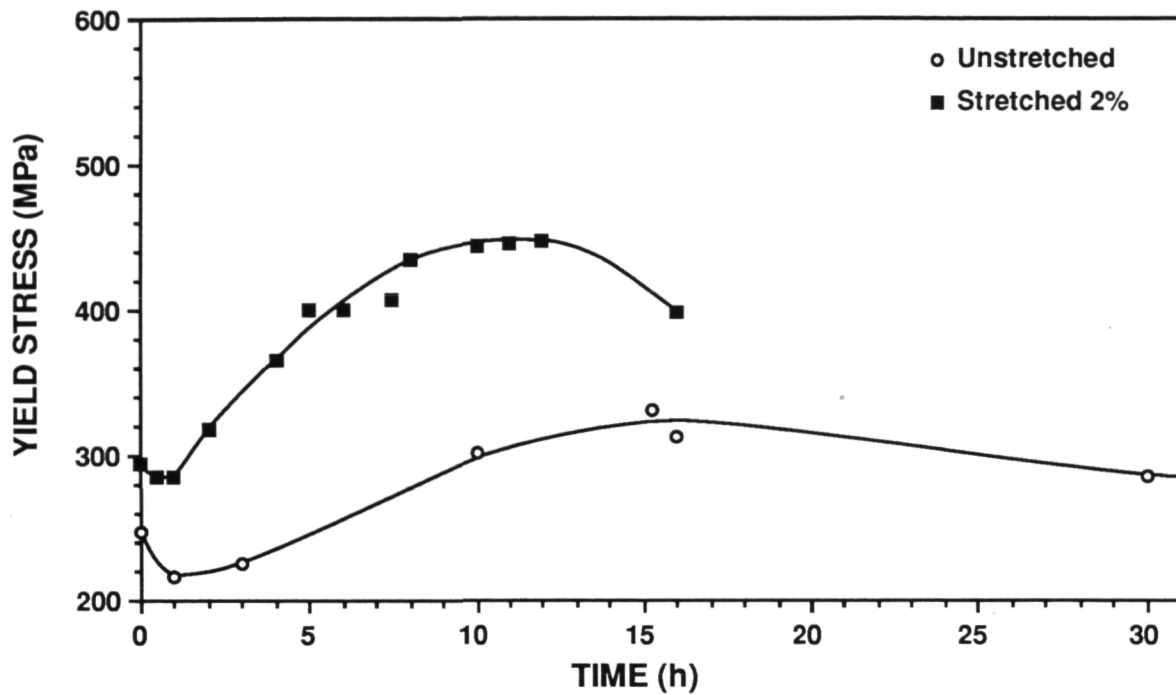
It is believed that for this T3 condition the major contribution to the strength of the composite is due the density of geometrically necessary dislocations from the initial stretching operation.

6.4.3 Aging Kinetics

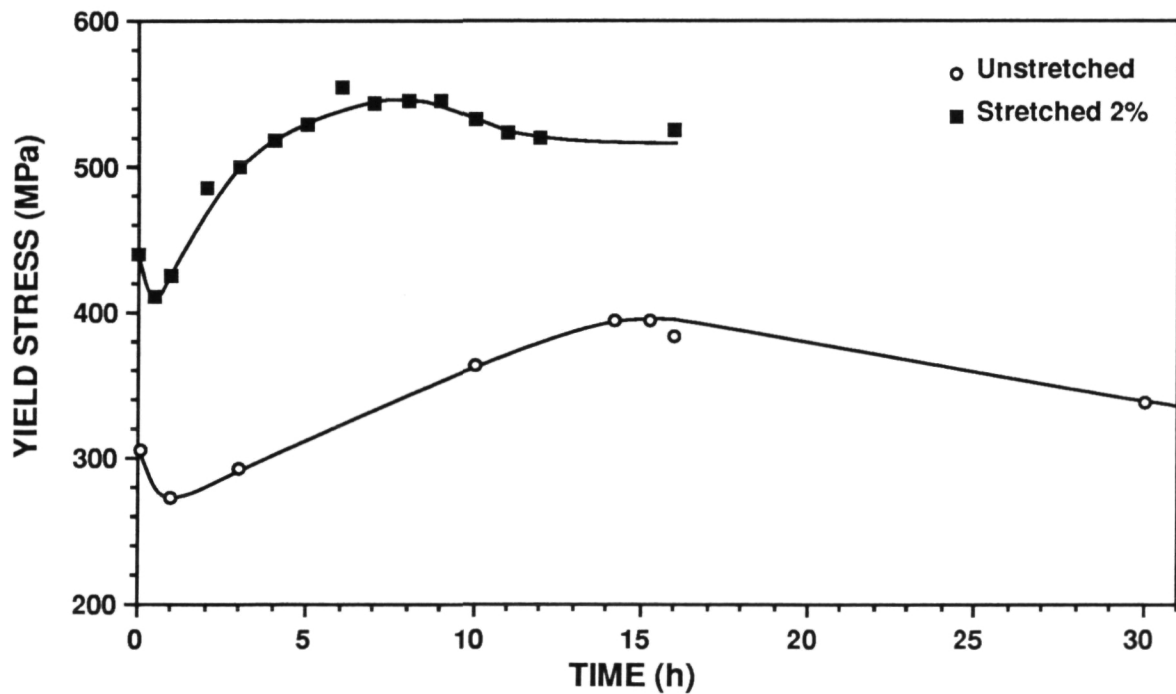
Having examined the role of geometrically necessary dislocations on strength we now examine the influence of the higher dislocation density on the kinetics of artificial aging. In Fig. 6.17 the aging kinetics of the unreinforced Al-4%Cu-1.5%Mg alloy and the alloy reinforced with 10 vol% 1.3 μm TiB₂ are shown with and without a 2% stretch prior to artificial aging. These data indicate the general effect of a stretch prior to artificial aging, i.e., the aging kinetics are accelerated and the peak strength is higher. These result from the presence of a higher dislocation density during the initial stages of aging in the stretched samples. Because the dislocations are heterogeneous nucleation sites for the precipitation of S', there are a larger number of finer precipitates in the stretched samples than in the unstretched samples. For the unreinforced alloy this result is consistent with observations made on commercial 2024 [57-58].

In Fig. 6.18 the variation of yield stress and elongation to fracture is shown for the Al-4%Cu-1.5%Mg alloys reinforced with various loadings of 0.3 μm TiB₂ following a stretch of 2%. The companion plots for Al-4%Cu-1.5%Mg alloys reinforced with 1.3 μm TiB₂ are shown in Fig. 6.19. For both sizes of TiB₂, additional reinforcement moves the yield stress higher while accelerating the aging curve. The acceleration in aging kinetics is dependent on the TiB₂ loading; higher TiB₂ loadings shift the aging curve to shorter times.

In Fig. 6.20 the aging curves for Al-4%Cu-1.5%Mg that is unreinforced, reinforced with 10 vol% of the small 0.3 μm TiB₂, and reinforced with 10 vol% of the larger 1.3 μm TiB₂ that have been stretched 2% prior to aging are replotted. The acceleration appears to be dependent on both the presence of particles and their size. The smaller TiB₂ produces a greater acceleration.

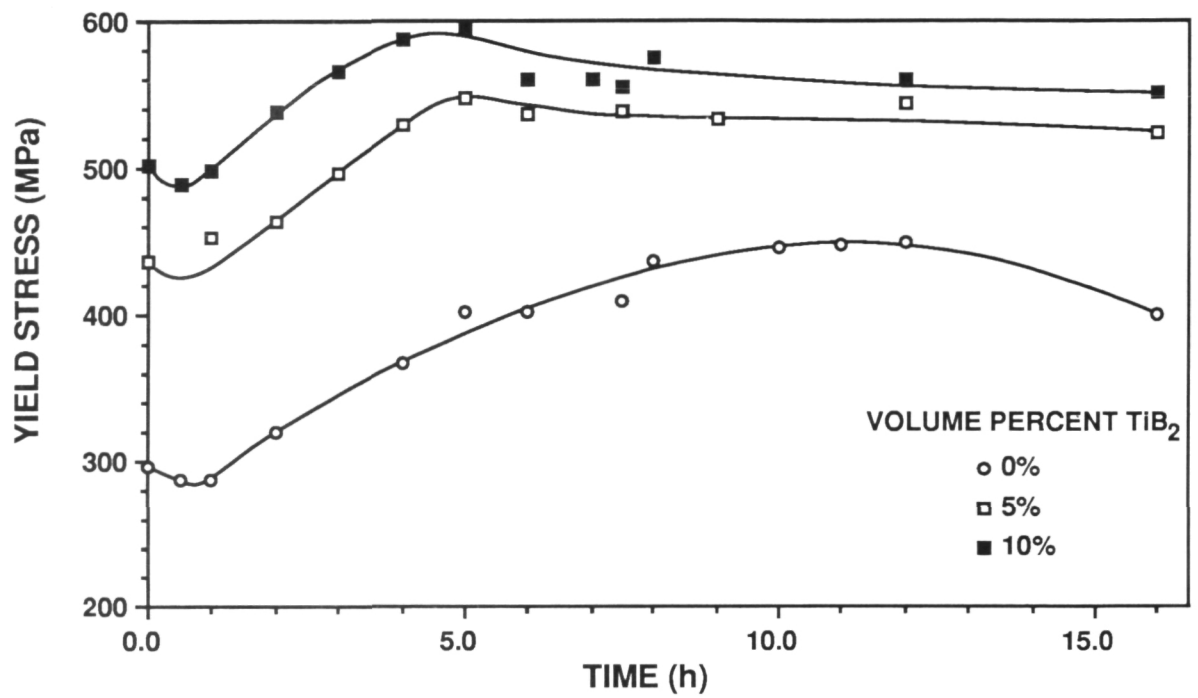


(a) Unreinforced

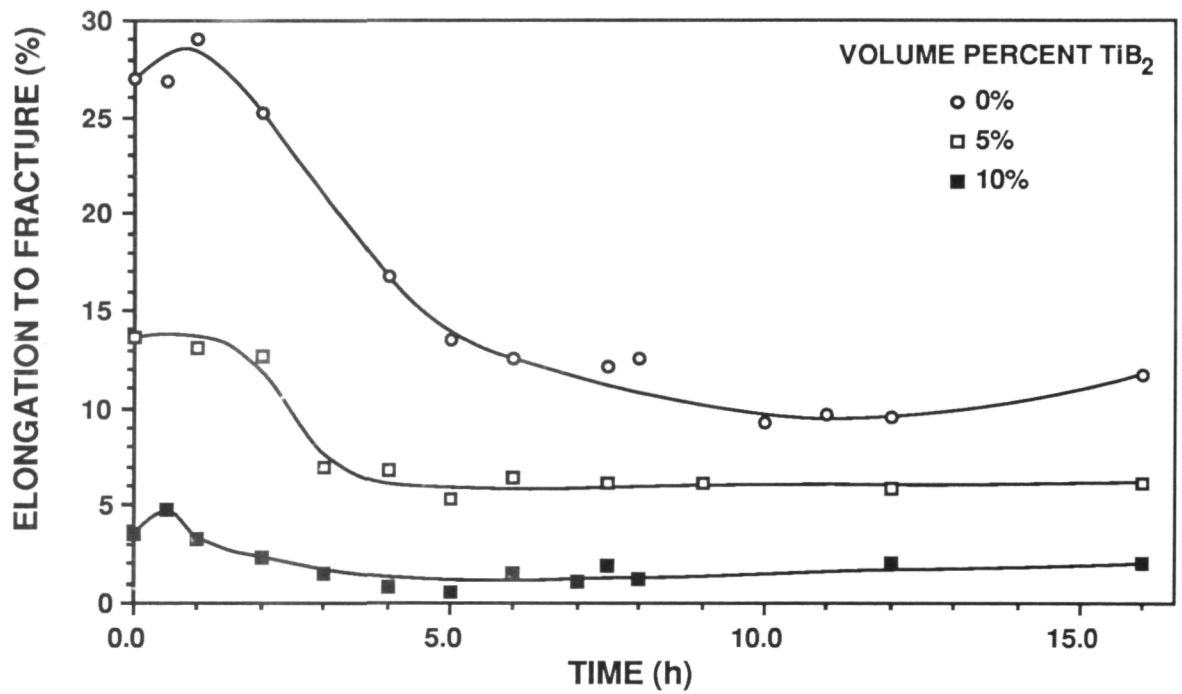


(b) 10 vol% 1.3μm TiB₂

Figure 6.17 Variation of tensile properties with time of artificial aging at 190°C for the Al-4%Cu-1.5%Mg alloys with and without cold work prior to aging.

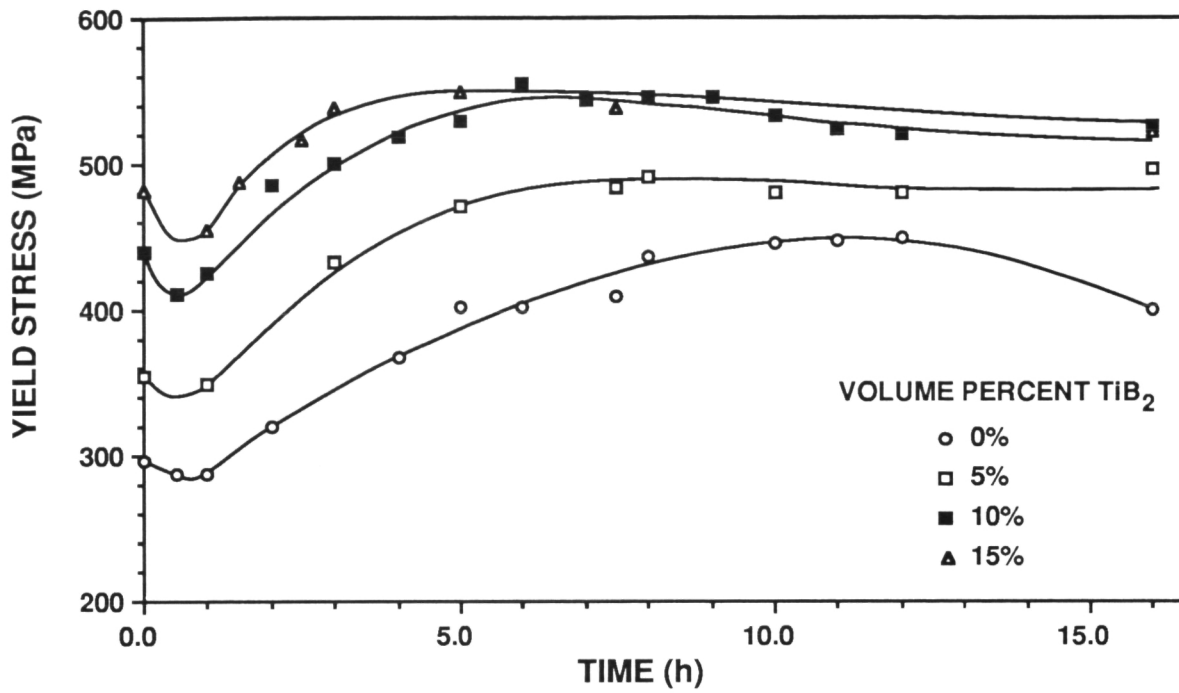


(a) Yield stress

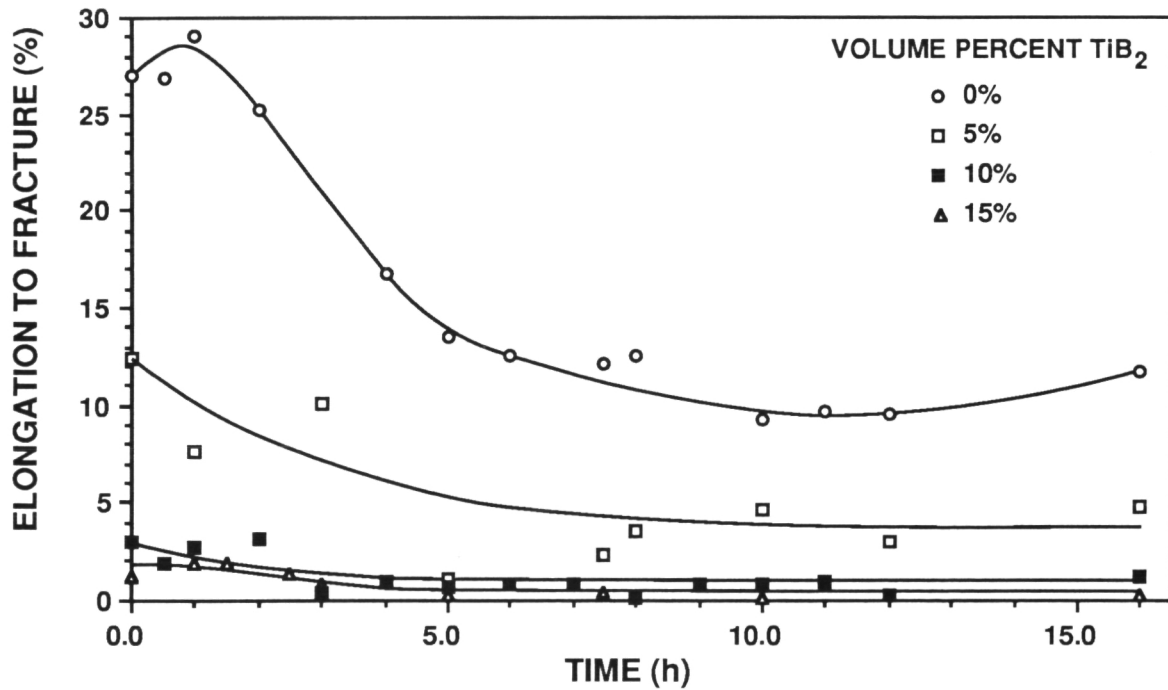


(b) Elongation to fracture

Figure 6.18 Variation of tensile properties with time of artificial aging at 190°C for the Al-4%Cu-1.5%Mg alloys containing 0.3 μm TiB_2 following 2% cold work.



(a) Yield stress



(b) Elongation to fracture

Figure 6.19 Variation of tensile properties with time of artificial aging at 190°C for the Al-4%Cu-1.5%Mg alloys containing 1.3 μm TiB_2 following 2% cold work.

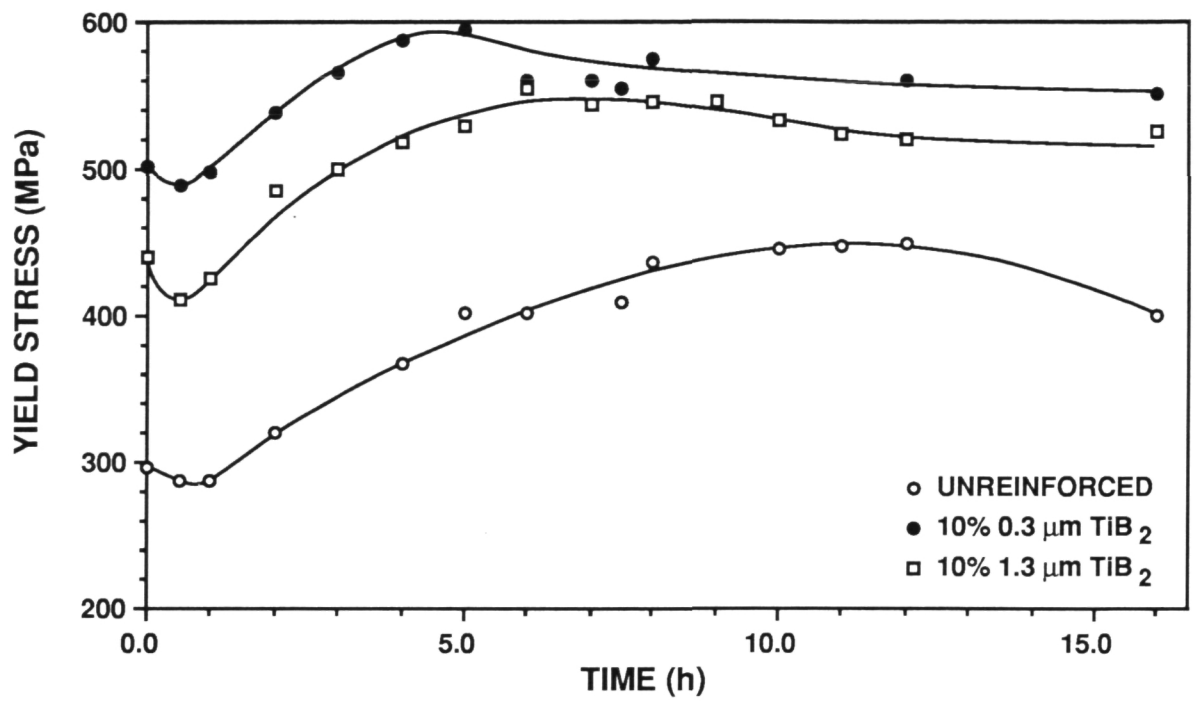


Figure 6.20 Variation of yield stress with time of artificial aging at 190°C for the Al-4%Cu-1.5%Mg alloys following 2% cold work.

6.4.4 Microstructure

In this section we will examine the microstructure of unreinforced Al-4%Cu-1.5%Mg and the alloy reinforced with 10 vol% 1.3 μm TiB_2 which were stretched 2% prior to aging. The yield stress of these alloys was presented in Fig. 6.20 as a function of aging time. Three aging conditions will be considered: the T3 condition (time equal to zero), 5 hours at 190°C (375°F), and 12 hours at 190°C (375°F). According to the mechanical properties shown in Fig. 6.20, 5 hours at 190°C is an underaged condition and 12 hours is the peak-aged condition for the unreinforced alloy. For the alloy reinforced with 10 vol% of 0.3 μm TiB_2 , 5 hours at 190°C is the peak-aged condition and 12 hours is the overaged condition. For the alloy reinforced with 10 vol% of 1.3 μm TiB_2 , 5 hours at 190°C is a slightly underaged condition and 12 hours is a slightly overaged condition.

Figure 6.21 shows the unreinforced Al-4%Cu-1.5%Mg alloy in the T3 condition. The TEM micrograph was taken using a multiple beam condition at a $\langle 001 \rangle$ zone axis. This diffraction condition will image any dislocations present. In the T3 condition both linear and helical dislocations are present, but the G.P. zones are not resolved. Figure 6.22 shows this alloy after aging at 190°C for 5 hours. Regions of S' precipitates are present in the upper right and lower left corners of this micrograph and the center shows a region of lower S' density that contains dislocations which have not had S' nucleate upon them yet. The selected area diffraction (SAD) pattern shown in Fig. 6.22(b) shows the presence of S' (compare with the indexed pattern in Fig. 6.2), while the excessive streaking in the [100] and [010] directions is an indication of how thin the S' precipitates are in these directions. In Fig. 6.23, which shows the microstructure after aging at 190°C for 12 hours, the S' laths have thickened and grown and are much more uniform in distribution and size. In this [001] orientation the two precipitate variants, which have the composite habit of [110] and $[1\bar{1}0]$, can be seen end on as thin laths. The precipitate variants with composite habits of [101] and $[\bar{1}01]$ are inclined to the beam in Fig. 6.23 and appear as corrugated laths.

Figure 6.24 shows the Al-4%Cu-1.5%Mg alloy reinforced with 10 vol% of 0.3 μm TiB_2 in the T3 condition. In the center of the micrograph is a 0.4 μm TiB_2 particle that is trailing several sets of dislocation loops. Linear dislocations and dislocation tangles are also visible. Qualitative comparison of Figs. 6.21 and 6.24 shows the much higher dislocation density in the reinforced alloy due to geometrically necessary dislocations produced by the stretching operation in the presence of the TiB_2 particulates. Figure 6.25 is a higher magnification view of the dislocation loops associated with the TiB_2 particle on the left side of the micrograph. Figure 6.26 shows this alloy after aging at 190°C for 5 hours. In the bright field micrograph, Fig. 6.26(a), two TiB_2 particles are visible, one on the right edge and the other toward the center with low angle boundary intersecting with it. A fine uniform distribution of S'

ORIGINAL PAGE
BLACK AND WHITE PHOTOGRAPH

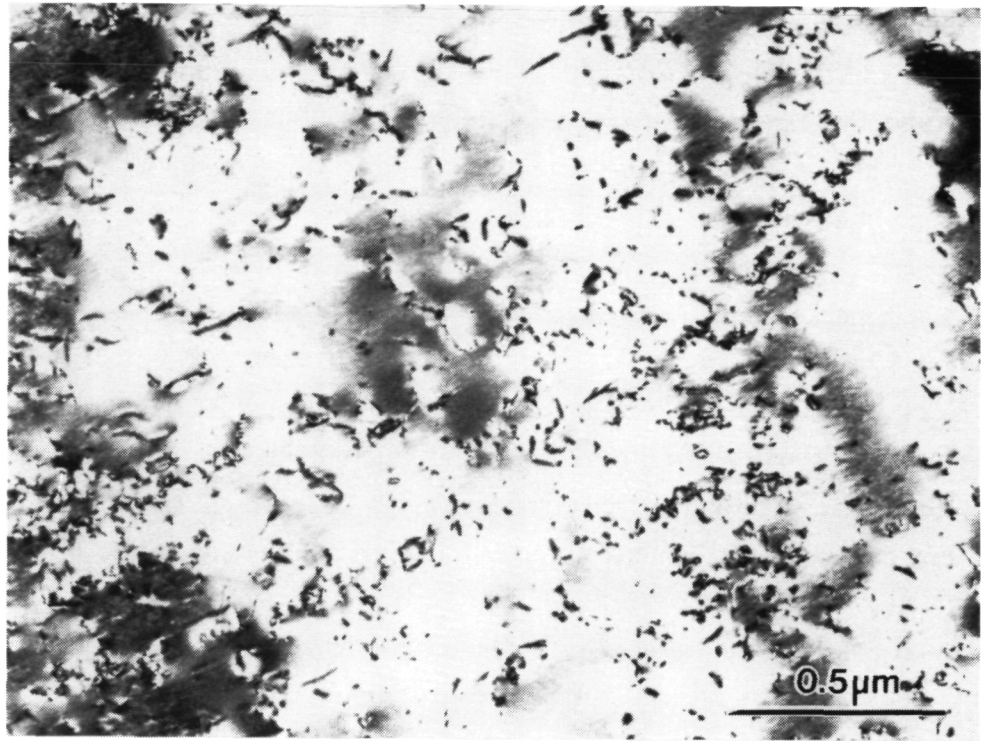
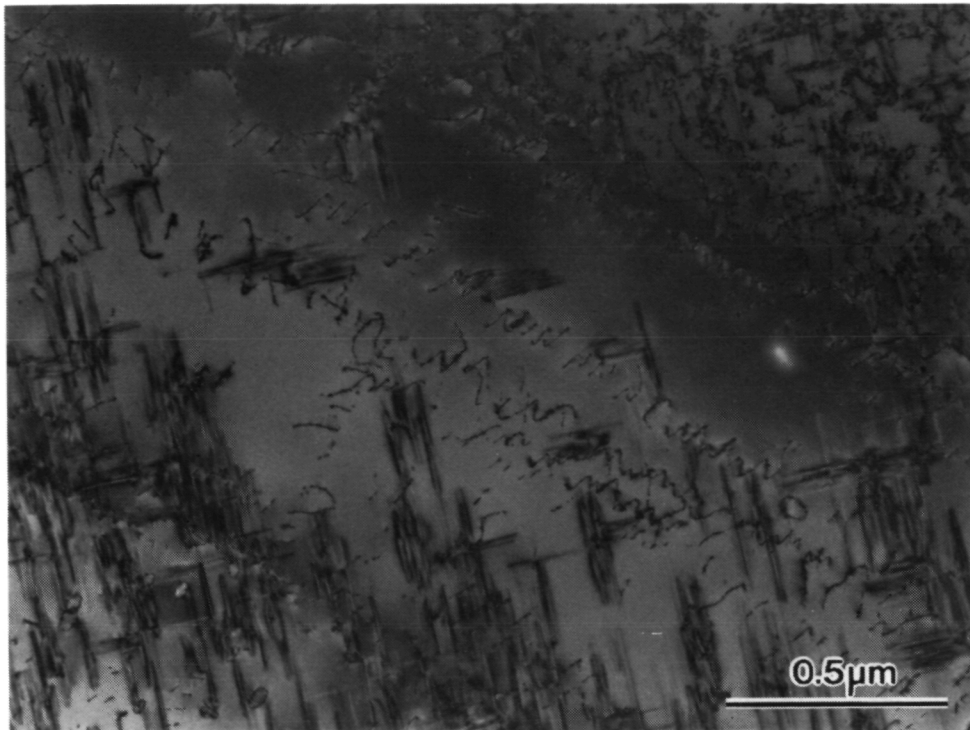
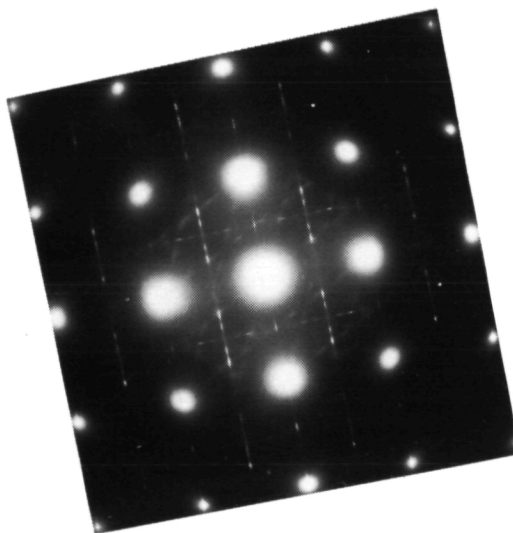


Figure 6.21 Unreinforced Al-4%Cu-1.5%Mg following 2% cold work and naturally aging.
Bright field image at $[001]_{\alpha}$ zone axis.



(a) Bright field image at $[001]_{\alpha}$ zone axis.



(b) SAD pattern at $[001]_{\alpha}$ zone axis.

Figure 6.22 Unreinforced Al-4%Cu-1.5%Mg following 2% cold work and artificially aged at 190°C for 5 hours.

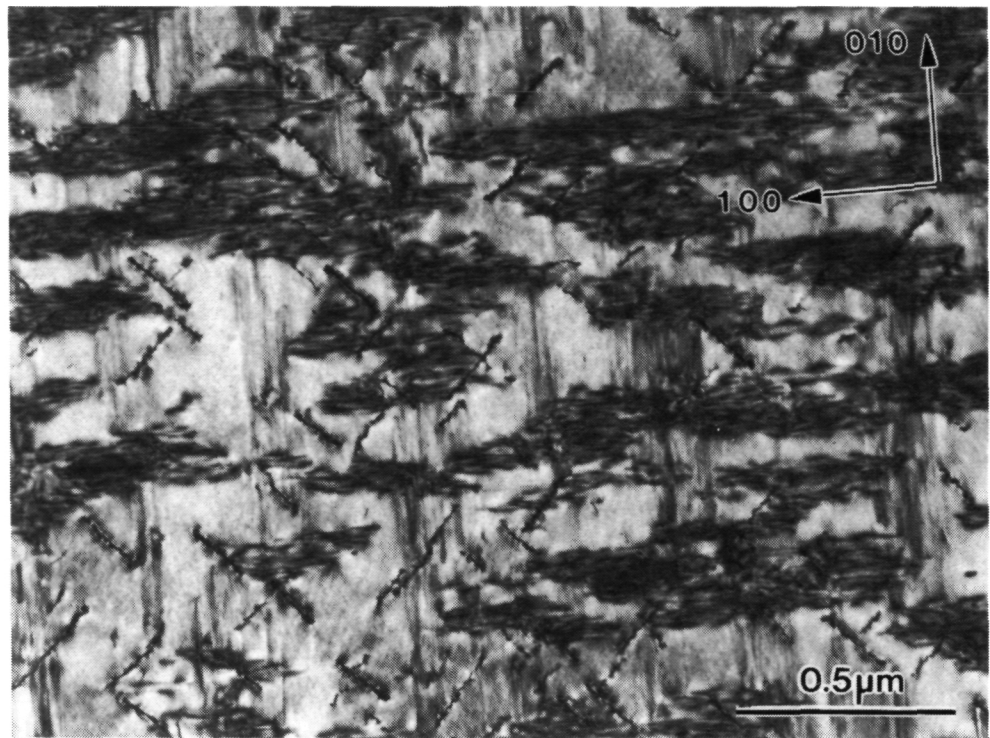


Figure 6.23 Unreinforced Al-4%Cu-1.5%Mg following 2% cold work and artificially aged at 190°C for 5 hours. Bright field image at $[001]_{\alpha}$ zone axis.

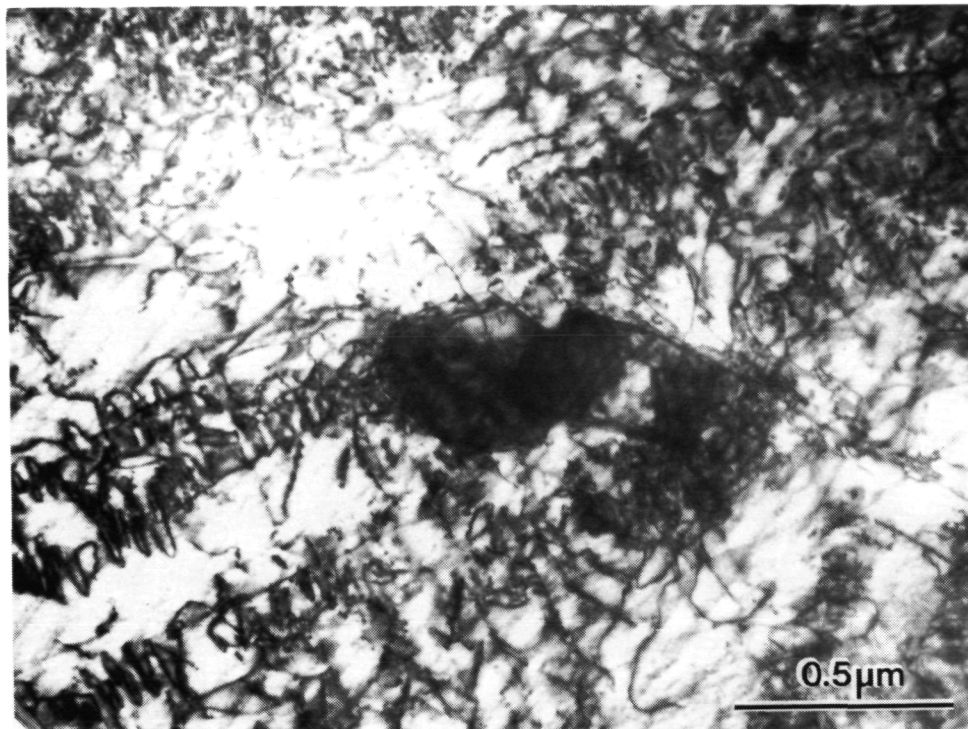


Figure 6.24 Al-4%Cu-1.5%Mg plus 10 vol% of 0.3 μm TiB_2 following 2% cold work and naturally aging. Bright field image at $[110]_\alpha$ zone axis.

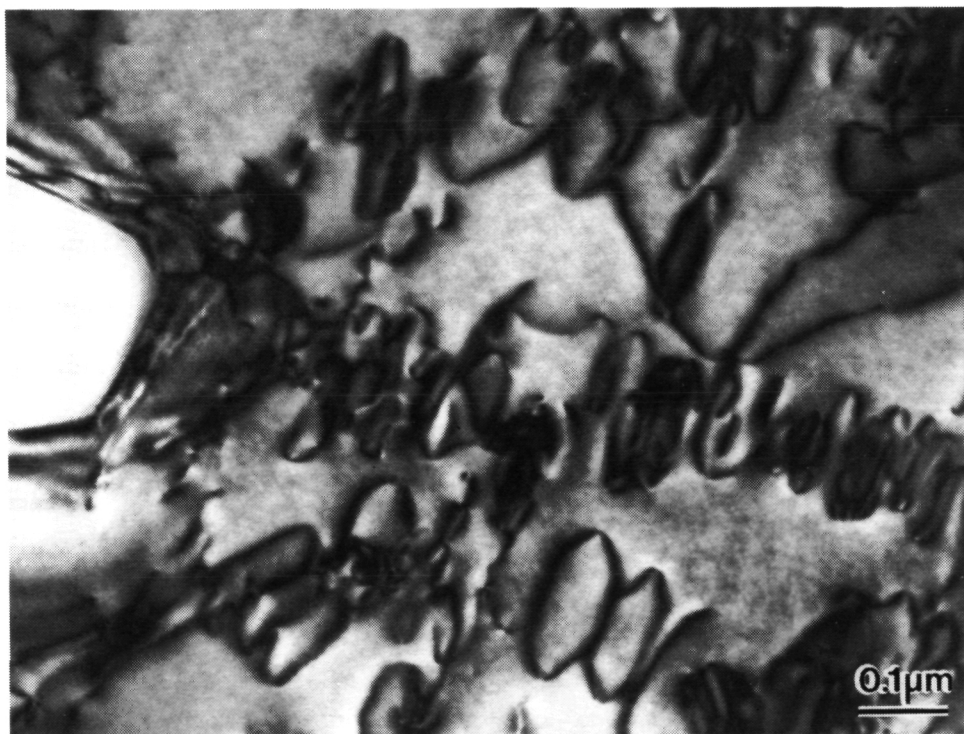
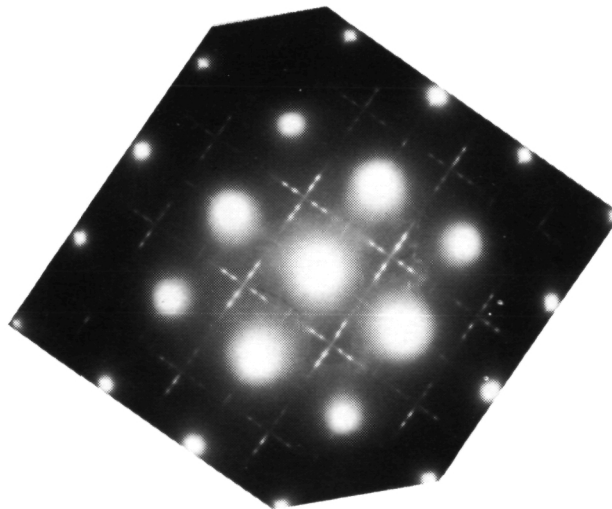


Figure 6.25 Al-4%Cu-1.5%Mg plus 10 vol% of 0.3 μm TiB_2 following 2% cold work and naturally aging. Bright field image at $[001]_\alpha$ zone axis.



(a) Bright field image at $[001]_{\alpha}$ zone axis.



(b) SAD pattern at $[001]_{\alpha}$ zone axis.

Figure 6.26 Al-4%Cu-1.5%Mg plus 10 vol% of 0.3 μm TiB₂ following 2% cold work and artificially aged at 190°C for 5 hours.

precipitates is also present. The SAD pattern {Fig. 26(b)} shows the presence of S'. The greater intensity of the S' spots, compared to those in Fig. 6.22(b), indicate that there is a greater volume fraction of S' in this sample than in the unreinforced alloy after the same length of aging. Comparing the size of the S' precipitates in Fig. 26(a), the peak-aged condition for the 10 vol% 0.3 μm alloy, versus those in Fig. 6.23, the peak-aged condition for the unreinforced alloy, illustrates the smaller size and higher number density of the S' in the reinforced alloy. A lower magnification image is presented in Fig. 6.27 that shows the uniformity of the S' distribution. It appears that neither the TiB_2 particles nor the grain boundaries directly affect the S' distribution and size. The microstructure after aging at 190°C for 12 hours is shown in Fig. 6.28. This micrograph contains a set of closely spaced TiB_2 particles and although this is a slightly overaged condition the uniform distribution of S' fine particles is maintained.

Figures 6.28 and 6.29 shows the Al-4%Cu-1.5%Mg alloy reinforced with 10 vol% of 1.3 μm TiB_2 in the T3 condition. Figure 6.28, which was taken at a [001] zone axis for comparison with Figs. 6.20, 6.23, and 6.24, contains a set of closely spaced TiB_2 particles at the bottom of the micrograph. Figure 6.29 is a set of two micrographs taken under two-beam conditions. In the center of the micrograph is a 1.0 μm TiB_2 particle which appears to have numerous dislocations associated with it. These appear to be predominantly linear dislocations and dislocation tangles in contrast to the dislocation loops observed in the alloys containing smaller TiB_2 particles. Figure 6.31 shows this alloy after aging at 190°C for 5 hours. A small TiB_2 particle is visible in the center of the bright field micrograph, Fig. 6.31(a) along with a fine uniform distribution of S' precipitates. The SAD pattern in Fig. 6.31(b) shows the presence of S'. Comparison of this microstructure with that of the other peak-aged microstructures (the 0.3 μm TiB_2 in Fig. 6.26 and the unreinforced alloy in Fig. 6.23) shows that the size and number density of S' in this alloy is intermediate between the alloy reinforced with 10 vol% 0.3 μm TiB_2 and the unreinforced alloy.

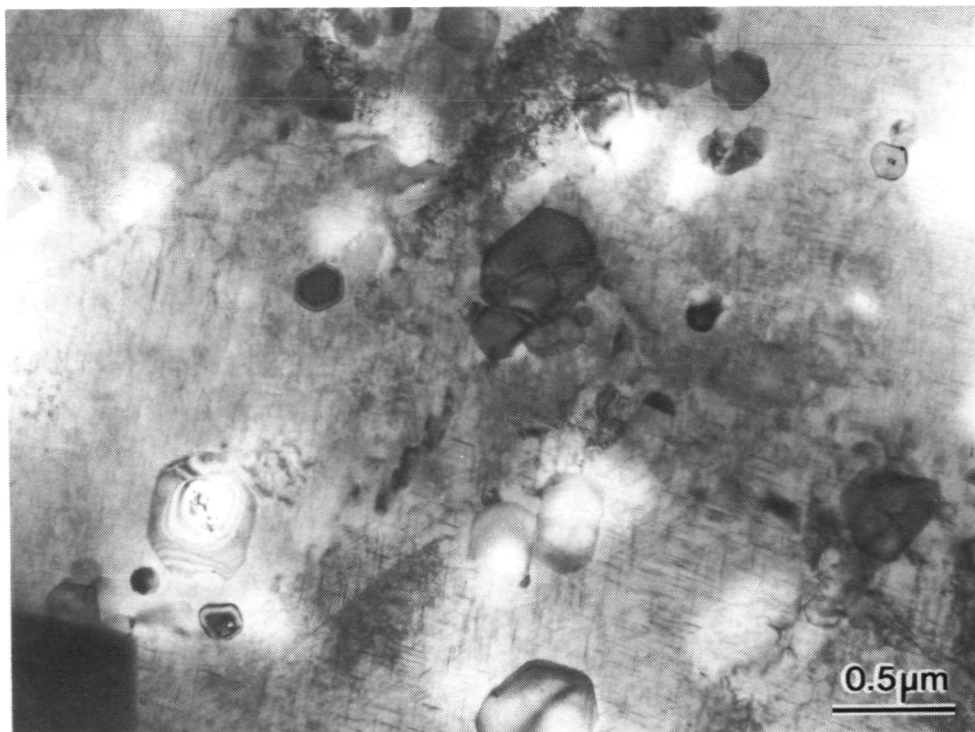


Figure 6.27 Al-4%Cu-1.5%Mg plus 10 vol% of 0.3 μm TiB₂ following 2% cold work and artificially aged at 190°C for 5 hours. Bright field image.

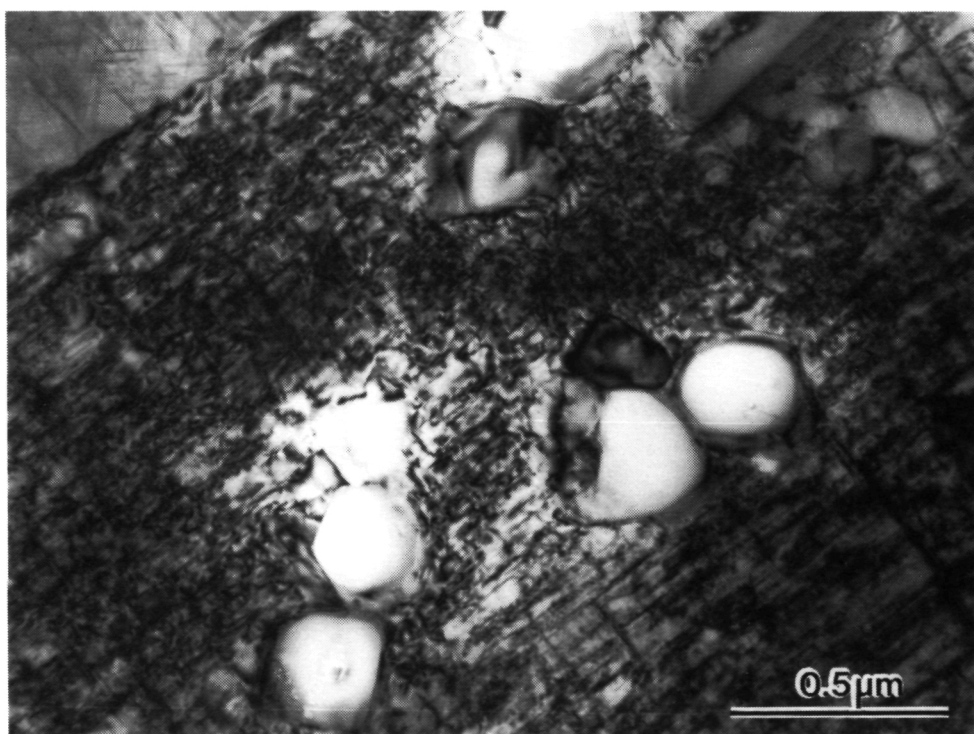


Figure 6.28 Al-4%Cu-1.5%Mg plus 10 vol% of 0.3 μm TiB₂ following 2% cold work and artificially aged at 190°C for 5 hours. Bright field image at [001]_α zone axis.

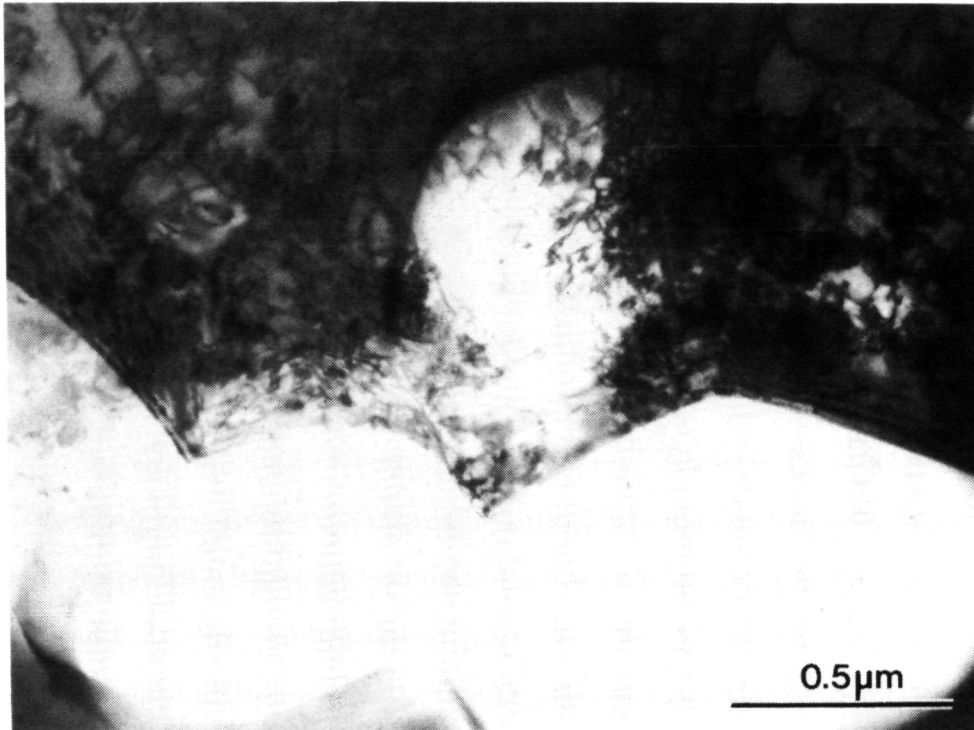
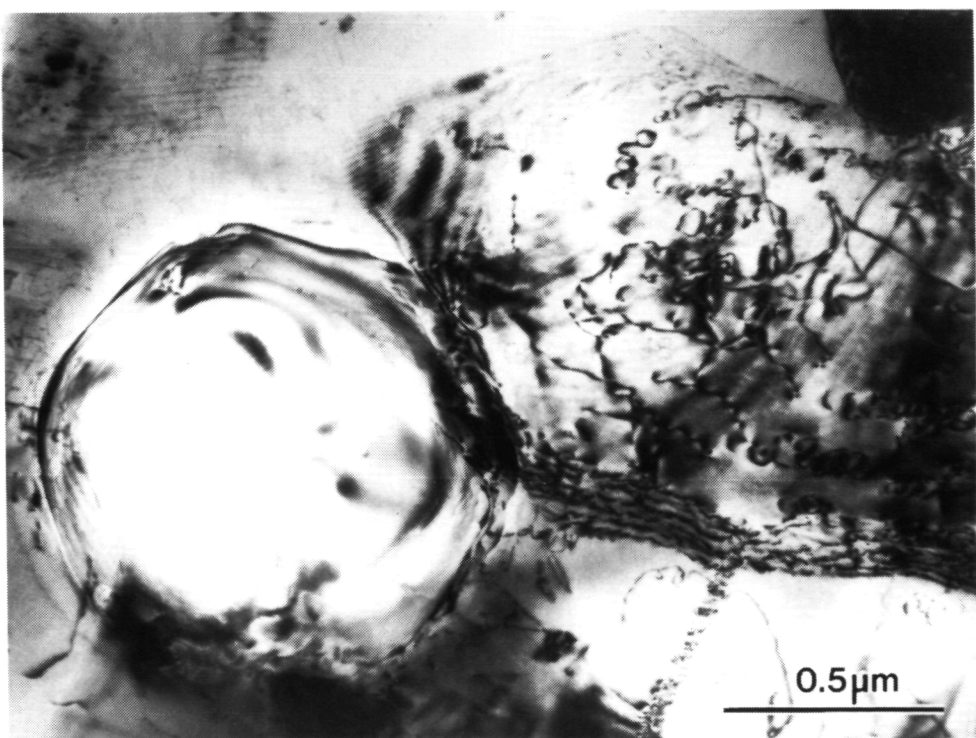


Figure 6.29 Al-4%Cu-1.5%Mg plus 10 vol% of 1.3 μm TiB₂ following 2% cold work and naturally aging. Bright field image at $[110]_{\alpha}$ zone axis.

ORIGINAL PAGE
BLACK AND WHITE PHOTOGRAPH

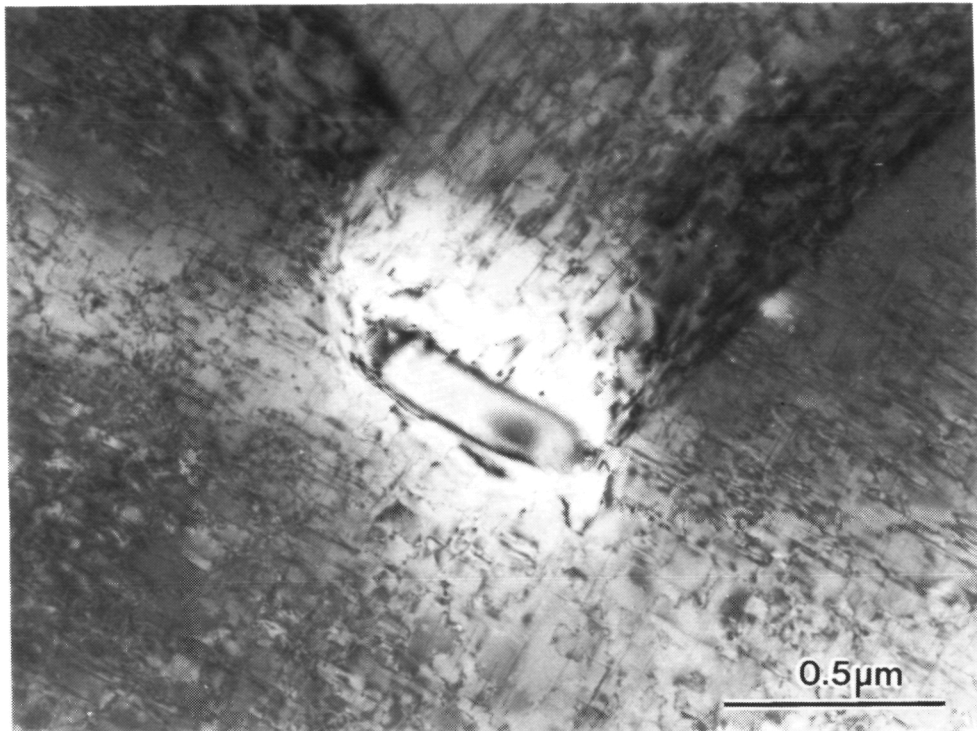


(a) 2-beam bright field image with $g=(\bar{1}11)$ near $[110]_{\alpha}$ zone axis.

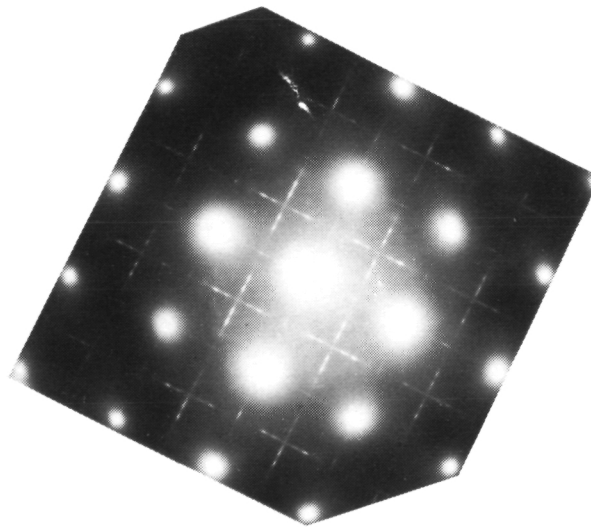


(b) 2-beam bright field image with $g=(1\bar{1}1)$ near $[110]_{\alpha}$ zone axis.

Figure 6.30 Al-4%Cu-1.5%Mg plus 10 vol% of 1.3 μm TiB₂ following 2% cold work and natural aging.



(a) Bright field image at $[001]_{\alpha}$ zone axis.



(b) SAD pattern at $[001]_{\alpha}$ zone axis.

Figure 6.31 Al-4%Cu-1.5%Mg plus 10 vol% of 1.3 μm TiB₂ following 2% cold work and artificially aged at 190°C for 5 hours.

7. STRENGTHENING MECHANISMS IN METAL MATRIX COMPOSITES

Although many aspects of MMCs are understood, there is no consensus on the mechanism responsible for the observed strength increase in discontinuous MMCs. In this chapter we would like to address possible explanations for the increase in yield strength in discontinuous MMCs, using several examples from this work as well as the work of others to illustrate our points. We will restrict ourselves to aluminum and aluminum alloys discontinuously reinforced with equiaxed particles in the range of 0.1 to 10 μm in diameter. Yielding at low temperatures, $T < 0.3T_m$, where deformation occurs by dislocation glide will be examined in Section 7.2 and high temperature deformation will be considered in Section 7.3.

7.1 Review of Possible Strengthening Mechanisms at Low Temperatures

7.1.1 Continuum Models

The models utilizing continuum mechanics include those with analytical solutions, such as the shear lag and the Eshelby type, and those with numerical ones.

The shear lag theory assumes that load transfer occurs between a high aspect ratio reinforcement and the matrix by means of shear stresses at the particle-matrix interface. By this mechanism the particle can act as a “reinforcement” to carry some of the load. The original model [60] only accounted for the shear transfer of load along the interface parallel to the applied load. Modifications have subsequently been made to account for the tensile transfer of load at the particle ends, a contribution which becomes more significant as the aspect ratio of the particle decreases [61-62,8]. According to the modified shear lag theory, the yield stress of the composite is

$$\sigma_y = \sigma_{ym} \left[1 + \frac{(L+t)A}{4L} \right] f + \sigma_{ym}(1-f) \quad (7.1)$$

where σ_{ym} is the yield stress of the unreinforced matrix, L is the length of the particle perpendicular to the applied stress, t is the length of the particle parallel to the applied stress, A is the particle aspect ratio, and f is the particle volume fraction.

For the equiaxed particles under consideration in this work, Eqn. 7.1 reduces to

$$\sigma_y = \sigma_{ym} \left(1 + \frac{1}{2} f \right). \quad (7.2)$$

There are several things to note with this form of the equation: it is linear with a very modest increase with increasing volume fraction and there is no dependence of the yield stress on particle size or other microstructural scale.

7.1.2 Single Dislocation-Particle Interaction Model

For small impenetrable particles a passing dislocation will bow between particles and finally by-pass the particle, leaving behind an “Orowan” loop. The effect of this process on the yield stress of the material is described by the Orowan relationship. As modified by Ashby and converted to tensile stresses for polycrystalline material this relationship is

$$\sigma_y = \frac{0.83MGb}{2\pi(1-\nu)^{1/2}} \frac{\ln(2r/r_0)}{(\lambda_s - 2r_s)} \quad (7.3)$$

where M is the Taylor factor, G the shear modulus, b the Burgers vector, ν Poisson's ratio, r the radius of the particles, r_0 the cut off radius or radius of the dislocation core, and $(\lambda_s - 2r_s)$ the mean interparticle separation on the slip plane [63]. For the interparticle separations typical of MMCs ($\geq 1 \mu\text{m}$) the strength increment with increasing volume fraction is small.

7.1.3 Multiple Dislocation-Particle Interaction Models: Dislocation Pile-Up Models

In a single-phase polycrystalline material the yield stress is proportional to $d^{-1/2}$, where d is the grain diameter. This is the Hall-Petch relationship, which arose from experimental observations on α -iron [64-65]. Experimental data of σ_y versus $d^{-1/2}$ show constant slopes but do not extrapolate to 0 as d becomes infinite. This discrepancy is typically dealt with by adding a stress, σ_0 , which is rationalized as either a frictional stress to the motion of dislocation glide or an internal back stress. This leads to the relation

$$\sigma_y = \sigma_0 + kd^{-1/2} \quad (7.4)$$

where k is the Hall-Petch slope. This relationship adequately describes the grain-size dependence of the flow stress in many materials and can be derived theoretically by calculating the stress concentration due to a dislocation pile-up at a grain boundary [66]. Lack of experimental observation of dislocation pile-ups in pure metals has led to the alternative model where the grain boundary is assumed to be a dislocation source [67,68].

The same $d^{-1/2}$ dependence of the yield stress has been observed in two-phase alloys where d is the characteristic microstructural dimension, e.g., the dimension that governs the slip distance. Examples include drawn ferrite, where d is the dislocation cell size; drawn perlite, where d is the interlamellar spacing of carbide; and polygonized aluminum, where d is

the cell size [69]. For bcc metals a very informative example is that of the competitive effects of cementite particles, grain boundaries, and subgrain boundaries on the behavior of spherodized cementite in a ferrite matrix as performed by Anand and Gurland [70]. Another example is the strengthening of deformation-processed composites such as drawn or rolled Cu-Nb, where under some conditions, the strength increase has been attributed to direct blocking of dislocation motion by the interphase boundaries leading to a $\lambda^{-1/2}$ relationship where λ is the interphase separation [71-73].

In summary, if the grain boundaries or subgrain boundaries impede dislocation motion, then the grain or subgrain size is the characteristic microstructural dimension; if the particles impede dislocation motion, then the interparticle separation is the characteristic microstructural dimension. In either case, if dislocation pile-up (or dislocation generation) is the operative strengthening mechanism, then an inverse square-root dependence on the characteristic microstructural dimension will be observed.

In the situation where the grain size and interparticle spacing have similar dimensions, dislocation pile-ups at both particle-matrix interfaces and grain boundaries may contribute. In such situations the ease of dislocation annihilation/generation at a particular interface is of issue. For instance Hornbogen and Staniek have shown that in a Fe-1%Cu alloy, dislocations were generated more profusely at the incoherent boundaries of the copper precipitates than at the grain boundaries of the matrix [74]. Thus, the behavior of the interphase barrier may be as important as the spacing of these boundaries.

7.1.4 Multiple Dislocation-Particle Interaction Models: Forest Hardening Models

Another aspect of the role of multiple dislocations is the role of dislocations on the work-hardening behavior of alloys at small strains. Kamat, Hirth, and Mehrabian [75] have examined the tensile properties of 2024 and 2014 reinforced with equiaxed alumina particles 5, 15, and 50 μm in diameter and suggest that at small strains, dislocation tangles form around the particles due to plastic incompatibility. These geometrically necessary dislocations link up to form dislocation cells with a diameter proportional to the interparticle spacing λ . They suggest that this should lead to a flow stress

$$\sigma = \alpha \frac{Gb}{\lambda} \quad (7.5)$$

where α is a proportionality constant.

It is possible that in some MMCs the reinforcement of the matrix does not significantly alter the onset of plastic deformation, rather the observed increase in the 0.2% offset yield

stress is due to an increase in the rate of work hardening at small strains. In these alloys a λ^{-1} dependence of the 0.2% offset yield stress would be observed.

7.2 Role of Particle Size and Volume Fraction

7.2.1 Al + TiB₂

As discussed in Chapter 3, high-purity aluminum was produced with 0.5, 2, 5, and 10 volume percent TiB₂ by ingot metallurgy using the XD™ process. The TiB₂ particles are equiaxed with average particle diameter of 0.3 μm . (Although the aluminum matrix is nominally 99.99% pure, there is some inherent solubility of Ti in the molten Al.) These alloys were hot forged in 3 orthogonal directions and then annealed/recrystallized at 500°C. Because of the lack of precipitates the matrix should deform by diffuse slip, which leads to the formation of dislocation cells and forest hardening.

In Fig. 7.1 the 0.2% offset yield and proportional limit are plotted against volume percent TiB₂. Although there is a minor increase of the proportional limit with increasing volume fraction TiB₂ the increase is slight compared with that in the 0.2% offset yield. In Fig. 7.2 the yield stress is plotted versus the grain size to the -1/2 power (Hall-Petch relationship) along with a least-squares fit of the data. The trend of increasing yield stress with decreasing grain size is observed, though the fit is poor. In Fig. 7.3 the yield stress is plotted against the theoretically calculated interparticle spacing to both the -1 power and the -1/2 power along with a least-squares fit of the data. Here the interparticle separation on the slip plane is $(\lambda_s^* - 2r_s)$ [75], where λ_s^* is the mean planar separation of particles defined by Kocks [76] as

$$\lambda_s^* = 1.25 r \sqrt{\frac{2\pi}{3f}} \quad (7.6)$$

and r_s is the mean radius of intersection of a random plane with a spherical particle of radius r which was given in the previous chapter

$$r_s = \sqrt{2/3} r. \quad (6.7)$$

In these pure aluminum alloys the fit of the data with $(\lambda_s^* - 2r_s)^{-1}$ is better than the fit with $(\lambda_s^* - 2r_s)^{-1/2}$. Thus, it is suggested that the observed increase in yield stress is due to forest hardening of the matrix resulting from the formation of dislocation cells having a diameter proportional to the interparticle spacing. Hence the apparent increase in yield strength is due to an increase in the initial strain hardening rate (as shown in Fig. 3.9) and not to a significant change in the point at which dislocations initially move.

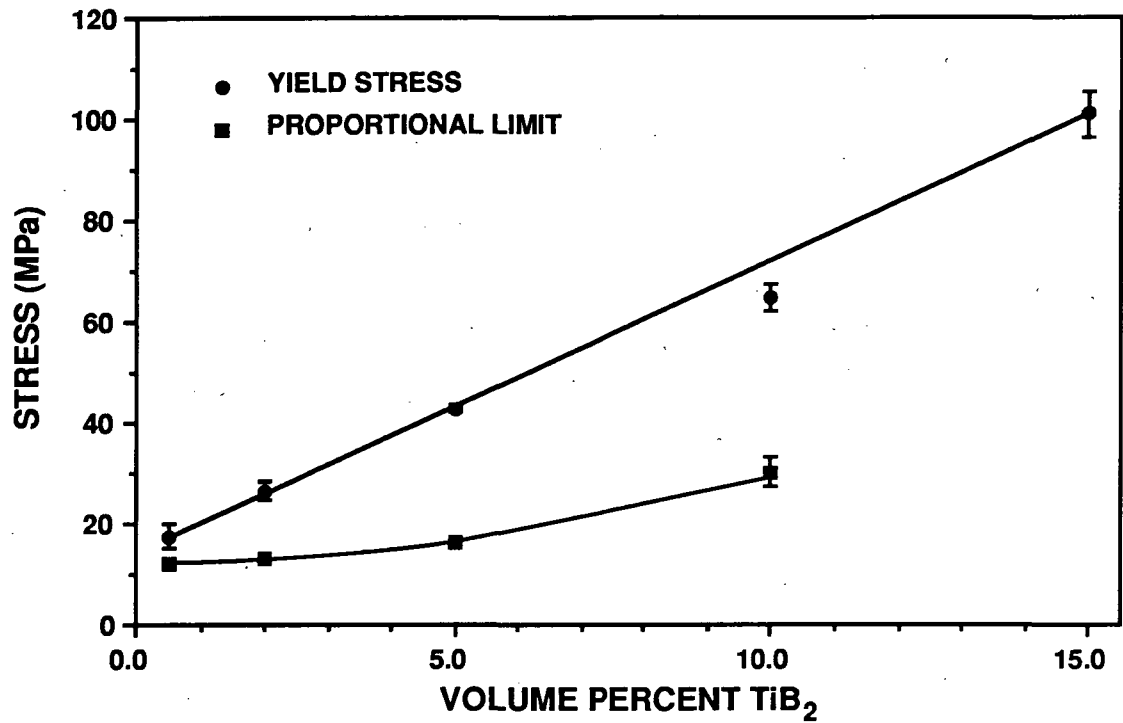


Figure 7.1 Yield stress and proportional limit versus particle loading for pure aluminum alloy with TiB₂.

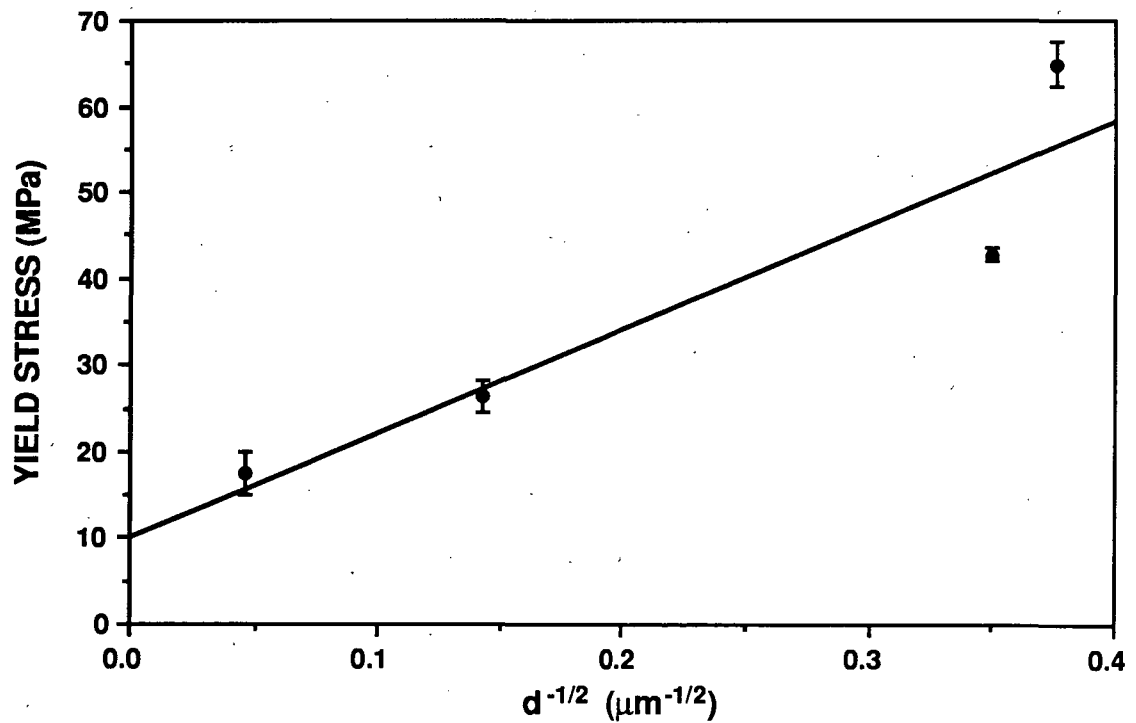
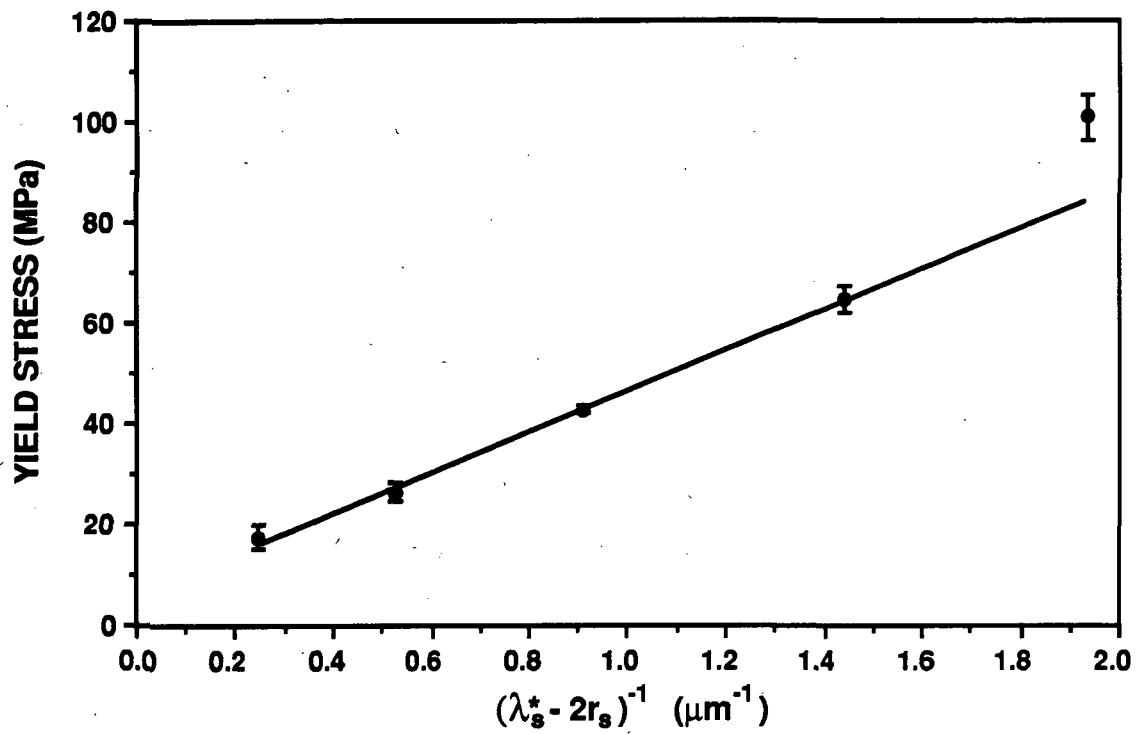
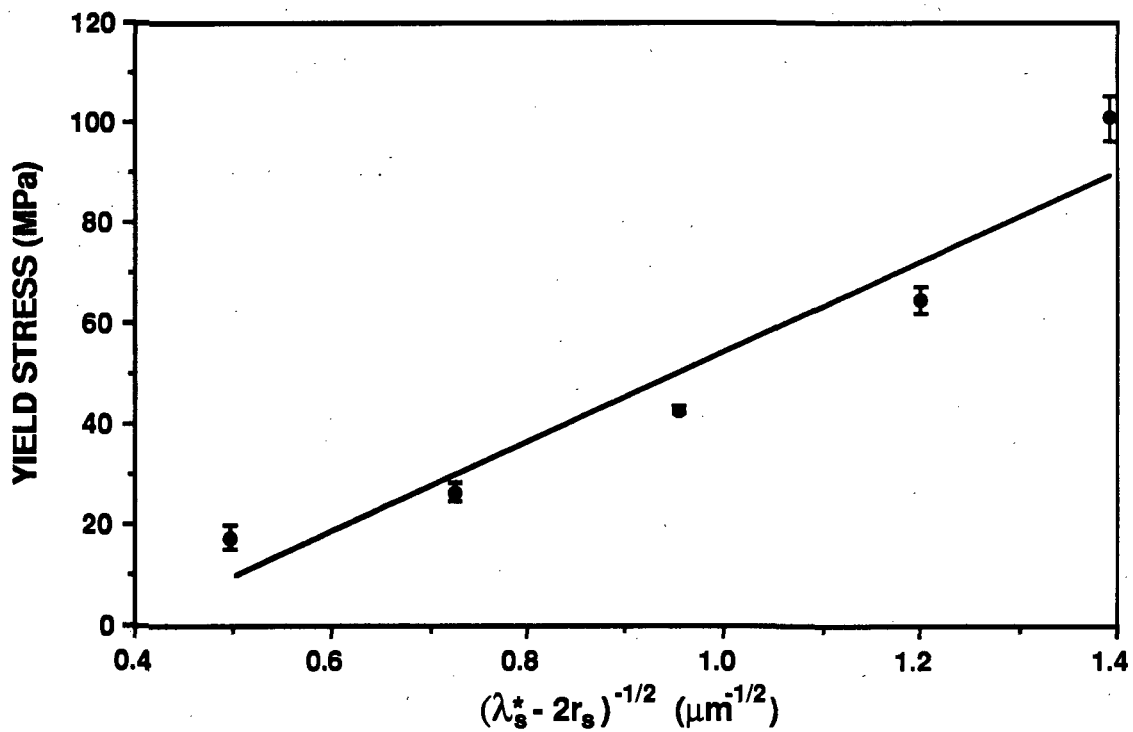


Figure 7.2 Yield stress versus the inverse square-root of grain size for pure aluminum alloy with TiB₂.



a) Yield stress versus the inverse of interparticle separation



(b) Yield stress versus the square-root of the inverse of interparticle separation

Figure 7.3 Yield stress as a function of the interparticle separation for pure aluminum alloy with TiB_2 .

7.2.2 Al-4%Cu-1.5%Mg + TiB₂: Planar Slip

As discussed in Chapter 4, Al-4wt%Cu-1.5wt%Mg alloys containing 0, 2, 5, 10, and 15 volume percent TiB₂ of two average particle diameters were produced. These alloys were extruded, solutionized at 493°C, water quenched, and then allowed to naturally age at room temperature. This heat treatment produces a dispersion of very fine G.P. zones that are sheared by the movement of dislocations so that the matrix deforms by planar slip.

The 0.2 offset yield stress of these alloys in the naturally aged, T4 condition, is shown in Fig. 7.4. The yield stress increases with increasing particle loading. At any given loading, the alloys with the small particles show a greater increase in strength than the alloys with larger particles. In Fig. 7.5 the yield stress is plotted along with the proportional limit of these same alloys. Note that the yield stress and the proportional limit increase at a similar rate with increasing volume fraction of TiB₂. Thus, the observed increase in strength is due to an increase in the initial resistance to the movement of dislocations and not a difference in the initial strain hardening rate.

As previously noted, the continuum models do not account for the observed particle size effect. Additionally, for equiaxed particles shear lag (Eqn. 7.2) predicts an increase in the yield stress that is significantly smaller than is observed experimentally; for the 15 vol% composite compare the 7.5% increase predicted by shear lag to the 45% increase observed.

Applicability of the various characteristic slip-length models was examined by plotting the yield stress against the various microstructural dimensions. The grain size for these alloys had been experimentally measured and is shown as a function of particle size and loading in Fig. 4.8. In Fig. 7.6 the yield stress is plotted versus the grain size to the -1/2 power (Hall-Petch relationship) along with a least-square fit of the data. The trend of increasing yield stress with decreasing grain size is observed, though the fit is poor. In Fig. 7.7 the yield stress is plotted against the measured interparticle spacing, $(\lambda - 2r_p)$, to both the -1 and the -1/2 powers along with a least-square fit of the data. Measurement of average interparticle spacing on a plane of polish, λ , was performed by the line intersect method using SEM micrographs [77]. Although the fit of the data with $(\lambda - 2r_p)^{-1}$ is reasonably good, the fit with $(\lambda - 2r_p)^{-1/2}$ is better with the data of different particle sizes and loadings falling on the same line.

The slope obtained in Fig. 7.7(a) differs from the Orowan slope predicted by Eqn. 7.3 by several orders of magnitude; thus the observed dependence on particle spacing is not due to Orowan strengthening. The data therefore suggest that the strength increase in these alloys, in this temper, is due to dislocation pile-ups through an interphase barrier-strengthening mechanism.

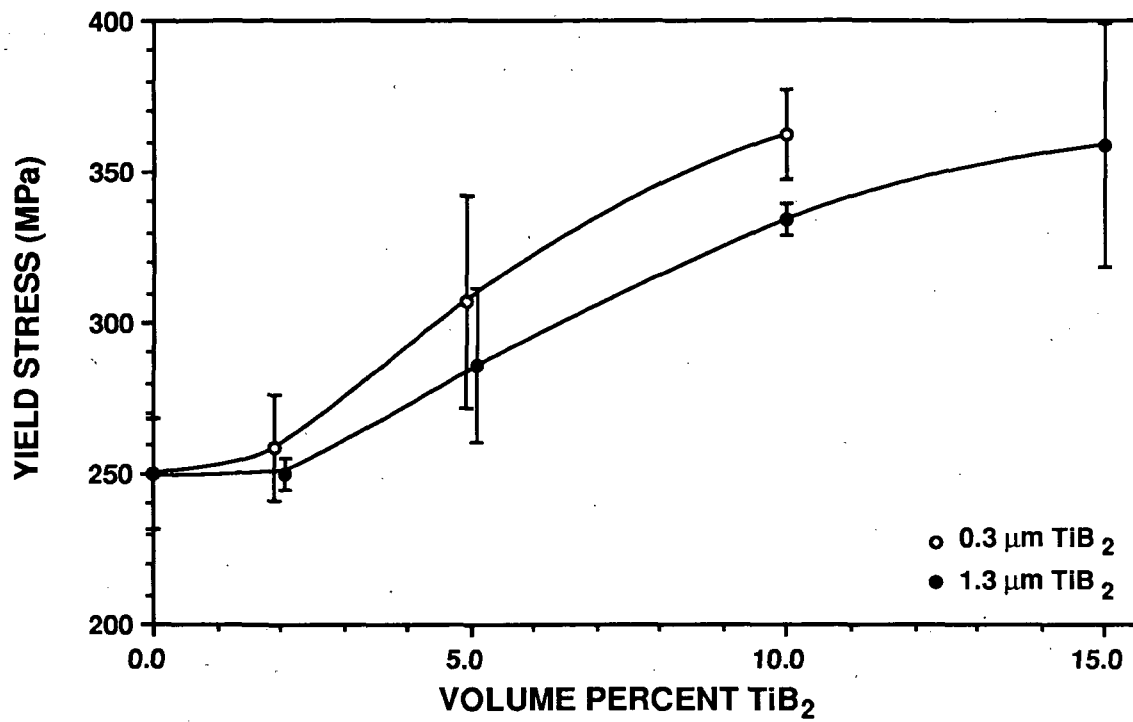
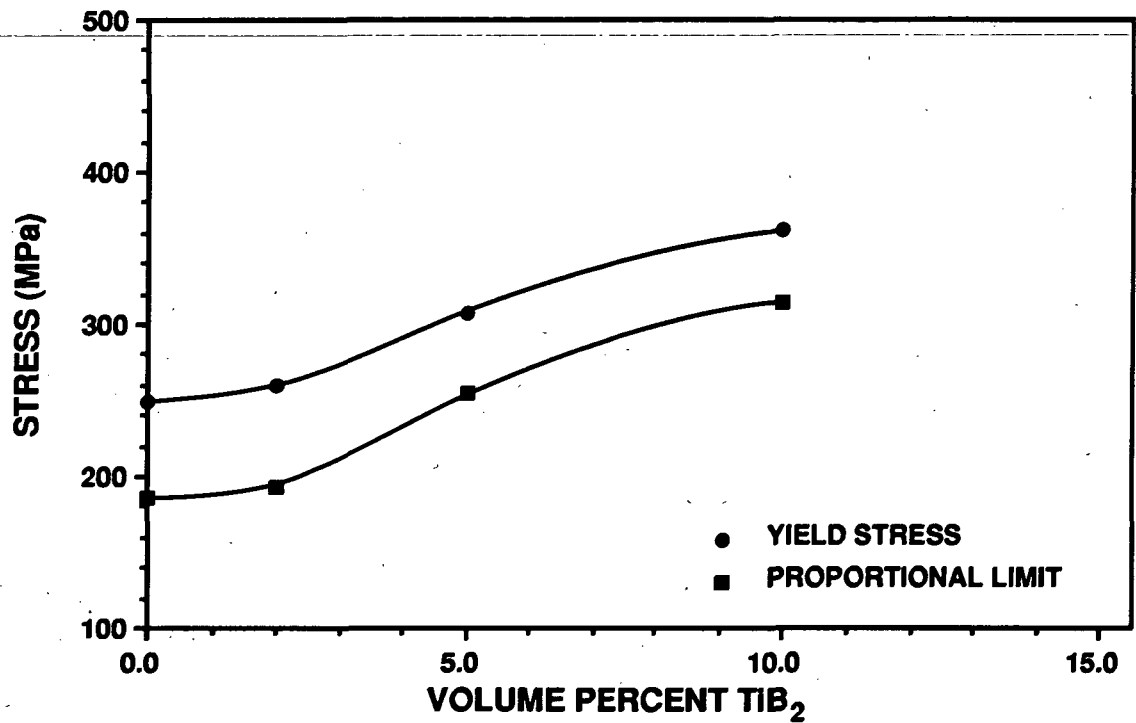
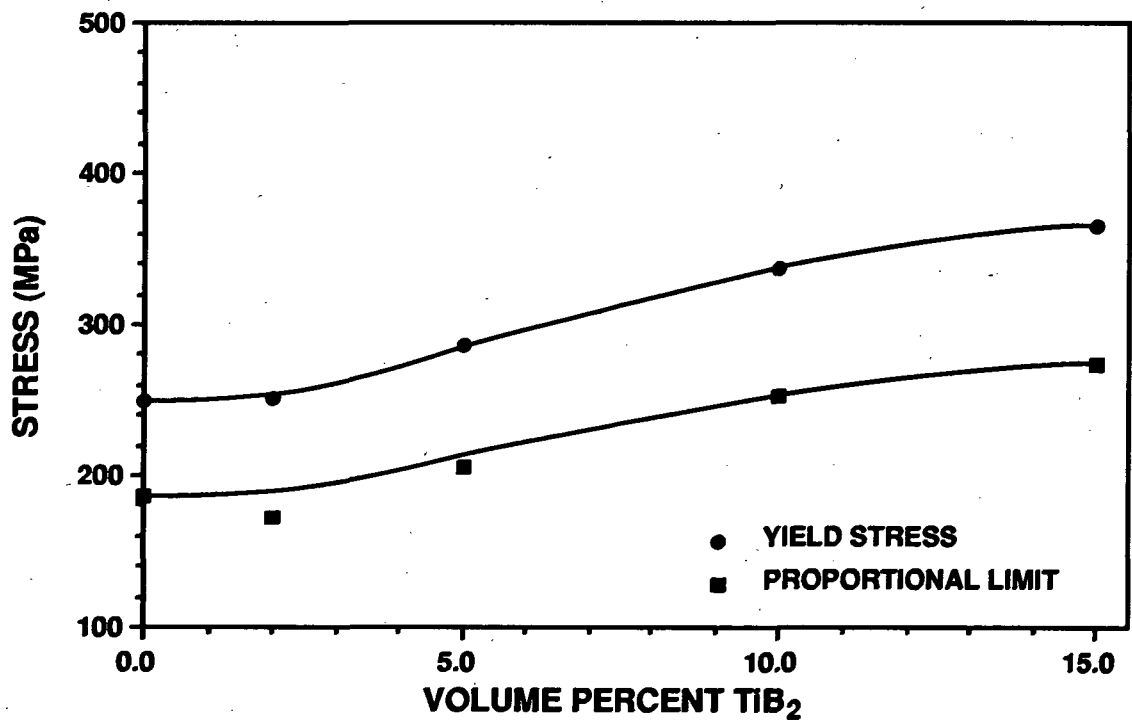


Figure 7.4 Variation of yield stress with volume percent of TiB_2 for Al-4%Cu-1.5%Mg alloys in naturally aged (T4) condition.



(a) Alloys containing $0.3 \mu\text{m}$ TiB_2



(b) Alloys containing $1.3 \mu\text{m}$ TiB_2

Figure 7.5 Variation of yield stress and proportional limit with volume percent for Al-4%Cu-1.5%Mg alloys in naturally aged (T4) condition.

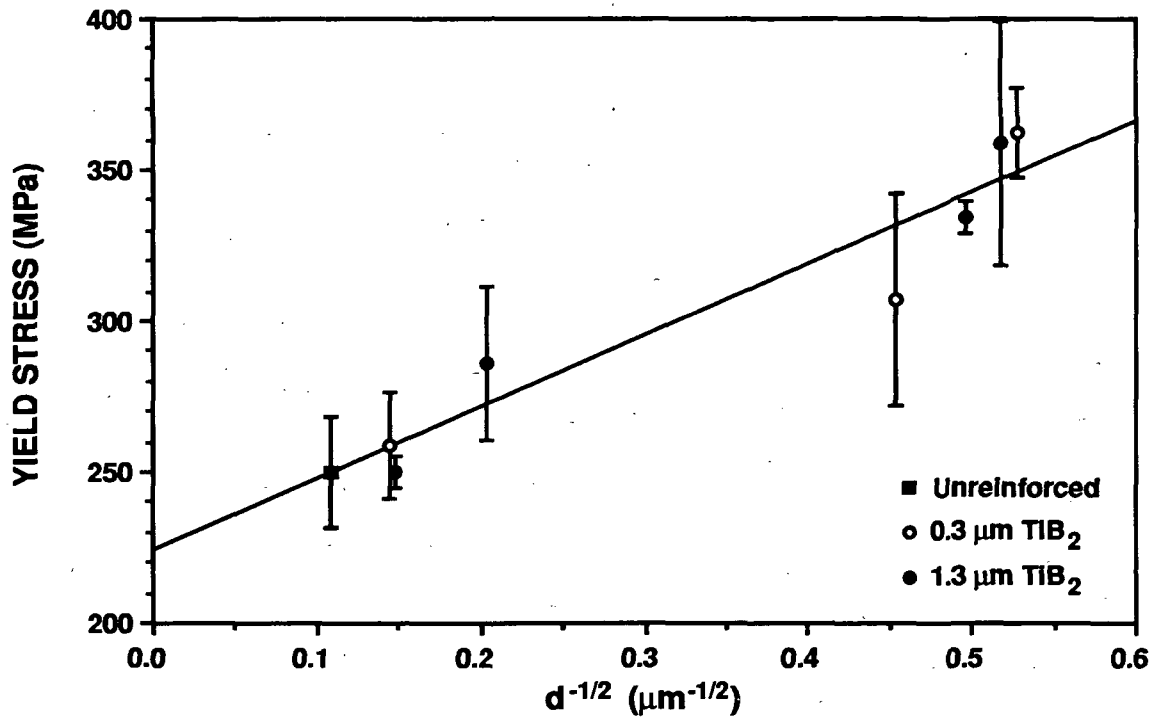
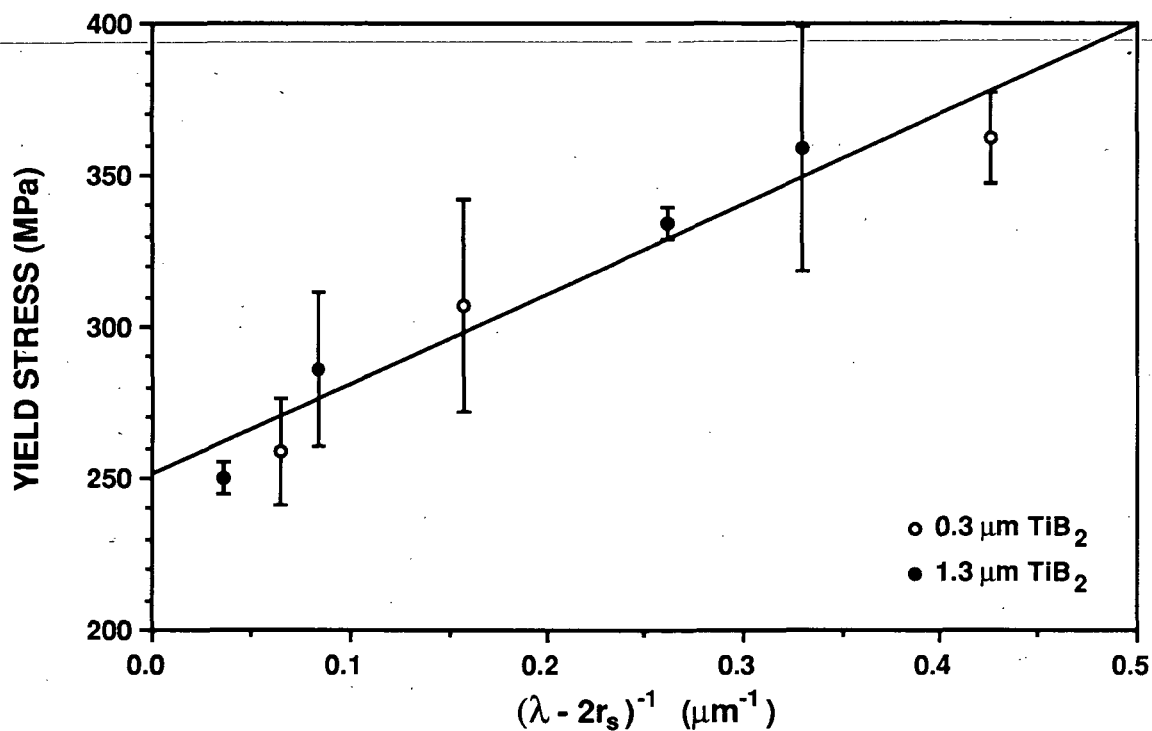
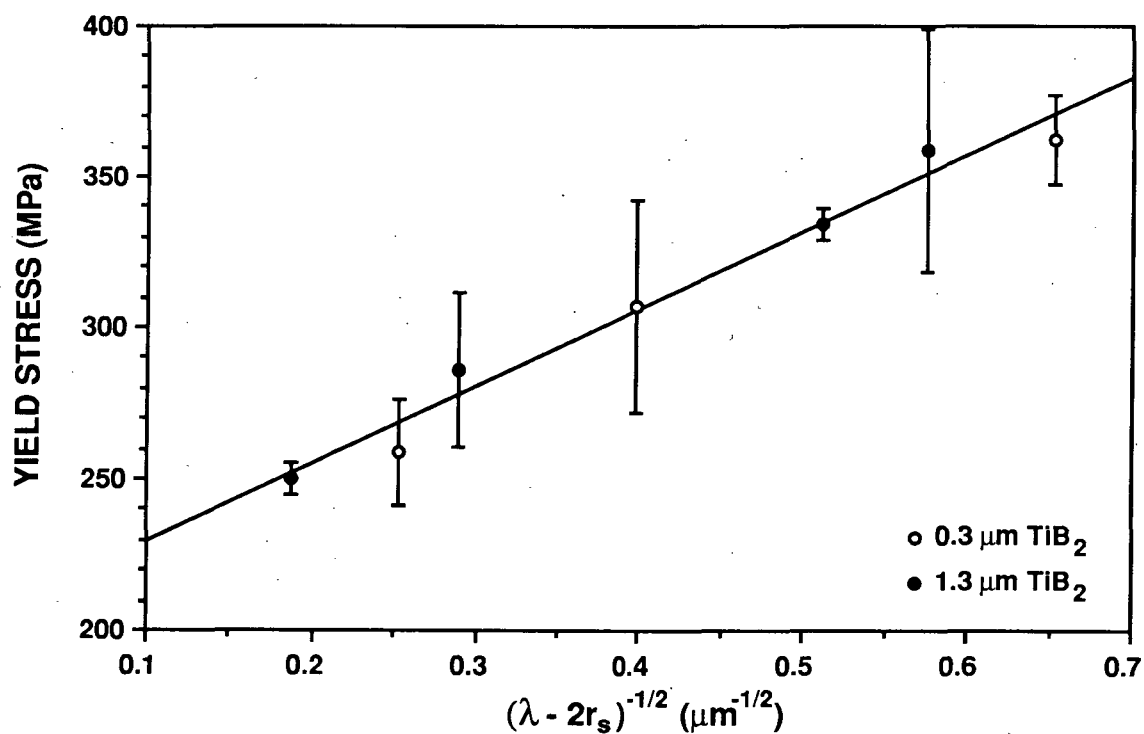


Figure 7.6 Yield stress versus the inverse square-root of grain size for Al-4%Cu-1.5%Mg alloys in naturally aged (T4) condition.



(a) Yield stress versus the inverse of interparticle separation



(b) Yield stress versus the square-root of the inverse of interparticle separation

Figure 7.7 Yield stress as a function of the interparticle separation for Al-4%Cu-1.5%Mg alloys in naturally aged (T4) condition.

7.2.3 Al-4%Cu-1.5%Mg + TiB₂: Wavy Slip

In a manner analogous to the analysis just considered for the T4 condition, in this section the behavior of Al-4%Cu-1.5%Mg alloys in the T6 condition is considered. Here the strengthening phase is primarily S' which should not be sheared by the movement of dislocations. Thus, in this condition the matrix deforms by wavy slip. The 0.2 offset yield stress of these alloys in the peak aged, T6 condition, is shown in Fig. 7.8. The yield stress increases with increasing particle loading. At any given loading, the alloys with the small particles show a greater increase in strength than the alloys with larger particles. In Figs. 7.9 the yield stress is plotted along with the proportional limit of these same alloys. Note as in the T4 condition the yield stress and the proportional limit increase at a similar rate with increasing volume fraction of TiB₂.

In Fig. 7.10 the yield stress is plotted versus the grain size to the -1/2 power (Hall-Petch relationship) along with a least-square fit of the data. In Fig. 7.11 the yield stress is plotted against the measured interparticle spacing, ($\lambda - 2r_s$), to both the -1 and the -1/2 powers along with a least-squares fit of the data. In all three plots the fit is poor. It is suggested that in this condition a combination of the slip distance as determined by grain size or interparticle spacing and the strength and spacing of the precipitates is controlling the strength of the alloy.

7.2.4 Al-4.5%Cu-1.5%Mg-0.6%Mn + Al₂O₃

As mentioned previously, Kamat, Hirth, and Mehrabian [75] have examined the tensile properties of Al-4.5%Cu-1.5%Mg-0.6%Mn (aluminum alloy 2024) reinforced with equiaxed alumina particles 5 μ m and 50 μ m in diameter and particle loadings of 2 to 20 vol%. The alloys were tested in the annealed condition or the O temper. In the O temper it is likely that plastic deformation will be by planar slip. In Fig. 7.12 the data of Kamat et al. are replotted for the 2024 alloys versus λ^{-1} and $\lambda^{-1/2}$. As with the Al-4%Cu-1.5%Mg+TiB₂ alloys, the fit of the data with λ^{-1} is reasonably good and the fit with $\lambda^{-1/2}$ is better. This suggests that the strength increase is due to dislocation pile-ups at Al₂O₃ particles. An alternative explanation is that the interparticle spacing may be controlling the grain size and hence a Hall-Petch relationship between interparticle spacing and yield stress is observed. Since the grain size of these alloys was not reported no definitive answer is possible.

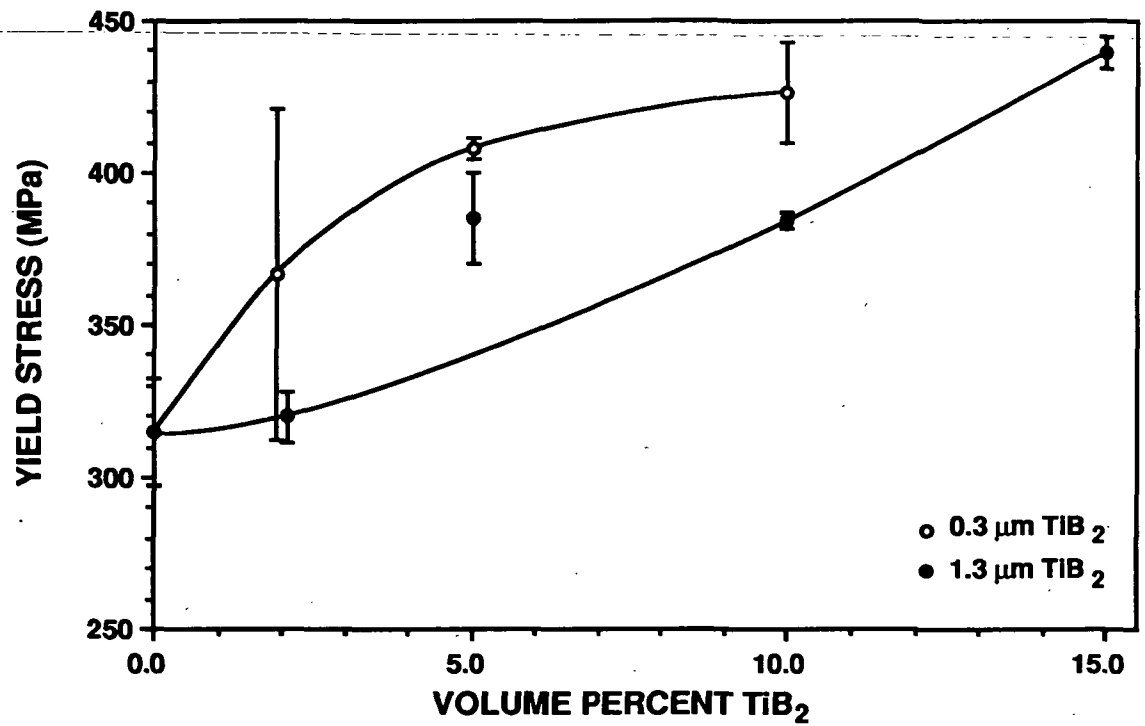
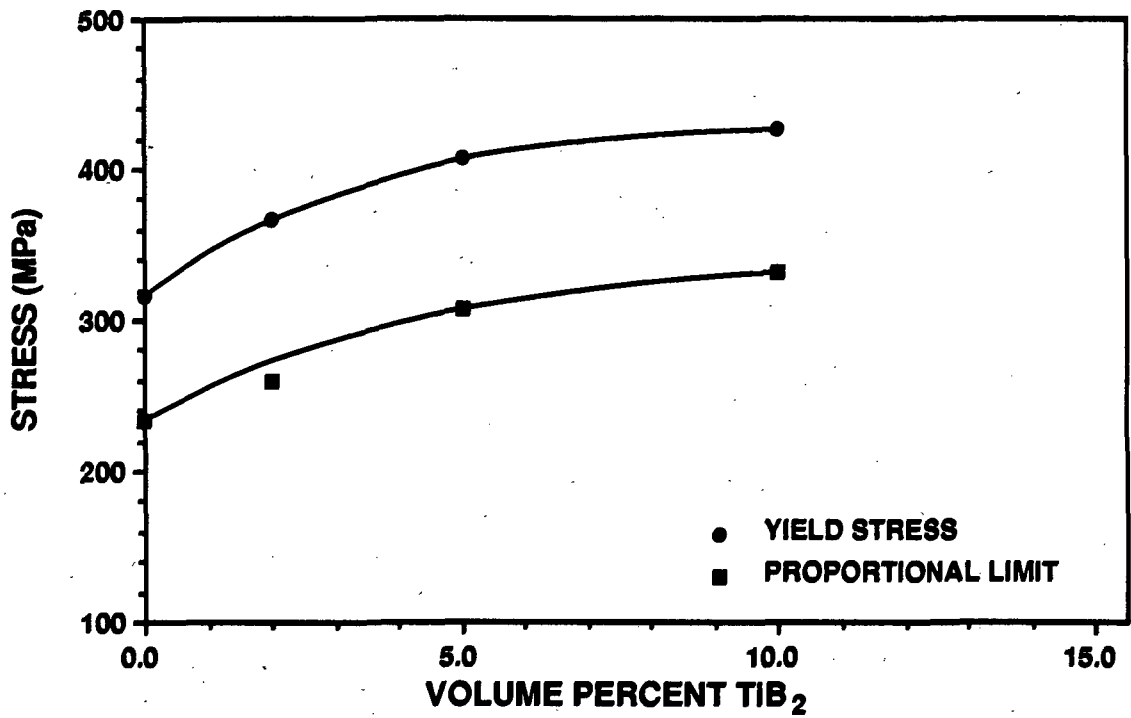
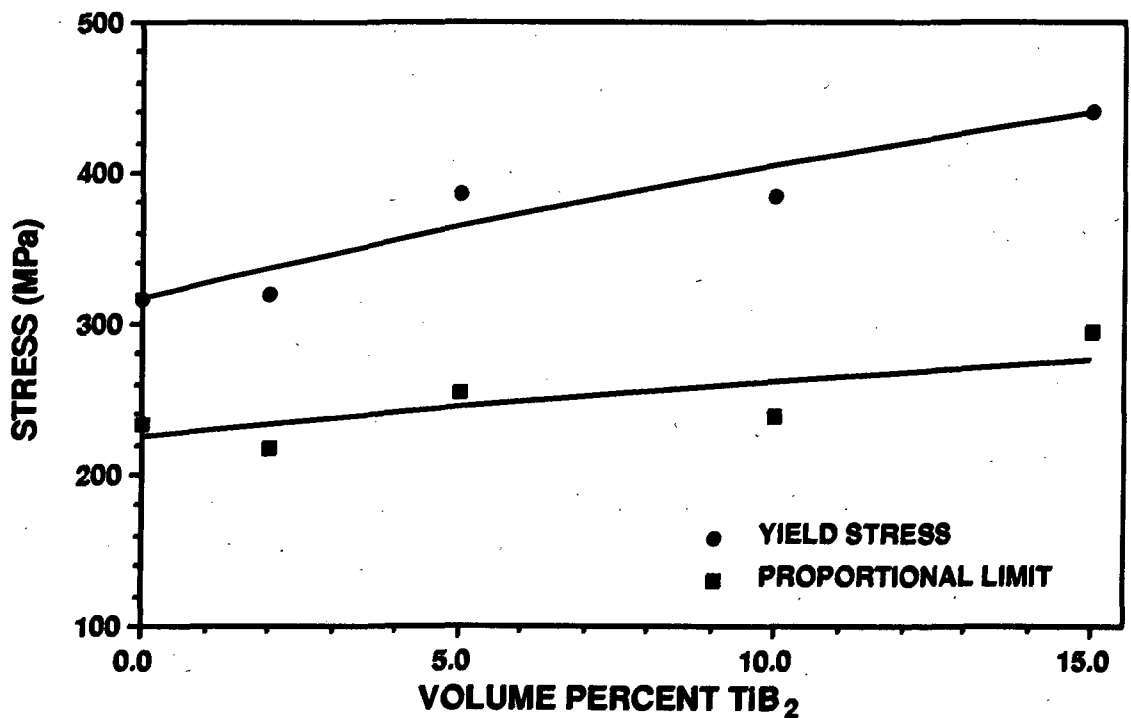


Figure 7.8 Variation of yield stress with volume percent of TiB_2 for Al-4%Cu-1.5%Mg alloys in peak-aged (T6) condition.



(a) Alloys containing $0.3 \mu\text{m}$ TiB_2



(b) Alloys containing $1.3 \mu\text{m}$ TiB_2

Figure 7.9 Variation of yield stress and proportional limit with volume percent for Al-4%Cu-1.5%Mg alloys in peak-aged (T6) condition.

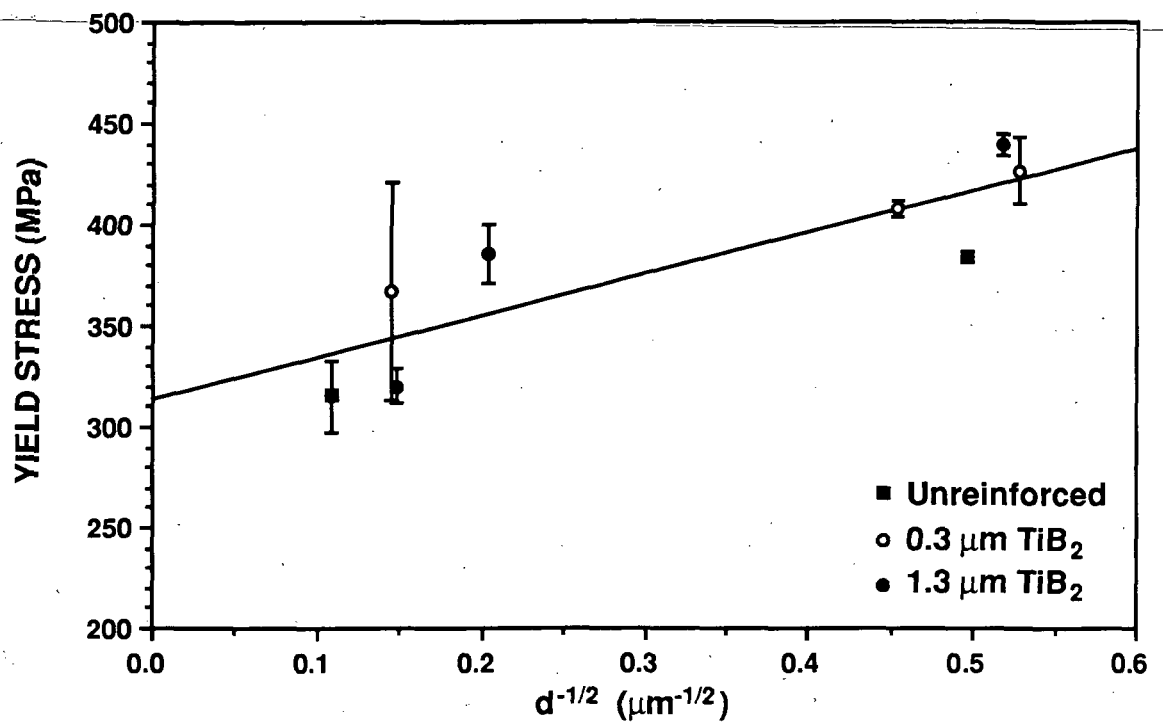
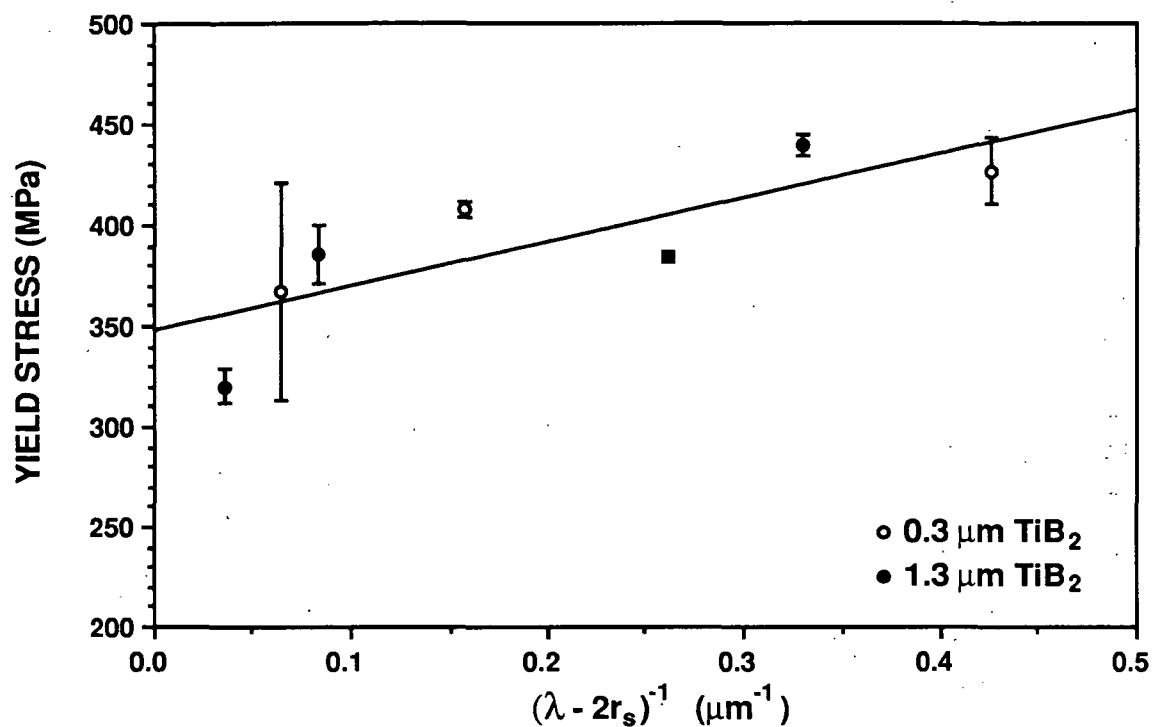
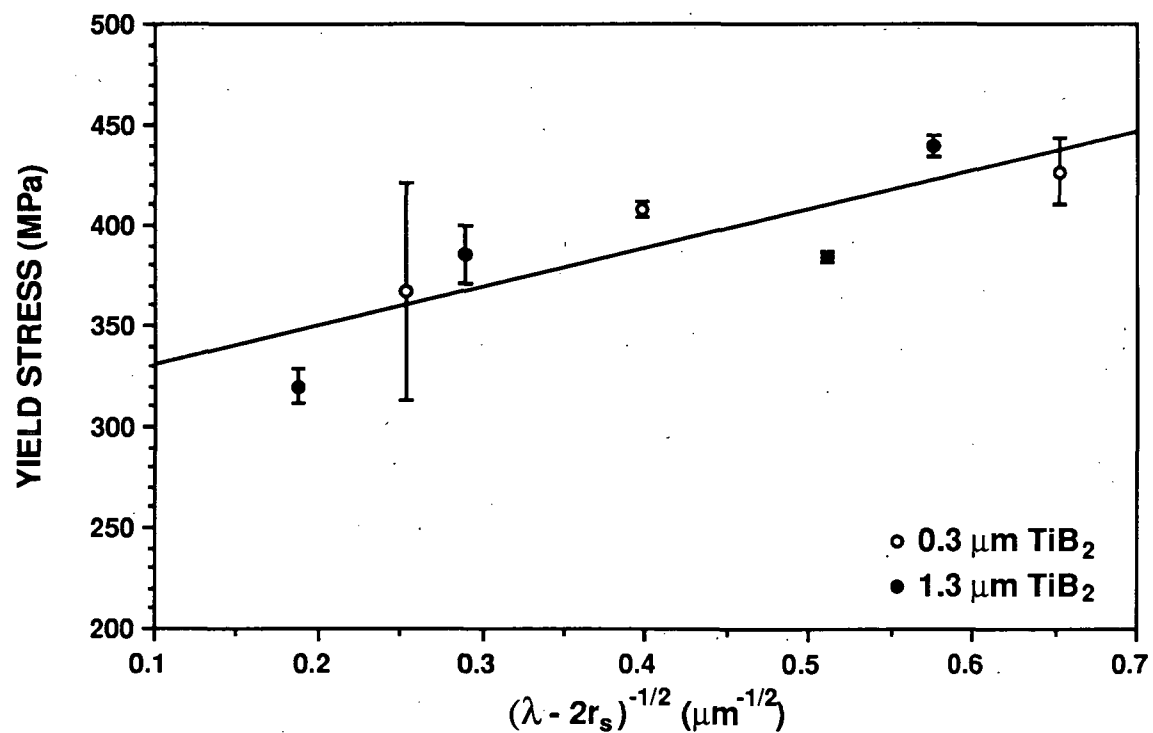


Figure 7.10 Yield stress versus the inverse square-root of grain size for Al-4%Cu-1.5%Mg alloys in artificially aged (T6) condition.

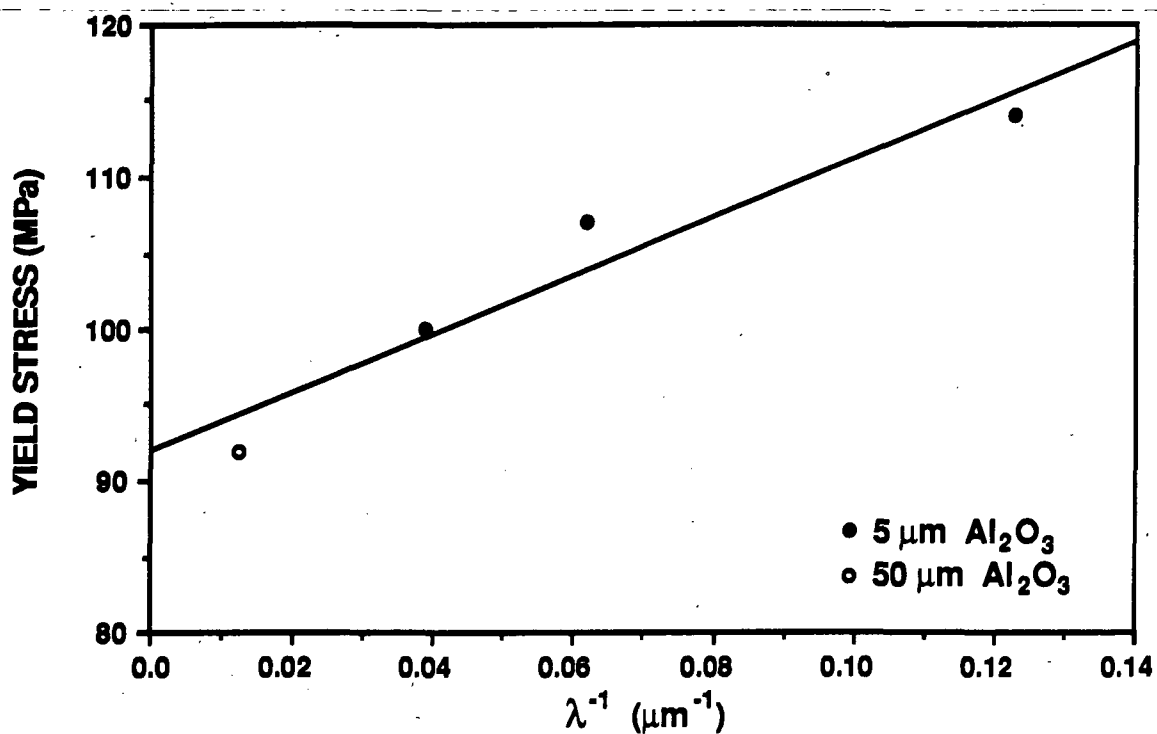


(a) Yield stress versus the inverse of interparticle separation

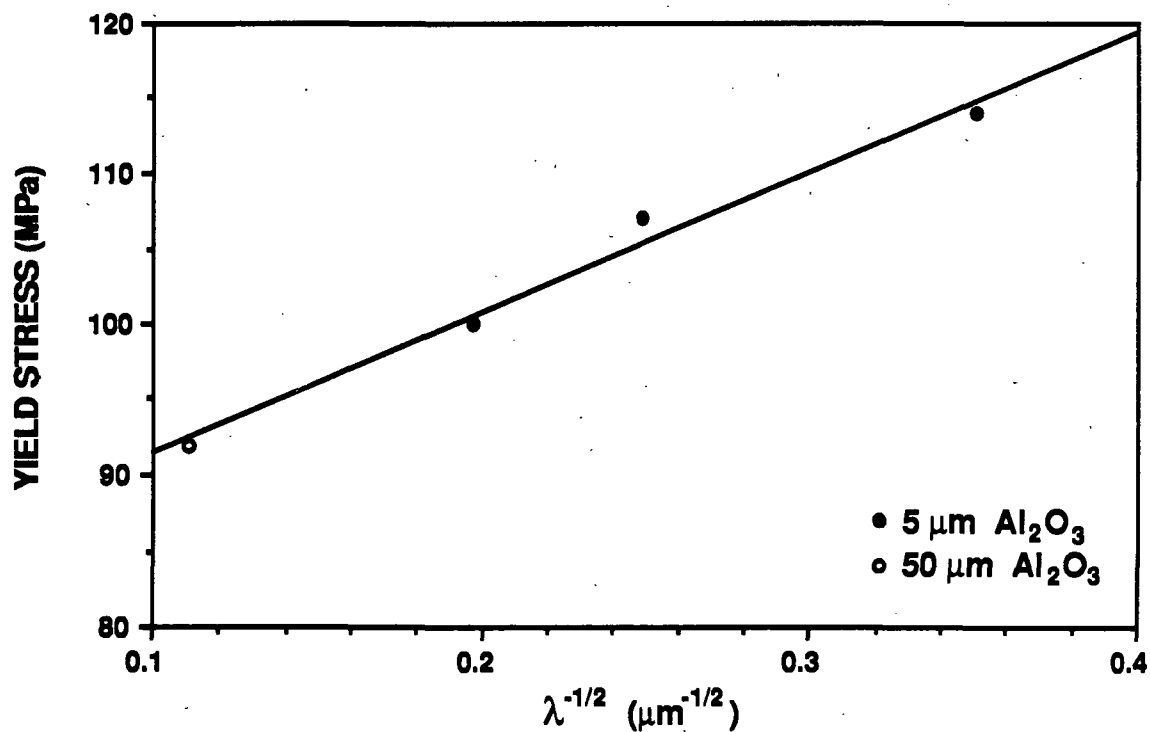


(b) Yield stress versus the square-root of the inverse of interparticle separation

Figure 7.11 Yield stress as a function of the interparticle separation for Al-4%Cu-1.5%Mg alloys in artificially aged (T6) condition.



(a) Yield stress versus the inverse of interparticle separation



(b) Yield stress versus the square-root of the inverse of interparticle separation

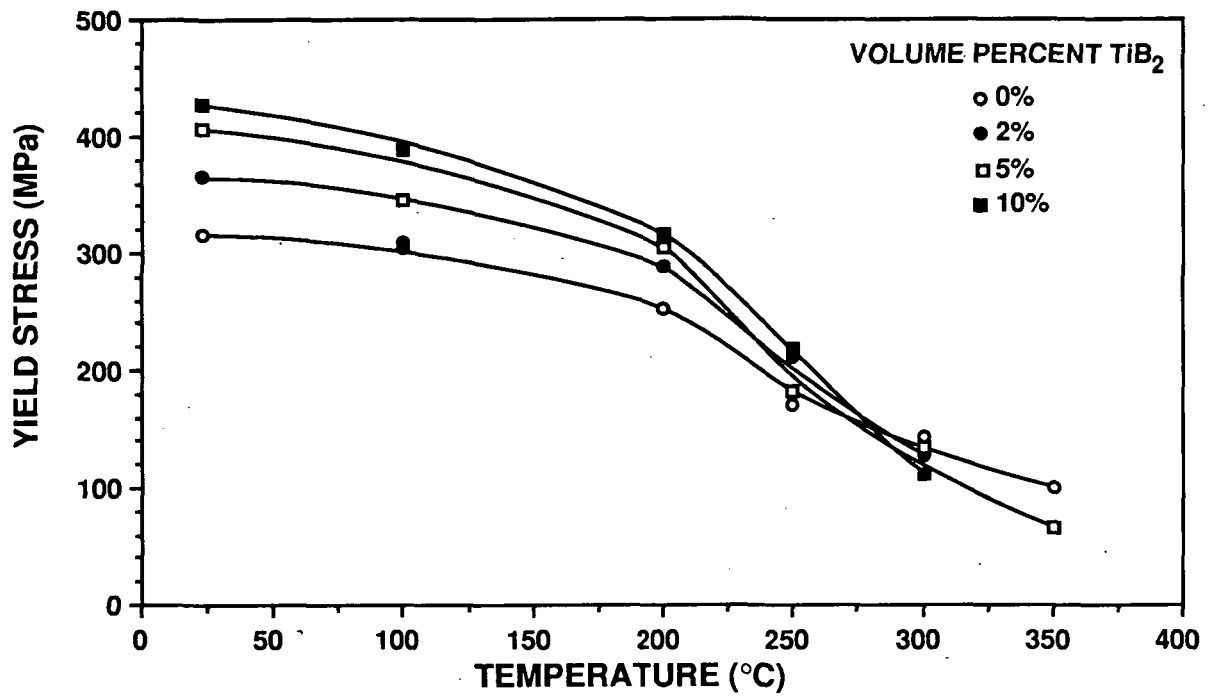
Figure 7.12 Yield stress as a function of the interparticle separation for 2024 in O temper condition. Data of Kamat, Hirth, and Mehrabian [75].

7.3 Elevated Temperature Properties

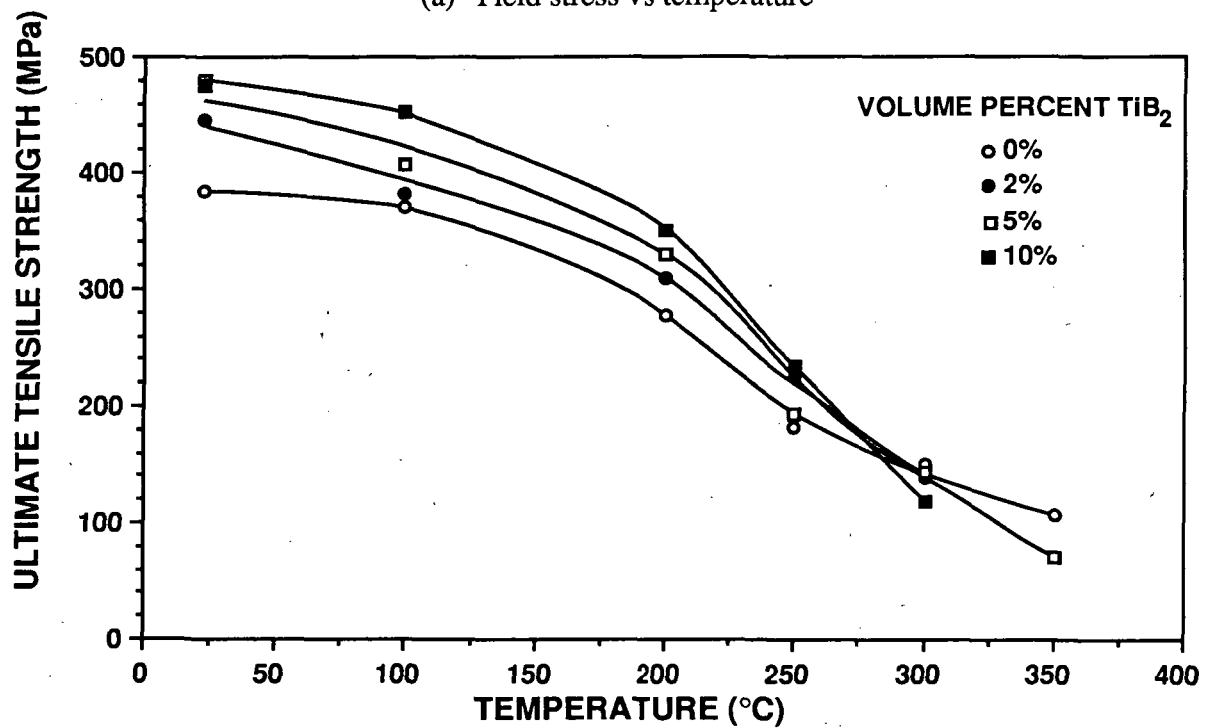
The elevated-temperature tensile properties of the XDTM reinforced Al-4%Cu-1.5%Mg alloys were examined as a function of particle size and loading. Alloys in the peak-aged (T6) condition were exposed to an elevated temperature for 0.5 h and then tested at a strain rate of $1.3 \times 10^{-3} \text{ sec}^{-1}$. For the alloys containing 0.3 μm TiB₂ particles, the 0.2% offset yield stress is shown as a function of temperature and TiB₂ loading in Fig. 7.13(a); the ultimate tensile strength is shown in Fig. 7.13(b), and the elongation to fracture in a 2.5 cm gauge length is shown in Fig. 7.13(c). Figures 7.14 shows the corresponding plots of yield stress, ultimate tensile strength, and elongation to fracture, respectively, as a function of test temperature, for the alloys containing 1.3 μm TiB₂ particles.

The general features of the yield stress vs temperature curves, shown in Figs. 7.13(a) and 7.14(a), are the same regardless of particle size and loading. With increasing temperature, the yield stress falls off gradually at first and then rapidly at temperatures above 200°C. The yield stress curves are displaced to higher stresses with increasing particle loading, although at very high temperatures (300°C) the yield stress of all the materials falls to a similar value. The rapid drop in yield stress regardless of particle loading at about 200°C indicates that the mechanisms of strengthening in the reinforced alloys can be defeated by thermally activated processes. This is consistent with the proposed mechanism of interphase barrier strengthening. At high temperatures, dislocations could cross-slip and the strength increase observed at low temperatures due to dislocation pile up would be defeated. It is also possible that at high temperatures the high grain boundary area and particle interface area act as sinks for dislocations, further reducing the dislocation pile ups. The annihilation of dislocation at grain and interphase boundaries would account for the apparent "cross over" in strength as a function of loading observed at 350°C.

As Figs. 7.13(c) and 7.14(c) show, the elongation to fracture was quite constant with increasing temperature, with a rapid increase in elongation at higher temperatures. The increase in elongation at high temperatures was more pronounced as the volume fraction of TiB₂ increases. Thus, elongation decreased with increasing particle loading at low temperatures, and increased with increasing particle loading at high temperatures.

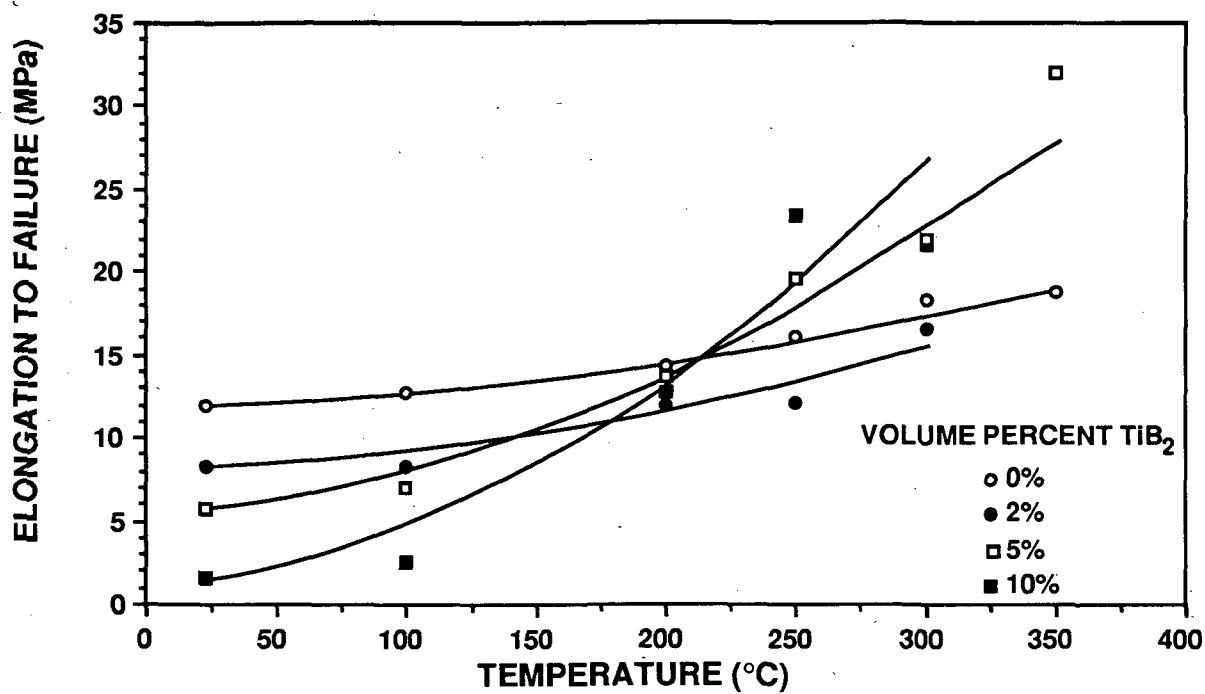


(a) Yield stress vs temperature



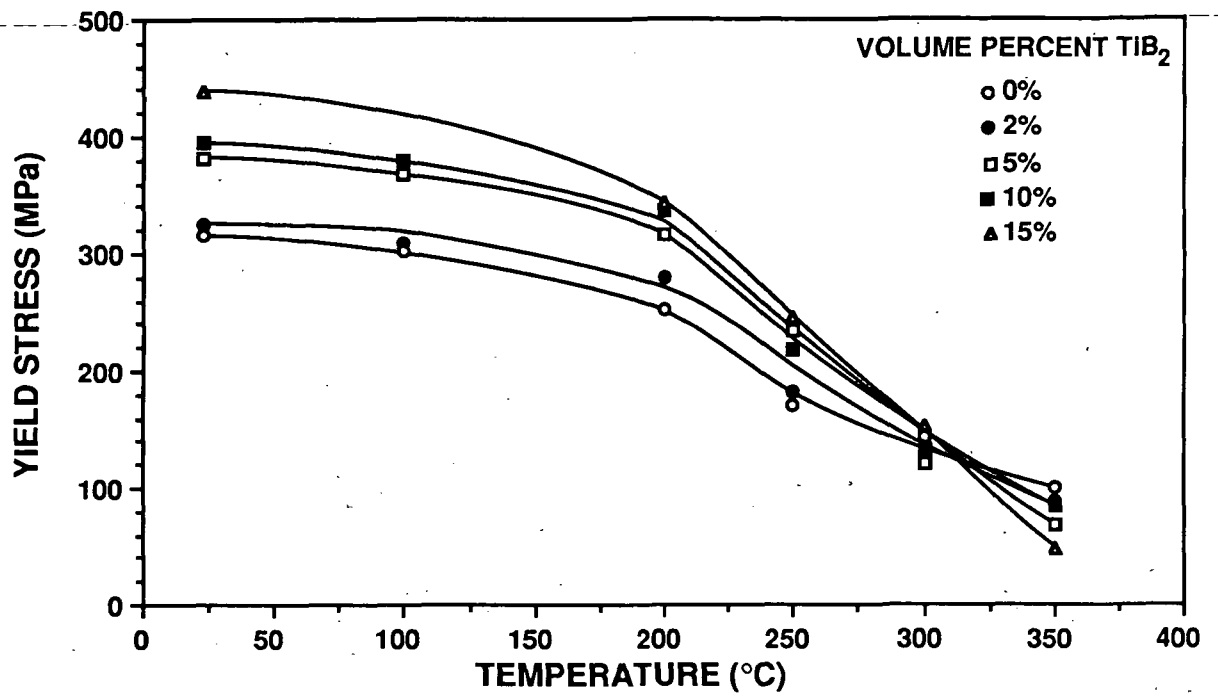
(b) Ultimate tensile strength vs temperature

Figure 7.13 Elevated temperature properties of Al-4%Cu-1.5%Mg with various loadings of $0.3 \mu\text{m}$ TiB_2 tested at a strain rate of $1.3 \times 10^{-3} \text{ s}^{-1}$ after a half-hour exposure at temperature.

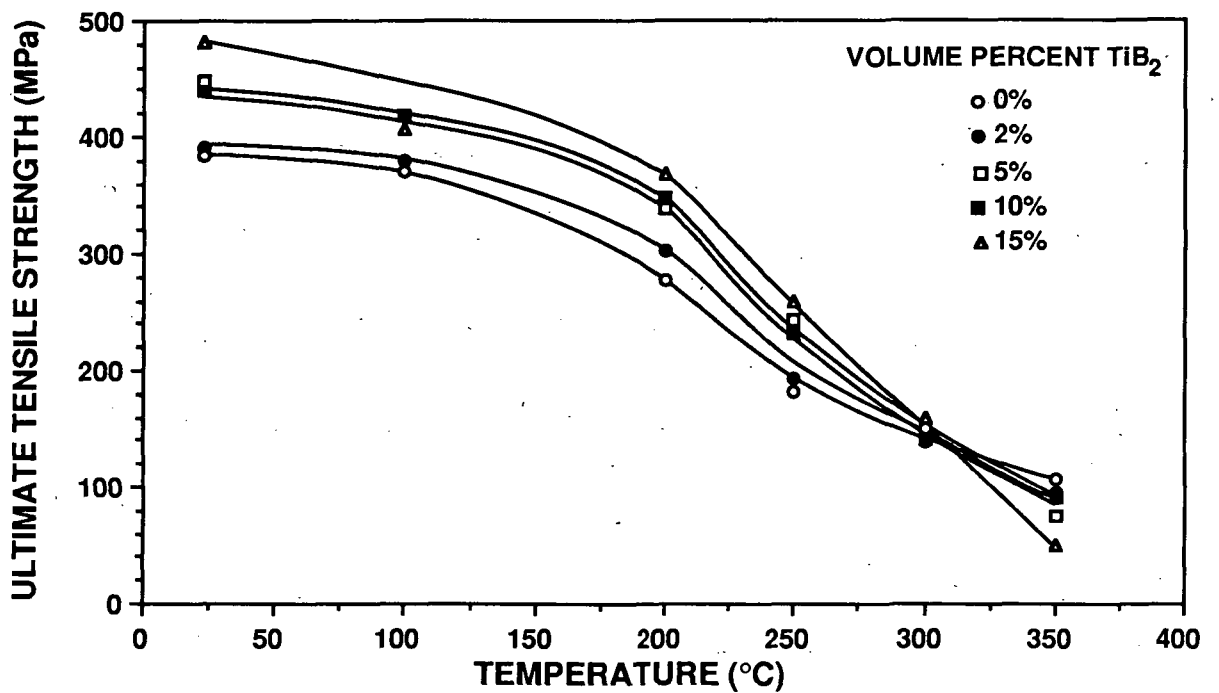


(c) Elongation to fracture vs temperature

Figure 7.13 Elevated temperature properties of Al-4%Cu-1.5%Mg with various loadings of 0.3 μm TiB₂ tested at a strain rate of $1.3 \times 10^{-3} \text{ s}^{-1}$ after a half-hour exposure at temperature.

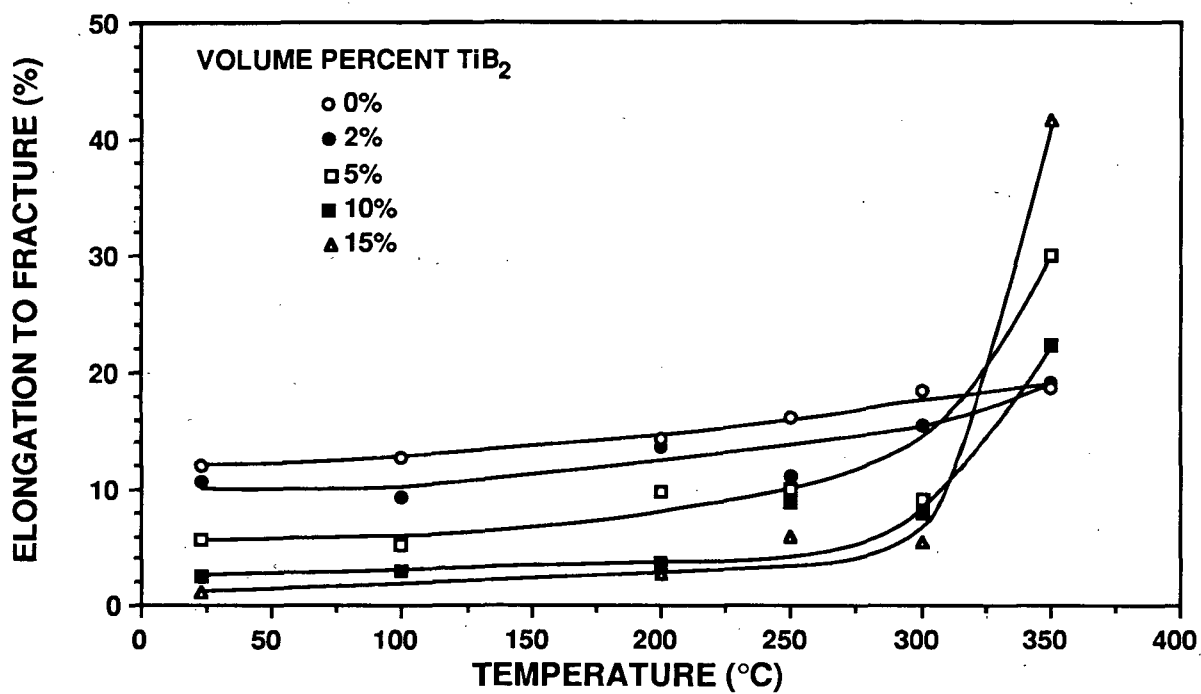


(a) Yield stress vs temperature



(b) Ultimate tensile strength vs temperature

Figure 7.14 Elevated temperature properties of Al-4%Cu-1.5%Mg with various loadings of 0.3 μm TiB₂ tested at a strain rate of $1.3 \times 10^{-3} \text{ s}^{-1}$ after a half-hour exposure at temperature.



(c) Elongation to fracture vs temperature

Figure 7.14 Elevated temperature properties of Al-4%Cu-1.5%Mg with various loadings of 1.3 μm TiB₂ tested at a strain rate of $1.3 \times 10^{-3} \text{ s}^{-1}$ after a half-hour exposure at temperature.

8. FRACTURE TOUGHNESS

The fracture toughness of aluminum alloys discontinuously reinforced with SiC particles has been considered by several authors [74,78-84]. Typical of these results, Flom and Arsenault [84] found that fracture toughness decreased with SiC volume fraction and appeared to be independent of particle size.

Attempts have been made to correlate fracture toughness with particle size, volume fraction, and matrix strength through interparticle spacing [74,84]. This model assumes that particles crack or decohere ahead of the major crack tip and that these cracks occur at small values of local strain. For SiC reinforced composites, where the fracturing of SiC particles is experimentally observed, this appears to be a viable approach.

In this chapter the fracture toughness of the XD™ reinforced Al-4%Cu-1.5%Mg alloys is examined as a function of particle size, loading, and artificial aging of the matrix. As we will see, a major difference between the SiC and TiB₂ reinforced material arises because TiB₂ does not fracture.

8.1 Measurement of Fracture Toughness and K_{IC}

Fracture toughness measurements were made using fatigue precracked compact tension samples according to ASTM standard E-399 [85]. Of the 56 samples tested, none failed during tensile precracking. However, most of the fracture toughness measurements were not valid to the ASTM E-399 standard because the samples were of insufficient thickness. The 1.58 cm (0.625 in.) thick extrusions were not thick enough to achieve plane strain conditions because of the combination of yield strength and toughness exhibited by most of these alloys. Valid plane-strain fracture toughness (K_{IC}) measurements were obtained only for the higher loading materials in the near peak-aged condition. They are listed in Table 8.1 as a function of aging time and TiB₂ loading. The near peak-aged 10 and 15 vol % TiB₂ containing alloys exhibit a K_{IC} of approximately 21 MPa \sqrt{m} (19 ksi \sqrt{in}).

To avoid the size constraints imposed by the plane-strain criteria of E-399, the equivalent energy fracture toughness (K_{ee}) will be used. This method is also a standardized ASTM procedure (ASTM E-992) and has been used successfully on steel samples. As Fig. 8.1 shows, the total energy under the curve to P_{max} was calculated and then a perfectly elastic load-displacement triangle with equal energy was created. The peak of the triangle (P_e in Fig. 8.1) corresponds to the load used to calculate the critical stress intensity. This is a standardized procedure that will work with even the most ductile materials.

Although the values of K_{ee} compare well with the valid K_{IC} measurements generated,

Table 8.1
Plane-strain fracture toughness (K_{IC}) of Al-4%Cu-1.5%Mg alloys
aged at 190°C from the T4 condition.

K_{IC} (MPa \sqrt{m})			
TiB ₂ Loading and Size	Aging Time (h)		
	10	16	30
10% 0.3 μm	21.7	-	24.6
10% 1.3 μm	22.0	-	-
15% 1.3 μm	20.7	19.6	19.1

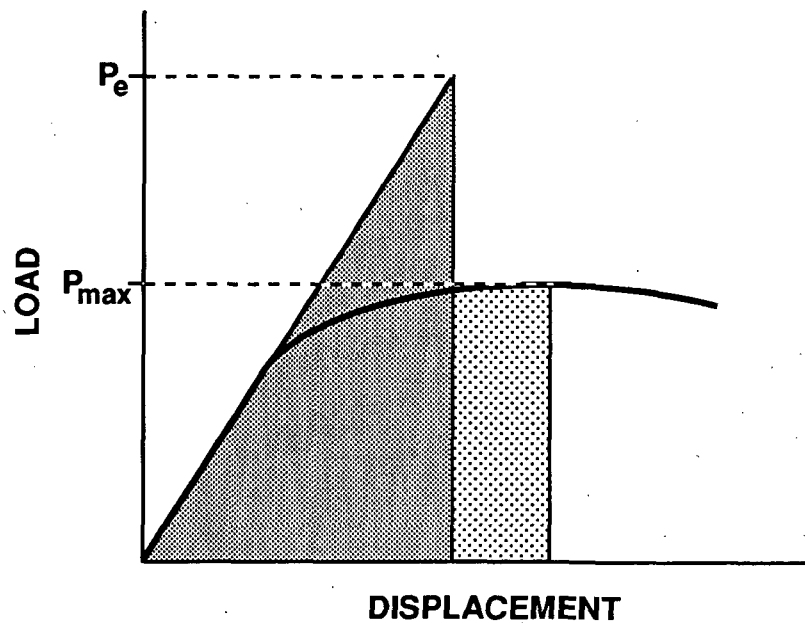


Figure 8.1 Schematic of load-displacement curve and construction of an ideally elastic material with an equivalent energy used to determine P_e .

they do not provide an absolute measure of the plane-strain fracture toughness.

8.2 Isothermal-Aging Response

Figures 8.2 and 8.3 show the equivalent energy fracture toughness as a function of aging time from the T4 condition at 190°C (375°F). The measurements for the alloys containing 0.3 μm diameter TiB_2 particles are shown in Fig. 8.2; and the measurements for the alloys with 1.3 μm TiB_2 particles are shown in Fig. 8.3. The fracture toughness decreased with aging, reaching a minimum slightly before the peak in strength. With overaging, fracture toughness increased slightly. This behavior is similar to conventional 2000-series alloys.

8.3 Effect of Loading and Particle Size

The K_{Ic} values for the T4 and T6 aged materials are plotted as a function of loading in Fig. 8.4. Although there is some noise, these data show that the fracture toughness initially drops off with the addition of TiB_2 volume fractions up to about 5%, and then remains nearly constant up to 15%. Thus, beyond the initial penalty, increased particle loadings did not severely affect fracture toughness. It also appears that the fracture toughness was insensitive to particle size in the range tested.

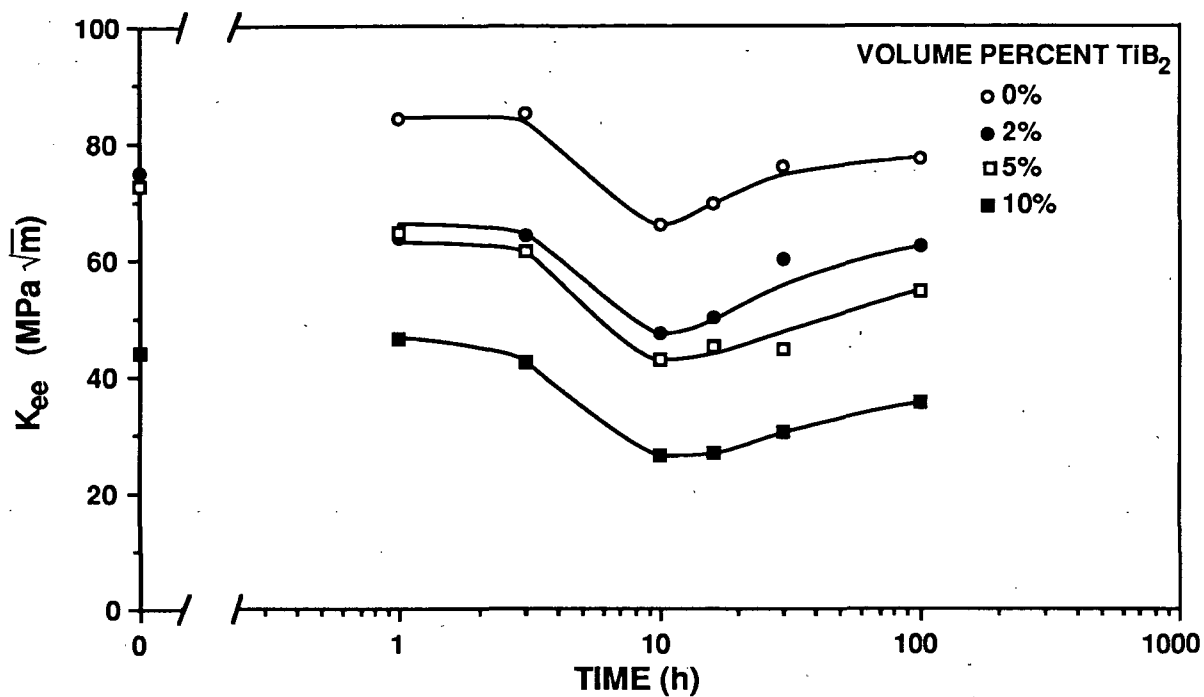


Figure 8.2 Equivalent energy fracture toughness vs aging time at 190°C for the Al-4%Cu-1.5%Mg alloys containing 0.3 μm TiB₂ particles.

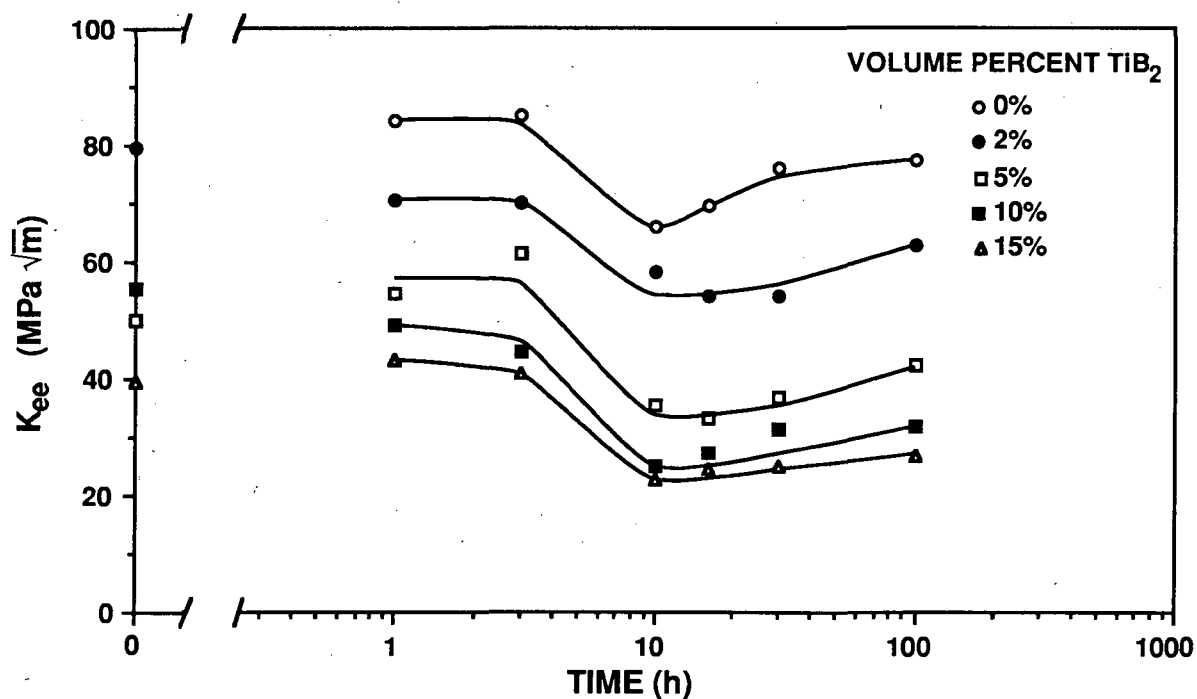
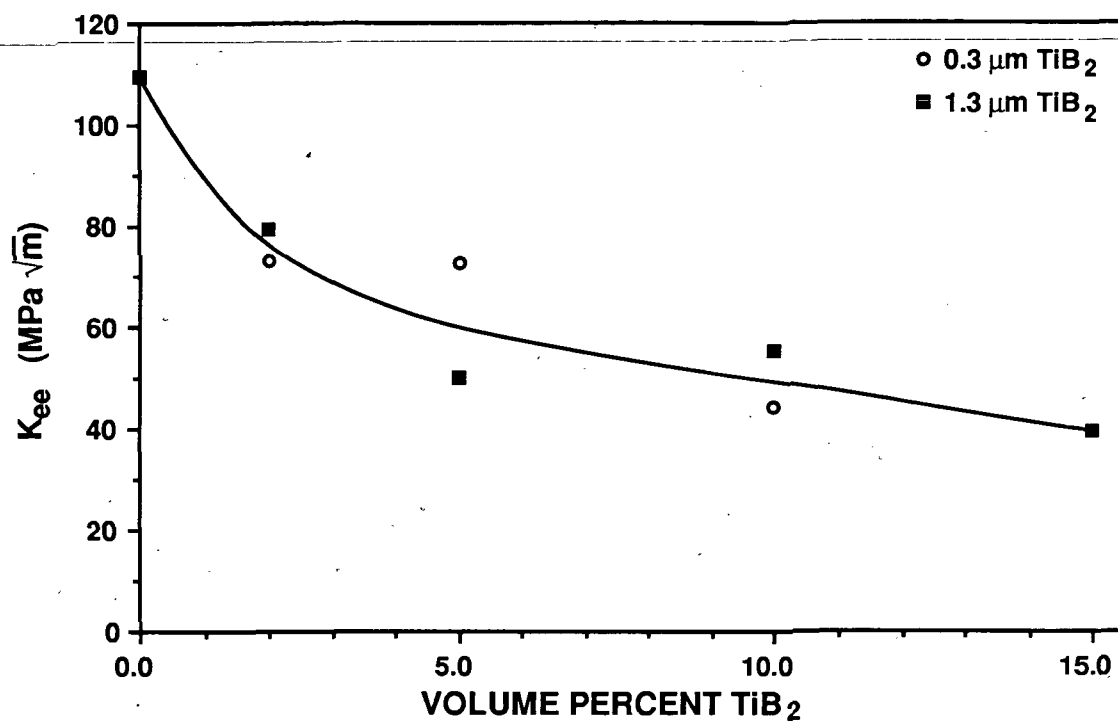
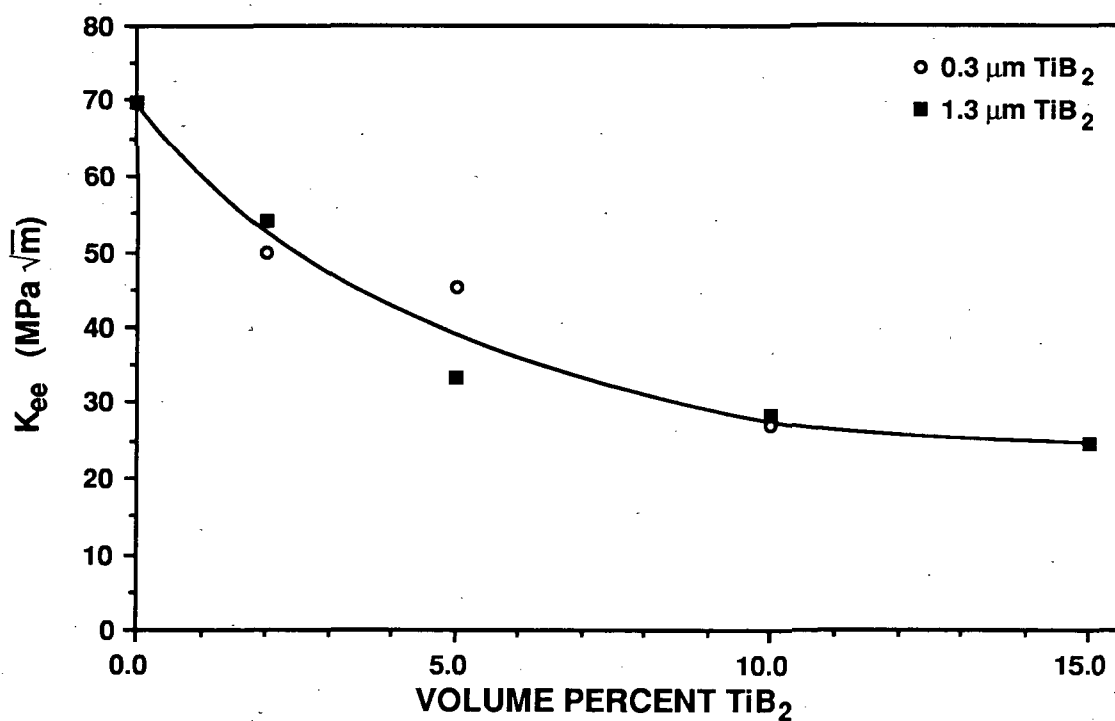


Figure 8.3 Equivalent energy fracture toughness vs aging time at 190°C for the Al-4%Cu-1.5%Mg alloys containing 1.3 μm TiB₂ particles.



(a) Naturally aged (T4) condition



(b) Peak-aged (T6) condition

Figure 8.4 Equivalent energy fracture toughness vs TiB_2 particle loading for the Al-4%Cu-1.5%Mg materials.

9. FATIGUE

Fatigue crack growth in SiC reinforced aluminum alloys has been examined by several investigators [80,81,86-90] whose studies show that the fracture of SiC particles either at or ahead of the crack tip is an important factor influencing the behavior of these alloys. At low stress intensity ranges (ΔK), Shang, Yu, and Ritchie [87] found that for an Al-Zn-Mg-Cu alloy with fine SiC, the fracture of SiC near the crack tip resulted in low levels of crack closure and rapid crack growth rates. For coarse SiC particles, fracture of SiC near the crack tip resulted in a rougher fracture surface, which promoted crack closure from asperity wedging, and improved crack growth resistance relative to the unreinforced alloy. At high ΔK , those near K_{IC} , crack growth rates are accelerated in the reinforced alloy due to the lower fracture toughness of the composite.

In this work the fatigue crack growth rate of Al-4%Cu-1.5%Mg alloys with various loadings and sizes of TiB_2 was examined per ASTM E647 [85] in the peak-aged (T6) condition. Compact tension specimens were machined from sections of the the extruded alloys. The crack plane orientation was L-T and the samples had a width of 5.1 cm (2.0 in.) and a nominal thickness of 0.64 cm (0.25 in.). The testing was done on a servo-hydraulic test machine in load control using a Haver sine waveform at a frequency of 10 Hertz and an R-ratio of 0.1 ($R=K_{min}/K_{max}$). The testing was done in "laboratory air" at 24°C and approximately 50% relative humidity. The specimens were precracked to an initial crack length over sample width of approximately 0.38. A standard K-increasing fatigue crack growth test was then conducted by keeping the load at a constant amplitude. Load, cycles, and crack mouth opening measurements were taken at intervals to determine the stress intensity and monitor the crack growth. From these, plots of crack length (a) versus number of cycles (n) and crack growth rate (da/dn) versus stress intensity range (ΔK) were produced.

In Fig. 9.1 the crack growth rate of the Al-4%Cu-1.5%Mg alloys reinforced with 0.3 μm TiB_2 is shown as a function of TiB_2 loading and ΔK ; the alloys are in the T6 temper and $R=0.1$. With increasing TiB_2 loading, the rate of crack extension for a given ΔK is greater. In Fig. 9.2, the analogous plot for the Al-4%Cu-1.5%Mg alloys reinforced with 1.3 μm TiB_2 is shown as a function of TiB_2 loading and ΔK . Examination of the fatigue fracture surface reveals a dimpled surface that contains TiB_2 particles in approximately 50% of the dimples. Observation of individual TiB_2 particles and matching fracture surfaces reveals no fractured particles.

To better view these data the curves are replotted in Fig. 9.3-9.5 as a function of TiB_2 size. Here the TiB_2 loading has been kept constant and the unreinforced alloy is included as a

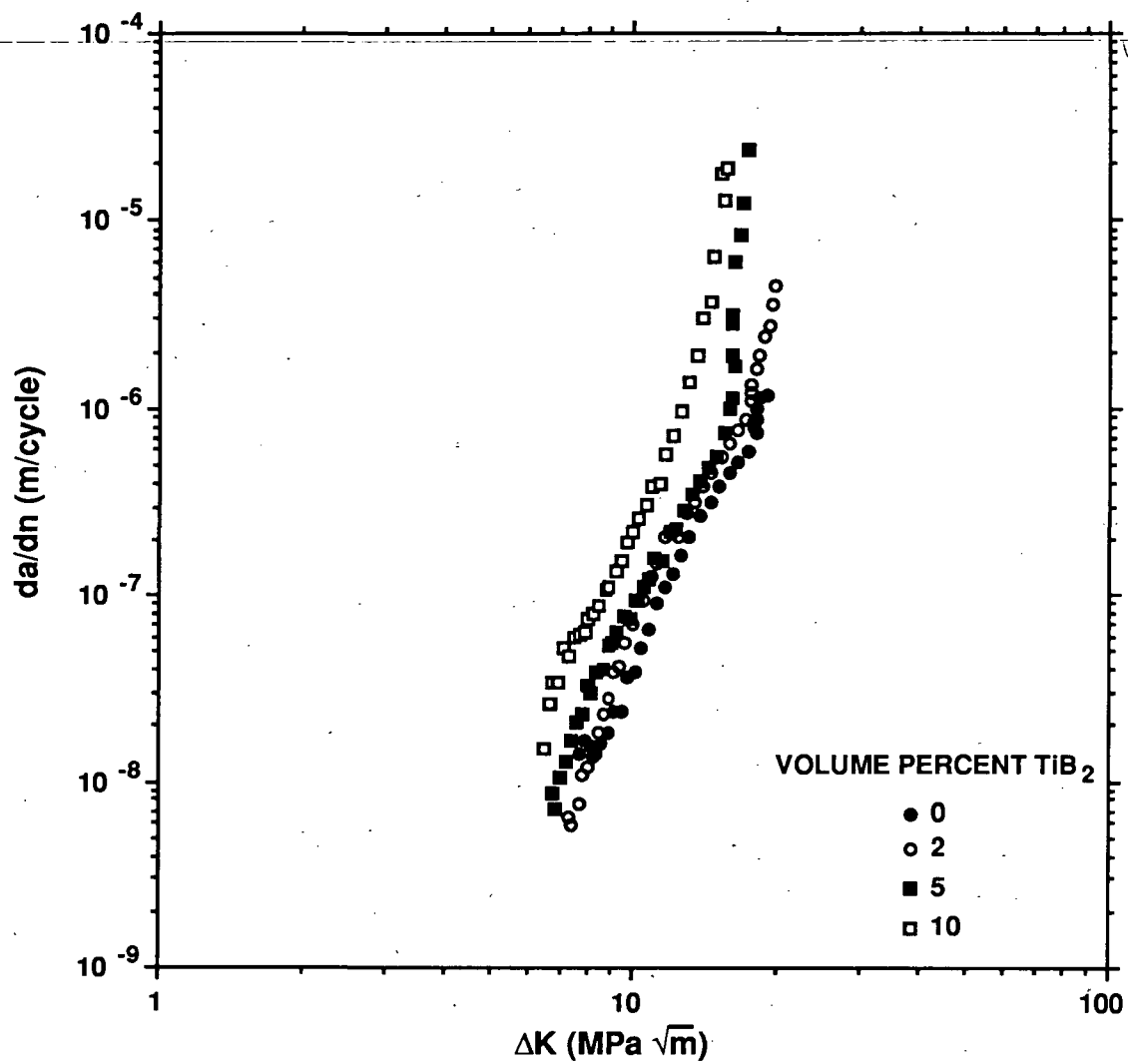


Figure 9.1 Fatigue crack growth rate of Al-4%Cu-1.5%Mg with 0.3 μm TiB₂.

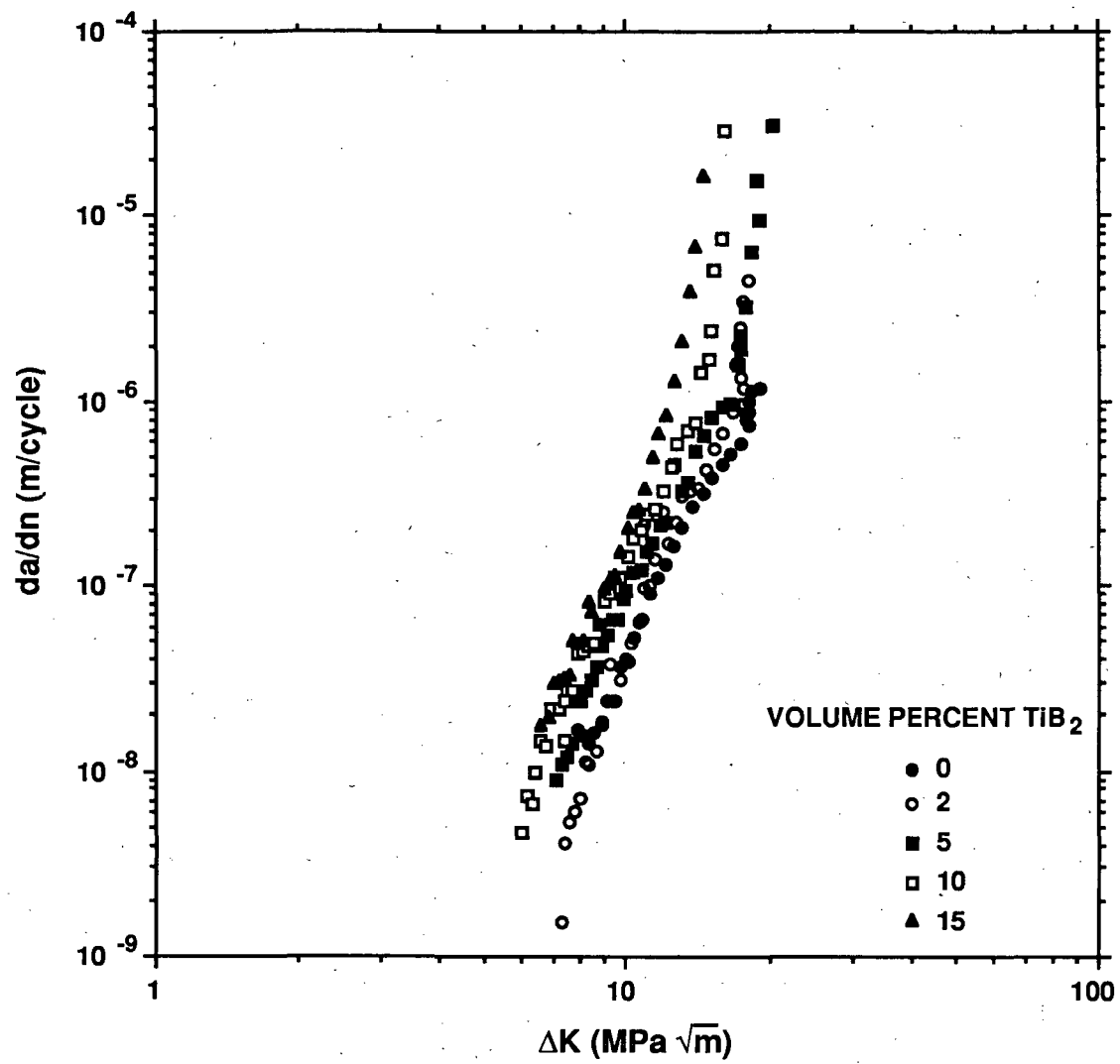


Figure 9.2 Fatigue crack growth rate of Al-4%Cu-1.5%Mg with 1.3 μm TiB_2 .

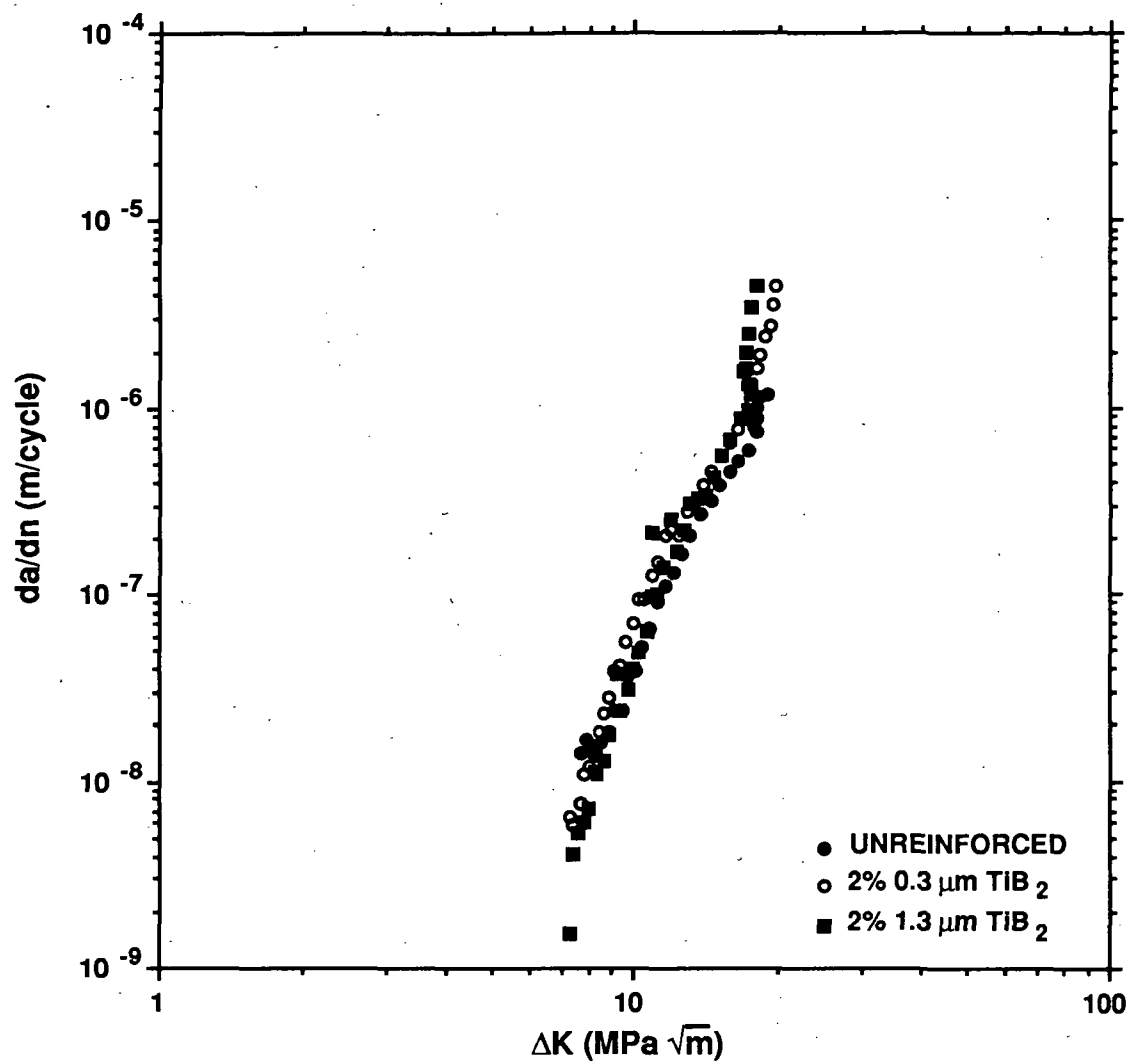


Figure 9.3 Fatigue crack growth rate of Al-4%Cu-1.5%Mg with 2 vol% TiB_2 .

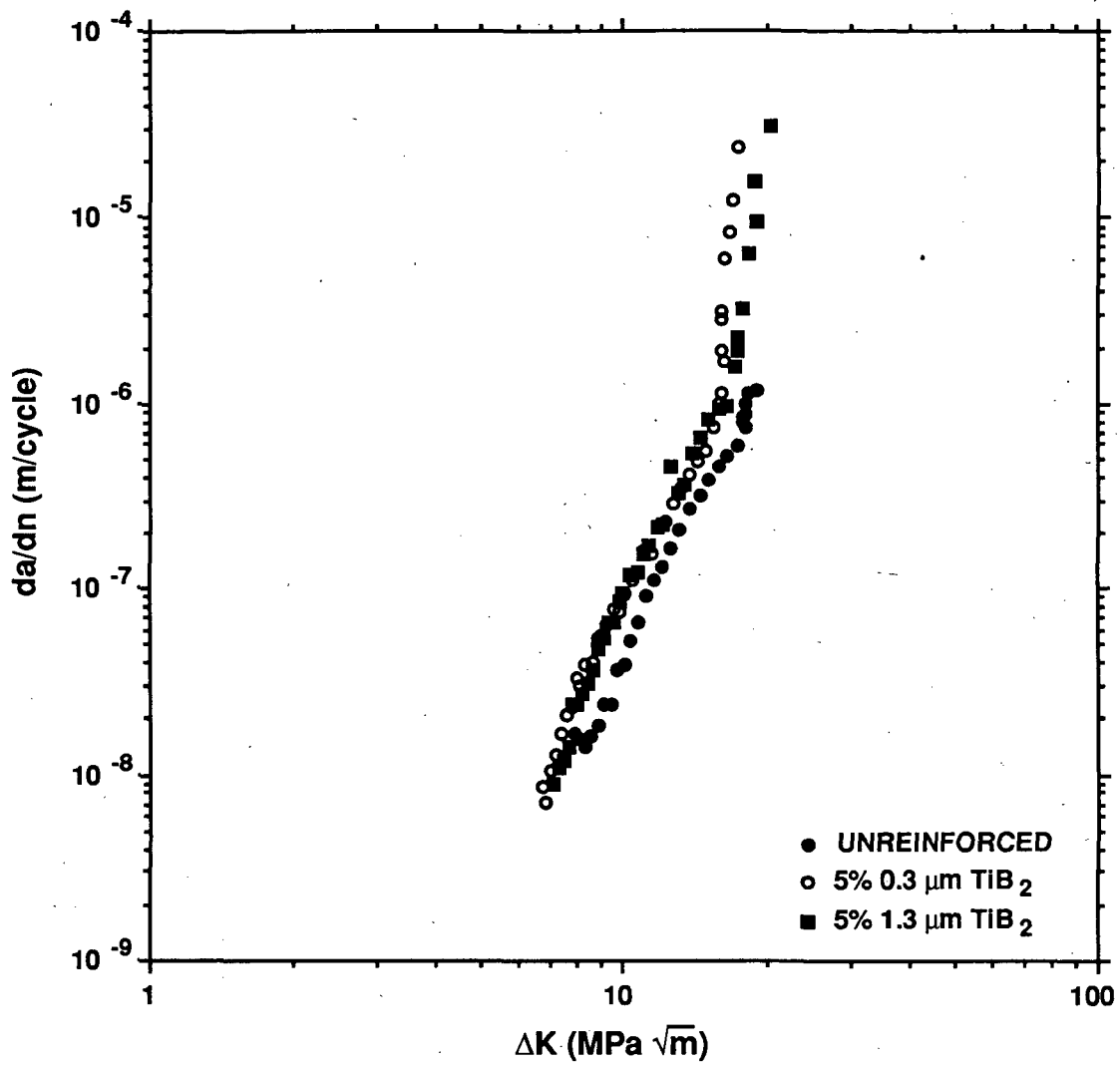


Figure 9.4 Fatigue crack growth rate of Al-4%Cu-1.5%Mg with 5 vol% TiB_2 .

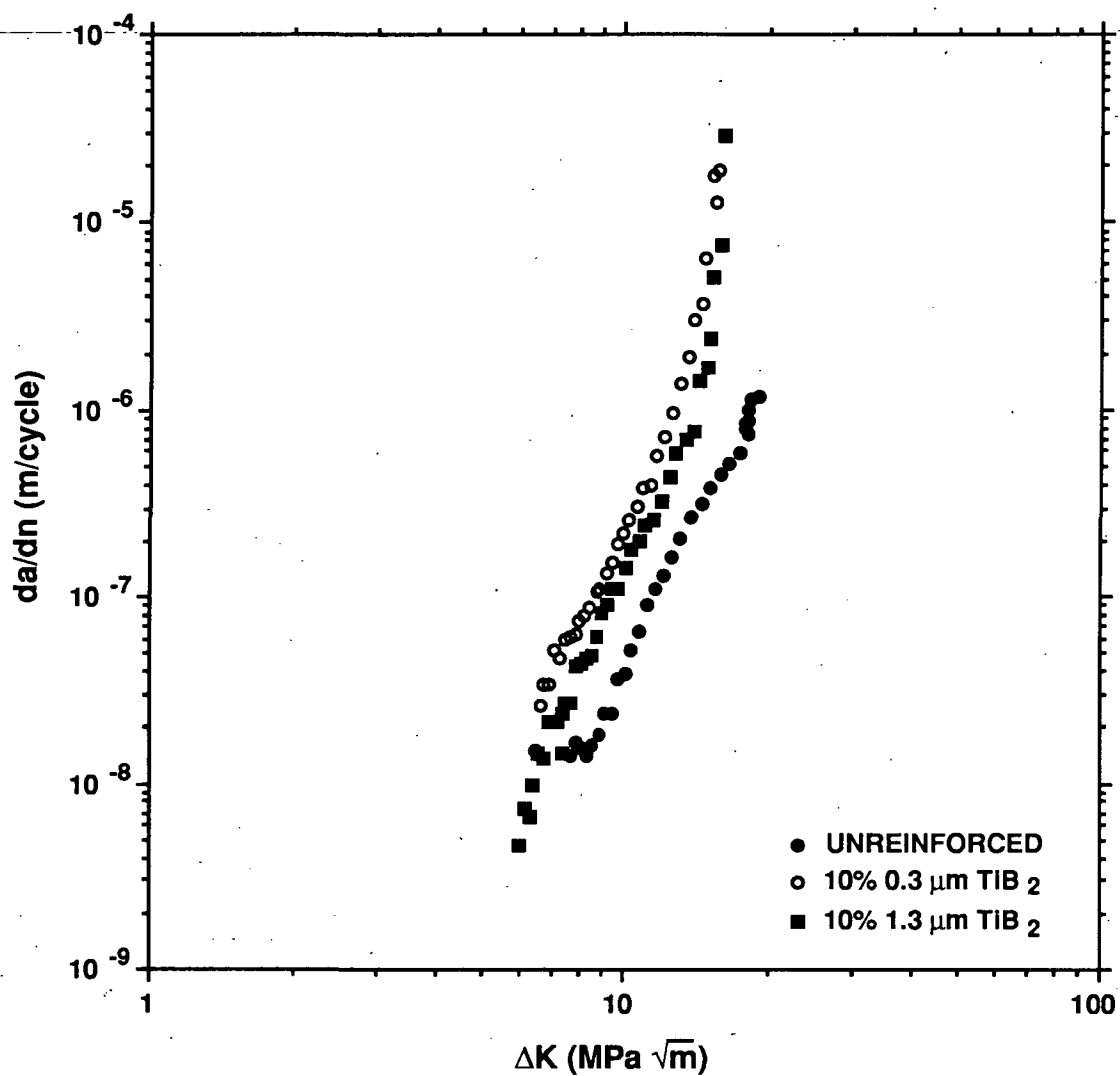


Figure 9.5 Fatigue crack growth rate of Al-4%Cu-1.5%Mg with 10 vol% TiB_2 .

reference line. For the same TiB₂ loading smaller particles result in a higher fatigue crack growth rate.

Each of the da/dn versus ΔK curves exhibits a linear stage II region. A least-squares fit of the data in this region to the Paris relationship

$$\frac{da}{dn} = C \Delta K^m \quad (9.1)$$

yields the coefficients presented in Table 9.1. There are no clear trends in either C or m with particle size or loading. Numerous authors have reported the empirical correlation

$$\ln(C) = a - b m \quad (9.2)$$

between C and m; this has been recently reviewed by Cotie and Garrett [91]. For aluminum and aluminum+SiC MMCs, Davidson [90] reports the correlation

$$\ln(C) = -16.1 - 2.2 m \quad (9.3)$$

for R=0.1. A least-squares fit of the data in Table 9.1 (shown in Fig. 9.6) yields the relation

$$\ln(C) = -15.9 - 2.3 m, \quad (9.4)$$

which agrees quite well with Davidson's observations.

In order to gain some insight into what effect particle fracture has on fatigue crack growth rate the present work is compared to 2124 reinforced with SiC whiskers. In Fig. 9.7 the data of Logsdon and Liaw [80] for a Al-4%Cu-2%Cu+20vol%SiC alloy in the T6 condition are plotted along with the Al-4%Cu-1.5%Cu alloy reinforced with 15 vol% of 1.3 μm TiB₂. Although Logsdon and Liaw do not report the SiC particle size for this alloy, Christman and Suresh [30] report a whisker size of 0.5 μm by 4 μm (after-extrusion) for a similar composite. The fatigue crack growth rate of the SiC reinforced alloy is significantly greater than the TiB₂ reinforced alloy. Although the particle size, morphology, and loading are different for the two composites, much of the difference is likely to stem from the brittle fracture of the reinforcing phase in the SiC MMC.

Table 9.1
Coefficients of least-squares fit to stage II data.

Loading (vol%)	Mean Size (μm)	Paris Coefficients	
		C (m/cycle)	m
Unreinforced		7.3×10^{-14}	5.8
2	0.3	4.8×10^{-15}	7.2
5	0.3	2.3×10^{-12}	4.6
10	0.3	3.8×10^{-13}	5.8
2	1.3	1.2×10^{-15}	7.6
5	1.3	5.2×10^{-13}	5.2
10	1.3	5.1×10^{-13}	5.4
15	1.3	2.2×10^{-15}	7.9

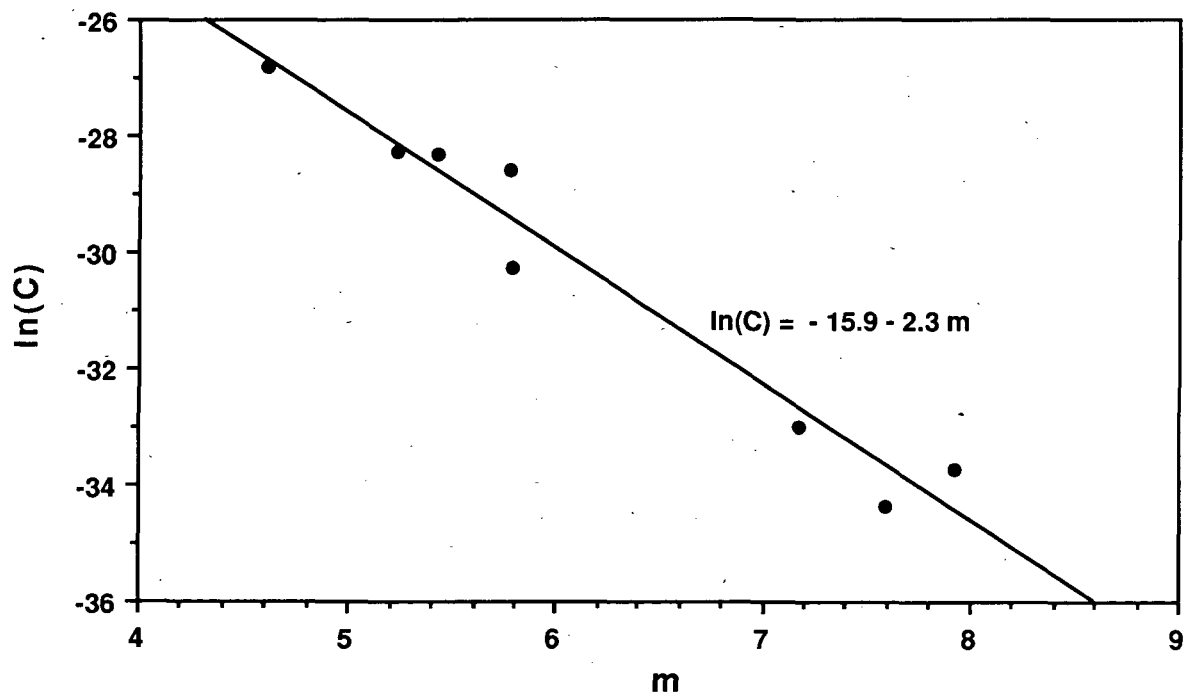


Figure 9.6 Plot of m versus $\ln(C)$ for stage II region of crack growth rate of Al-4%Cu-1.5%Mg with and without TiB_2 .

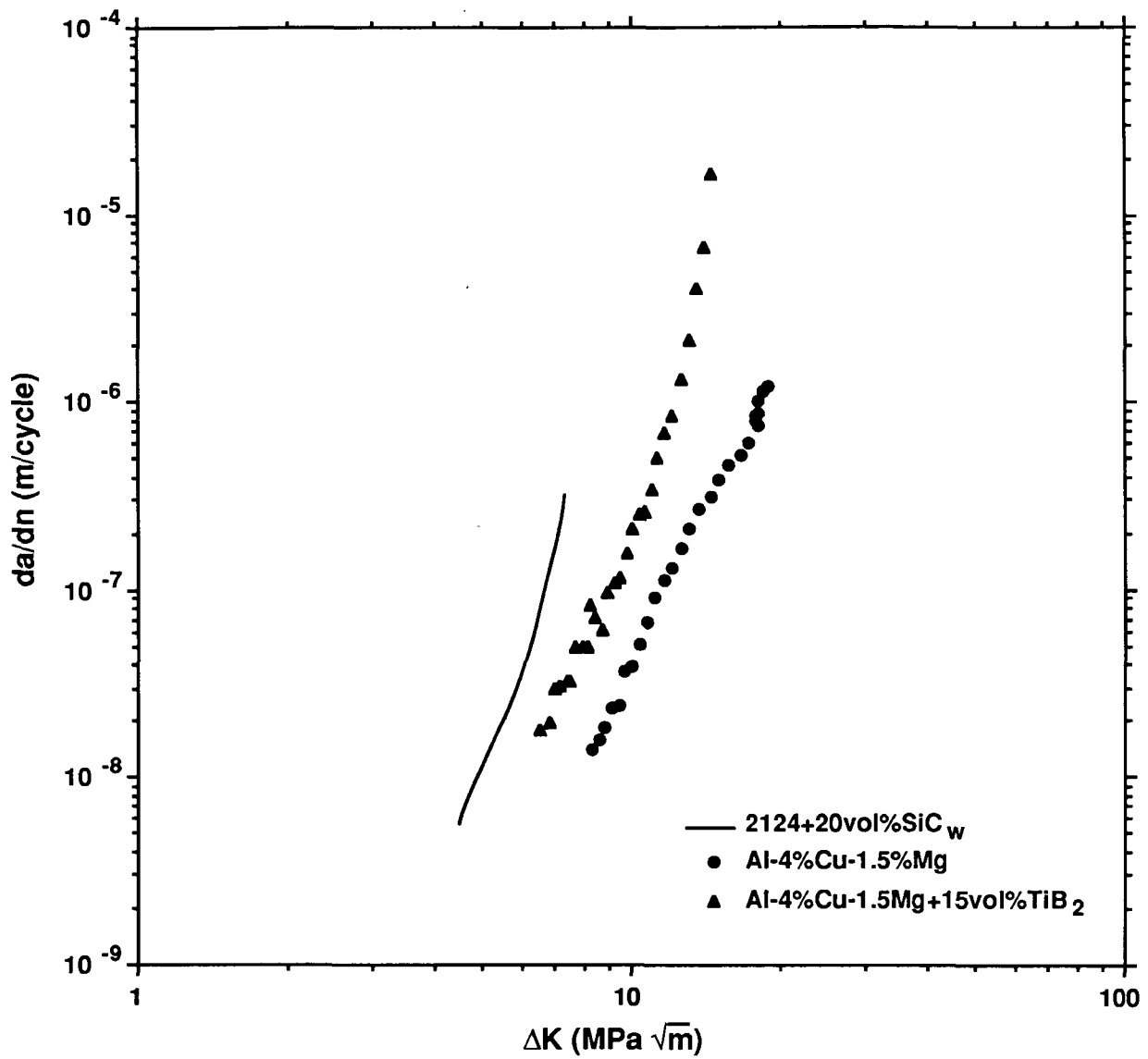


Figure 9.7 Fatigue crack growth rate of 2124+20vol%SiC whiskers compared to Al-4%Cu-1.5%Mg+15vol% TiB₂ and unreinforced alloy. All alloys in T6 condition with R=0.1. 2124+SiC data from Logsdon and Liaw [80].

10. SUMMARY

The influence of reinforcement size, volume fraction, and matrix deformation behavior on the strength, fracture toughness, fatigue crack growth rate, and high-temperature strength of a precipitation strengthened aluminum metal matrix composite (MMC) was examined.

Pure aluminum reinforced with 0.5 to 15 vol% TiB₂ particles that are 0.3 μm in diameter were produced by the XD™ process. The alloys were cast, hot forged in 3 orthogonal directions, and annealed at 500°C. The TiB₂ particle distribution is uniform indicating that the particles were not pushed by the solidification front during casting. The grain size of the annealed alloys was strongly influenced by the amount of TiB₂ in the alloy. For instance the grain size drops from 435 μm for the 0.5% alloy to 7 μm for the 10% alloy. The grain size dependence on TiB₂ is most likely due to two contributions: refinement of the initial cast structure and pinning of grain boundaries during the high temperature anneal.

The tensile properties of these pure aluminum composites was also strongly affected by the amount of TiB₂ present. Higher particle loadings significantly increased the yield stress; from 18 MPa for the 0.5% alloy to 102 MPa for the 15% alloy. The elongation to failure dropped with increasing particle loading, from 45% for the 0.5 vol% alloy to 12% for the 15 vol% alloy, although the fracture mode remained ductile rupture.

The proportional limit increased only slightly with increasing TiB₂ content while the initial strain hardening rate was much higher for the higher loading alloys. This result, combined with a linear dependence of the yield stress on the inverse of the interparticle spacing, suggests that for these alloys, which deform by diffuse dislocation slip, the formation of dislocation cells and forest hardening is responsible for the observed increase in yield stress. Although Hall-Petch strengthening cannot be ruled out, it does not explain the observed strain hardening or proportional limit behavior.

Al-4%Cu-1.5%Mg reinforced with 0 to 15 vol% TiB₂ particles either 0.3 μm or 1.3 μm in diameter were also produced by the XD™ process. The alloys were cast, extruded, and then heat treated. Significant particle pushing occurred during solidification of the Al-4%Cu-1.5%Mg alloy with 0.3 μm TiB₂; this resulted in a poor TiB₂ distribution. Particle pushing was not observed in the alloy with 1.3 μm TiB₂ and the particle distribution is very uniform. The pushing of 0.3 μm diameter TiB₂ by this Al-Cu-Mg alloy and not in pure aluminum is due to the lack of a mushy zone in the pure metal.

The Young's modulus increased with increases in TiB₂ loading. The dependence of the modulus on volume fraction and the elastic constants of the particle and matrix are predicted by the lower bound of the Hashin-Shtrikman model.

Dislocation punching due to CTE mismatch of TiB_2 and the aluminum matrix for alloys quenched from the solutionizing temperature was investigated. The size of the particle was the critical factor in determining whether or not dislocations were punched out upon quenching. The critical particle diameter appears to be approximately $0.6\text{ }\mu\text{m}$ for aluminum plus TiB_2 quenched from 500°C ; for particles below this diameter, dislocation punching was not observed whereas it was for particles with larger diameter. This critical particle diameter is consistent with the predictions of the Ashby-Johnson model for dislocation punching due to a transformation strain.

The isothermal-aging response of the precipitation strengthened Al-4%Cu-1.5%Mg alloys was not accelerated by the presence of TiB_2 . Although some dislocation punching was observed in alloys with large TiB_2 , the overall dislocation density in these alloys was similar to the dislocation density in unreinforced alloys. It is believed that the dislocations punched due to CTE mismatch act as vacancy sinks. With fewer vacancies, fewer dislocation loops are formed by vacancy condensation, and the overall dislocation density remains the same although the morphology of the dislocations are different.

Stretching the alloys between solutionizing and artificial aging produced a significant acceleration of the aging response of the TiB_2 reinforced alloys. The cold work created additional geometrically necessary dislocations which served as heterogeneous nucleation sites for the precipitation of S' . This led to accelerated aging, a finer precipitate size, and an increase in the strength of the alloy. The degree of acceleration was a function of the particle size and loading; small particles and high loading produced the greatest acceleration in the aging kinetics.

The tensile properties were also examined as a function of particle size and loading. Strength increased with TiB_2 loading, and at equivalent loadings, the alloy with the smaller TiB_2 particles showed greater strength. The elongation to fracture decreased with increased TiB_2 loading and appeared to be independent of particle size.

For the Al-4%Cu-1.5%Mg alloys in the T4 temper, the yield stress and the proportional limit increased at a similar rate with increasing volume fraction of TiB_2 . The observed increase in strength is therefore due to an increase in the initial resistance to the movement of dislocations and not a difference in the initial strain hardening rate. The continuum models such as shear-lag theory significantly underestimate the strength increase observed with increasing loading and do not account for the observed particle size effect. Because the Al-4%Cu-1.5%Mg matrix deforms by planar dislocation slip in the T4 temper, the applicability of the various characteristic slip-length (dislocation pile-up) models was examined. The fit between yield stress and the square-root of the inverse grain size is poor; thus Hall-Petch strengthening is improbable. Although a trend is observed between the yield stress and the

inverse of the interparticle spacing, the slope obtained by this fit differs from that predicted by the Orowan relationship by several orders of magnitude. Thus, the observed dependence on particle spacing is not due to Orowan strengthening. A linear relationship between the yield stress and the square root of the interparticle spacing was observed with the data of different particle sizes and loadings falling on the same line. Therefore, the data suggest that the strength increase in these alloys, in this temper, is due to dislocation pile-ups through an interphase barrier-strengthening mechanism.

For the Al-Cu-Mg alloys in the T6 temper the matrix deforms by wavy slip. In these alloys the linear relationship between the yield stress and the square root of the interparticle spacing was not observed. This suggests that in this temper a the slip distance defined by a combination of particle spacing, grain size, precipitate spacing, and precipitate resistance to shearing is controlling the strength of the alloy.

The tensile properties of Al-4%Cu-1.5%Mg+TiB₂ alloys were examined as a function of temperature. With increasing temperature the yield stress fell off gradually at first, and then dropped rapidly at temperatures above 200°C (400°F). Increased TiB₂ loadings displaced the yield stress curves to higher stresses; although at very high temperatures, 350°C (650°F), the yield stresses of all the materials fell to a similar value. The rapid drop in yield stress regardless of particle loading at about 200°C indicates that the mechanisms of strengthening in the reinforced alloys can be defeated by thermally activated processes. This is consistent with the proposed mechanism of interphase barrier strengthening. At high temperatures, dislocations could cross-slip and the strength increase observed at low temperatures due to dislocation pile-up would be defeated. It is also possible that at high temperatures the high grain boundary and particle interface area act as sinks for dislocations, further reducing dislocation pile-ups.

Fracture toughness of the Al-4%Cu-1.5%Mg+TiB₂ alloys was also examined as a function of particle size, loading, and matrix temper. Fracture toughness decreased with TiB₂ additions up to 5% and then leveled off from 5% to 15%; it also decreased with artificial aging. There was no apparent dependence of the fracture toughness on particle size, but this may be an artifact due to the nonuniform particle distribution of the alloys reinforced with 0.3 μm TiB₂.

Fatigue crack growth rate of the Al-4%Cu-1.5%Mg+TiB₂ alloys in the T6 condition was also examined as a function of the particle size and loading. Fatigue crack growth rate increased with increasing particle loading and smaller particle size.

11. REFERENCES

- [1] J.M. Brupbacher, L. Christodoulou, and D.C. Nagle, "Process for Forming Metal-Ceramic Composites," U.S. Patent No. 4,710,348 (1987).
- [2] L. Christodoulou, D.C. Nagle, and J.M. Brupbacher, "Metal-Second Phase Composites," U.S. Patent No. 4,716,030 (1990).
- [3] L. Christodoulou, D.C. Nagle, and J.M. Brupbacher, "Process for Forming Metal-Second Phase Composites and Product Thereof," U.S. Patent No. 4,751,048 (1988).
- [4] D.M. Stefanescu, B.K. Dhindaw, S.A. Kacar, and A. Moitra, "Behavior of Ceramic Particles at Solid-Liquid Metal Interface in Metal Matrix Composites," *Met. Trans.*, **19A**; 2847 (1988).
- [5] S.N. Omenyi and A.W. Neumann, "Thermodynamic Aspects of Particle Engulfment by Solidifying Melts," *J. Appl. Phys.*, **47**(9), 3956 (1976).
- [6] J.W. McCoy and F.E. Wawner, "Dendritic Segregation in Particle-Reinforced Cast Aluminum Composites," Cast Reinforced Metal Composites, eds. S.G. Fishman and A.K. Dhingra, ASM Int., Metals Park, OH, p. 237 (1988).
- [7] Z. Hashin and S. Shtrikman, "A Variational Approach to the Theory of the Elastic Behavior of Multiphase Materials," *J. Mech. Phys.: Solids*, **11**(2); 127 (1963).
- [8] M. Taya and R.J. Arsenault, "A Comparison Between a Shear Lag Type Model and an Eshelby Type Model in Predicting the Mechanical Properties of a Short Fiber Composite," *Scripta Metall.*, **21**; 349 (1987).
- [9] W.J. Lackey, D.P. Stinton, G.A. Cerny, L.L. Fehrenbacher, and A.C. Schaffhauser, "Ceramic Coatings for Heat Engine Materials - Status and Future Needs," ORNL/TM-8959, Oak Ridge National Laboratory, Oak Ridge, TN (1983).
- [10] J.D. Eshelby, "Elastic Inclusions and Inhomogeneities," Progress in Solid Mechanics, vol. III, eds. Sneddon and Hill, p. 89 (1961).
- [11] G.C. Weatherly, "Loss of Coherency of Growing Particles by the Prismatic Punching of Dislocation Loops," *Philos. Mag.*, **17**; 791 (1968).
- [12] L.M. Brown, G.R. Woolhouse, and L.E. Valdré, *Philos. Mag.*, "Radiation-induced Coherency Loss in a Cu-Co Alloy," **17**; 781 (1968).
- [13] L.M. Brown and G.R. Woolhouse, "The Loss of Coherency of Precipitates and the Generation of Dislocations," *Philos. Mag.*, **21**; 329 (1970).
- [14] M.F. Ashby and L. Johnson, "On the Generation of Dislocations at Misfitting Particles in a Ductile Matrix," *Philos. Mag.*, **20**; 719 (1969).
- [15] G.C. Weatherly, " " *Met. Sci.*, **2**; 237 (1968).

- [16] M.F. Ashby, S.H. Gelles, and L.E. Tanner, "The Stress at which Dislocations are Generated at a Particle-Matrix Interface," *Philos. Mag.*, **19**; 757 (1969).
- [17] V.A. Philips, "Electron-Microscope Observation on Precipitation in a Cu-3.1 wt pct Co Alloy," *Trans. TMS-AIME*, **230**; 967 (1964).
- [18] R. Hill, The Mathematical Theory of Plasticity, Oxford Univ. Press, London, 1950.
- [19] A. Mendelson, Plasticity - Theory and Applications, p. 135, MacMillan, New York (1968).
- [20] C.A. Hoffman, *J. Eng. Mater. Tech.*, **95**; 55 (1973).
- [21] J.K. Lee, Y.Y. Earmme, H.I. Aaronson, and K.C. Russell, "Plastic Relaxation of the Transformation Strain Energy of a Misfitting Spherical Precipitate: Ideal Plastic Behavior," *Metall. Trans.*, **11A**; 1837 (1980).
- [22] J.W. Christian, The Theory of Transformations in Metals and Alloys - Part I, 2nd ed., p. 200, Pergamon Press, Oxford (1975).
- [23] Y.Y. Earmme, W. C. Johnson, and J.K. Lee, "Plastic Relaxation of the Transformation Strain Energy of a Misfitting Spherical Precipitate: Linear and Power-Law Strain Hardening," *Metall. Trans.*, **12A**; 1521 (1981).
- [24] C.T. Kim, J.K. Lee, and M.R. Plichta, "Plastic Relaxation of Thermoelastic Stress in Aluminum/Ceramic Composites," *Metall. Trans.*, **21A**; 673 (1990).
- [25] M. Taya and T. Mori, "Dislocations Punched-Out Around a Short Fiber in a Short Fiber Metal Matrix Composite Subjected to Uniform Temperature Change," *Acta Metall.*, **35**; 155 (1987).
- [26] I. Dutta, D.L. Bourell, and D. Latimer, "A Theoretical Investigation of Accelerated Aging in Metal-Matrix Composites," *J. Composite Mater.*, **22**; 829 (1988).
- [27] R.J. Arsenault and N. Shi, "Dislocation Generation Due to Differences Between the Coefficients of Thermal Expansion," *Mater. Sci. Eng.*, **81**; 175 (1986).
- [28] Y. Flom and R.J. Arsenault, "Deformation in Al-SiC Composites Due to Thermal Stresses," *Mater. Sci. Eng.*, **75**; 151 (1985).
- [29] M. Volgelsang, R.J. Arsenault, and R. M. Fisher, "An *In Situ* HVEM Study of Dislocation Generation at Al/SiC Interfaces in Metal Matrix Composites," *Metall. Trans.*, **17A**; 379 (1986).
- [30] T. Christman and S. Suresh, "Microstructural Development in an Aluminum Alloy-SiC Whisker Composite," *Acta Metall.*, **36**; 1691 (1988).
- [31] L.F. Mondolfo, Aluminum Alloys: Structure and Properties, Butterworth Co., London, pp. 497-505 (1976).
- [32] H.W.L. Phillips, Annotated Equilibrium Diagrams of Some Aluminum Alloy Systems, Institute of Metals, London, pp. 27-35 (1959).

- [33] C.R. Brooks, Heat Treatment, Structure, and Properties of Nonferrous Alloys, ASM, Metals Park, OH, pp. 121-137 (1982).
- [34] Y.A. Bagaryatsky, Zhur. Tech. Fiziki, **18**; 827 (1948).
- [35] K.H. Hardy, "The Ageing Characteristics of Some Ternary Aluminium-Copper-Magnesium Alloys with Copper: Magnesium Weight Ratios of 7:1 and 2.2:1," J. Inst. Metals, **83**; 17 (1954-55).
- [36] J.M. Silcock, "The Structural Aging Characteristics of Al-Cu-Mg Alloys with Copper Magnesium Weight Ratios of 7:1 and 2.2:1," J. Inst. Metals, **89**; 203 (1960-61).
- [37] A.A. Slekeyev, L.B. Ber, L.G. Klimovich, and O.S. Korobov, "On the Structure of the Zones in Alloy Al-Cu-Mg," Phys. Met. Metall, **46**(3); 80 (1979). {translated from Fiz. Metal. Metalloved., **46**(3); 548 (1978)}
- [38] Y. Gefen, M. Rosen, and A. Rosen, "Aging Phenomena in Duraluminum 2024 Studied by Resistometry and Hardness," Mater. Sci. Eng., **8**; 181 (1971).
- [39] M. Rosen, E. Horowitz, L. Swartzendruber, S. Fick, and R. Mehrabian, "The Aging Process in Aluminum Alloy 2024 Studied by Means of Eddy Currents," Mater. Sci. Eng., **53**; 191 (1982).
- [40] R.N. Wilson and P.G. Partridge, "The Nucleation and Growth of S' Precipitates in an Aluminum-2.5% Copper-1.2% Magnesium Alloy," Acta Metall., **13**; 1321 (1965).
- [41] G.C. Weatherly and R.B. Nicholson, "Loss of Coherency of Growing Particles by the Prismatic Punching of Dislocation Loops," Philos. Mag., **17**; 801 (1968).
- [42] L.K. Ives, L.J. Swartzendruber, W.J. Boettinger, M. Rosen, S.D. Ridder, F.S. Biancaniello, R.C. Reno, D.B. Ballard, and R. Mehrabian, "NBS: Processing/Microstructure/Property Relationships in 2024 Aluminum Alloy Plates," U.S. Dept. of Commerce, National Bureau of Standards, Technical Report NBSIR 83-2669 (1983).
- [43] D.L. Robinson and M.S. Hunter, "Interrelation of TEM Microstructure, Composition, Tensile Properties, and Corrosion Resistance of Al-Cu-Mg-Mn Alloys," Metall. Trans., **3**; 1147 (1972).
- [44] F. Cuisiat, P. Duval, and R. Graf, Scripta Metall., "Etude des Premiers Stades de Decomposition d'un Alliage Al-Cu-Mg," **18**; 1051 (1984).
- [45] J. Yan, L. Chunzhi, and Y. Minggao, "On the Crystal Structure of S' Phase in Al-Cu-Mg Alloy," J. Mater. Sci. Let., **9**; 421 (1990).
- [46] A.K. Gupta, P. Gaunt, and M.C. Chaturvedi, "The Crystallography and Morphology of the S'-Phase Precipitate in an Al(CuMg) Alloy," Philos. Mag. A, **55**; 375 (1987).

- [47] C.B. Zhang, W. Sun, and H.Q. Ye, "Investigation of the Crystallography and Morphology of the S' Precipitate in an Al(CuMg) Alloy by HREM," *Philos. Mag. Let.*, **59**; 265 (1989).
- [48] T.G. Nieh and R.F. Karlak, "Aging Characteristics of B₄C Reinforced 6061-Aluminum," *Scripta Metall.*, **18**; 25 (1984).
- [49] I. Dutta and D.L. Bourell, "A Theoretical and Experimental Study of Aluminum Alloy 6061-SiC Metal Matrix Composite to Identify the Operative Mechanism for Accelerated Aging," *Mater. Sci. Eng.*, **A112**; 67 (1989).
- [50] H.J. Rack, "Age Hardening Behavior of SiC Whisker Reinforced 6061 Aluminum," *Sixth Int. Conf. on Composite Materials*, eds. F.L. Matthews, N.C.R. Buskell, J.M. Hodgkinson, and J. Morton, Elsevier App. Sci., London, vol. 2, p. 382 (1987).
- [51] S. Suresh, T. Christman, and Y. Sugimura, "Accelerated Aging in Cast Al Alloy-SiC Particulate Composites," *Scripta Metall.*, **23**; 1599 (1989).
- [52] E. Hunt, P.D. Pitcher, and P.J. Gregson, "Precipitation Reaction in 8090 SiC Particulate Reinforced MMC," *Scripta Metall.*, **24**; 937 (1990).
- [53] T.G. Nieh, C.M. McNally, J. Wadsworth, D.L. Yaney, and P.S. Gilman, "Mechanical Properties of a SiC Reinforced Aluminum Composite Prepared by Mechanical Alloying," *Dispersion Strengthened Aluminum Alloys*, eds. Y.-W. Kim and W.M. Griffith, TMS, Warrendale, PA, p. 681 (1988).
- [54] J.M. Papazian, "Effects of SiC Whiskers and Particles on Precipitation in Aluminum Metal Matrix Composites," *Metall. Trans. A*, **19A**; 2945 (1988).
- [55] J.L. Petty-Galis and R.D. Goolsby, "Calorimetric Evaluation of the Effects of SiC Concentration on Precipitation Processes in SiC Particulate-Reinforced 7091 Aluminum," *J. Mater. Sci.*, **24**; 1439 (1989).
- [56] C.M. Friend, I. Horsfall, S.D. Luxton, and R.J. Young, "The Effect of Fibre/Matrix Interfaces on the Age-Hardening Characteristics of δ -Alumina Fibre Reinforced AA6061," *Cast Reinforced Metal Composites*, eds. S.G. Fishman and A. K. Dhingra, ASM Int., Metals Park, OH (1988).
- [57] N. Sen and D.R.F. West, "Some Factors Influencing S' Precipitation in Al-Cu-Mg and Al-Cu-Mg-Ag Alloys," *J. Inst. Metals*, **97**; 87 (1969).
- [58] *Aluminum: Properties and Physical Metallurgy*, ed. J.E. Hatch, pp. 188-191, ASM, Metals Park, OH (1984).
- [59] M.F. Ashby, "The Deformation of Plastically Non-homogeneous Materials," *Philos. Mag.*, **21**; 399 (1970).
- [60] A. Kelly, *Strong Solids*, Clarendon Press, Oxford, p. 123 (1966).

- [61] V.C. Nardone and K.M. Prewo, "On the Strength of Discontinuous Silicon Carbide Reinforced Aluminum Composites," *Scripta Metall.*, **20**; 43 (1986).
- [62] V.C. Nardone, "Assessment of Models Used to Predict the Strength of Discontinuous Silicon Carbide Reinforced Aluminum Alloys," *Scripta Metall.*, **21**; 1313 (1987).
- [63] P. Kelly, *Int. Metall. Rev.*, **18**; 31 (1973).
- [64] E.O. Hall, *Proc. Phys. Soc.*, **B64**; 747 (1951).
- [65] N.J. Petch, *J. Iron Steel Inst.*, **174**; 25 (1953).
- [66] J.D. Eshelby, F.C. Frank, and F.R.N. Nabarro, " , " *Philos. Mag.*, **42**; 351 (1951).
- [67] J.C.M. Li and Y.T. Chou, "The Role of Dislocation in the Flow Stress Grain Size Relationships," *Metall. Trans.*, **1**; 1145 (1970).
- [68] N. Hansen, "Polycrystalline Strengthening," *Metall. Trans.*, **16A**; 2167 (1985).
- [69] L. Anand and J. Gurland, "Effect of Internal Boundaries on the Yield Strengths of Spheroidized Steels," *Metall. Trans.*, **7A**; 191 (1976).
- [70] G. Wassermann, " , " 2nd International Conference on the Strength of Metals and Alloys, ASM, Metals Park, OH, p. 1188 (1970).
- [71] P.D. Funkenbusch and T.H. Courtney, "Microstructural Strengthening in Cold Worked In Situ Cu-14.8 vol% Fe Composites," *Scripta Metall.*, **15**; 1349 (1981).
- [72] W.A. Spitzig, A.R. Pelton, and F.C. Laabs, "Characterization of the Strength and Microstructure of Heavily Cold Worked Cu-Nb Composites," *Acta Metall.*, **35**; 2427 (1987).
- [73] E. Hornbogen and G. Staniek, "Grain-Size Dependence of the Mechanical Properties of an Age-Hardening Fe-1%Cu-Alloy," *J. Mater. Sci.*, **9**; 879 (1974).
- [74] S.V. Kamat, J.P. Hirth, and R. Mehrabian, "Mechanical Properties of Particulate-Reinforced Aluminum-Matrix Composites," *Acta Metall.*, **37**; 2395 (1989).
- [75] J.W. Martin, Micromechanisms in Particle-Hardened Alloys, pp. 41-44, Cambridge Univ. Press, London (1980).
- [76] U.F. Kocks, "A Statistical Theory of Flow Stress and Work-Hardening," *Philos. Mag.*, **13**; 541 (1966).
- [77] E.E. Underwood, Quantitative Stereology, Addison-Wesley, Reading MA (1970).
- [78] D.F. Haddon and C.R. Crowe, "Fracture Toughness of SiC/Al Metal Matrix Composites," Strength Met. Alloys, Proc. Int. Conf., 7th, ed. H.J. McQueen, Pergamon Press, Oxford, p. 1515 (1985).
- [79] D. L McDaniels, "Analysis of Stress-Strain, Fracture, and Ductility Behavior of Aluminum Matrix Composites Containing Discontinuous Silicon Carbide Reinforcement," *Metall. Trans.*, **16A**; 1105 (1985).

- [80] W.A. Logsdon and P.K. Liaw, "Tensile Fracture Toughness and Fatigue Crack Growth Rate Properties of Silicon Carbide Whisker and Particulate Reinforced Aluminum Metal Matrix Composites," *Eng. Fract. Mechanics*, **24**; 737 (1986).
- [81] D.L. Davidson, "Fracture Characteristics of Al-4 Pct Mg Mechanically Alloyed with SiC," *Metall. Trans.*, **18A**; 2115 (1987).
- [81] J.J. Lewandowski, C. Liu, and W.H. Hunt, Jr., "Microstructural Effects on the Fracture Micromechanisms in 7XXX Al P/M-SiC Particulate Metal Matrix Composites," Processing and Properties for Powder Metallurgy Composites, eds. P. Kumar, K. Vedula and A. Ritter, The Metallurgical Society, Warrendale, PA, p. 117 (1988).
- [82] D.L. Davidson, "Fracture Surface Roughness as a Gauge of Fracture Toughness: Aluminum-Particulate SiC Composites," *J. Mater. Sci.*, **24**; 681 (1989).
- [83] J.J. Lewandowski, C. Liu, and W.H. Hunt, Jr., "Effects of Matrix Microstructure and Particle Distribution on Fracture of an Aluminum Metal Matrix Composite," *Mater. Sci. Eng.*, **A107**; 241 (1989).
- [84] Y. Flom and R.J. Arsenault, "Effect of Particle Size on Fracture Toughness of SiC/Al Composite Material," *Acta Metall.*, **37**; 2413 (1989).
- [85] ASTM Annual Book of Standards, Am. Soc. Test. Mater. (1987).
- [86] T. Christman and S. Suresh, "Effects of SiC Reinforcement and Aging Treatment on Fatigue Crack Growth in an Al-SiC Composite," *Mater. Sci. Eng. A*, **102**; 211 (1988).
- [87] J.K. Shang, W. Yu, and R.O. Ritchie, "Role of Silicon Carbide Particles in Fatigue Crack Growth in SiC-particulate-reinforced Aluminum Alloy Composites," *Mater. Sci. Eng. A*, **102**; 181 (1988).
- [88] J.K. Shang and R.O. Ritchie, "Crack Bridging by Uncracked Ligaments during Fatigue-Crack Growth in SiC-Reinforced Aluminum-Alloy Composites," *Metall. Trans.*, **20A**; 897 (1989).
- [89] J.K. Shang and R.O. Ritchie, "On the Particle-Size Dependence of Fatigue-Crack Propagation Thresholds in SiC-Particulate-Reinforced Aluminum-Alloy Composites: Role of Crack Closure and Crack Trapping," *Acta Metall.*, **37**; 2267 (1989).
- [90] D.L. Davidson, "Micromechanisms of Fatigue Crack Growth and Fracture Toughness in Metal Matrix Composites," Report 1989; Avail. from NTIS, Gov. Rep. Announce Index **89**(11), Abstr. No 930,253 (1989).
- [91] M.B. Cortie and G.G. Garrett, "On the Correlation Between the C and m in The Paris Equation for Fatigue Crack Propagation," *Eng. Fract. Mech.*, **30**; 49 (1988).

Report Documentation Page

1. Report No. NASA CR-4365		2. Government Accession No.		3. Recipient's Catalog No.	
4. Title and Subtitle The Mechanisms of Dispersion Strengthening and Fracture in Al-Based XD TM Alloys				5. Report Date May 1991	
				6. Performing Organization Code	
7. Author(s) R. M. Aikin, Jr.				8. Performing Organization Report No. MML TR 90-63c	
				10. Work Unit No. 505-63-50-02	
9. Performing Organization Name and Address Martin Marietta Laboratories 1450 South Rolling Road Baltimore, Maryland 21227				11. Contract or Grant No. NAS1-18531	
				13. Type of Report and Period Covered Contractor Report	
12. Sponsoring Agency Name and Address National Aeronautics and Space Administration Langley Research Center Hampton, VA 23665-5225				14. Sponsoring Agency Code	
15. Supplementary Notes Langley Technical Monitor: William D. Brewer Final Report - Part I					
16. Abstract The influence of reinforcement size, volume fraction, and matrix deformation behavior on room and elevated temperature strength; the fracture toughness; and the fatigue crack growth rate of metal matrix composites of Al-4%Cu-1.5%Mg with TiB ₂ have been examined. The influence of reinforcement volume fraction has also been examined for pure aluminum with TiB ₂ . Inter-particle spacing appears to be the factor that controls the strength of these alloys, with the exact nature of the dependence relying on the nature of dislocation slip in the matrix (planar versus diffuse). The isothermal aging response of the precipitation strengthened Al-4%Cu-1.5%Mg alloys was not accelerated by the presence of TiB ₂ . Cold work prior to artificial aging created additional geometrically necessary dislocations which served as heterogeneous nucleation sites leading to accelerated aging, a finer precipitate size, and an increase in the strength of the alloy.					
17. Key Words (Suggested by Author(s)) Metal Matrix Composites				18. Distribution Statement Unclassified - Unlimited Subject Category 26	
19. Security Classif. (of this report) Unclassified		20. Security Classif. (of this page) Unclassified		21. No. of pages 154	
				22. Price A08	

National Aeronautics and
Space Administration
Code NTT

Washington, D.C.
20546-0001

Official Business
Penalty for Private Use, \$300

NASA

National Aeronautics and
Space Administration

Washington, D.C.
20546

**SPECIAL FOURTH CLASS MAIL
BOOK**

Postage and Fees Paid
National Aeronautics and
Space Administration
NASA-451

Official Business
Penalty for Private Use \$300



L1 001 CR-4365 910502S090569A

NASA

SCIEN & TECH INFO FACILITY

ACCESSIONING DEPT

P O BOX 8757 BWI ARPRT

BALTIMORE MD 21240

NASA

POSTMASTER: If Undeliverable (Section 158
Postal Manual) Do Not Return